

**Chemical and Dynamical Processes in the
Atmospheres of
I. Ancient and Present-Day Earth
II. Jupiter and Galilean Satellites
III. Extrasolar “Hot Jupiters”**

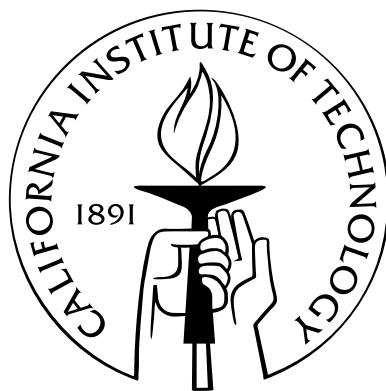
Thesis by

Mao-Chang Liang

In Partial Fulfillment of the Requirements

for the Degree of

Doctor of Philosophy



California Institute of Technology

Pasadena, California

2006

(Defended Nov 7, 2005)

© 2006

Mao-Chang Liang

All Rights Reserved

Acknowledgements

I would like to thank my family for not stopping me from doing academic research; they completely supported my decision. (In Chinese culture, children's plans are mostly under their parents' control.) I would also like to acknowledge my master's thesis advisor, Professor Fred Lo, for teaching me how to be a good scientist and researcher. The major thing I learned from him is that, to be a good scientist, one has to remember that theory and experiments are equally important. For working on theory, one has to think of what experiments can support your theory; for experimentalists, to interpret the results requires a deep understanding of the background physics or theory. This clearly is seen from my Ph.D. advisors, Professors Yuk Yung and Geoff Blake, who work closely with theorists and experimentalists. Their great help in launching my research career has been invaluable. I would then want to thank my girlfriend, Bows Chiou, and colleagues Mark Allen, Mimi Gerstell, Xun Jiang, Anthony Lee, Chris Parkinson, Run-Lie Shia, and many others for their insightful comments/discussion on my research. Financial support from National Aeronautics and Space Administration (NASA) and National Science Foundation (NSF) are acknowledged.

Abstract

When exposed to stellar UV radiation, chemical processes will be governed not only by temperature/pressure but also the spectrum of the incoming dissociative photon flux; the system will approach kinetic, or photochemical, equilibrium, instead of thermochemical equilibrium. Over the previous decades, photochemistry has proven to be a powerful tool for predicting the chemical composition in the atmospheres of solar planets and their satellites. For example, the ozone layer in our own atmosphere (stratosphere) is a photochemical product of oxygen. In this thesis, I apply a photochemical model to the study of a variety of astronomical objects: the Earth, Jupiter, the Galilean satellite Callisto, and extrasolar “hot Jupiters” (HD 209458b). For the Earth, a method for utilizing the isotopic composition of CO₂ and N₂O to monitor global changes due to these two greenhouse gases is developed. For objects other than the Earth, the model facilitates in the interpretation of data acquired by remote (telescopic) and *in situ* (spacecraft) measurements. The ultimate goal is to understand the conditions of chemical and physical environments in protoplanetary nebulae, which will provide clues as to the formation of planetary systems; the synthesis of organic compounds which could lead to the appearance of life; and the evolution of planetary atmospheres such as the formation of Titan’s nitrogen-rich atmosphere.

Contents

Acknowledgements	iii
Abstract	iv
1 Introduction	1
2 An Overview of Kinetic Models	8
2.1 Chemical Reactions	9
2.2 Caltech/JPL Multi-Dimensional Kinetics Models	10
2.2.1 One-Dimensional Model	11
2.2.2 Two-Dimensional Model	14
2.2.3 Modified Two-Dimensional Model	16
I Ancient and Present-Day Earth	22
3 A Semianalytic Model for Photo-Induced Isotopic Fractionation in Simple Molecules	23
3.1 Introduction	24
3.2 Method	26

3.2.1	The Reflection Principle	26
3.2.2	Analytic Solution for Diatomic Molecules	27
3.2.3	Triatomic Molecules	33
3.2.4	Temperature Dependence	36
3.3	Applications	37
3.3.1	Diatomic Molecules: HCl and HI	37
3.3.2	Linear Triatomic Molecule: N ₂ O	41
3.3.3	Nonlinear Triatomic Molecule: O ₃	42
3.4	Applications to the Atmosphere	43
3.5	Conclusion	45
4	Isotopic Composition of Stratospheric Ozone	68
4.1	Introduction	69
4.2	Atmospheric Models	73
4.2.1	One-Dimensional Model	73
4.2.2	Ozone Formation	75
4.2.3	Ozone Photolysis	77
4.3	Results	79
4.3.1	Vertical Profiles	79
4.3.2	Three-Isotope Plots	81
4.4	Conclusion	82
5	Oxygen Isotopic Composition of Carbon Dioxide in the Middle At-	
	mosphere	105

5.1	Introduction	106
5.2	Exchange Reactions between O(¹ D) and CO ₂	108
5.3	Sources of O(¹ D)	110
5.4	One-Dimensional Model	111
5.5	Three-Box Model	112
6	Production of Oxidants in the Atmosphere of a Snowball Earth	120
6.1	Introduction	121
6.2	Hypothesis	123
6.3	Atmospheric Chemical Processes	123
6.4	Biological Implications	125
II	Jupiter and the Galilean Satellites	134
7	Meridional Transport in the Stratosphere of Jupiter	135
7.1	Introduction	136
7.2	Two-Dimensional Transport Model	137
7.3	Simulation Results	139
7.4	Conclusion	142
8	Atmosphere of Callisto	151
8.1	Introduction	152
8.2	Model Description	154
8.3	General Results	156

8.3.1	Electron Density and Hydrogen Abundance	156
8.3.2	Carbon Dioxide and Carbon Monoxide	158
8.3.3	Atomic Carbon and Atomic Oxygen	159
8.4	Discussion	160
8.5	Summary	163
 III Extrasolar “Hot Jupiters”		180
 9 Source of Atomic Hydrogen in the Atmosphere of HD 209458b		181
9.1	Introduction	182
9.2	Model	183
9.3	Results	185
9.3.1	OH and O Radicals	185
9.3.2	CO ₂ and CH ₄	186
9.3.3	H and H ₂ O	188
9.4	Conclusion	189
 10 On the Insignificance of Photochemical Hydrocarbon Aerosols in the Atmospheres of Close-in Extrasolar Giant Planets		198
10.1	Introduction	199
10.2	Model	201
10.3	Results	203
10.4	Discussion	205

List of Figures

- 3.1 Photolysis Model—Schematic diagram of the direct photodissociation process, illustrating the Born-Oppenheimer approximation and the Reflection Principle (dashed lines). “L” and “H” refer to the standard and isotopically substituted species, respectively. Ψ_0 , V_g , and V_e denote the vibrationally averaged ground state wavefunction, ground state electronic potential, and dissociating electronic potential, respectively. . . . 55
- 3.2 Photolysis Model—Schematic diagram illustrating the steps in the application of the photodissociation model, described in section 3.2. The vertical axis refers to the physical quantity in the upper-left corner in each panel; the horizontal axis denotes the photon frequency ν . “L” and “H” denote the standard and isotopically substituted species, respectively. The full procedure is divided into five steps: (a)-(e). See text for details. 56

- 3.3 Photolysis Model—Applications of the new photodissociation algorithm to the diatomic molecules HCl/DCl and HI/DI. The first three panels present the decomposition of the individual cross sections into their isotope-dependent (G) and isotope-independent (γ) components. The bottom two panels present various fits to the D/H fractionation factor(s). The dissociation cross sections in Figures 3.3a and 3.3f have been divided by the maximum cross sections of the standard species HCl and HI, with $\sigma_P = 3.4 \times 10^{-18} \text{ cm}^2$ and $\sigma_P = 8.2 \times 10^{-18} \text{ cm}^2$, respectively. The various model fits in Figures 3.3d and 3.3i denote the state decomposition from the spin-orbit coupling of Cl and I. The final fits incorporating γ are given in Figures 3.3e and 3.3j. 57
- 3.4 Photolysis Model— a: The $^{14}\text{N}^{14}\text{N}^{16}\text{O}$ photodissociation cross section, measured by *Yoshino et al.* [1984] at 295 K, and normalized to the peak $\sigma_P = 1.4 \times 10^{-18} \text{ cm}^2$. The gaussian fit is shown by the dotted line. b: The form of γ for N_2O . A fourth-order polynomial fit is shown by the dotted line, which has a functionality similar to the HCl and HI systems (see Figures 3.3c and 3.3h). 58
- 3.5 Photolysis Model—Comparison of the predicted ϵ using our new algorithm to YM97’s ZPE model, Johnson et al.’s *ab initio* calculation, and laboratory measurements (with $2\text{-}\sigma$ error bar overplotted) for four N_2O isotopologues/isotopomers. The solid curve depicts the temperature-independent model described in section 3.2.4. 59

3.6	Photolysis Model—Comparison of the temperature dependence of ϵ using the three state temperature-dependent model (section 3.2.4) to Johnson et al.'s <i>ab initio</i> calculation for N ₂ O isotopologues/isotopomers at 295 and 233 K.	60
3.7	Photolysis Model— a: The dissociation cross sections of ¹⁶ O ¹⁶ O ¹⁶ O and ¹⁸ O ¹⁸ O ¹⁸ O as measured by <i>Parisse et al.</i> [1996], at 295 K and normalized to $\sigma_P = 1.2 \times 10^{-17}$ cm ² . The decomposed γ is shown in panel b. . . .	61
3.8	Photolysis Model—Comparison of the predicted ϵ to the YM97's ZPE model and laboratory measurements [<i>Parisse et al.</i> , 1996] for O ₃ isotopologues and isotopomers.	62
3.9	Photolysis Model—Applications of the predicted fractionations of the dissociation cross sections of nitrous oxide's isotopologues/isotopomers in the Earth's lower and upper stratosphere. $\ln(f) = -0.6$ was used to delineate the boundary, where f is the ratio of the remaining N ₂ O to that of the initial N ₂ O in the upwelling air parcel. White bar: Atmospheric measurements, with 1- σ error bars overplotted. Light gray bar: This work. Dark gray bar: Johnson et al.'s <i>ab initio</i> calculations. Black bar: The ZPE model of YM97.	63
4.1	Ozone—Profiles of temperature (solid line) and eddy diffusion coefficient (dashed line) used in the calculation. These two profiles are taken from <i>Allen et al.</i> [1981]. Dotted line represents a temperature profile equal to the solid line reduced by 8%.	93

4.2	Ozone—Profile of rate coefficient k_{83} , which is used to account for the net loss of ozone by catalysis in the stratosphere. See text and Table 4.1 for details.	94
4.3	Ozone—Calculated ozone formation and oxygen exchange rate coefficients (solid lines). Null fractionation is shown by dotted lines for reference. The filled circles are laboratory measurements of <i>Mauersberger et al.</i> [1999] and <i>Janssen et al.</i> [1999]. The open circles are from the calculation by <i>Gao and Marcus</i> [2002].	95
4.4	Ozone—Enrichments resulting from the formation processes. Filled symbols are laboratory measurements: circles were measured by <i>Morton et al.</i> [1990], and triangles by <i>Mauersberger et al.</i> [1999]. The open circles were calculated by <i>Gao and Marcus</i> [2002].	96
4.5	Ozone—Fractionation factors calculated using the MZPE model in the Hartley band at 195 (dashed lines) and 295 K (solid lines). Results calculated using the <i>Yung and Miller</i> [1997] model are shown by dotted lines. The fractionation factor is defined by $1000 \times (\sigma/\sigma_0 - 1)$, where σ_0 and σ are the photoabsorption cross sections of normal and isotopically substituted molecules, respectively.	97
4.6	Ozone—Fractionation factors calculated using the MZPE model in the Chappuis band at 295 K (solid lines). Results calculated using the <i>Yung and Miller</i> [1997] model are shown by dotted lines.	98

- 4.7 Ozone—Enrichments for the species indicated in the upper-left corner of each panel. Enrichments calculated using the formation and photolysis models are shown by solid and dashed lines, respectively. The dotted lines are the laboratory measurements [*Morton et al.*, 1990]. 99
- 4.8 Ozone—Total enrichments calculated by integrating the formation and photolysis models. The error bars in the atmospheric measurements are for 1- σ . The diamonds are mass-spectroscopic measurements [*Krankowsky et al.*, 2000; *Mauersberger et al.*, 2001; *Lämmerzahl et al.*, 2002], and asterisks are FTIR measurements by *Irion et al.* [1996] 100
- 4.9 Ozone—Three-isotope plot of ozone in the regions between 20 and 35 km. Diamonds are balloon-borne mass spectrometer measurements [*Krankowsky et al.*, 2000; *Mauersberger et al.*, 2001; *Lämmerzahl et al.*, 2002]. The solid and dashed lines are the calculated formation- and photolysis-induced enrichments, respectively. The dotted line is the laboratory measurements [*Morton et al.*, 1990]. 101
- 4.10 Ozone—Three-isotope plot of ozone in the regions between 20 and 35 km, using the temperature profile shown by dotted line in Figure 4.1. Dotted line shows the profiles obtained using the reference temperature profile. One- σ error bars are overplotted. 102

- 5.1 Carbon Dioxide—Three-isotope plot of oxygen in CO₂, from which the tropospheric values have been subtracted. The atmospheric measurements are from *Lämmerzahl et al.* [2002] (circles) and from *Thiemens et al.* [1995] (asterisks). The solid line depicts the model, and the change in slope at A corresponds to altitudes of ~60-80 km. At higher altitudes (and for fractionations greater than these fiducial values), the slope $m(\text{A-B})$ is ~0.3 – as expected from oxygen photolysis. Another change of slope in the calculation occurs at B for altitudes of ~90 km and higher. Over this range, molecular diffusion dominates, and the slope becomes mass dependent, that is ~0.5 (dash-dotted line). Inset: vertical profiles of $\delta^{18}\text{O}(\text{CO}_2)$. The dotted line represents the results excluding the fractionation of O(¹D) from O₂ photolysis over the solar Lyman- α emission. 117
- 5.2 Carbon Dioxide—A three-box mixing model for CO₂ in the middle atmosphere. The solid line represents the mixing of boxes 1 (troposphere) and 2 (stratosphere) only, while the symbols denote additional mixing with box 3 to varying extent. Squares: no mixing with box 3. Triangles: 0.05% of air from box 3. Diamonds: 0.1% of air from box 3. The two arrows indicate the direction in which the fractionation changes as the age of the air is increased. 118

- 5.3 Carbon Dioxide—The notation and symbols are the same as those in Figures 5.1 and 5.2. The solid line illustrates the fractionation expected from the interaction of CO₂ and O₃ only, while the dotted line presents an example of how the three isotope slope can be flattened by the mixing of air from boxes 2 (stratosphere) and 3 (mesosphere). 119
- 6.1 Snowball—Profiles of H₂O (dotted), H₂O₂ (solid), O₃ (dashed), O₂ (dash-dotted), H₂ (triple dot-dashed), CO (thin long-dashed), and CO₂ (thick long-dashed) calculated with the reference model, in which the surface temperature is 240 K, temperature gradient is -10 K km⁻¹, and constant temperature is 150 K above the tropopause (~10 km). The downward and escape fluxes of H₂O₂ and H₂ are ~5×10⁸ and 10¹⁰ cm⁻² s⁻¹, respectively. The mixing ratio of H₂O above the tropopause is set equal to that at the tropopause. 132
- 6.2 Snowball—Sensitivity of surface H₂ abundance on the deposition rate of H₂O₂ by diffusion. The abundance of O₂ as high as that in Figure 6.1 is maintained by CO₂ photolysis. Horizontal dotted line denotes the rate inferred by Kalahari Mn Field [*Kirschvink et al.*, 2000]; four billion tons of Mn were found over an area of 10⁶⁻⁷ km², which corresponds to an average deposition rate of ~3×10⁸ cm⁻² s⁻¹ in 100 Myr. 133

- 7.1 Jupiter—Relative abundances of C_2H_2 (upper) and C_2H_6 (lower) at 5 mbar as a function of latitude. Asterisks are the Cassini measurements [Kunde *et al.*, 2004]. Diamonds and circles are, respectively, high-latitude Cassini measurements that do include (diamonds) and do not include (circles) auroral longitudes. The calculated abundances of C_2H_2 and C_2H_6 are normalized to those at the equator. Solid line represents model results with the reference K_{yy} : constant $2 \times 10^{10} \text{ cm}^2 \text{ s}^{-1}$ below the 5 mbar altitude level and $2 \times 10^9 \text{ cm}^2 \text{ s}^{-1}$ above (model B). Dotted line represents the cosine function of latitude. 147
- 7.2 Jupiter—Timescales for the chemical loss of C_2H_2 (solid lines) and C_2H_6 (dashed lines) and for vertical transport (dotted line). The vertical transport timescale is defined by H^2/K_{zz} , where K_{zz} and H are the vertical diffusion coefficients of CH_4 and atmospheric scale height, respectively; values of time constants are derived from our reference model. Thick and thin lines represent values at latitudes 10° and 70° , respectively. The horizontal arrow indicates the 5 mbar level where the peak in the contribution function for the Cassini measurements of C_2H_2 and C_2H_6 lies. The vertical long-dashed line is a meridional mixing time equal to R_J^2/K_{yy} , where R_J is the radius of Jupiter and $K_{yy} = 2 \times 10^{10} \text{ cm}^2 \text{ s}^{-1}$. The shaded area shows the photochemical production region for the hydrocarbons. 148

7.3	Jupiter—2-D volume mixing ratio profiles of C_2H_2 (left) and C_2H_6 (right) calculated with the reference K_{yy} (model B).	149
8.1	Callisto—Vertical profiles of oxides: O_2 (solid line), O (dotted line), CO_2 (dashed line), and CO (dash-dotted line).	171
8.2	Callisto—Vertical profiles of H_2O (solid line), OH (dotted line), H_2 (dashed line), and H (dash-dotted line).	172
8.3	Callisto—Vertical profiles of total photoabsorption rates for O_2 (solid line), H_2O (dotted line), CO_2 (dashed line), and CO (dash-dotted line).	173
8.4	Callisto—Vertical profiles of total electron density (dark solid line), O_2^+ (dashed line), H_2O^+ (dotted line), CO_2^+ (dash-dotted line), and O^+ (long-dashed line) in our reference model (enhanced surface chemical reactions). A model with no chemical reactions enhanced on the surface is shown for comparison (light solid line). Triangles are Galileo spacecraft flyby experiments. The reported error bars are overplotted.	174
8.5	Callisto—Callisto’s surface shows abundant evidence for mass wasting of a dark mantling material. Pits (at A) suggest ground collapse due to loss of subsurface volatiles. A 4 km wide landslide deposit (at B) attests to the mobility of the dark material. Bright crater walls and local topographic highs are probably exposures of water frost cold trapped on relatively bright “bedice” which is believed to underlie the dark mantle. (Galileo Solid State Imager observation C9CSCRATER01, image s0401505526; resolution 160 m/pixel.)	175

8.6	Callisto—Profiles of H ₂ O diffusive flux as a function of temperature for temperature gradient of 200 K cm ⁻¹ . The two dotted lines represents maximum H ₂ O diffusion rates (horizontal line) and the required surface temperature of 150 K (vertical line).	176
9.1	HD 209458b—Vertical profile of temperature (solid line), total density (dashed line), and initial constituent number densities (H ₂ O: dotted line, CO: dash-dot line, CH ₄ : dash-dot-dot line).	194
9.2	HD 209458b—Comparison of mixing ratios of OH (solid line) and O (dotted line) radicals in models A, B, and C.	195
9.3	HD 209458b—Comparison of mixing ratios of H (solid line), CH ₄ (dotted line), H ₂ O (dashed line), CO (dash-dot line), and CO ₂ (dash-dot-dot line) in models A, B, and C.	196
9.4	HD 209458b—Production rate of H (dark lines) and photolysis rate of H ₂ O (gray lines) in models A, B, and C.	197
10.1	HD 209458b—Vertical temperature profiles of the reference model (solid line), <i>Barman et al.</i> [2002, dashed line], <i>Fortney et al.</i> [2003, dash-dotted], and Jupiter (dotted line). We assume the profiles of <i>Barman et al.</i> [2002] and <i>Fortney et al.</i> [2003] are isothermal above their reported pressure levels.	213
10.2	HD 209458b—Major photochemical pathways for forming C and C ₂ species.	214

10.3	HD 209458b—Comparison of volume mixing ratios of C_2H_2 (upper panel), C_2H_4 (middle panel), and C_2H_6 (lower panel) for models A, D, E, and Jupiter (solid, dashed, dash-dotted, and dotted lines, respectively). The high C_2H_2 mixing ratio at the top of the atmosphere is due to the high photolysis rate of CO.	215
------	--	-----

List of Tables

3.1	Photolysis Model—Vibrational Frequencies for HCl, HI, N ₂ O, and O ₃	64
3.2	Photolysis Model—Parameters Obtained from Gaussian Fitting	65
3.3	Photolysis Model—Parameters for HCl and HI at Two Dissociation Channels	66
3.4	Photolysis Model—Parameters for Decomposed Cross Section and <i>f</i> Factor of N ₂ O	67
4.1	Ozone—List of Chemical Reactions	103
4.1	Ozone—List of Chemical Reactions	104
7.1	Summary of Model Results	150
8.1	Callisto—Lists of Major Reactions	177
8.1	Callisto—Lists of Major Reactions	178
8.2	Callisto—Abundances of C, O, CO, H, and H ₂	179
10.1	HD 209458b—Initial Chemical Abundances of CH ₄ , CO, and H ₂ O for Models A-E.	216

10.2	HD 209458b—Mixing Ratios of CH ₄ , C ₂ H ₂ , C ₂ H ₄ , and C ₂ H ₆ for Models A-E at 0.1 mbar. Jupiter’s Results at 2 μbar are Included for Comparison.	217
------	--	-----

Chapter 1

Introduction

Research from the previous several decades shows photochemistry to be a powerful and unique tool for explaining/predicting the chemical composition in the atmospheres of planets and their satellites. One famous example is the ozone layer in our atmosphere. Ozone is produced via the Chapman reaction; atomic oxygen generated by the photolysis of molecular oxygen can react with molecular oxygen and a third molecule (primarily molecular nitrogen and oxygen) to form ozone. The process is governed by local photochemistry, and the concentration of ozone is determined by the density of oxygen and the number of available dissociative photons. In biology, photochemistry is also crucial for providing energy to life on the surface, including ourselves, because (micro-)organisms cannot extract energy from a system that is in “thermal” equilibrium.

This thesis is composed of three parts, in the sequence of objects nearby to objects outside our solar system. In part one, I present topics on Earth Science (§3-6), mainly in atmospheric regions above the tropopause. In the second part, chemical and dynamical processes in the atmospheres of the outer planets and their satellites are discussed (§7-8). Finally, distant objects outside the solar system (§9-10), close-in extrasolar giant planets, or so-called “hot Jupiters,” are examined.

To provide a context for this work, I briefly introduce the tool I adopt in this thesis, which is California Institute of Technology/Jet Propulsion Laboratory KINETICS model (Caltech/JPL) in §2, before turning to the science in chapters 3-10.

On the Earth, isotopic composition of trace molecules is a useful tool for quantifying biogeochemical cycles. Here, two examples are presented: the N_2O and CO_2

biogeochemical cycles. Measurements of the $^{15}\text{N}/^{14}\text{N}$ and $^{18}\text{O}/^{16}\text{O}$ ratios in N_2O from two major tropospheric sources, tropical rain forest soils and fertilized soils, show that ^{15}N and ^{18}O are depleted relative to the mean tropospheric N_2O . This implies sources of heavy N_2O , enriched in ^{15}N and ^{18}O , must be present to balance the light N_2O from soils. One such source is the back flux of N_2O from the stratosphere, which is enriched in heavy N_2O , which is discussed in Chapter 3. However, these returned fluxes of heavy N_2O are so large that a large oceanic N_2O flux is needed to balance the heavy stratospheric N_2O . Similarly, $^{13}\text{C}/^{12}\text{C}$ and $^{18}\text{O}/^{16}\text{O}$ in CO_2 have been used to quantify the uptake fluxes of CO_2 between the ocean and land and to estimate the terrestrial gross primary production (GPP) in the photosynthesis by plants, respectively. Like N_2O , back fluxes of CO_2 from the stratosphere, also enriched in heavy isotopologues, are possible tools for quantifying the biogeochemical cycles involving CO_2 . This stratospheric “signature” has been proposed for estimating the gross carbon flux from the surface.

Chapter 3 presents a method to predict the isotopic fractionation in simple molecules under the influence of UV radiation. The model is based on the Born-Oppenheimer approximation and the Reflection Principle. It has the main advantage of using commonly available input data, namely the photolysis cross sections for the standard isotopologue/isotopomer and the ground state isotope-specific spectroscopic constants. This new approach is demonstrated with applications to the diatomic molecules HCl and HI and the triatomic molecules N_2O and O_3 .

Chapter 4 presents a kinetic calculation for the isotopic composition of stratospheric

ozone; this chapter is a critical first step to an understanding of the isotopic composition of oxygen in CO₂, which is demonstrated in the following chapter. The calculated enrichments of ⁴⁹O₃ and ⁵⁰O₃ are in agreement with atmospheric measurements made at mid-latitudes. The overall magnitude of the ozone enrichments (~10%) is large compared with that commonly known in atmospheric chemistry and geochemistry. The heavy oxygen atom that results from ozone photolysis is therefore useful as a tracer of chemical species and pathways that involve ozone or its derived products. For example, the mass anomalies of oxygen in two greenhouse gases, CO₂ and N₂O, are likely the consequences of the transfer of heavy oxygen atoms from ozone.

The isotopic composition of long-lived trace gases provides a window into atmospheric transport and chemistry. Carbon dioxide is a particularly powerful tracer, because its abundance remains >100 ppmv in the mesosphere. Chapter 5 therefore presents a study of the isotopic composition of CO₂ in the middle atmosphere. We find that the heavy oxygen atom exchange between O₃ and CO₂, through the reaction $^{18}\text{O}(^1\text{D}) + \text{C}^{16}\text{O}^{16}\text{O} \rightarrow ^{16}\text{O} + \text{C}^{16}\text{O}^{18}\text{O}$, can explain the observations made above ~20 km. In the stratosphere, O₃ photolysis is the major source of O(¹D). In the mesosphere, we discover that O₂ photolysis over the solar Lyman- α line is a source of heavy O(¹D) more important than O₃. Incorporating these two O(¹D) sources into stratospheric and mesospheric chemical transport models, we quantitatively predict the unusual enhancements of ¹⁷O and ¹⁸O in CO₂ from the middle atmosphere. One application of this “anomalous” oxygen signature in CO₂ is to study biogeochemical cycles, in particular to constrain the gross carbon fluxes between the atmosphere and

terrestrial biosphere.

I next undertake a study of the photochemical processes in the ancient Earth atmosphere, about 2.4 billion years (Gyr) ago. Chapter 6 has potentially significant implications for the origin of oxygen photosynthesis. One of the major mysteries in the history of life is the origin of the enzymatic systems that protect cells from the oxidative damage of molecular oxygen. Protection from such oxidative damage is necessary before oxygenic photosynthesis could evolve, but oxygenic photosynthesis is virtually the only source of this oxidant. The chicken-and-egg nature of this problem was recognized in 1977 by Bill Schopf at UCLA, who noted that without oxygen-mediating enzymes, the first photosynthetic cell to release O_2 would kill itself. We show that glacial conditions in an anaerobic atmosphere can lead to the sequestration of large quantities of hydrogen peroxide in glacial ice. It has also been proposed that H_2O_2 played a crucial role in the origin and evolution of oxygenic photosynthesis, since it is capable of being both a powerful oxidant and a reductant. The transformation of H_2O_2 to O_2 is fully within the oxidative capabilities of reaction centers within existing anoxygenic photosynthetic bacteria. The existence of the Pongola glaciation ~ 2.9 Gyr ago, and perhaps unrecognized earlier glacial episodes, argue that oxygen would also have been available to drive the evolution of enzymatic tolerance long before the appearance of the first (clear evidence) oxygen-producing phototrophs ~ 2.4 Gyr ago.

In Part II, I focus on a discussion of the chemical and dynamical processes in the atmospheres of Jupiter and Callisto (one of Galilean satellites). Chapter 7 is based on the Cassini (a spacecraft mission to Saturnian system) measurements of

latitude dependence of two hydrocarbons, C_2H_2 and C_2H_6 , to quantify the meridional transport in the stratosphere of Jupiter. A two-dimensional photochemical calculation coupled with mass transport due to vertical and meridional mixing is performed. In general, this model study suggests that the meridional transport timescale above a transitional altitude between 5 and 10 mbar is >1000 years and the timescale could be as short as 10 years below the 10 mbar level. The long meridional transport time derived in the regions above the 5 mbar level is inconsistent, by 2 orders of magnitude, with that obtained from the spreading of gaseous molecules deposited after the impact of the Shoemaker-Levy 9 comet.

In Chapter 8, I discuss the Galileo (a spacecraft mission to Jovian system) flybys of Callisto in 1999, during which a CO_2 atmosphere and an ionosphere were detected. To explain the observed electron profile, we find that an atmosphere 20-100 times denser than the CO_2 atmosphere must be introduced. Later, Hubble Space Telescope (HST) observations of this atmosphere provided another constraint on the abundance of atomic oxygen. The atomic oxygen produced from O_2 photodissociation was 2 orders of magnitude greater than the reported upper limit. The introduction of reactive hydrogen chemistry assuming a surface abundance of H_2O of $\sim 2 \times 10^9 \text{ cm}^{-3}$ (4×10^{-8} mbar) is required to reduce the excess atomic O abundance. The calculated atomic O column density is $> 5 \times 10^{12} \text{ cm}^{-2}$, which is about the observed upper limit, suggesting that we should be able to detect O in the atmosphere of Callisto. In this chapter, the inferred enhanced chemical processes are also discussed, that predicts oxidants near the surface can be produced in large quantities. With ice convection,

oxidants produced on the surface can be delivered to the liquid ocean, if one exists, underneath the surface and thus provide the required energy for underlying ecosystem.

The last two chapters are for the exploration of atmospheric chemical processes in extrasolar planets (Part III). Since the discovery of the so-called “hot Jupiters,” such close-in planets are generally believed to be undergoing hydrodynamic escape. If true, these planets would provide a new laboratory for refining our knowledge of hydrodynamic escape processes in our solar system, such as the possible loss of nearly an Earth’s ocean of water on early Venus, the hydrogen problems in the ancient Earth’s atmosphere, the nitrogen abundance in the atmosphere of Titan, etc. The source of hydrogen is central to these issues. Chapter 9 shows that atomic hydrogen produced from H_2 dissociation via an H_2O -mediated catalytic process is efficient in the atmospheres of “hot Jupiters.” Then in Chapter 10, we further discover that the production of hydrocarbon aerosols is insignificant, suggesting that we will be able to detect the chemical composition in those atmospheres down to the limit of Rayleigh scattering and/or cloud tops of high temperature condensates.

Chapter 2

An Overview of Kinetic Models

Abstract

In this Chapter, I briefly introduce the tool adopted here for the study of chemical and dynamical processes in planetary atmospheres. This numerical tool can roughly be decomposed into two parts: photochemistry and the transport of chemical species. Quantitative studies of integrating photochemistry and chemical transport, which I describe below, were pioneered by *Colegrove et al.* [1965], to simulate the distribution of atomic oxygen in the middle atmosphere of the Earth. Later, *Strobel* [1973] applied the same method to the outer solar system planets. This tool for examining the chemical composition in the atmospheres of (exo)planets and their satellites has been proven to be of great success.

2.1 Chemical Reactions

There are four kinds of chemical reactions in kinetics: (1) photodissociation ($AB + h\nu \rightarrow A + B$), (2) combination ($A + B + M \rightarrow AB + M$), (3) disproportionation ($AB + CD \rightarrow AC + BD$), and (4) exchange and transfer ($A + BC \rightarrow AB + C$), where $h\nu$ denotes dissociative photons and M is a third particle that carries away some of the excess energy of reaction. For photodissociation reactions, the model calculates appropriate J values (s^{-1}) by integrating the products of cross sections and the solar flux over the relevant wavelengths. For each bimolecular reaction, the rate constant is available from laboratory measurements and/or theoretical calculations. The rate coefficients for three-body combination reactions are interpolated between the low-pressure, three-body values k_0 ($cm^6 s^{-1}$) and high-pressure, two-body limiting values k_∞ ($cm^3 s^{-1}$), with a simple expression that leads to the limiting

values at low and high densities of

$$k = \frac{k_0 k_\infty}{k_\infty + k_0 [M]} F_c^\beta \quad (2.1)$$

$$\beta = [1 + (\log_{10} \frac{k_0 [M]}{k_\infty})^2]^{-1}, \quad (2.2)$$

where $[M]$ is the total atmospheric density (cm^{-3}) and k is in units of $\text{cm}^6 \text{s}^{-1}$. We assume $F_c \approx 0.6$ [DeMore *et al.*, 1992], unless otherwise noted. (F_c is a coefficient which characterizes the broadening of the falloff curve, induced by the energy dependence of the rate coefficient for unimolecular dissociation of the energized adduct.) The chemical reaction rates ($\text{cm}^{-3} \text{s}^{-1}$; P , chemical production rates, and L , chemical loss rates) for photodissociation, two-body (bimolecular) and three-body (termolecular) reactions are $J[AB]$, $k[AB][CD]$, and $k[A][B][M]$, respectively.

2.2 Caltech/JPL Multi-Dimensional Kinetics Models

The Caltech/JPL multi-dimensional model (KINETICS) was built to answer fundamental questions concerning the chemical composition and dynamical processes responsible for the transport and mixing of chemical species in planetary atmospheres. Are gravity waves primarily responsible for vertical mixing? Are planetary waves mainly responsible for horizontal mixing? Is there a difference in mixing between tropics and mid-latitudes? Is the polar region isolated? How do similar processes in planetary atmospheres compare?

Transport and mixing of chemical species in a planetary atmosphere are well defined if the dynamics are determined. Conversely, if the distribution of trace species and their

chemistry are known, we can infer the dynamical processes operating in the atmosphere.

I will briefly give an overview of the fundamental concepts that give rise to one-dimensional (1-D) and two-dimensional (2-D) modeling of chemistry and transport. These models simplify full transport in three dimensions by averaging over latitudes and longitudes and longitudes, respectively. While atmospheric transport is essentially a three-dimensional (3-D) process, the demand for computing power and the lack of knowledge of physical inputs hamper the development of general circulation models (GCM) for chemical species in planetary atmospheres. The 1-D and 2-D models, combining physical insight, computational flexibility, and observed tracer data, have made fundamental contributions to our understanding of Earth and planetary atmospheres. 3-D models for planets are at the nascent stage, but advancing rapidly.

2.2.1 One-Dimensional Model

Colegrove et al. [1965] introduced a 1-D photochemical model to simulate the distribution of atomic oxygen in the middle atmosphere of the Earth. The model solves the continuity equation of mass:

$$\frac{\partial n_i}{\partial t} + \frac{\partial \varphi_i}{\partial z} = P_i - L_i, \quad (2.3)$$

where n_i is the number density for the species i , φ_i the vertical flux, P_i the chemical production rate, and L_i the chemical loss rate, all evaluated at time t and altitude z . The vertical transport φ_i is given by

$$\varphi_i = -\frac{dn_i}{dz}(D_i + K_{zz}) - n_i\left[\frac{D_i}{H_i} + \frac{K_{zz}}{H_{atm}}\right] - n_i\frac{dT}{dz}\left[\frac{(1 + \alpha_i)D_i + K_{zz}}{T}\right] + n_i w_i, \quad (2.4)$$

where H_i is the species' scale height, H_{atm} the atmospheric scale height, α_i the thermal diffusion parameter, T the temperature, and w_i the zonally averaged vertical velocity (see *Chamberlain and Hunten* [1987] for details). We usually set w_i equal to zero. $D_i(z)$ and $K_{zz}(z)$ are, respectively, the molecular and eddy diffusion coefficients. The former is rigorously based on fundamental physics and laboratory measurements, and the latter is usually derived empirically from observations of tracers in the atmosphere. A notable example of the success of this approach is the derivation of a $K_{zz}(z)$ profile with a non-trivial vertical structure for the terrestrial mesosphere and lower thermosphere by *Allen et al.* [1981] using chemical tracer data. *Lindzen* [1981] independently derived a similar vertical structure based on the dynamics of the breaking of gravity waves.

For Jovian planets, the vertical eddy mixing is usually parameterized by $K_0 n(z)^{-\gamma}$, where $n(z)$ is the atmospheric density at altitude z , being caused by the propagation and dissipation of gravity waves generated in the deep atmosphere. The exponent $\gamma \approx 0.5$, determined from the conservation of energy in propagating waves, and K_0 is obtained empirically by fitting tracers' vertical profiles. For molecular diffusion, we follow the expression

$$D_i(n) = A_{H_2} T^{(S_{H_2}-1)} \frac{B}{n} \sqrt{M_{H_2}/M_i}, \quad (2.5)$$

where $A_{H_2} = 3.64 \times 10^{-5} \text{ cm}^2 \text{ s}^{-1} \text{ K}^{-S_{H_2}}$, $S_{H_2} = 1.75$, $B = 7.3439 \times 10^{21} \text{ cm}^{-3} \text{ K}$, and $M_{H_2} = 2.01594 \text{ amu}$; M_i is the mass of target in amu [*Marrero and Mason*, 1972].

The numerical solution of the 1-D model follows standard techniques. After discretization, equations (2.3)-(2.4) reduce to a single finite difference equation that is first order in time (t) and second order in space (z). Chemistry is linearized by successive iteration using Newton's method. The entire system is then block-tridiagonal and can be inverted without

further approximation. Convergence of chemical species is within a fractional error of 10^{-4} for all species, as can be verified by comparing the numerical solutions against analytic solutions [Landry *et al.*, 1991]. The 1-D photochemical model has been successfully applied to Jupiter for over three decades [e.g., see Wallace and Hunten, 1973; Strobel, 1973; Gladstone *et al.*, 1996; also books by Atreya, 1986; Yung and DeMore, 1999 and recent review by Moses *et al.*, 2004].

In the Earth’s atmosphere, the availability of nuclear debris data from nuclear bomb testing in the late 1950’s and early 1960’s stimulated the development of 2-D models for meridional transport and stratosphere-troposphere exchange. Reed and German [1965]’s pioneering model is based on mixing length theory, but takes into account counter-gradient transport by making use of all four components of the eddy diffusivity tensor. A fundamental breakthrough in 2-D modeling occurred a decade later when Andrews and McIntyre [1976, 1978] showed that atmospheric waves that are linear, steady, and frictionless do not contribute to net transport. Only non-linear, dissipative, and transient waves contribute to the so-called “transformed Eulerian mean” (TEM) transport. See Andrews *et al.* [1987] for various approximately equivalent versions of TEM, including the “residual circulation.” There are at least two ways to compute the TEM circulation: one way is to obtain the “Eliassen-Palm flux” from a GCM; another way is to approximately equate the TEM circulation with the diabatic circulation [Dunkerton, 1978]. The latter option allows us to relate the meridional transport to radiative processes in the atmosphere. There is another consequence of the Andrews and McIntyre’s theory: the horizontal eddy coefficient is simply related to the gradient of potential vorticity, and hence is readily derived from GCM products [Tung, 1982]. In the following decade, the 2-D TEM models became the “work horse” in the Earth’s atmosphere for assessing the impact of anthropogenic perturbation

of the ozone layer by chlorofluorocarbons [e.g., see *Garcia and Solomon, 1983; Ko et al., 1985*].

The spatial distribution of the aforementioned chemical tracers reflects a balance between chemistry and transport in the upper troposphere and middle atmosphere of Jupiter, where our knowledge of chemistry is superior to that of transport. Therefore, quantitative modeling of the observed distribution of the chemical tracers can be used to improve our knowledge of transport processes. To achieve this goal, we need a 2-D model that is flexible enough to integrate all recent advances yet robust enough to allow for parameterization to fill in gaps of knowledge.

2.2.2 Two-Dimensional Model

Lee et al. [1998], *Allen et al. [2000]* and *Edgington et al. [2000]* have discussed preliminary efforts at 2-D modeling of chemistry and transport in the atmosphere of Jupiter. We have developed a new hybrid 2-D model (H-2D), based on the Caltech/JPL 2-D model for the terrestrial atmosphere.

The details of the H-2D model are described in Appendix A of *Morgan et al. [2004]*. In earlier work [e.g., *Shia et al., 1989; Yung and Miller, 1997; Morgan et al., 2004*], the diabatic circulation was computed from radiative heating rates. We recently developed an innovative method for deriving the TEM circulation from the outputs of a GCM using mapping on isentropic surfaces. We have applied this method successfully to obtain the TEM circulation in the terrestrial atmosphere [*Jiang et al., 2004*] and the Jovian atmosphere [*Yung et al., 2003*]. The chief advantage of this approach versus previous models [*Garcia and Solomon, 1983; Ko et al., 1985*] is that it is directly derived from a 3-D GCM.

The heritage of the Jupiter H-2D model is our 2-D model for the terrestrial atmosphere.

The present model is a time dependent treatment of the global atmosphere in two dimensions (pressure and latitude), composed of four modules: the chemical module, the solar radiative module, the infrared radiative module, and the transport module. Because of the modular design of the earlier 1-D model, the generalization to 2-D required only limited restructuring. The photochemical module, the solar radiative module, and the infrared radiative module are all used in the 2-D model as in the 1-D model, with only minor code adjustments. It is a special feature of our model that the 1-D and 2-D models are unified, with arbitrary dimensions in pressure and latitude.

The continuity equation in 2-D

$$\frac{\partial \chi}{\partial t} + v \frac{\partial \chi}{\partial y} + w \frac{\partial \chi}{\partial z} - \frac{1}{\cos \theta} \frac{\partial}{\partial y} [\cos \theta K_{yy} \frac{\partial \chi}{\partial y}] - e^{\xi} \frac{\partial}{\partial z} [e^{-\xi} K_{zz} \frac{\partial \chi}{\partial z}] = \frac{Q}{[M]} \quad (2.6)$$

is solved for all long-lived species (e.g., N₂O), where χ is the mixing ratio for the species, $\xi = z/H_{atm}$, and v , w , K_{yy} , and K_{zz} denote the horizontal velocity, vertical velocity, horizontal eddy diffusivity, and vertical eddy diffusivity, respectively. $Q (= P - L)$ is the net chemical production rate. The abundance of short-lived species [e.g., O(¹D)] are computed through local chemical equilibrium. The aim of the transport module is to provide the advection fields, v and w .

Equation 2.6 is solved first by discretizing it in space and time and marching forward by time-splitting. That is, in a time step the different processes of chemistry, diffusion, and advection in different directions are calculated sequentially. As long as the time step is small enough compared with the timescale of the different processes, the model simulations are independent of the order of the processes being calculated and the model simulations are acceptable. The validity of the numerical method for solving the continuity equation

was tested against analytic solutions first derived by our group [*Shia et al.*, 1990].

2.2.3 Modified Two-Dimensional Model

For 1-D problems, the Caltech/JPL KINETICS integrates the continuity equation with chemistry and diffusion by solving the resulting matrix equation using a matrix inversion method, which allows quite large time steps. Due to the limitation of computing power when the model was expanded to 2-D (for a detailed model description, see above and *Morgan et al.* [2004]) more than 10 years ago, the time splitting (or process splitting) procedure was adopted, as described above, which requires a small time step as compared with the time scale of the different processes.

In recent applications, the model has been used to investigate the upper region of planetary atmospheres where molecular diffusion in the vertical direction becomes the dominating transport mechanism. This reduces the time step from hours to tens of seconds. The “quasi 2-D” model is an approach to solve this problem. Two kinds of “quasi 2-D” are available.

First, taking advantage of the existing 1-D model approach, the vertical diffusion and chemistry are solved by inverting the matrix. The “quasi 2-D” method is a series of 1-D models at different latitudes coupled with horizontal diffusion where advection in the horizontal and vertical direction solved one-by-one in the same time step. The results are tested against analytic solutions [*Shia et al.*, 1990]. This method is advantageous when the advection and horizontal eddy mixing are less important than vertical mixing. The condition is met in atmosphere of Jupiter, and the Cassini measurements of C_2H_2 and C_2H_6 latitudinal profiles at the ~ 5 mbar level are well reproduced by this model (see §7).

Second, to take further advantage of the computational efficiency of the 1-D solver, the horizontal diffusion and horizontal and vertical advection are integrated into Q in equation

2.6. This method is particularly powerful when the advection and horizontal eddy mixing are as important as (or more significant than) the vertical mixing, such as the chemical transport in the atmosphere of Titan, which is currently under investigation with this new model.

Bibliography

Allen, M., Y.L. Yung, and J.W. Waters, Vertical Transport and Photochemistry in the Terrestrial Mesosphere and Lower Thermosphere (50-120 km), *Journal of Geophysical Research-Space Physics*, 86 (NA5), 3617-3627, 1981.

Allen, M., Y.T. Lee, A. Friedson, G. Orton, and R. West, Transport in the Jovian Stratosphere, *Bulletin American Astronomical Society*, 32, 1008, 2000.

Andrews, D.G., and M.E. McIntyre, Planetary Waves in Horizontal and Vertical Shear: The Generalized Eliassen-Palm Relation and the Mean Zonal Acceleration, *Journal of the Atmospheric Sciences*, 33, 2031-2048, 1976.

Andrews, D.G., and M.E. McIntyre, Generalized Eliassen-Palm and Charney-Drazin Theorems for Waves on Axisymmetric Mean Flows in Compressible Atmospheres, *Journal of the Atmospheric Sciences*, 35, 175-185, 1978.

Andrews, D.G., J.R. Holton, and C.B. Leovy, Middle Atmospheric Dynamics, Academic Press, 1987.

Atreya, S.K., Atmospheres and Ionospheres of the Outer Planets and their Satellites, Berlin, New York: Springer-Verlag, 1986.

Chamberlain, J.W., and D.M. Hunten, Theory of Planetary Atmospheres, New York: Academic Press, 1987.

- Colegrove, F.D., W.B. Hanson, and F.S. Johnson, Eddy Diffusion and Oxygen Transport in Lower Thermosphere, *Journal of Geophysical Research*, 70(19), 4931-4941, 1965.
- DeMore, W. B., S. P. Sander, D. M. Golden, R. F. Hampson, M. J. Kurylo, C. J. Howard, A. R. Ravishankara, C. E. Kolb, and M. J. Molina 1992, Chemical Kinetics and Photochemical Data for Use in Stratospheric Modeling. Evaluation Number 10, JPL Publication 92-20, Jet Propulsion Laboratory.
- Dunkerton, T.J., On the Mean Meridional Mass Motions of the Stratosphere and Mesosphere, *Journal of the Atmospheric Sciences*, 35, 2325-2333, 1978.
- Edgington, S.G., R.A. West, A.J. Friedson, and S.K. Atreya, A 2-D Photochemical Model with Meridional Circulation, *Bulletin American Astronomical Society*, 32, 1013, 2000.
- Garcia, R.R., and S. Solomon, A Numerical-Model of the Zonally Averaged Dynamical and Chemical-Structure of the Middle Atmosphere, *Journal of Geophysical Research-Oceans and Atmospheres*, 88 (NC2), 1379-1400, 1983.
- Gladstone, G.R., M. Allen and Y.L. Yung, Hydrocarbon Photochemistry in the Upper Atmosphere of Jupiter, *Icarus*, 119(1), 1-52, 1996.
- Jiang, X., C.D. Camp, R.L. Shia, D. Noone, C. Walker, and Y.L. Yung, Quasi-Biennial Oscillation and Quasi-Biennial Oscillation-Annual Beat in the Tropical Total Column Ozone: A Two-Dimensional Model Simulation, *Journal of Geophysical Research-Atmospheres*, 109 (D16), art. no. 4377, 2004.
- Ko, M.K.W., K.K. Tung, D.K. Weisenstein, and N.D. Sze, A Zonal Mean Model of Stratospheric Tracer Transport in Isentropic Coordinates - Numerical Simulations for

- Nitrous-Oxide and Nitric-Acid, *Journal of Geophysical Research-Atmospheres*, 90(ND1), 2313-2329, 1985.
- Landry, B., M. Allen, and Y. L. Yung. (1991). Troposphere Stratosphere Interactions in a One-Dimensional Model of Jovian Photochemistry. *Icarus* 89(2): 377-383.
- Lee, Y.T., M.A. Allen, A.J. Friedson, and R.A. West, A 2-D model of C₂H₆ in the Jovian stratosphere, *Bulletin American Astronomical Society*, 30, 1067, 1998.
- Lindzen, R.S., Turbulence and Stress Owing to Gravity-Wave and Tidal Breakdown, *Journal of Geophysical Research-Oceans and Atmospheres*, 86(NC10), 9707-9714, 1981.
- Marrero, T. R., and E. A. Mason 1972, Gaseous Diffusion Coefficients, *J. Phys. Chem. Ref. Data*, 1, 3-118.
- Morgan, C.G., M. Allen, M.C. Liang, R.L. Shia, G.A. Blake, and Y.L. Yung, Isotopic Fractionation of Nitrous Oxide in the Stratosphere: Comparison between Model and Observations, *Journal of Geophysical Research-Atmospheres*, 109(D4), art. no. 4305, 2004.
- Moses, J.I., et al., The Stratosphere of Jupiter, *Jupiter: The Planet, Satellites and Magnetosphere*, Cambridge University Press, 29-157, 2004.
- Reed, R.J., and K.E. German, A Contribution to the Problem of Stratospheric Diffusion by Large-Scale Mixing, *Monthly Weather Review*, 93, 313-321, 1965.
- Shia, R.L., Y.L. Yung, M. Allen, R.W. Zurek, and D. Crisp, Sensitivity Study of Advection and Diffusion Coefficients in a 2-Dimensional Stratospheric Model Using Excess C-14 Data, *Journal of Geophysical Research-Atmospheres*, 94(D15), 18467-18484, 1989.

- Shia, R.L., Y.L. Ha, J.S. Wen, and Y.L. Yung, 2-Dimensional Atmospheric Transport and Chemistry Model - Numerical Experiments with a New Advection Algorithm, *Journal of Geophysical Research-Atmospheres*, 95(D6), 7467-7483, 1990
- Strobel, D.F., photochemistry of NH_3 in Jovian atmosphere, *Journal of the Atmospheric Sciences*, 30(6), 1205-1209, 1973.
- Tung, K.K., On the Two-Dimensional Transport of Stratospheric Trace Gases in Isentropic Coordinates, *Journal of the Atmospheric Sciences*, 39(10), 2330-2355, 1982.
- Yung, Y.L., and W.D. DeMore, Photochemistry of Planetary Atmospheres, Oxford University Press, 1999.
- Yung, Y.L., and C.E. Miller, Isotopic Fractionation of Stratospheric Nitrous Oxide, *Science*, 278(5344), 1778-1780, 1997.
- Yung, Y.L., X. Jiang, A.Y. Lee, R.L. Shia, and T.E. Dowling, Stratosphere and Troposphere Exchange using Chemical Tracers: A Comparative Study between Earth and Jupiter, *EOS Transactions American Geophysical Union*, 84(46), A12A-0071, p.113, 2003a
- Wallace, L., and D.M., Hunten, Lyman-alpha albedo of Jupiter, *Astrophysical Journal*, 182(3), 1013-1031, 1973.

Part I

Ancient and Present-Day Earth

Chapter 3

A Semianalytic Model for Photo-Induced Isotopic Fractionation in Simple Molecules

Mao-Chang Liang, Geoffrey A. Blake, and Yuk L. Yung

Journal of Geophysical Research-Atmospheres, 109(D10), D10308, 2004.

Abstract

We have developed a semi-analytic model for computing photo-induced isotopic fractionation in simple molecules of interest to the atmospheric science community. The method is based on the Born-Oppenheimer approximation and the Reflection Principle. It has the main advantage of using commonly available input data, namely the photolysis cross sections for the standard isotopologue/isotopomer and the ground state isotope-specific spectroscopic constants. The isotopic fractionation arises principally from the spectral shift induced by the small difference in zero point energy between isotopologues/isotopomers and the contraction of the wavefunction due to heavier isotope substitution. The latter effect dominates photolytic fractionation away from the cross section maxima. Our new approach is demonstrated with applications to the diatomic molecules HCl and HI and the triatomic molecules N₂O and O₃. Agreement between the model and measurements is excellent. New modelling results for the fractionation of ¹⁵N¹⁵N¹⁶O in the stratosphere using the Caltech/JPL two-dimensional model are presented.

3.1 Introduction

Stable isotopic fractionation has been known since the 1930's. Mass-dependent fractionation was first recognized by *Urey* [1947], who demonstrated that the physical basis of isotopic fractionation was "well correlated with the energy states of molecules as secured from spectral data by the use of statistical mechanics" [*Urey*, 1947, p. 563]. Subsequent work has improved the calculation of partition functions and fractionation factors [*Richet et al.*, 1977; *Kaye*, 1987].

The isotopic fractionation of a trace species is diagnostic of its chemical and transport

history. Stable isotopes have therefore played an important role in the quantitative understanding of atmospheric transport and chemistry. Recently, measurements of isotopic fractionation of many trace species in the terrestrial atmosphere have been reported with an accuracy < 1 per mil (one part in thousand). Examples include O_3 [Mauersberger, 1987; Johnston and Thiemens, 1997; Mauersberger et al., 2001], CO_2 [Brenninkmeijer et al., 1995; Lämmerzahl et al., 2002], CO [Brenninkmeijer et al., 1995; Huff and Thiemens, 1998; Röckmann et al., 1999], CH_4 [Brenninkmeijer et al., 1995; Irion et al., 1996], and N_2O [Yoshida and Matuso, 1983; Kim and Craig, 1993; Cliff and Thiemens, 1997; Rahn and Wahlen, 1997; Cliff et al., 1999; Yoshida and Toyoda, 2000; Röckmann et al., 2001a,b]. The fractionations observed in the D/H ratio in the atmospheres of planets and satellites in the solar system have provided useful constraints on the evolution of their atmospheres [Geiss and Reeves, 1981; Frost et al., 1982; Owen et al., 1986; Kaye, 1987; Owen et al., 1988; Owen, 1992; Yung and Dissly, 1992; Debergh, 1993; Vidal-Madjar et al., 1998; Yung and Kass, 1998; Miller and Yung, 2000]. Most of these measurements require an understanding of the fundamental kinetic and photolytic processes that take place in the atmosphere(s) for their interpretation [e.g., McLinden et al., 2003; Morgan et al., 2004].

Isotopic fractionation has also been extensively studied using *ab initio* calculations [e.g., van Harreveld and van Hemert, 2000; Johnson et al., 2001] and analytic models [e.g., Yung and Miller, 1997, YM97 hereafter; Gao and Marcus, 2001; Blake et al., 2003]. Here, we present a semi-analytic computational model of the fractionation induced by the photodissociation of simple molecules. Comparison with available laboratory data is made in section 3.3, and the implications for atmospheric chemistry are discussed in section 3.4.

3.2 Method

In this section, we present our algorithm for calculating the dissociation cross sections of isotopically substituted species. We assume that the cross section for the standard isotopic species is known and invoke the Reflection Principle and the Born-Oppenheimer approximation to simplify the calculations. Example applications of this new method will be given in section 3.3.

3.2.1 The Reflection Principle

Photodissociation can be approximately classified as either direct or indirect. As a photon interacts with a molecule, absorption processes can leave it in an excited electronic state. If the lifetime of the upper state is much shorter than the vibrational period(s), the process is called direct fragmentation. If the lifetime is much longer than the vibrational period(s), the process is called indirect fragmentation. Spectroscopically, the (direct) photodissociation model presented in this work is valid only if the width of the spectrum is comfortably larger than the fundamental vibrational frequency (frequencies). The photodissociation cross section can thus be simply computed by mapping the square of the initial wavefunction onto the energy axis through the potential energy surface of the dissociative state. This is the essence of the Reflection Principle. To first order, the potential energy curve for a dissociating diatomic molecule can be represented by a linear function in the region not far from the equilibrium nuclear distance of the molecule's ground state. At sufficiently low temperatures the population of molecules in excited vibrational states is negligible, and the initial state can be approximated by the ground state wavefunction alone. For example, at room temperature $\sim 90\%$ of N_2O molecules are in the vibrational ground state

and $\sim 10\%$ reside in the first excited bending state. Based on the Reflection Principle with a simplified upper state potential energy surface, the dissociation cross section turns out to be an energy weighted gaussian function if the initial state is the ground state – for which a simple harmonic oscillator gaussian provides a reasonable description of the true (anharmonic) wavefunction for small excursions from the vibrationally averaged molecular structure.

A schematic of the one-dimensional Reflection Principle as applied to the direct photodissociation of diatomic molecules is illustrated in Figure 3.1 [see also *Schinke, 1993*]. In the Born-Oppenheimer approximation, both the position and the momentum of the nuclei are conserved during photoexcitation. Accordingly, vertical lines can be used to map the square of the vibrational ground state wavefunction ($|\Psi_0|^2$) onto the energy axis (that is, the nuclear geometry remains constant). The transitions are best drawn from potential curve to potential curve (dashed lines), and the photon energy is given by $h\nu = V_e - V_g$, where V_e and V_g are the dissociative and ground state electronic potentials, respectively. Within the Born-Oppenheimer approximation, the potential curves (V_e and V_g) are independent of isotopic substitution.

3.2.2 Analytic Solution for Diatomic Molecules

The change of mass of the isotopically substituted species from that of the more abundant standard species is usually less than 10%. This results in a small difference in the vibrational frequencies. *Yung and Miller [1997]* first modelled the fractionation in the photodissociation of nitrous oxide by shifting the whole spectrum by an amount equal to ΔZPE , where ΔZPE is the difference in zero point energy (ZPE) between the the standard species and isotopically substituted species. However, the fractionation predicted via this method is approximately

half that observed in laboratory measurements and atmospheric observations. Isotopic substitution not only changes the ZPE of a given isotopologue/isotopomer, but also modifies the shape of the corresponding vibrational wavefunction. The modification of wavefunction has a significant effect on the dissociation cross section, especially away from the peak of the spectrum. Photodissociation models based on these modified wavefunctions have the correct form, and much more closely reproduce the laboratory measurements of isotopic fractionation [*Blake et al.*, 2003].

For direct photolysis, the dissociation cross section can be approximated by the square of the transition dipole moment-weighted initial state wavefunction. Here, we adopt the classical view of the photodissociation process to simplify the calculation: the linear momentum is independent of the spatial coordinate. The overall dissociation cross section is then the sum of all trajectories leading to the dissociation, with a particular weight for each path in phase space. The statistical weight is usually given by the Wigner distribution function [e.g., *Wigner*, 1932]. For a harmonic oscillator in the ground state, the distribution function, $P_W(R, P)$, is

$$P_W(R, P) = (\pi\hbar)^{-1} \exp[-2\alpha(R - R_0)^2/\hbar] \exp[-P^2/(2\alpha\hbar)], \quad (3.1)$$

where R is the instantaneous nuclear distance, P is the related linear momentum, \hbar is the Planck constant, and R_0 is the vibrationally averaged nuclear distance in the ground state [e.g., *Dahl*, 1983]. For the line-width component in $P_W(R, P)$, α is defined as

$$\alpha \equiv \mu\omega/2 = (k/\omega^2)\omega/2 \propto 1/\text{ZPE}, \quad (3.2)$$

where μ is the reduced mass, ω is the vibrational frequency, and k is the corresponding

curvature of the ground state potential energy curve (the so-called spring or force constant, defined as the second derivative of V_g near R_0). The rightmost proportionality of equation (3.2) is given by the Born-Oppenheimer approximation, i.e., k is unchanged by isotopic substitution. This classical distribution function of the vibrational ground state is the product of two gaussians defined in phase space, one centered at the vibrationally averaged nuclear distance R_0 , the other centered at $P = 0$. Since direct photodissociation occurs instantaneously in the Born-Oppenheimer approximation, the internal coordinate (R) and the corresponding momentum (P) of the parent molecule remain unchanged during the excitation process [Mulliken, 1971].

The dissociation cross section is given by the product of the distribution function (equation (3.1)) and the square of the transition dipole moment. For simplicity, we first assume that the transition dipole moment is independent of R , P , and isotopic substitution. The dissociation cross section σ can then be calculated as a function of photon energy E [e.g., Schinke, 1993] by:

$$\sigma(E) \propto E \int dP \int dR \exp[-2\alpha(R - R_0)^2/\hbar] \exp[-P^2/(2\alpha\hbar)] \delta(H - E), \quad (3.3)$$

where H is the Hamiltonian defined for the dissociative process. Note that we have omitted the square of the transition dipole moment from equation (3.3). By integrating equation (3.3), we obtain

$$\begin{aligned} \sigma(E) &\propto E\alpha^{1/2} \exp[-2\alpha(R_t - R_0)^2/\hbar] / V'_{R_t} \\ &= E\beta^{1/2} \exp[-2\beta(E - V_0)^2/\hbar], \end{aligned} \quad (3.4)$$

where $V_0=V_e(R_0)$, V'_R is the absolute value of the derivative of $V_e(R)$ with respect to R , R_t is the classical turning point defined by $H(R_t, P) = E$, $\beta = \alpha/V_{R_t}'^2$, and $V'_{R_t} = V'_R|_{R_t}$. If the dissociation potential can be linearized as

$$V_e(R) \approx V_e(R_0) - V'_{R_0}(R - R_0) \equiv V_0 - V'_0(R - R_0), \quad (3.5)$$

the resulting σ is approximated by

$$\sigma(E) \propto E\beta^{1/2}\exp[-2\beta(E - V_0)^2/\hbar] , \quad (3.4')$$

where $V'_0 = V'_{R_0}$ and $\beta = \alpha/V_0'^2$. We see that the above equation is simply an energy-weighted gaussian function if the dissociating potential is linear with R . If the slope of $V_e(R)$, V'_R , is not strongly varying, that is,

$$V'_R = V'_0 + \eta, \quad (3.6)$$

where $\eta = \eta(R) \ll V'_0$, the cross section σ in equation (3.4) can be further simplified to

$$\begin{aligned} \sigma(E) &\propto E\alpha^{1/2}\exp[-2\alpha(E - V_0)^2/(\hbar V_{R_t}'^2)]/V_{R_t}' \\ &= E\alpha^{1/2}\exp[-2\alpha(E - V_0)^2/(\hbar(V'_0 + \eta)^2)]/(V'_0 + \eta) \\ &\approx EG(\alpha, V_0, E)\gamma(V_0, E), \end{aligned} \quad (3.7)$$

where G and γ are defined by

$$G(\alpha, V_0, E) \equiv \beta^{1/2}\exp[-2\beta(E - V_0)^2/\hbar] \quad (3.8)$$

$$\gamma(V_0, E) \equiv \exp[4\alpha_0\eta(E - V_0)^2/(\hbar V_0'^3)]. \quad (3.9)$$

The factor $\beta=\alpha/V_0'^2$ in equation (3.8) is used for normalization, and α_0 in equation (3.9) denotes the α for the standard species. Within the Born-Oppenheimer approximation and for a linearized upper state potential, isotopic substitution changes α (or β) only. The ZPE of the heavier isotopologue/isotopomer is smaller than that of the standard species. Thus, G of the heavier isotopologue/isotopomer will be narrower and sharper than that of the standard species. The function γ is equal to 1 if the dissociation potential is a linear function of the internuclear distance, i.e., $\eta = 0$, and if the dipole transition matrix element is independent of geometry. Typically, the dissociation potential is flatter and transition dipole smaller with increasing internuclear distance, and γ should therefore decrease toward larger R . If the transition dipole is assumed to vary linearly with distance and $V_e(R)$ is approximated with a quadratic function, the function γ varies as the fourth power of the transition frequency.

The fractionation factor $\epsilon(E \equiv h\nu)$ is defined by the difference in cross sections between the isotopically substituted (typically with a heavier isotope, and so designated H) and standard species (or L),

$$\begin{aligned} \epsilon(E; \text{per mil}) &\equiv 1000 \left(\frac{\sigma_H(E)}{\sigma_L(E)} - 1 \right) \\ &\approx 1000 \left[\frac{G(\alpha(H), V_0(H), E)}{G(\alpha(L), V_0(L), E)} - 1 \right] \\ &= 1000 \left[\frac{\beta(H)^{1/2} \exp[-2\beta(H)(E - V_0(H))^2/\hbar]}{\beta(L)^{1/2} \exp[-2\beta(L)(E - V_0(L))^2/\hbar]} - 1 \right], \end{aligned} \quad (3.10)$$

where γ is neglected since in most cases it is much less sensitive to isotopic substitution than is G . This will be demonstrated quantitatively in section 3.3. Thus, the form of the

isotopic fractionation induced by direct photolysis is nearly gaussian in nature, but for small effects the exponential can be expanded through the quadratic term in order to qualitatively demonstrate the effect of wavefunction reshaping.

Both β and V_0 are isotopically sensitive, with the wavelength shift of cross section maxima related to the change in the vibrationally averaged bond length, $\Delta R_0 = R_0(L) - R_0(H)$, and the steepness of the repulsive upper state potential. For a Morse ground state potential, the change in bond length can be approximated by

$$\Delta R_0 \approx \frac{\Delta \text{ZPE}}{\text{ZPE}} \left(\frac{a_e}{4B_e} \right) R_0$$

where the rotational constant of a vibrational state i is given by $B_v = B_e + a_e(i + 1/2)$. The shift in energy is simply $\Delta \nu_0 \approx V_0' \Delta R_0$, and for HI the product $(V_0' a_e R_0)/(4B_e \text{ZPE}) = 1.03$. Thus, $\Delta \nu_0 \approx \Delta \text{ZPE}$, as assumed by YM97. Using this approximation, the overall $\epsilon(\nu)$ can be written as

$$\epsilon(\nu; \text{per mil}) \approx \epsilon_1(\nu) + \epsilon_2(\nu) \quad . \quad (3.11)$$

Here, ϵ_1 and ϵ_2 have the approximate form

$$\epsilon_1(\nu) \equiv 1000 \frac{1}{W^2} \Delta \text{ZPE} (\nu - \nu_0 - \Delta \text{ZPE}/2) \quad (3.11a)$$

$$\epsilon_2(\nu) \equiv 1000 \frac{1}{2W^2} \frac{\Delta \text{ZPE}}{\text{ZPE}} (\nu - \nu_0 - \Delta \text{ZPE})^2, \quad (3.11b)$$

where W is the full-width-half-maximum (FWHM) of the fitted gaussian function, and ν_0

is the frequency of the standard species at which the dissociation cross section is maximum. Physically, ϵ_1 follows from the shift in energy induced by the ZPE of the various species, and ϵ_2 is the correction due to the change of the shape of the wavefunction. For large fractionation values, the full gaussian form of equation (3.10) should be used.

3.2.3 Triatomic Molecules

The method developed above for diatomic molecules can be extended to triatomic compounds. There are four normal modes for linear triatomic molecules (the bending mode is doubly degenerate) and three for nonlinear triatomics. The corresponding vibrational frequencies, ω_i , for the molecules studied in this paper are tabulated in Table 3.1, where i equals 1, 2, and 3 for symmetric stretching, bending, and asymmetric stretching, respectively.

For the photolysis of a linear molecule $A-B-C \rightarrow A-B + C$, the following dissociation coordinate system is usually used: r , R , and θ denote the A-B bond distance, the distance between the center of mass of A-B and C, and the angle between r and R . On average, θ is zero for a linear molecule in the vibrational ground state. The dissociation potential is again expanded through its first derivatives to yield

$$V_e(r, R, \theta) \approx V_0 - V'_r(r - r_0) - V'_R(R - R_0) - V'_\theta(\theta - \theta_0), \quad (3.12)$$

where the subscript “0” refers to the vibrationally averaged value, and V'_r , V'_R , and V'_θ are the partial derivatives of V_e with respect to their suffix. Within the Born-Oppenheimer approximation, the dissociation cross section can be calculated by means of the Reflection Principle and has the same form as equation (3.4) [see *Schinke, 1993*], but β must be

redefined as

$$\beta = (V_r'^2/\alpha_r + V_R'^2/\alpha_R)^{-1} \quad (3.13)$$

for a linear molecule since the expression for the generalized β accounts only for the modes directly related to the dissociation. The bending mode, to a first approximation, is not important for linear molecules because the vibrational motion is perpendicular to the dissociation coordinate R . The α_r and α_R are defined in accordance with equation (3.2), and so may be simply related to the ZPE, or

$$\beta^{-1} = \sum V_i'^2/\alpha_i \propto \sum (V_i'^2/k_i)\omega_i \propto \sum \omega_i = \text{ZPE}' \quad (3.14)$$

if the prefactors $(V_i'^2/k_i)$ in front of ω_i are the same, where α_i is the α for each normal mode and ZPE' is the sum of all vibrational frequencies significantly participating in the dissociation (equal to $\omega_1 + \omega_3$ for a linear molecule). The fractionation factor ϵ for a linear molecule is thus analogous to equation (3.10). Expanded through the quadratic term, ϵ can again be represented by

$$\epsilon(\nu; \text{per mil}) \approx \epsilon_1(\nu) + \epsilon_2'(\nu) \quad , \quad (3.15)$$

where ϵ_1 is defined as in equation (3.11a) and ϵ_2' is given by

$$\epsilon_2'(\nu) \equiv 1000 \frac{1}{2W^2} \frac{\Delta\text{ZPE}'}{\text{ZPE}'} (\nu - \nu_0 - \Delta\text{ZPE})^2.$$

$\Delta\text{ZPE}'$ is the difference of ZPE' between the standard species and the isotopically substi-

tuted species.

For a nonlinear molecule, the bending mode is no longer perpendicular to R . We amend equations (3.13) and (3.14), for which the bending mode contribution must be included in β , which is redefined by

$$\beta = (V_r'^2/\alpha_r + V_R'^2/\alpha_R + V_\theta'^2/\alpha_\theta)^{-1}. \quad (3.16)$$

The fractionation factor ϵ is the same as that defined in equation (3.15), but now ZPE' and $\Delta ZPE'$ are equal to ZPE and ΔZPE , respectively. The summation in equation (3.14) for nonlinear molecules thus runs over all the vibrational frequencies. Note that the above calculations are valid only for the dissociation process $A-B-C \rightarrow A-B + C$, and cannot be used to describe the $A-B-C \rightarrow A-C + B$ channel. The latter is much less likely, and as much we will not consider it here. For example, in the photolysis of water and nitrous oxide, the channels $H_2O \rightarrow OH + H$ and $N_2O \rightarrow N_2 + O(^1D)$ account for essentially 100% for the dissociation.

As shown schematically in Figure 3.2, in actual practice the calculation of isotopic fractionation from the known dissociation cross section of the standard species is divided into five steps:

1. The dissociation cross section of the standard isotopologue/isotopomer is divided by the corresponding dissociating photon frequency ν (see equation (3.7)) to obtain σ/ν .
2. The experimental values of σ/ν from (a) are then fitted with a three-parameter gaussian function, yielding a best guess for the wavefunction G . Values of γ are obtained from the ratio of σ/ν to G , as described in equations (3.7)-(3.9), and then fitted to a fourth-order polynomial (shown in dotted line).

3. Once derived, the functional forms of G and γ are derived for the isotopically substituted species using the values of ZPE and ZPE' tabulated in Table 3.1. As a guide to the reader, schematic illustrations of G and γ for the standard and substituted species are shown with the dotted and solid lines, respectively.

4. The photodissociation cross section for the isotopically substituted species is then constructed by multiplying G , γ , and ν . In the figure, the dotted line again shows the dissociation cross section of the standard species for comparison.

5. Finally, the fractionation factor ϵ is calculated from equation (3.10).

3.2.4 Temperature Dependence

Temperature-Independent Model—Typical atmospheric chemical reactions take place at < 300 K, and we can often assume that all the molecules lie in the ground state. According to equation (3.7), in such cases the measured cross section can be fitted by G and γ , and the resulting fractionation can be calculated from equation (3.15) with an appropriate adjustment of ZPE' (tabulated in Table 3.1).

Temperature-Dependent Model—In some molecules, the dissociation cross section of the standard species has been measured at more than one temperature, permitting the influence of vibrationally excited states to be directly examined. The contribution from each state can be approximated by the assumption of statistical equilibrium [e.g., *Selwyn et al.*, 1981]. At room temperature or below, levels up to the second excited state of the lowest energy vibration typically capture nearly all of the total population. The dissociation is the sum of the contributions from these three states:

$$\sigma(T, \nu) = \sum_i g_i(T) \sigma_i(\nu) \text{ and} \quad (3.17)$$

$$\sum_i g_i(T) = 1, \quad (3.17a)$$

where the subscript i ranges from 0 to 2 (vibrational ground state to second vibrational excited state) and $g_i(T)$ is the population weighting for the i -th state at temperature T .

The fractionation factor ϵ is expressed by

$$\epsilon(T, \nu; \text{per mil}) \approx 1000 \left[f \frac{g_0(H)G_0(H) + g_1(H)G_1(H) + g_2(H)G_2(H)}{g_0(L)G_0(L) + g_1(L)G_1(L) + g_2(L)G_2(L)} - 1 \right], \quad (3.18)$$

where f is a scaling factor which is energy independent and can be determined when the fractionation factor has been measured at any one temperature or from the temperature-independent model. Physically, this factor accounts for subtle variations in the transition dipole surface or anharmonicities in the actual bound state wavefunctions. Such variations are ignored in equations (3.10) and (3.18), but manifest themselves in the differing γ shown in Figures 3.3, 3.4, and 3.7.

3.3 Applications

3.3.1 Diatomic Molecules: HCl and HI

Diatomic molecules form the simplest tests of the Born-Oppenheimer photolysis model, and here HCl/DCl and HI/DI are used for a quantitative demonstration of our approach. Strictly speaking, HCl and HI do not follow the assumptions laid out in section 3.2, in that there are two upper states thanks to the strong spin-orbit interactions in Cl and I. As a result of these interactions, there are two channels ($^2P_{3/2}$ and $^2P_{1/2}$) leading to the dissociation of the parent molecule [e.g., *Ascenzi et al.*, 1999; *Brown and Balint-Kurti*, 2000]. The

branching ratio for the dissociation of heavier isotopologue (DCl and DI) via the excited state $^2P_{1/2}$ channel of Cl/I is smaller as a consequence of the increased adiabaticity of the DCl/DI photodissociation (thanks to the slower relative speed between D and Cl/I as compared to H and Cl/I for the same kinetic energy). This spin-orbit coupling means that two states must be considered in the photodissociation process, with different branching ratios as a function of hydrogen isotopic substitution. We will address these complications below, but first proceed with the formalism developed in section 3.2 since it captures the essential details of the isotopic behavior of hydrogen halide photodissociation.

Figure 3.3a shows the measured dissociation cross sections σ for HCl and DCl [*Bahou et al.*, 2001]. These cross sections have been normalized by the peak cross section of HCl, σ_P , where $\sigma_P = 3.4 \times 10^{-18} \text{ cm}^2$. The first step in computing the DCl cross section is to employ equation (3.7), which consists of three factors, $E \equiv h\nu$, G , and γ . In order to obtain G in equation (3.8), the normalized dissociation cross section is divided by the photon energy ν . The resulting data are then fitted by a gaussian with parameters ν_0 , W , and the peak amplitude (see Figure 3.3b), whose values are tabulated in Table 3.2.

As Figures 3.3a and 3.3b show, the DCl spectrum has a higher peak and narrower width than that of HCl. This result is consistent with equation (3.8), in which the shape of the spectrum reflects the shape of the ground state wavefunction within the Born-Oppenheimer approximation. Figure 3.3c shows the respective $\gamma(\nu)$, which are computed as the ratio $\sigma/(EG)$. Near the peak of the dissociation cross section, $\gamma \approx 1$. As anticipated by equation (3.9), in which η is more (positive)negative at higher(lower) energies, $\gamma < 1$ to the far red of the cross section maxima and > 1 to the blue.

The same analysis is applied to HI and DI and is shown in Figures 3.3f, 3.3g, and 3.3h. The dissociation cross sections of HI and DI have been measured by *Ogilvie* [1971]. Here they

have been normalized to the HI cross section peak, $\sigma_P = 220 \text{ mol}^{-1} \text{ cm}^{-1} = 8.2 \times 10^{-18} \text{ cm}^2$. Note that the γ for the standard species, HCl and HI, is not so different from that for the isotopically substituted species, DCl and DI, as expected. At energies far from the peak of the cross section, the change of G between isotopologues is much more significant than that of γ , and it is therefore safe to omit γ [as in equation (3.10)] for the computation of ϵ . Figures 3.3d and 3.3i show the fractionation factor ϵ for HCl/DCl and HI/DI. The dashed line shows the predicted ϵ using equation (3.10), with the YM97 ZPE model shown for comparison (dotted line). The results using our new method have the right form and magnitude to fit to the measured ϵ (cross symbol), but the predictions are shifted in energy with respect to the measurements thanks to the two spin-orbit states of the dissociating potential. The solid line depicts the prediction when adopting the experimental cross section maxima for the ΔZPE in equation (3.11a); the computation of the shape of the isotopically substituted spectrum still follows the scheme described in section 3.2.

The spin-orbit splitting is not large enough to resolve spectrally, but is manifest as a blueshift of the HCl/HI dissociation spectrum relative to that of DCl/DI thanks to the increased importance of the excited halogen $^2P_{1/2}$ channel. This blueshift is quite noticeable for HCl/DCl (see Figure 3.3a), while the peak positions of the dissociation cross sections of HI and DI are comparable (Figure 3.3f).

If we assume that the dissociations of DCl and DI are fully adiabatic, that is, that the DCl/DI dissociation occurs only via the ground $^2P_{3/2}$ channel of Cl/I, then the dissociation cross section of HCl/HI via the ground Cl/I channel can be calculated from the DCl/DI dissociation cross section by means of equation (3.7). The actual branching ratio of the dissociation of DCl via the excited Cl channel is ~ 0.2 at $\sim 193 \text{ nm}$ (see *Tonokura et al.*, 1992), and so this approximation should be a good first step. The expected G of HCl

dissociation via the ground Cl channel is represented by equation (3.8) and shown by the dotted line in Figure 3.3b. The branching ratio of HCl via the excited Cl channel is ~ 0.3 overall [Tonokura *et al.*, 1992], and the contribution from the excited Cl channel can be computed by the difference of HCl's G and the G via the ground state Cl channel. Gaussian fits to the spectra so obtained yield peaks offset by $\sim 3700 \text{ cm}^{-1}$, and the width is increased by $\sim 7\%$ relative to that of the ground state. We note that the change of the width may be due to the change of the slope in the dissociation potential surface. The fitted values are tabulated in Table 3.3. As the dash-dotted line of Figure 3.3d shows, the resulting ϵ is in excellent agreement with measurements. In fact, ϵ is simply the fractionation of the fitted G between HCl and DCl because the nongaussian γ function is largely insensitive to isotopic substitution (e.g., Figure 3.3c).

The same algorithm is applied to HI and DI and the results are shown in Figures 3.3f-3.3i. By considering the two dissociation channels for HI/DI, the improvement of ϵ (shown in dash-dotted line) is not as great as that for HCl/DCl simply because HI/DI photodissociation is more adiabatic than that for HCl/DCl. The greater error of HI/DI at low energy end is due to the neglect of γ . The spectra of γ for HI and DI are shown in Figure 3.3h: the difference at low energy end is clearly somewhat greater than that for HCl and DCl. When including γ , as described in equations (3.7) and (3.9), the predicted ϵ matches the measurements well, as shown in Figures 3.3e and 3.3j. The lowest energies correspond to the largest internuclear distances where the effects of anharmonicity are greatest. Improved fits should therefore be possible with numerical wavefunctions derived from fits to the full suite of isotope specific rovibrational spectroscopic constants.

3.3.2 Linear Triatomic Molecule: N₂O

The cross sections of ¹⁴N¹⁴N¹⁶O have been examined by many authors. Here we use the measurements of *Selwyn et al.* [1981], *Yoshino et al.* [1984], and *Merienne et al.* [1990]. *Yoshino et al.* [1984] measured the cross section in the wavelength range 170–222 nm at room temperature; their results are shown in Figure 3.4. The cross section has been normalized to the peak of the ¹⁴N¹⁴N¹⁶O spectrum, $\sigma_P = 1.4 \times 10^{-18}$ cm². The Yoshino et al. cross sections are first used to determine those of the other isotopologues/isotopomers by means of the temperature-independent model (section 3.2.4), with the room temperature results presented in Figure 3.5. Our prediction (solid line) is in good agreement with the measurements. YM97’s ZPE model and the *Johnson et al.* [2001]’s *ab initio* model are shown for comparison. YM97’s model underestimates ϵ by more than a factor of 2, while Johnson et al.’s *ab initio* calculations agree well with the measurements except for 546 and 556. The *ab initio* prediction of ϵ for 546 is even worse than YM97’s, most likely due to the assumption of a fixed N-N bond length in the dissociation process [*McLinden et al.*, 2003]. Our prediction underestimates ϵ by 10-20 per mil for 456 and $\sim 15\%$ for 556. According to equation (3.4), the dissociation cross section is determined by the slope of the dissociation potential and the gaussian width of the ground state wavefunction. So, if the Born-Oppenheimer approximation is invalid (thanks to curve crossings in the excited state, for example), the prediction of ϵ will be accordingly imprecise. Non-uniform prefactors in front of the ω_i in equation (3.14) may also contribute to this underestimation.

This simple one-state model cannot account for the cross section variations seen in the laboratory. *Selwyn et al.* [1981], for example, measured cross sections over the wavelength range 172–197 nm at six temperatures ranging from 150–500 K, while *Merienne et al.* [1990] carried out measurements over the wavelength range 200–240 nm at 3 temperatures

ranging from 220–296 K. The combined data [Selwyn *et al.*, 1981; Merienne *et al.*, 1990] yields temperature-independent cross sections for three vibrational states [Selwyn *et al.*, 1981]. The application of the temperature-dependent fractionation approach to N_2O is shown in Figure 3.6, where $^{14}\text{N}^{14}\text{N}^{16}\text{O}$, $^{14}\text{N}^{14}\text{N}^{18}\text{O}$, $^{15}\text{N}^{14}\text{N}^{16}\text{O}$, $^{14}\text{N}^{15}\text{N}^{16}\text{O}$, and $^{15}\text{N}^{15}\text{N}^{16}\text{O}$ are renamed 446, 448, 546, 456, and 556 for simplicity.

Figure 3.6 shows the predicted fractionation factor at 295 and 233 K using the temperature-dependent model described in section 3.2.4. Parameters for the state-decomposed cross sections and scaling factors f are given in Table 3.4. The latter account for small dipole moment surface variations with isotopic substitution. Our predictions are in good agreement with the *ab initio* calculations except for 546 and 556. The prediction for 556 at 233 K reproduces well the single mass spectrometric measurement from laboratory photolysis experiments [Kaiser *et al.*, 2003], and implies the algorithm and the assumption of ZPE' and $\Delta\text{ZPE}'$ (see section 3.2.4) used to calculate the cross sections as well as the fractionation factors are reasonable.

3.3.3 Nonlinear Triatomic Molecule: O_3

The dissociation cross sections of $^{16}\text{O}^{16}\text{O}^{16}\text{O}$ (666) and $^{18}\text{O}^{18}\text{O}^{18}\text{O}$ (888) have been measured by Parisse *et al.* [1996] at 295 K and are shown in Figure 3.7. Here, the cross sections have been normalized to the peak value of $\sigma(666)$, $\sigma_P = 1.2 \times 10^{-17} \text{ cm}^2$. Our model as well as YM97's ZPE model is applied, with results shown in Figure 3.8. O_3 is a nonlinear molecule, and so the reshaping of the wavefunction uses the full $\Delta\text{ZPE}'$'s since all three vibrational modes contribute significantly to the dissociation. The prediction of our model for 888 is in excellent agreement with the measurements. Figure 3.8 shows the fractionation factors for 667 ($^{16}\text{O}^{16}\text{O}^{17}\text{O}$), 676 ($^{16}\text{O}^{17}\text{O}^{16}\text{O}$), 668 ($^{16}\text{O}^{16}\text{O}^{18}\text{O}$), 686 ($^{16}\text{O}^{18}\text{O}^{16}\text{O}$), and 888.

The results show that the heavier isotopologues/isotopomers are substantially enriched by long wavelength ozone photolysis, with values that are significantly underestimated by the YM97's ZPE model.

3.4 Applications to the Atmosphere

Isotopic fractionation in the atmosphere plays an important role in constraining sources and sinks of atmospheric gases and for tracing the evolution of the atmosphere. Here we will briefly discuss some of the applications of this work.

HCl—Hydrogen chloride was discovered in the Venusian atmosphere at altitudes above the clouds (> 65 km above the surface) [*Connes et al.*, 1967], and the photochemistry of HCl has been studied extensively since then [*Prinn*, 1971; *McElroy et al.*, 1973; *Yung and DeMore*, 1982; *Bahou et al.* 2001]. The observed D/H ratio in the Venusian atmosphere is nearly 100 times greater than that in the terrestrial atmosphere [e.g., *Donahue et al.*, 1982; *McElroy et al.*, 1982]. Since the water vapor in the Venusian atmosphere is trapped below 60 km, mainly by H_2SO_4 , the major carrier of H in the upper atmosphere is HCl. Hence, the enrichment of deuterium in the Venusian atmosphere may be due the photolytic fractionation between DCl and HCl. Indeed, the photolytic rate of DCl turns out to be only 16% that of HCl for the conditions above the cloud layer [*Bahou et al.*, 2001]. This difference in the photolytic rates may contribute significantly to the enhancement of D/H ratio in the Venusian atmosphere above the clouds.

HI—Despite the importance of iodine chemistry in the terrestrial atmosphere [e.g., *Vogt et al.*, 1999], neither HI nor DI has been measured. We hope this work may stimulate interest in these two species.

N_2O —Nitrous oxide is a potent greenhouse molecule as well as the major source of NO_x in the upper atmosphere. It is produced mainly from land ($\sim 2/3$) and oceanic microbial activity ($\sim 1/3$) as a by-product of nitrification and denitrification reactions. Human activity plays an important role in the N_2O budget, in which about one-third of the current emissions are anthropogenic [IPCC, 2001]. The isotopic composition of N_2O has been extensively studied [Yoshida and Matsuo, 1983; Kim and Craig, 1993; Cliff and Thiemens, 1997; Rahn and Wahlen, 1997; Cliff *et al.*, 1999; Yoshida and Toyoda, 2000; Röckmann *et al.*, 2001a,b], and global modelling has been carried out to determine the spatial distribution, isotopic fractionation and budget of N_2O [McLinden *et al.*, 2003; Morgan *et al.*, 2004]. However, only singly substituted isotopologues/isotopomers 456, 546, 447, and 448 have been modelled to date.

Here, we extend the modelling to a doubly substituted isotopologue, 556. Our newly developed model is in good agreement with the measurements (Figures 3.5 and 3.6). The application to the Earth's stratosphere was carried out using the Caltech/JPL two-dimensional KINETICS model with an appropriate stream function. A detailed description of this model has been given in Morgan *et al.* [2004]. As shown in Figure 3.9, 556 is $\sim 50\%$ more enriched than 456 both in the lower stratosphere and in the upper stratosphere. Lower and upper stratospheric regions were separated at $\ln(f) = -0.6$, where f is the ratio of the remaining N_2O to that of the initial N_2O in the upwelling air parcel. As expected, the enrichment of this doubly substituted species is larger than those of singly substituted species, and reflects the fractionation levels induced by photolysis in both the 456 and 546 isotopologues [Kaiser *et al.*, 2003]. The latest generation of multi-collector stable isotope mass spectrometers are certainly capable of making high precision measurements on multiply substituted atmospheric trace gases [Eiler and Schauble, 2004], but our predicted results remain to be

verified by atmospheric measurements. Further, we know little about the biological production of doubly substituted N_2O . The major production mechanisms are nitrification and denitrification, with distinctive isotopic signatures [see *Stein and Yung*, 2003]. The doubly substituted species may offer additional information of the dependence of the production of N_2O as a function of the environmental conditions such as temperature, pH, and oxidation state. New laboratory measurements are needed to establish these fractionation patterns.

O_3 —The roles of O_3 as UV shield and as a greenhouse gas are well known. The production rate of O_3 in the stratosphere is mass-independent (i.e., $\delta^{17}\text{O} \approx \delta^{18}\text{O}$), and a chemical mechanism consistent with these properties has been identified by *Gao and Marcus* [2001]. In the stratosphere, the photo-induced isotopic fractionation for O_3 is clearly mass-dependent, according to our model. The conclusion is robust since the prediction for 888 is in excellent agreement with the laboratory measurements (see Figure 3.8). Interestingly, the isotopomer dependence (686 versus 668, for example) of photolysis is opposite to that of the chemical reactions which form ozone. As a result, both the overall fractionation and the isotopic patterns in the isotopomers will be altitude-dependent, and any detailed analysis of the atmospheric data must account for both the kinetic and photolysis components. Further work that compares the model results to observations is in progress.

3.5 Conclusion

We present a simple and flexible semi-analytic model based on the Born-Oppenheimer approximation and the Reflection Principle for the photo-induced isotopic fractionation in polyatomic molecules of interest to atmospheric chemistry. Only direct photolysis through a single excited state is treated; other types of photodissociation (predissociation, coupled

states photodissociation, and the like) cannot be examined within this formalism. Fortunately, the applicability of the direct photodissociation limit can be tested by comparing the time scales for dissociation and vibration from the experimental data themselves – ideally $\Delta\nu_{h\nu} \gg \nu_{\text{vib}}$, where $\Delta\nu_{h\nu}$ is the full width half maximum of the photodissociation cross section(s) and ν_{vib} is (are) the fundamental vibrational frequency (frequencies).

The small changes of a molecule’s ZPE as a function of isotopic substitution have two consequences: displacing the peak of the spectrum by an amount roughly equal to ΔZPE and the modification of the shape of the vibrational wavefunction. The model quantitatively predicts the dissociation cross section for the isotopologues of the diatomic and triatomic molecules investigated here (HCl, HI, N₂O, O₃), yet is sufficiently simple to be included in detailed chemistry/circulation codes that can be used to examine the sources and sinks of important atmospheric constituents. For example, *Blake et al.* [2003] and *Morgan et al.* [2004] have modelled the stratospheric enrichments of nitrous oxide, and the model values are in good agreement with measurements. This also implies that our understanding of the stratospheric circulation is largely satisfactory. Our model may be generalized to more complex systems by taking the “effective” normal modes of molecules into account. Validity can be checked by comparing the characteristic width to the fundamental vibrational frequency (frequencies).

Bibliography

- Ascenzi, D., P.M. Regan, and A.J. Orr-Ewing, The Ultraviolet Photodissociation of DCl: H/D Isotope Effects on the Cl(²P) Atom Spin-Orbit Branching, *Chemical Physics Letters*, *310*, 477-484, 1999.
- Bahou, M., C. Y. Chung, Y. P. Lee, B. M. Cheng, Y. L. Yung, and L. C. Lee, Absorption Cross Sections of HCl and DCl at 135–232 nanometers, *Astrophysical Journal Letters*, *559*, L179-L182, 2001.
- Blake, G.A., M.C. Liang, C.G. Morgan, and Y.L. Yung, A Born-Oppenheimer Photolysis Model of N₂O Fractionation, *Geophysics Research Letters*, *30*,(12) 1656, doi:10.129/2003GL016932, 2003.
- Brenninkmeijer, C.A.M., D.C. Lowe, M.R. Manning, R.J. Sparks, and P.F.J. vanVelthoven, The ¹³C, ¹⁴C and ¹⁸O Isotopic Composition of CO, CH₄, and CO₂ in the Higher Southern Latitudes Lower Stratosphere, *Journal of Geophysics Research*, *100*(D12), 26163-26172, 1995.
- Brown, A., and G.G. Balint-Kurti, Spin-Orbit Branching in the Photodissociation of HF and DF. I. A Time-Dependent Wave Packet Study for Excitation from v=0, *Journal of Chemical Physics*, *113*(5), 1870-1878, 2000.
- Cliff, S.S., C.A.M. Brenninkmeijer, and M. H. Thiemens, First Measurement of the ¹⁸O/¹⁶O

- and $^{18}\text{O}/^{16}\text{O}$ Ratios in Stratospheric Nitrous Oxide: A Mass-Independent Anomaly, *Journal of Geophysical Research*, *104*,(D13) 16171-16175, 1999.
- Cliff, S.S., and M. H. Thiemens, The $^{18}\text{O}/^{16}\text{O}$ and $^{17}\text{O}/^{16}\text{O}$ Ratios in Atmospheric Nitrous Oxide: A Mass-Independent Anomaly, *Science*, *278*, 1774-1776, 1997.
- Connes, P., J. Connes, W.S. Benedict, L.D. Kaplan, Traces of HCl and HF in the Atmosphere of Venus, *Astrophysical Journal*, *147*, 1230-1237, 1967.
- Dahl, J.P., Dynamical Equations for the Wigner Functions, *Energy Storage and Redistributions in Molecules*, ed. J. Hinze, Plenum Press, New York, 1983.
- Debergh, C., The D/H ratio and the Evolution of Water in the Terrestrial Planets, *Origins of Life and Evolution of the Biosphere*, *23*(1), 11-21, 1993.
- Donahue, T.M., J.H. Hoffman, R.R. Hodges, and A.J. Watson, Venus Was Wet—A Measurement of the Ratio of Deuterium to Hydrogen, *Science*, *216*, 630-633, 1982.
- Eiler, J.M., and E. Schauble, $^{18}\text{O}^{13}\text{C}^{16}\text{O}$ in Earth's Atmosphere, *Geochimica et Cosmochimica Acta*, *68*, 4767-4777, 2004.
- Frost, R.L., J.E. Beckman, G.D. Watt, G.J. White, and J.P. Phillips, Limits on the D:H Mod Ratio in the Interstellar Medium for Molecular Observations, in *Submillimeter Wave Astronomy*, Cambridge Univ. Press, New York, 1982.
- Gao, Y.Q., and R.A. Marcus, Strange and Unconventional Isotope Effects in Ozone Formation, *Science*, *293*, 259-263, 2001.
- Geiss, J., and H. Reeves, Deuterium in the Solar System, *Astronomy and Astrophysics*, *93*, 1-2, 1981.

- Huff, A.K., and M.H. Thiemens, $^{17}\text{O}/^{16}\text{O}$ and $^{18}\text{O}/^{16}\text{O}$ Isotope Measurements of Atmospheric Carbon Monoxide and its Sources, *Geophysics Research Letters*, 25(18), 3509-3512, 1998.
- IPCC, Climate Change: The Scientific Basis, Cambridge Univ. Press, edited by J. T. Houghton et al., 2001.
- Irion, F.W., E.J. Moyer, M.R. Gunson, C.P. Rinsland, Y.L. Yung, H.A. Michelsen, R.J. Salawitch, A.Y. Chang, M.J. Newchurch, M.M. Abbas, M.C. Abrams, and R. Zanders, Stratospheric Observations of CH_3D and HDO from ATMOS Infrared Solar Spectra: Enrichments of Deuterium in Methane and Implications for HD, *Geophysics Research Letters*, 23(17), 2381-2384, 1996.
- Johnson, M. S., G. Billing, A. Gruodis, and M. Janssen, Photolysis of Nitrous Oxide Isotopomers Studied by Time-Dependent Hermite Propagation, *Journal of Physical Chemistry A*, 105, 8672-8680, 2001.
- Johnston, J.C., and M.H. Thiemens, The Isotopic Composition of Tropospheric Ozone in Three Environments, *Journal of Geophysics Research*, 102(D21), 25395-25404, 1997.
- Kaiser, J., T. Röckmann, C.A.M. Brenninkmeijer, and P.J. Crutzen, Wavelength Dependence of Isotope Fractionation in N_2O Photolysis, *Atoms. Chem. Phys. Discuss.*, 2, 1735-1763, 2002.
- Kaiser, J., T. Röckmann, and C.A.M. Brenninkmeijer, Assessment of $^{15}\text{N}^{15}\text{N}^{16}\text{O}$ as a Tracer of Stratospheric Processes, *Geophysics Research Letters*, 30(2), 1046, doi:10.1029/2002GL016253, 2003.

- Kaye, J.A., Mechanisms and Observations for Isotope Fractionation of Molecular Species in Planetary Atmosphere, *Review of Geophysics*, 25(8), 1609-1658, 1987.
- Kim, K. R., and H. Craig, ^{15}N and ^{18}O Characteristics of Nitrous Oxide: A Global Perspective, *Science*, 262, 1855-1857, 1993.
- Lämmerzahl, P., T. Röckmann, C.A.M. Brenninkmeijer, D. Krankowsky, and K. Mauersberger, Oxygen Isotope Composition of Stratospheric Carbon Dioxide, *Geophysics Research Letters*, 29(12), 10.1029/2001GL014343, 2002.
- Mauersberger, K., Ozone Isotope Measurements in the Stratosphere, *Geophysics Research Letters*, 14(1), 80-83, 1987.
- Mauersberger, K., P. Lämmerzahl, and D. Krankowsky, Stratospheric Ozone Isotope Enrichments-Revisited, *Geophysics Research Letters*, 28(16), 3155-3158, 2001.
- McElroy, M.B., N.D. Sze, and Y.L. Yung, Photochemistry of Venus Atmosphere, *Journal of the Atmospheric Sciences*, 30(7), 1437-1447, 1973.
- McElroy, M.B., M.J. Prather, and J.M. Rodriguez, Escape of Hydrogen from Venus, *Science*, 215, 1614-1615, 1982.
- McLinden, C.A., M.J. Prather, and M.S. Johnson, Global Modeling of the Isotopic Analogues of N_2O : Stratospheric Distributions, Budgets, and the ^{17}O - ^{18}O Mass-Independent Anomaly, *Journal of Geophysics Research*, 108(D8), 4233, doi:10.1029/2002JD002560, 2003.
- Merienne, M., B. Coguart, and A. Jenouvrier, Temperature Effect on the Ultraviolet Absorption of CFCl_3 , CF_2Cl_2 , and N_2O , *Planetary and Space Science*, 38, 617-625, 1990.

- Miller, C.E., and Y.L. Yung, Photo-Induced Isotopic Fractionation, *Journal of Geophysics Research*, 105(23), 29039-29051, 2000.
- Morgan, C., M. Allen, M.C. Liang, R.L. Shia, G.A. Blake, and Y.L. Yung, Isotopic Fractionation of Atmospheric Nitrous Oxide, *Journal of Geophysics Research*, 109, D04305, doi:10.1029/2003JD003402, 2004.
- Mulliken, R. S., Role of Kinetic Energy in the Franck-Condon Principle, *Journal of Chemical Physics*, 55, 309-314, 1971.
- Ogilvie, J.F., Semi-Experimental Determination of a Repulsive Potential Curve for Hydrogen Iodide, *Transactions of the Faraday Society*, 67, 2205, 1971.
- Owen, T., Deuterium in the Solar-System, *Symposium - International Astronomical Union*, 150, 97-101, 1992.
- Owen, T., B.L. Lutz, and C. Debergh, Deuterium in the Outer Solar System: Evidence for 2 Distinct Reservoirs, *Nature*, 320, 244-246, 1986.
- Owen, T., J.P. Maillard, C. Debergh, and B.L. Lutz, Deuterium on Mars: The Abundance of HDO and the Value of D/H, *Science*, 240, 1767-1770., 1988.
- Parisse, C., J. Brion, and J. Malicet, UV Absorption Spectrum of Ozone: Study of the Isotope Effect in the Hartley System, *Chemical Physics Letters*, 248, 31-36, 1996.
- Prinn, R.G., Photochemistry of HCl and Other Minor Constituents in Atmosphere of Venus, *Journal of the Atmospheric Sciences*, 28(6), 1058, 1971.
- Rahn, T., and M. Wahlen, Stable Isotope Enrichment in Stratospheric Nitrous Oxide, *Science*, 278, 1776-1778, 1997.

- Rahn, T., H. Zhang, M. Wahlen, and G.A. Blake, Stable Isotope Fractionation during Ultraviolet Photolysis of N₂O, *Geophysics Research Letters*, *25*, 4489-4492, 1998.
- Richet, P., Y. Bottinga, and M. Javoy, Review of Hydrogen, Carbon, Nitrogen, Oxygen, Sulfur, and Chlorine Stable Isotope Fractionation Among Gaseous Molecules, *Annual Review of Earth and Planetary Sciences*, *5*, 65-110, 1977.
- Röckmann, T., C.A.M. Brenninkmeijer, P.J. Crutzen, and U. Platt, Short-Term Variations in the ¹³C/¹³C Ratio of CO as a Measure of Cl Activation during Tropospheric Ozone Depletion Events in the Arctic, *Journal of Geophysics Research*, *104*(D1), 1691-1697, 1999.
- Röckmann, T., C. A. M. Brenninkmeijer, M. Wollenhaupt, J. N. Crowley, and P. J. Crutzen, Measurement of the Isotopic Fractionation of ¹⁵N¹⁴N¹⁶O, ¹⁴N¹⁵N¹⁶O, and ¹⁴N¹⁴N¹⁸O in the UV Photolysis of Nitrous Oxide, *Geophysics Research Letters*, *27*, 1399-1402, 2000.
- Röckmann, T., J. Kaiser, J. N. Crowley, C. A. M. Brenninkmeijer, and P. J. Crutzen, The Origin of the Anomalous or “Mass-Independent” Oxygen Isotope Fractionation in Tropospheric N₂O, *Geophysics Research Letters*, *28*, 503-506, 2001a.
- Röckmann, T., J. Kaiser, C. A. M. Brenninkmeijer, J. N. Crowley, R. Borchers, W. A. Brand, and P. J. Crutzen, Isotopic Enrichment of Nitrous Oxide (¹⁵N¹⁴N¹⁶O, ¹⁴N¹⁵N¹⁶O, ¹⁴N¹⁴N¹⁸O) in the Stratosphere and in the Laboratory, *Journal of Geophysics Research*, *106*, 10403-10410, 2001b.
- Schinke, R., *Photodissociation Dynamics*, Cambridge Univ. Press, New York, NY, 1993.
- Selwyn, G., and H. S. Johnston, Ultraviolet Absorption Spectrum of Nitrous Oxide as a

- Function of Temperature and Isotopic Substitution, *Journal of Chemical Physics*, *74*, 3791-3803, 1981.
- Stein, L.Y., and Y.L. Yung, Production, Isotopic Composition, and Atmospheric Fate of Biologically Produced Nitrous Oxide, *Annual Review of Earth and Planetary Sciences*, *31*, 329-356, 2003.
- Tonokura K., Y. Matsumi, M., Kawasaki, S. Tasaki, and R. Bersohn, Photodissociation of Hydrogen Chloride at 157 and 193 nm: Angular Distributions of Hydrogen Atoms and Fine-Structure Branching Ratios of Chlorine Atoms in the 2P_j Levels, *Journal of Chemical Physics*, *97*(11), 8210-8215, 1992.
- Turatti, F., D.W.T. Griffith, S.R. Wilson, M.B. Esler, T. Rahn, H. Zhang, and G.A. Blake, Positionally Dependent ^{15}N Factors in the UV Photolysis of N_2O Determined by High Resolution FTIR Spectroscopy, *Geophysics Research Letters*, *27*, 2489-2492, 2000.
- Urey, H.C., The Thermodynamic Properties of Isotopic Substances, *Journal of the Chemical Society*, 562-581, 1947.
- van Harrevelt R., and M.C. van Hemert, Photodissociation of Water. II. Wave Packet Calculations for the Photofragmentation of H_2O and D_2O in the \tilde{B} Band, *Journal of Chemical Physics*, *112*(13), 5787-5808, 2000.
- Vidal-Madjar, A., R. Ferlet, and M. Lemoine, Deuterium Observations in the Galaxy, *Space Science Reviews*, *84*(1-2), 297-308, 1998.
- Vogt, R., R. Sander, R. Von Glasow, and P.J. Crutzen, Iodine chemistry and its Role in Halogen Activation and Ozone Loss in the Marine Boundary Layer: A Model Study, *Journal of Atmospheric Chemistry*, *32*(3), 375-395, 1999.

- Wigner, E., On the Quantum Correction for Thermodynamic Equilibrium, *Physical Review*, *40* 749-759, 1932.
- Yoshida, N., and S. Matsuo, Nitrogen Isotope Ratio of Atmospheric N₂O as a Key to the Global Cycle of N₂O, *Geochemical Journal*, *17*(5), 231-239, 1983.
- Yoshida, N., and S. Toyoda, Constraining the Atmospheric N₂O Budget from Intramolecular Site Preference in N₂O Isotopomers, *Nature*, *405*, 330-334, 2000
- Yoshino, K., D. E. Freeman, and W. H. Parkinson, High resolution Absorption Cross-Section Measurements of N₂O at 295-299 K, *Planetary and Space Science*, *32*, 1219-1222, 1984.
- Yung, Y.L., W.B. DeMore, Photochemistry of the Stratosphere of Venus—Implications for Atmospheric Evolution, *Icarus*, *51*(2), 199-247, 1982.
- Yung, Y.L., and R.W. Ditsly, Deuterium in the Solar-System, *ACS Symposium Series*, *502*, 369-389, 1992.
- Yung, Y.L., and D.M. Kass, Deuteronomy? A puzzle of Deuterium and Oxygen on Mars, *Science*, *280*, 1545-1546, 1998.
- Yung, Y.L., and C.E. Miller, Isotopic Fractionation of Stratospheric Nitrous Oxide, *Science*, *278*, 1778-1780, 1997.
- Zhang, H., P.O. Wennberg, V.H. Wu, G.A. Blake, Fractionation of ¹⁴N¹⁵N¹⁶O and ¹⁵N¹⁴N¹⁶O during Photolysis at 213 nm, *Geophysics Research Letters*, *27*(16), 2481-2484, 2000.

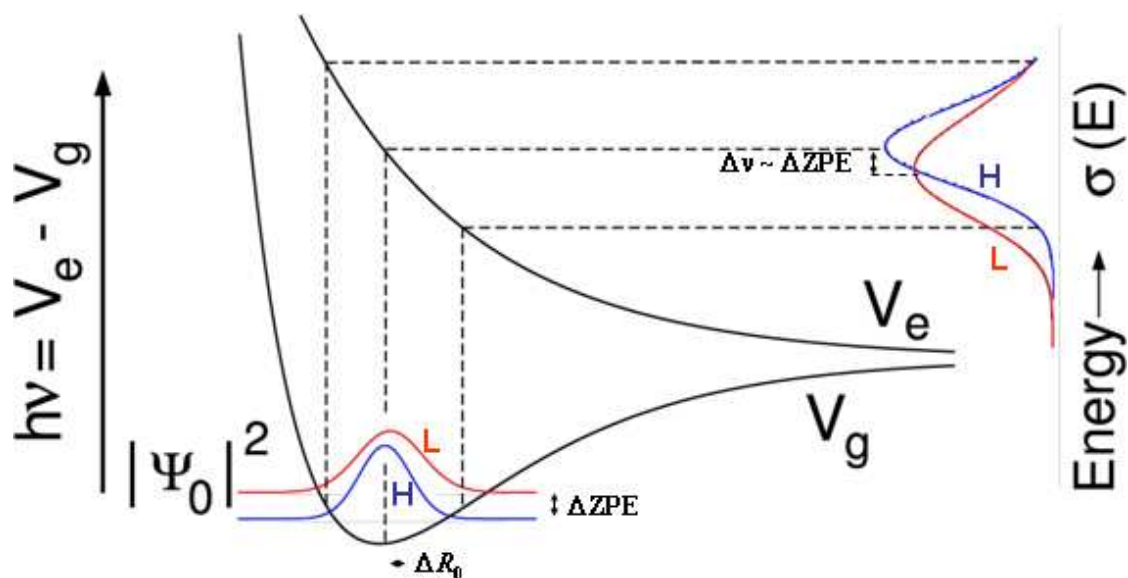


Figure 3.1 Photolysis Model—Schematic diagram of the direct photodissociation process, illustrating the Born-Oppenheimer approximation and the Reflection Principle (dashed lines). “L” and “H” refer to the standard and isotopically substituted species, respectively. Ψ_0 , V_g , and V_e denote the vibrationally averaged ground state wavefunction, ground state electronic potential, and dissociating electronic potential, respectively.

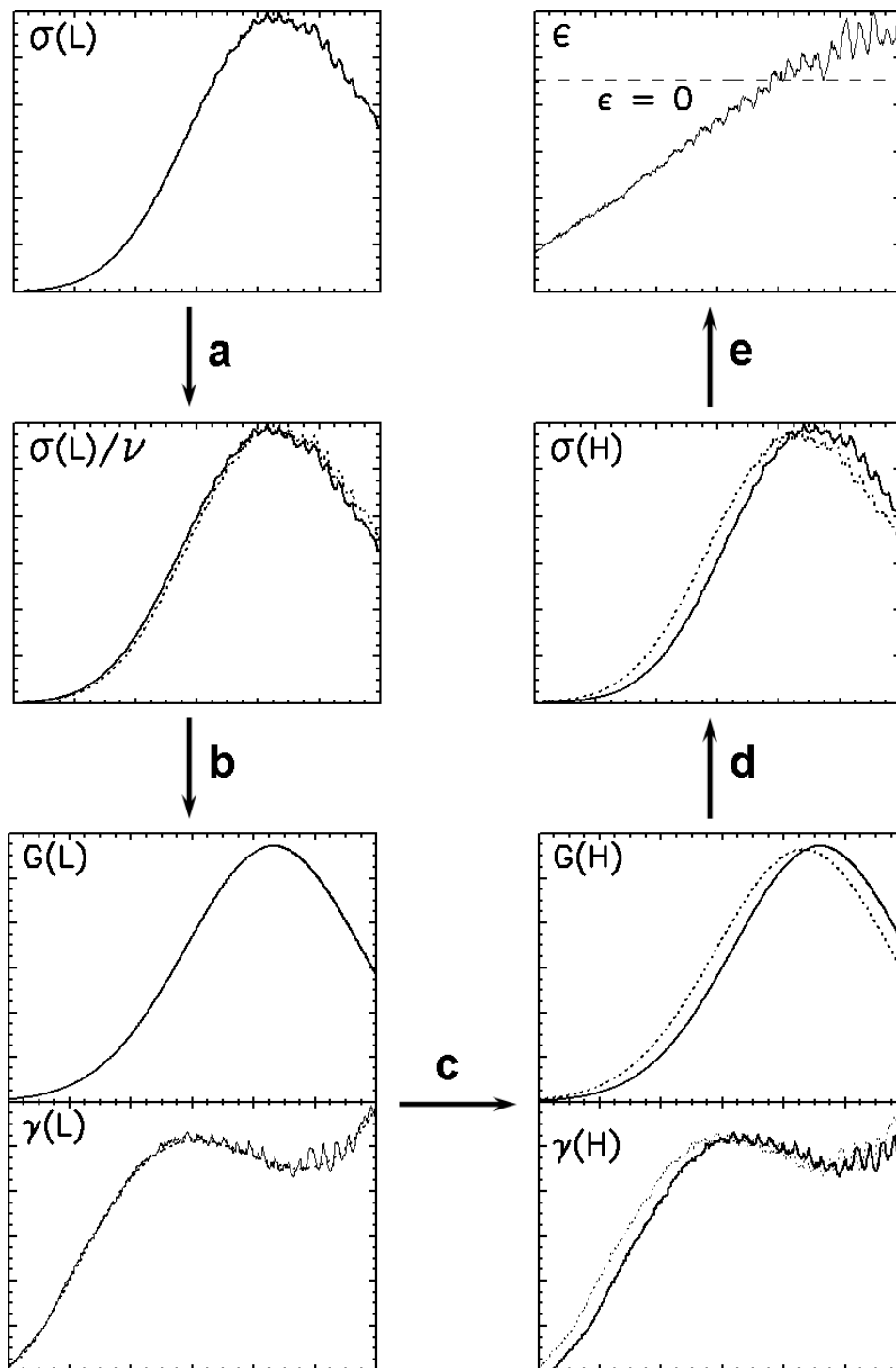


Figure 3.2 Photolysis Model—Schematic diagram illustrating the steps in the application of the photodissociation model, described in section 3.2. The vertical axis refers to the physical quantity in the upper-left corner in each panel; the horizontal axis denotes the photon frequency ν . “L” and “H” denote the standard and isotopically substituted species, respectively. The full procedure is divided into five steps: (a)-(e). See text for details.

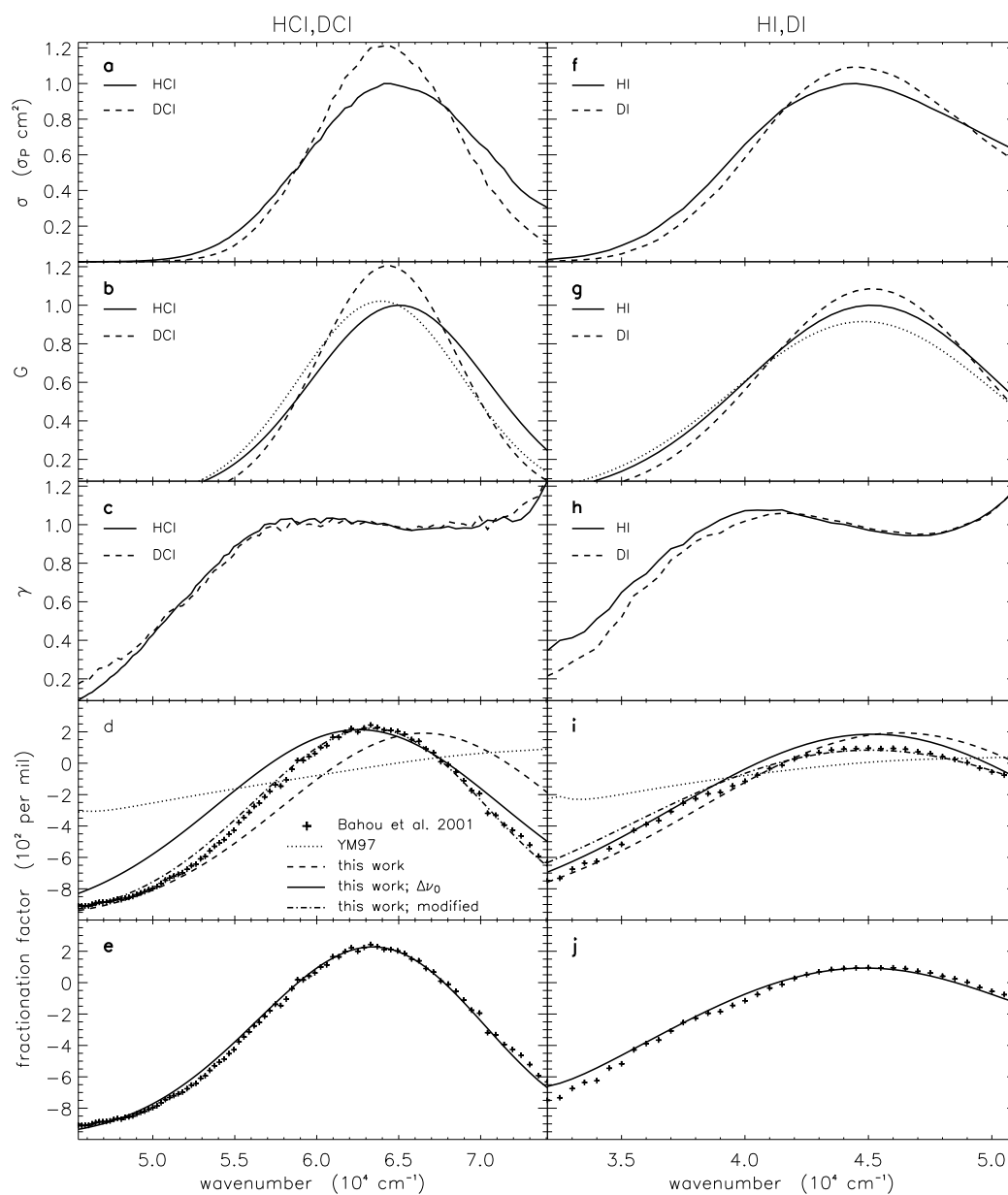


Figure 3.3 Photolysis Model—Applications of the new photodissociation algorithm to the diatomic molecules HCl/DCI and HI/DI. The first three panels present the decomposition of the individual cross sections into their isotope-dependent (G) and isotope-independent (γ) components. The bottom two panels present various fits to the D/H fractionation factor(s). The dissociation cross sections in Figures 3.3a and 3.3f have been divided by the maximum cross sections of the standard species HCl and HI, with $\sigma_P = 3.4 \times 10^{-18} \text{ cm}^2$ and $\sigma_P = 8.2 \times 10^{-18} \text{ cm}^2$, respectively. The various model fits in Figures 3.3d and 3.3i denote the state decomposition from the spin-orbit coupling of Cl and I. The final fits incorporating γ are given in Figures 3.3e and 3.3j.

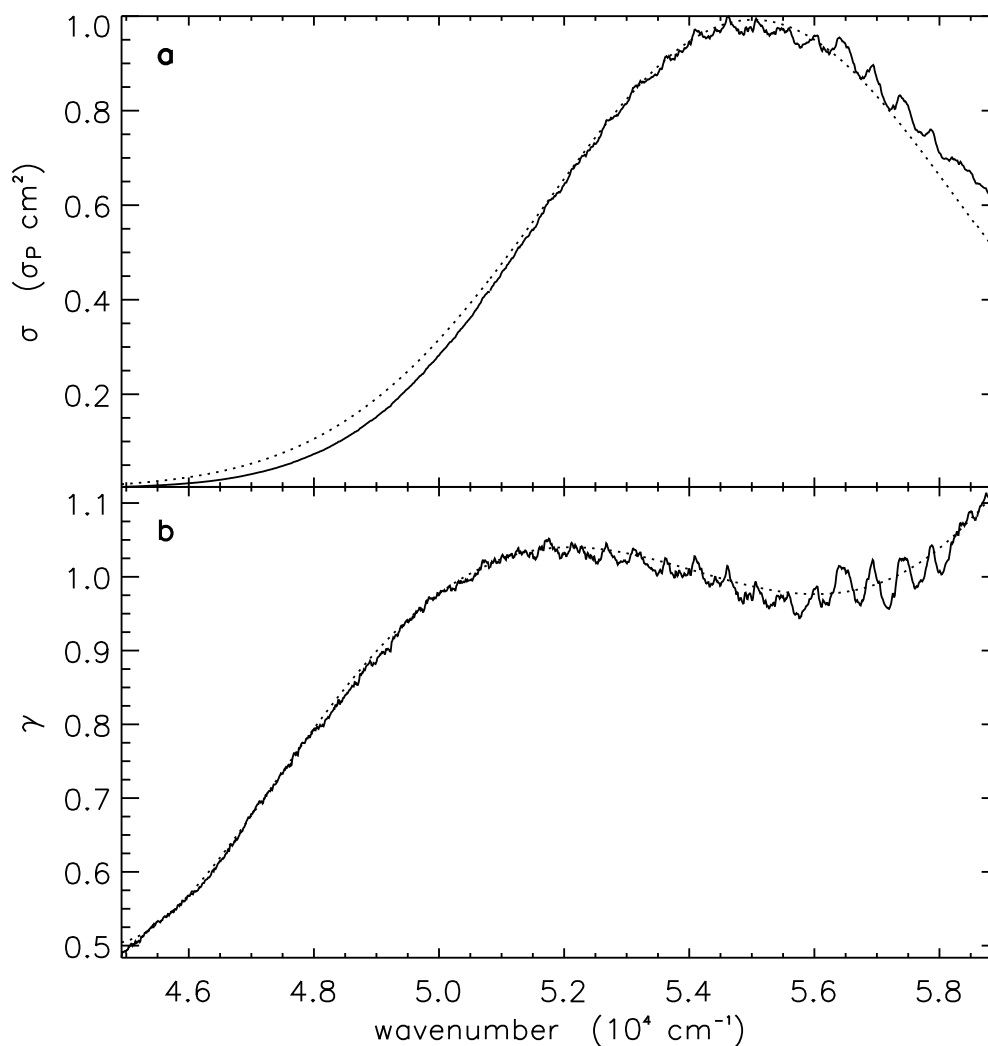


Figure 3.4 Photolysis Model— a: The $^{14}\text{N}^{14}\text{N}^{16}\text{O}$ photodissociation cross section, measured by *Yoshino et al.* [1984] at 295 K, and normalized to the peak $\sigma_P = 1.4 \times 10^{-18} \text{ cm}^2$. The gaussian fit is shown by the dotted line. b: The form of γ for N_2O . A fourth-order polynomial fit is shown by the dotted line, which has a functionality similar to the HCl and HI systems (see Figures 3.3c and 3.3h).

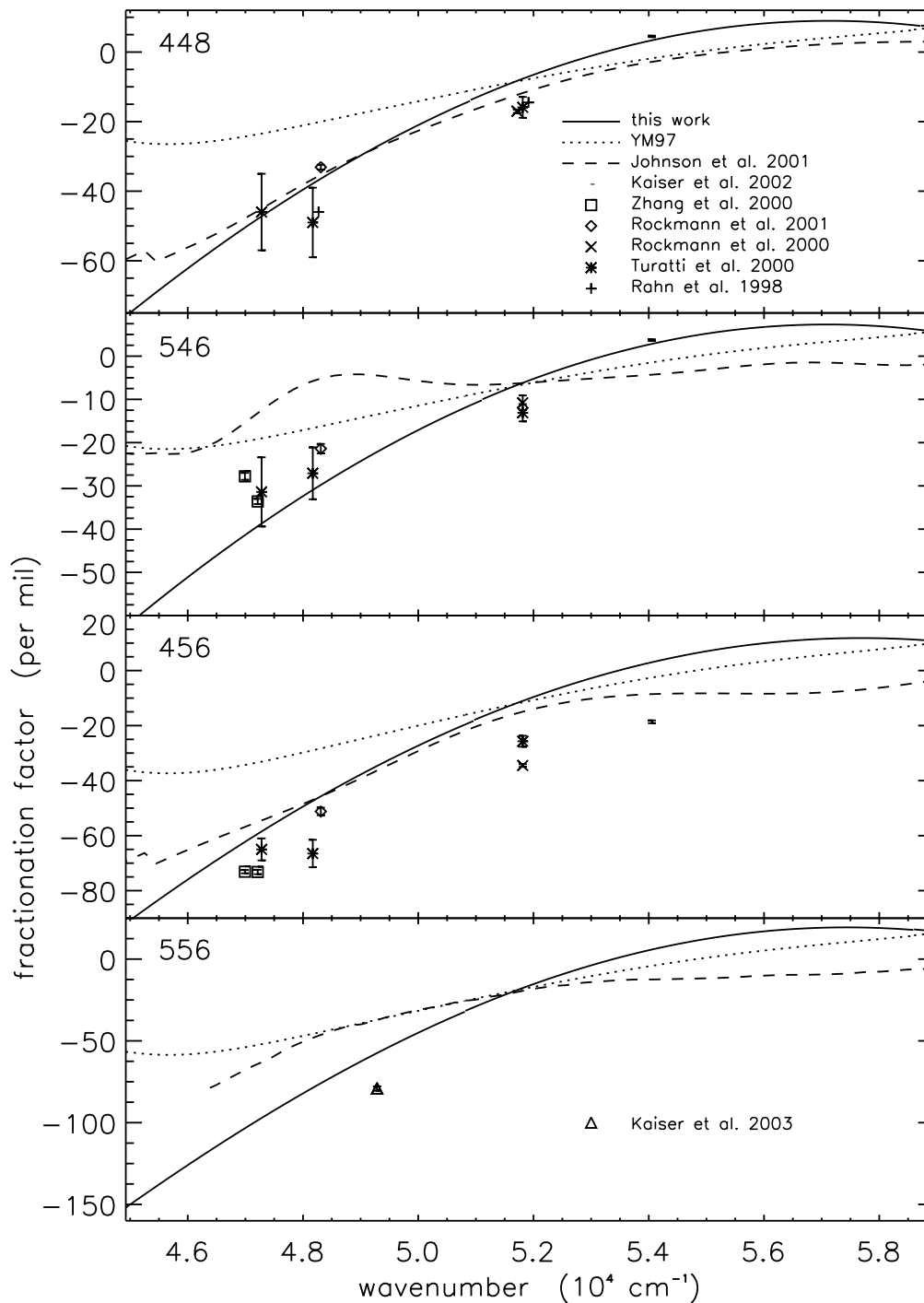


Figure 3.5 Photolysis Model—Comparison of the predicted ϵ using our new algorithm to YM97’s ZPE model, Johnson et al.’s *ab initio* calculation, and laboratory measurements (with $2\text{-}\sigma$ error bar overlotted) for four N_2O isotopologues/isotopomers. The solid curve depicts the temperature-independent model described in section 3.2.4.

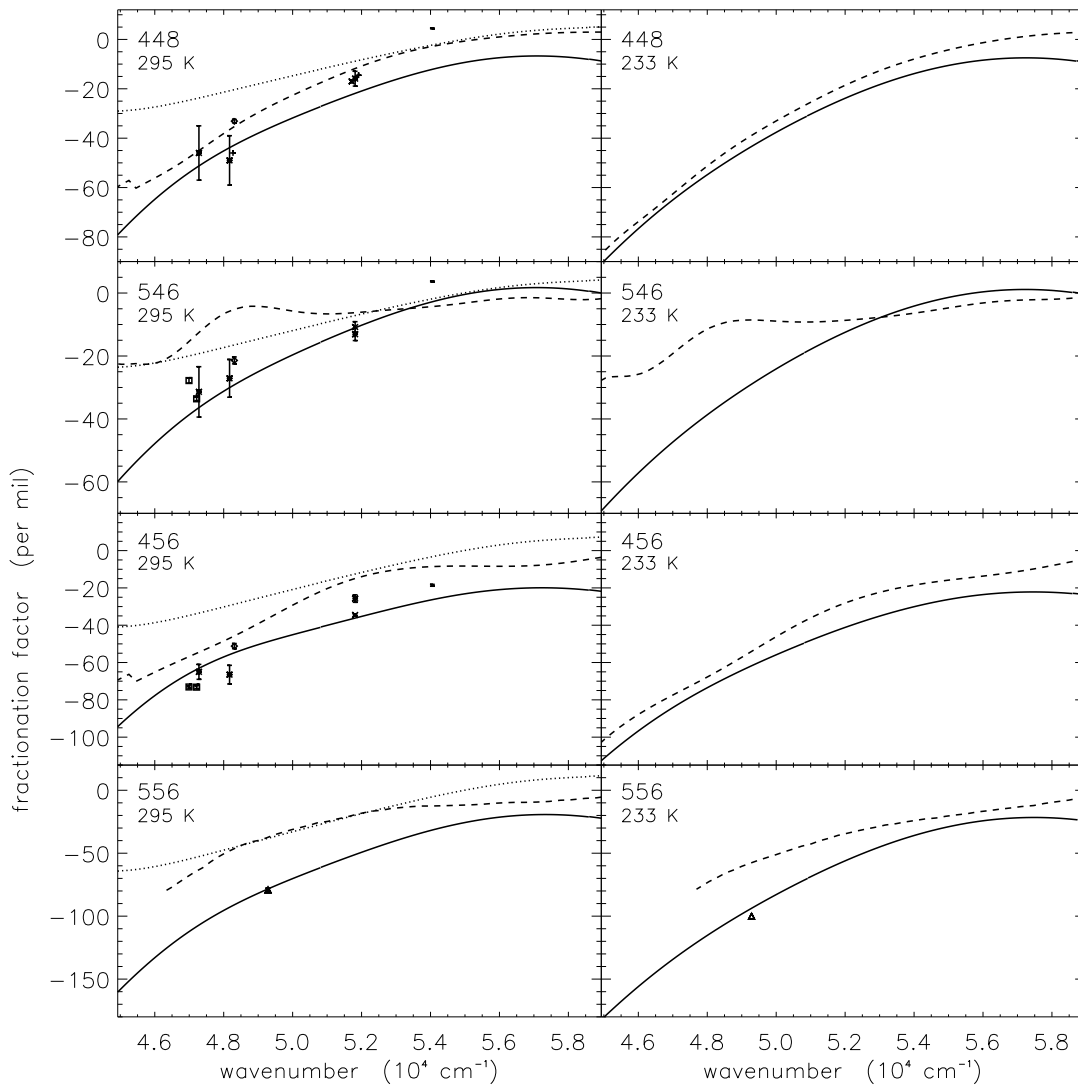


Figure 3.6 Photolysis Model—Comparison of the temperature dependence of ϵ using the three state temperature-dependent model (section 3.2.4) to Johnson et al.’s *ab initio* calculation for N_2O isotopologues/isotopomers at 295 and 233 K.

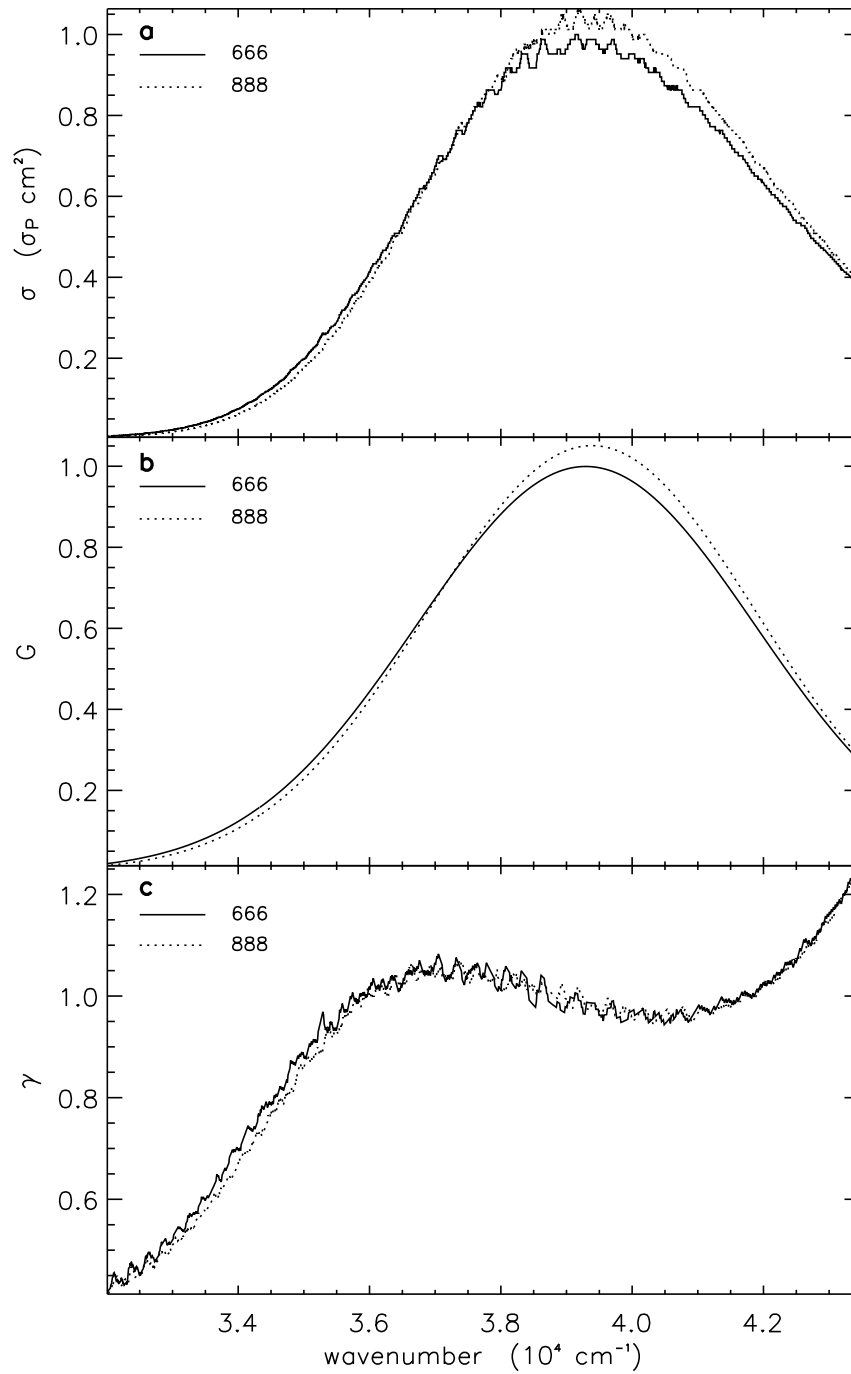


Figure 3.7 Photolysis Model— a: The dissociation cross sections of $^{16}\text{O}^{16}\text{O}^{16}\text{O}$ and $^{18}\text{O}^{18}\text{O}^{18}\text{O}$ as measured by *Parisse et al.* [1996], at 295 K and normalized to $\sigma_P = 1.2 \times 10^{-17} \text{ cm}^2$. The decomposed γ is shown in panel b.

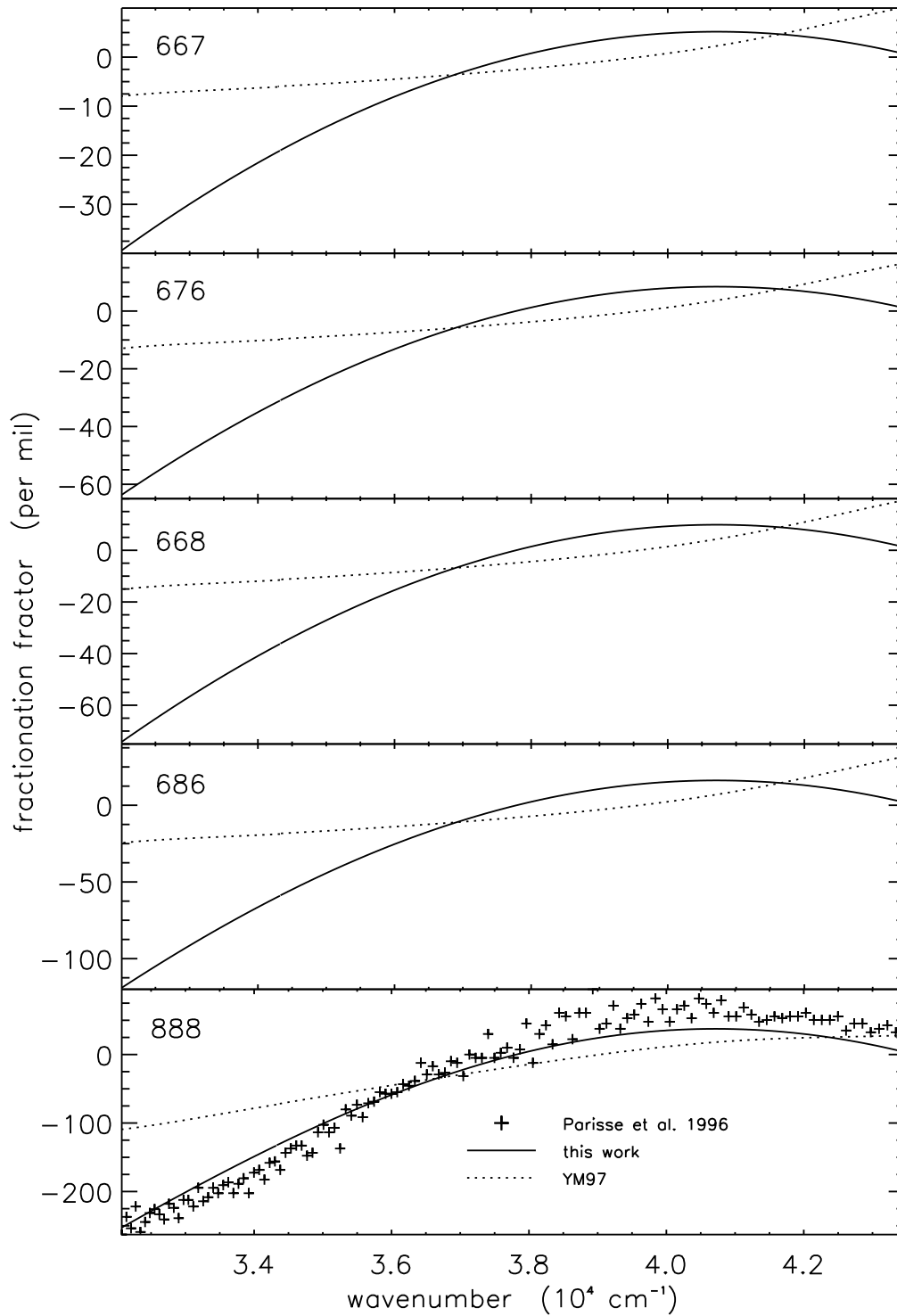


Figure 3.8 Photolysis Model—Comparison of the predicted ϵ to the YM97's ZPE model and laboratory measurements [*Parisse et al.*, 1996] for O_3 isotopologues and isotopomers.

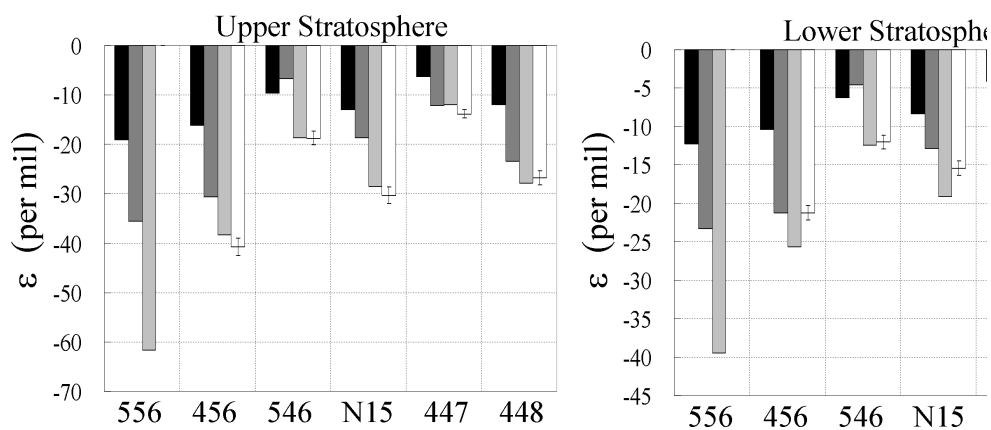


Figure 3.9 Photolysis Model—Applications of the predicted fractionations of the dissociation cross sections of nitrous oxide’s isotopologues/isotopomers in the Earth’s lower and upper stratosphere. $\ln(f) = -0.6$ was used to delineate the boundary, where f is the ratio of the remaining N_2O to that of the initial N_2O in the upwelling air parcel. White bar: Atmospheric measurements, with $1\text{-}\sigma$ error bars overplotted. Light gray bar: This work. Dark gray bar: Johnson et al.’s *ab initio* calculations. Black bar: The ZPE model of YM97.

Table 3.1. Photolysis Model—Vibrational Frequencies for HCl, HI, N₂O, and O₃

molecule	isotopologue	ω_1	ω_2	ω_3	ZPE	ZPE'
HCl	– ¹ HCl	2964.5	1482.3	1482.3
	– ² DCl	2131.6	1065.8	1065.8
HI	– ¹ HI	2289.2	1144.6	1144.6
	– ² DI	1629.7	814.9	814.9
N ₂ O	– ¹⁴ N ¹⁴ N ¹⁶ O	1284.9	588.7	2223.8	2343.1	1754.3
	– ¹⁴ N ¹⁴ N ¹⁷ O	1264.7	586.3	2220.1	2328.7	1742.4
	– ¹⁴ N ¹⁴ N ¹⁸ O	1246.9	584.1	2216.7	2315.9	1731.8
	– ¹⁵ N ¹⁴ N ¹⁶ O	1280.4	575.5	2177.7	2321.1	1735.8
	– ¹⁴ N ¹⁵ N ¹⁶ O	1269.9	585.3	2201.6	2304.5	1729.0
	– ¹⁵ N ¹⁵ N ¹⁶ O	1265.3	571.9	2154.7	2281.9	1710.0
O ₃	– ¹⁶ O ¹⁶ O ¹⁶ O	1103.1	700.9	1042.1	1423.1	1423.1
	– ¹⁶ O ¹⁶ O ¹⁷ O	1095.7	692.4	1035.4	1411.7	1411.7
	– ¹⁶ O ¹⁶ O ¹⁸ O	1090.4	684.6	1028.1	1401.5	1401.5
	– ¹⁶ O ¹⁷ O ¹⁶ O	1087.8	697.1	1024.4	1404.7	1404.7
	– ¹⁶ O ¹⁸ O ¹⁶ O	1074.3	693.3	1008.5	1388.0	1388.0
	– ¹⁸ O ¹⁸ O ¹⁸ O	1041.6	661.5	984.8	1343.9	1343.9

Note. — The units are in cm⁻¹.

Table 3.2. Photolysis Model—Parameters Obtained from Gaussian Fitting

molecule	isotopologue	ν_0	W	amplitude
HCl	– ^1HCl	65034.6	5401.1	1.000
	– ^2DCl	64345.7	4252.1	1.205
HI	– ^1HI	45123.8	5085.7	1.000
	– ^2DI	45133.3	4469.0	1.085
N_2O	– $^{14}\text{N}^{14}\text{N}^{16}\text{O}$	55027.7	3321.7	1.000
O_3	– $^{16}\text{O}^{16}\text{O}^{16}\text{O}$	39291.1	2586.5	1.000
	– $^{18}\text{O}^{18}\text{O}^{18}\text{O}$	39383.9	2514.6	1.052

Note. — The units for ν_0 and W are in cm^{-1} . The amplitude of the isotopically substituted species has been normalized by that of the standard species.

Table 3.3. Photolysis Model—Parameters for HCl and HI at Two Dissociation Channels

molecule	ν_0^1	W^1	ν_0^2	W^2
HCl	63929.9	5017.1	67599.2	5369.7
HI	44803.6	5296.6	45621.5	4644

Note. — The superscripts 1 and 2 are for the dissociation via the ground Cl and excited Cl channels, respectively. The decomposition is based on the adiabatic dissociation of DCl and DI with the branching ratio of 0.3 for HCl and HI via the excited Cl/I channel.

Table 3.4. Photolysis Model—Parameters for Decomposed Cross Section and f Factor of N₂O

state	amplitude	ν_0	W	
0	1.00	55450.5	3166.3	
1	3.46	54536.7	3105.4	
2	3.51	50165.0	2338.7	
species	448	546	456	556
f	0.981	0.992	0.960	0.953

Note. — The peak amplitude of the vibrational ground state (0) is 1.2×10^{-19} cm².

Chapter 4

Isotopic Composition of Stratospheric Ozone

Mao-Chang Liang, Fredrick W. Irion, Jason D. Weibel, Charles E.

Miller, Geoffrey A. Blake, and Yuk L. Yung

Journal of Geophysical Research-Atmospheres, 111(D2), D02302, 2006.

Abstract

We present a kinetic calculation for the isotopic composition of stratospheric ozone. The calculated enrichments of $^{49}\text{O}_3$ and $^{50}\text{O}_3$ are in agreement with atmospheric measurements made at mid-latitudes. Integrating the kinetic fractionation processes in the formation and photolysis of ozone, we obtain enrichments of $\sim 7.5\text{-}10.5$ and $\sim 7.5\text{-}12.5\%$ (referenced to atmospheric O_2) for $\delta^{49}\text{O}_3$ and $\delta^{50}\text{O}_3$, respectively, at altitudes between 20 and 35 km; the photolysis in the Hartley band of ozone is responsible for the observed altitude variation. The overall magnitude of the ozone enrichments ($\sim 10\%$) is large compared with that commonly known in atmospheric chemistry and geochemistry. The heavy oxygen atom in ozone is therefore useful as a tracer of chemical species and pathways that involve ozone or its derived products. For example, the mass anomalies of oxygen in two greenhouse gases, CO_2 and N_2O , are likely the consequences of the transfer of heavy oxygen atoms from ozone.

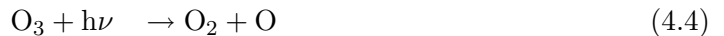
4.1 Introduction

It has been more than 20 years since the discovery of the heavy ozone anomaly [*Mauersberger, 1981; Thiemens and Heidenreich, 1983*]. The overall magnitude of the ozone enrichments is large compared with that commonly known in atmospheric chemistry and geochemistry. The heavy oxygen atom in ozone is therefore useful as a tracer of chemical species and pathways that involve ozone or its derived products. A quantitative analysis of the isotopic compositions in stratospheric ozone constitutes the mainbody of this paper. The enrichment, δ , is defined by

$$\delta(\%) = 100 \times \left(\frac{R_{smp}}{R_{std}} - 1 \right), \quad (4.1)$$

where R_{smp} is the ratio of the abundances of an isotopically substituted species and its normal molecule and R_{std} is the same ratio in a standard sample. In this paper, the species of interest are ozone and atomic and molecular oxygen. Since molecular oxygen is the largest oxygen reservoir in the atmosphere and its isotopic composition is very stable, we choose the oxygen isotopic composition in atmospheric O_2 as our standard, rather than the more commonly employed V-SMOW (Vienna Standard Mean Ocean Water). The magnitudes of the atmospheric $\delta^{16}O^{17}O$ and $\delta^{16}O^{18}O$ are 1.175 and 2.35% referenced to V-SMOW, respectively, while the values are zero as referenced to O_2 itself.

For simplicity, we define $O = {}^{16}O$, $P = {}^{17}O$, and $Q = {}^{18}O$. Thus, OOP, OPO, OOQ, and OQO represent ${}^{16}O^{16}O^{17}O$, ${}^{16}O^{17}O^{16}O$, ${}^{16}O^{16}O^{18}O$, and ${}^{16}O^{18}O^{16}O$, respectively. The doubly isotope substituted molecules are of negligible importance for the purposes of this paper, and ${}^{50}O_3$ is therefore primarily OOQ and OQO. In the stratosphere, the chemistry is governed primarily by the Chapman reactions:



It has been known that equations (4.3) and (4.4) can result in noticeable ozone isotopic fractionation [*Gao and Marcus, 2001; Liang et al., 2004*].

Using a balloon-borne mass spectrometer, *Mauersberger* [1981] reports stratospheric enrichments of 0-40% in ${}^{50}O_3$, with a broad maximum between 28 and 38 km and a minimum

at 20 km. The error was 15% at 30 km, increasing above and below that altitude. Recently, Mauersberger and colleagues acquired new data with the error lowered to $\sim 5\%$ [Schueler *et al.*, 1990; Krankowsky *et al.*, 2000; Mauersberger *et al.*, 2001; Lämmerzahl *et al.*, 2002] from ten balloon flights with more than 40 samples. The measured magnitude of the enrichments of ozone is $\sim 10\%$, a value consistent with that obtained from ground-based and space-based Fourier transform infrared spectrometers (FTIR) [Irion *et al.*, 1996; Meier and Notholt, 1996]. Experimentally, Thiemens and Heidenreich [1983] first discovered that the formation of O_3 follows a slope of ~ 1 in three-isotope plots of ozone, instead of the typical ~ 0.5 dependence. Subsequent measurements demonstrated that the three-body reaction between O and O_2 (equation (4.3)) in their electronic ground states results in large enrichments for the heavier isotopologues [Morton *et al.*, 1990]. Later isotope specific reaction measurements further showed that the interaction channels to form asymmetric isotopomers are the major players in explaining the ozone isotopic anomaly [Janssen *et al.*, 1999; Mauersberger *et al.*, 1999; Janssen *et al.*, 2001; Janssen *et al.*, 2003].

At room temperature, the measured enrichments of $^{49}\text{O}_3$ and $^{50}\text{O}_3$ in the production of ozone (equation (4.3)) are ~ 11 and 13% , respectively [Thiemens and Heidenreich, 1983; Heidenreich and Thiemens, 1985; Thiemens and Jackson, 1988; Morton *et al.*, 1990; Anderson *et al.*, 1997; Mauersberger *et al.*, 1999; Janssen *et al.*, 1999; Janssen *et al.*, 2003]. This result is by far the largest fractionation known in atmospheric chemistry and geochemistry and is in apparent contradiction to typical formation processes, in which the heavier molecules are depleted [e.g., Kaye and Strobel, 1983]. Recently, the introduction of the symmetry factor η has successfully explained this phenomenon as observed in the laboratory [Hathorn and Marcus, 1999; Hathorn and Marcus, 2000; Gao and Marcus, 2001; Gao and Marcus, 2002; Gao *et al.*, 2002], where η is applied to parameterize the deviation of the statisti-

cal density of states for symmetric isotopomers compared with asymmetric isotopomers. However, no quantitative atmospheric models including these formation processes or their impact on the isotopic composition of other species have been reported. With newly available high resolution measurements of ozone isotopic composition made at mid-latitudes, it is found that the magnitude of the enrichments increases with altitude [*Krankowsky et al.*, 2000; *Mauersberger et al.*, 2001; *Lämmerzahl et al.*, 2002]. *Mauersberger* and colleagues [e.g., *Mauersberger et al.*, 2001] attempted to explain the altitude variation of the enrichments by temperature variation. The inferred temperature range at altitudes between ~ 20 and 35 km is ~ 200 -260 K, which is much warmer than what is generally expected in the stratosphere for these latitudes and seasons: ~ 210 -230 K.

In general, the temperature gradient in the stratosphere is about 1 K km^{-1} . If the observed enrichment variation of heavy ozone is due entirely to the temperature variation in the stratosphere, the required temperature gradient is $\sim 5 \text{ K km}^{-1}$, based on the averaged variation of enrichments with temperature of $0.06\% \text{ K}^{-1}$ measured in the laboratory [*Morton et al.*, 1990]. Therefore, a process other than the temperature gradient is needed to account for this variation. It has been shown by *Bhattacharya et al.* [2002] that the photolysis-induced fractionation (equation (4.4)) at low pressures, such as those in the stratosphere, can result in high enrichment. In their paper, they defined a turn-over time $\tau = [\text{O}_3]/[\text{O}_3]'$, where $[\text{O}_3]$ is the ozone density at a given time t and $[\text{O}_3]' = d[\text{O}_3]/dt$ is the corresponding dissociation rate, to explain this additional fractionation. With this turn-over time, *Bhattacharya et al.* were able to reproduce the altitude variations of the enrichments of heavy ozone and predicted an enrichment of about 14% at 40 km. Instead of applying this artificial turn-over time, we use the dissociation cross sections for isotopic substituted species calculated by the method described previously [*Blake et al.*, 2003; *Liang*

et al., 2004; *Miller et al.*, 2005].

This chapter is organized as follows. We describe the basics of the model incorporating the ozone enrichments from both formation and photolysis processes in §4.2. The kinetic study for isotopically substituted ozone in the stratosphere is computed using the Caltech/JPL KINETICS one-dimensional diffusive chemical model. A detailed analysis of the model results and their comparison with atmospheric measurements is presented in §4.3.

4.2 Atmospheric Models

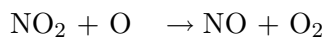
4.2.1 One-Dimensional Model

The one-dimensional Caltech/JPL KINETICS model is used in our study. A detailed description of the model has been given previously [e.g., *Allen et al.*, 1981]. Here, we summarize the most essential features only. The atmosphere is assumed to be in hydrostatic equilibrium, and the mass continuity equation is solved:

$$\frac{\partial n_i}{\partial t} + \frac{\partial \varphi_i}{\partial z} = P_i - L_i, \quad (4.7)$$

where n_i is the number density of species i , φ_i the transport flux, P_i the chemical production rate, and L_i the chemical loss rate, all evaluated at time t and altitude z . We are interested in a steady state solution, i.e., $\langle \partial n_i / \partial t \rangle \rightarrow 0$, in a diurnally averaged model. For the Earth's atmosphere, the homopause is located at 100 km above the surface, while the region of interest is well below it, i.e., altitudes $\lesssim 60$ km. Eddy mixing is therefore the dominant term in φ_i . The profiles of temperature and eddy diffusion coefficients are taken from *Allen et al.* [1981] and are reproduced in Figure 4.1.

The model atmosphere consists of 66 layers evenly distributed from the surface to 130 km. Since the stratosphere is the region of principal interest, the chemistry is governed mainly by the Chapman reactions (equations (4.2)-(4.6)). Table 4.1 lists the reactions and rate coefficients used in this study. The reaction $\text{O}_3 + \text{X} \rightarrow \text{PROD} + \text{X}$ (R83) and its isotopic variants (R84-R87) simulate the net loss of ozone by NO_x , HO_x , and ClO_x catalysts. “X” simply denotes that the reaction is catalyzed. The catalytic processes will drive the decomposition of ozone to O_2 . Since O_2 is the largest oxygen reservoir, we do not trace the catalyzed products. The rate coefficients are assumed to be isotopically invariant and are calculated from the following five reactions:



We obtain the reaction rates from a complete version of oxygen chemistry model in the stratosphere [*Jiang et al., 2004; Morgan et al., 2004*], multiply by 2, and then divide by the O_3 concentrations in that model. The factor of 2 indicates that either O or O_3 loss will eventually lead to the loss of ozone. The sum of the products for the above five reactions is used as the rate coefficient in R83-R87 and shown in Figure 4.2. With these catalytic reactions, the resulting O_3 profiles within the simplified chemistry are in good agreement with that obtained by complete chemical models.

When we switch off the fractionation in the rate coefficients in Table 4.1, the enrichments

of O and O₃ relative to O₂ vanish, as expected, while O(¹D) has a finite value of $\sim 0.5\%$. This deviation is a consequence of the non-negligible abundances of OP and OQ. The abundances of OP and OQ relative to O₂ in the Earth's atmosphere are $\sim 8 \times 10^{-4}$ and 4×10^{-3} , respectively. The typical definition of isotopic compositions of O(¹D) assumes that O(¹D) is the derivative of O₃ only [e.g., see *Yung et al.*, 1997]. However, O(¹D) can also be produced from the photolysis of OPO, OOP, OQO, and OOQ (R3, R7, R9, and R13). It turns out that the abundances of OP and OQ determine the enrichment of O(¹D). The $\sim 0.5\%$ value is simply $-(8 \times 10^{-4} + 4 \times 10^{-3})$.

4.2.2 Ozone Formation

We follow Gao and Marcus' approach to calculate the rate coefficients relevant to our study [*Gao and Marcus*, 2001; 2002]. Since the pressure of interest is less than 50 mbar (altitudes greater than 20 km), the formation rates of ozone are close to their low-pressure limit, that is the pressure dependence is insignificant; the difference of enrichments for heavier ozone is $< 0.5\%$ between 10 and 50 mbar [e.g., see *Morton et al.*, 1990]. It is also because of the low pressure in the region of interest that the coefficient can be well calculated by the free-rotor model [see *Gao and Marcus*, 2002 for details] in which the interaction between atomic and molecular oxygen is simplified. Hence, for simplicity, we calculate the rate coefficients using a free-rotor approach.

It is important to note that the production rate of asymmetric molecules is not simply the sum of the rate coefficients of two reactive channels measured in the laboratory or calculated in the theory. For example, the products of OOQ and QOO are the results of

two different reaction channels:



The fractionation in the production of OOQ is not the sum of the fractionations of the rate coefficients in the above two reactions. When there is rapid exchange reaction between atomic and molecular oxygen, one can multiply the second reaction by the equilibrium constant in the reaction $\text{O} + \text{OQ} \rightleftharpoons \text{Q} + \text{OO}$ [e.g., see equations (2.11)-(2.13) of *Hathron and Marcus, 1999* or equation (2.36) of *Gao and Marcus, 2002*]. The product after multiplying by an additional factor of 2 is used in R29 (and R28 for OOP production) of Table 4.1. The factor 2 indicates that OOQ can be formed by attaching Q to OO from either side.

The ozone layer is located mainly at altitudes between 20 and 50 km (50-1 mbar), and its mixing ratio peaks at ~ 30 km (~ 10 mbar). Because of the weak pressure-dependence in the enrichments of ozone in the stratosphere, we calculate the rate coefficients of ozone production at 10 mbar where the mixing ratio of ozone peaks. The enrichment is rather sensitive to temperature, however. The variation of the enrichments from 140 to 300 K is about 4-5% in the low pressure limit, or $\sim 0.03\% \text{ K}^{-1}$ (or $0.06\% \text{ K}^{-1}$ when incorporating O + O₂ exchange reactions) [*Morton et al., 1990*].

The parameters η and ΔE are taken to be the same as those suggested by *Gao and Marcus* [2001], that is $\eta = 1.13$ at 140 K and 1.18 at 300 K, we use linear interpolation in between, and $\Delta E = 260 \text{ cm}^{-1}$. The reaction rate coefficients are calculated and shown in Figure 4.3 along with laboratory measurements and theoretical calculations. The exchange rate coefficients of O and O₂ are given in the lowermost panels. The dotted lines in the

figure represent the reference case in which the fractionation in the rate coefficients is removed. The calculated enrichments of ozone are plotted in Figure 4.4. The laboratory measurements [Morton *et al.*, 1990; Mauersberger *et al.*, 1999] and the published calculated values [Gao and Marcus, 2002] are overplotted by filled and open symbols, respectively. We note that the calculation of δQ agrees with experiments better than that for δP . While the errors for δQ are $\lesssim 5\%$, the errors of δP can be as large as 50%. Further improvement in the theory of temperature-dependent and isotope-specific formation rates of ozone are therefore needed.

4.2.3 Ozone Photolysis

The absorption cross sections and photolysis quantum yields of OOP, OPO, OOQ, and OQO have not yet been measured. A zero point energy-based semi-analytic model (MZPE model, hereafter) is applied to calculate the cross sections for the above species [Blake *et al.*, 2003; Liang *et al.*, 2004; Miller *et al.*, 2005]. In the Earth’s atmosphere, the photolysis of ozone is primarily in the Hartley and Chappuis bands, where the latter dominates in the regions $\lesssim 35$ km. The calculation in the Hartley band at room temperature was reported by Liang *et al.* [2004] and is reproduced here by the solid lines in Figure 4.5. We also perform the same calculation in the Chappuis band, and the results are shown in Figure 4.6.

In each band, there are two channels for the dissociation of asymmetric molecules. For example, in the Hartley band OOQ can be dissociated into either $O(^1D) + OQ(^1\Delta_g)$ or $O_2(^1\Delta_g) + Q(^1D)$. We assume these two branches are equally weighted. Whether this assumption is valid does not affect the results obtained in this paper. The robustness of this assumption arises from the fact that the abundance of ozone is negligible compared with that of molecular oxygen, and fast exchange reactions between atomic and molecular oxygen

quickly wash out the isotopic fractionations in the photolytic products of ozone. However, the subsequent reactions involving $O(^1D)$ can be seriously modified by this assumption, but are beyond the scope of this paper. We will show in the companion paper [Liang *et al.*, 2005] that the assumption of equally-weighted channels in the photolysis of ozone can explain the observed isotopic compositions of CO_2 in the middle atmosphere.

Temperature variation may be a factor important to the photolysis-induced fractionation. For example, N_2O shows a non-negligible temperature variation [e.g., Liang *et al.*, 2004]. To verify the sensitivity to temperature, we also calculate the fractionation of the cross sections of heavy ozone at 195 K. The absorption ozone cross section of normal ozone at 195 K was taken from Freeman *et al.* [1984] and Yoshino *et al.* [1988; 1993]. The results of the fractionation are shown by the dashed lines in Figure 4.5. Unlike N_2O , ozone shows a negligible temperature dependence, at least in the Hartley band. So, for simplicity, we ignore the temperature dependence of photoabsorption cross sections in our model.

It has been shown that the ozone photodissociation in the Huggins band can result in fractionation as large as $\sim 30\%$ [Miller *et al.*, 2005]. However, the process takes place at UV wavelengths longer than 300 nm, where the cross section is small. The photodissociation coefficients in the Huggins band are orders of magnitude less than those in the Hartley and Chappuis bands. The overall contribution from this band is relatively small, and we ignore it in this paper.

4.3 Results

Following equation (4.1), the enrichment of heavy ozone in this paper is defined by

$$\delta\text{OQO} (\%) = 100 \times \left(\frac{2[\text{OQO}/\text{O}_3]}{[\text{OQ}/\text{O}_2]} - 1 \right) \quad (4.8)$$

$$\delta\text{OOQ} (\%) = 100 \times \left(\frac{[\text{OOQ}/\text{O}_3]}{[\text{OQ}/\text{O}_2]} - 1 \right) \quad (4.9)$$

$$\delta\text{Q} (\%) = (\delta\text{OQO} + 2\delta\text{OOQ})/3. \quad (4.10)$$

A similar definition holds for OPO and OOP, but with substitution of Q by P. Here, we assume conventional statistical weights for symmetric (OPO and OQO) and asymmetric (OOP and OOQ) molecules.

In this chapter, we concentrate on the stratosphere, where the diurnal temperature variation is small. In the troposphere near the surface, the overall δP and δQ are $\sim 6.5\text{-}8$ and $8\text{-}9\%$, respectively [Krankowsky *et al.*, 1995; Johnston and Thiemens, 1997]. The measured variation of the enrichments of ozone is as large as $\sim 0.5\%$. The overall enrichments can roughly be explained by the formation at ~ 300 K [Morton *et al.*, 1990]. With $0.06\% \text{ K}^{-1}$ temperature variations, the inferred temperature variation is ~ 10 K.

4.3.1 Vertical Profiles

Figures 4.7 and 4.8 show the calculated enrichments for ozone isotopomers and isotopologues. We see that the formation-induced enrichments alone can roughly explain the magnitude of the observed values. These figures indicate that the enrichments due to the formation of symmetric molecules are about a factor of two smaller than those of asymmetric molecules, while the opposite is true for photolysis-induced enrichments. Enrichments

resulting from photolysis are about an order of magnitude less than those from formation.

Formation—The enrichments of symmetric molecules show little altitude dependence, while those for asymmetric molecules increase with altitude above ~ 20 km (solid lines of Figure 4.7). For symmetric molecules (OPO and OQO), the enrichment gradients are negligible: $\lesssim 0.003\% \text{ K}^{-1}$. For asymmetric molecules (OOP and OOQ), the gradients are a factor of about 20 greater, $\sim 0.06\% \text{ K}^{-1}$, consistent with the laboratory measurements [Morton *et al.*, 1990]. The magnitudes of the enrichments for symmetric molecules are smaller than those for asymmetric molecules, and their abundance is also a factor of two less than that of asymmetric variants. Therefore, the overall enrichments as well as their temperature variations are contributed primarily by asymmetric molecules. The dotted lines in the bottom two panels of Figure 4.7 represent laboratory measured enrichments for P and Q [Morton *et al.*, 1990]. The values are consistent with those in Figure 4.4.

Photolysis—The enrichments of the isotopomers and isotopologues of ozone from photolysis are shown by the dashed lines in Figure 4.7. The enrichments peak at ~ 35 km and are significant only at altitudes between 20 and 50 km, where the ozone layer peaks. The magnitude of the fractionation is sensitive to the wavelength of incident UV photons (see Figure 4.4). Therefore, it is expected that the attenuation of UV radiation can result in large vertical variations of the enrichments. At high altitudes, the photolysis is primarily through photons at the maximum of the Hartley band, where the fractionation is small. Lower in the atmosphere, absorption in the long-wavelength wing of the Hartley band becomes important, and fractionation is large in this region. Below the ozone peak, photolysis in the Chappuis band dominates, and there is little fractionation (Figure 4.6).

Overall Enrichments—The isotopic fractionation from both formation and photolysis are presented in Figure 4.8. We see that the combined enrichments better match the

observations.

4.3.2 Three-Isotope Plots

Figure 4.9 shows a three-isotope plot of ozone at altitudes between 20 and 35 km. The slope measured in the laboratory is ~ 0.6 (dotted line), but the associated error is significant and the slope varies with temperature [see Figure 4.3 of *Morton et al.*, 1990]. The slope for a linear least squares fit to the atmospheric measurements is ~ 1 . The slope in the formation processes in our model is ~ 0.8 , close to but not quite unity (solid line). The slope from the photolysis is mass-dependent, or ~ 0.5 (inset).

It is shown that the enrichment variations from formation are about 1.5% for δQ and about 1% for δP . The observations show a factor of ~ 3 broader. If temperature variation is the key to the observed variation of the enrichments, the required variation is >60 K, an unreasonable value in the stratosphere. However, we show next that the photolysis-induced enrichments can account for these variations. As shown in the inset of Figure 4.9, the variations of δQ and δP are ~ 3 and 1.5%, respectively.

In the altitude range 22 to 33 km, the observed enrichments for P and Q are, respectively, ~ 7 -10 and ~ 7 -11%, while the calculated values are ~ 8 -10.5 and ~ 8 -12.5%. For OPO and OOP, the variations are ~ 1.5 and ~ 2.5 %. For OQO and OOQ, they are ~ 2 and ~ 4 %. It is important to note that the calculated overall enrichments are about 1-1.5% (dotted line of Figure 4.10) in excess of the measurements, suggesting that other processes as important as photolysis may be missing in our study.

Since the photolysis lifetime of stratospheric ozone is only about one hour, the transport does little to change the vertical profiles of the enrichments. To lower the calculated values, we could reduce the effect from either formation or photolysis. For the formation channel,

we show in Figure 4.10 that an 8% reduction (~ 20 K) of temperature in our reference profile, shown by the dotted line in Figure 4.1, reproduces the observations well. From photolysis we need to increase the ozone column above 40 km by a factor of >5 , which can then move the peaks of the photolysis-induced enrichments upward by ~ 5 km, thus reducing the enrichments in the regions between 20 and 35 km. However, both are unlikely, because the required modification in the temperature and ozone abundance in the stratosphere is beyond the uncertainties of the current knowledge of the stratosphere. More laboratory measurements on the formation and photolysis rate coefficients for ozone are urgently needed to refine our calculations.

4.4 Conclusion

In this paper, we have modeled processes affecting the isotopic composition of heavy ozone in detail. The enrichments resulting from the formation processes which are on the order of 10% are by far the most significant in the known chemical and geochemical fractionation mechanism. At altitudes between 20 and 35 km, the enrichments for $^{49}\text{O}_3$ and $^{50}\text{O}_3$ are 7-9% and 7-11%, respectively. *Krankowsky et al.* [2000] and *Mauersberger et al.* [2001] attribute the altitude variation to the temperature variation in the stratosphere, and the estimated temperature ranges 200-260 K. However, the expected temperature in the stratosphere is between ~ 210 and 230 K. *Bhattacharya et al.* [2002] proposed that the ozone dissociation provides additional fractionation to the existing enrichments resulting from formation processes. They introduced an *ad hoc* parameter of turn-over time to simulate the photodissociation-induced enrichments. With this turn-over time, they were able to reproduce the observed altitudinal variations of the enrichments of heavy ozone.

To avoid this artificial parameter, we use the calculated dissociation cross sections for isotopically substituted species. The cross sections are calculated by means of the MZPE model [e.g., see *Liang et al.*, 2004 for details]. With this, we are able to calculate the enrichments of heavy ozone quantitatively. We perform a modeling study using one-dimensional Caltech/JPL KINETICS code which takes the optical depths from the molecular absorption (mainly oxygen and ozone in the stratosphere) properly into account. The altitude variation of heavy ozone enrichments is thereby reproduced. When incorporating this additional effect into the formation-induced enrichments, the overall values of the enrichments are systematically 1-1.5% in excess of the observation. With large modifications to the temperature profile (8% reduction) and ozone column (>5 times enhancement above 40 km) in the stratosphere, we would be able to reproduce the observations. It is also possible that we have overestimated the enrichments from photolysis, though the MZPE model calculation has successfully reproduced the laboratory measured cross section of $^{18}\text{O}^{18}\text{O}^{18}\text{O}$ [see Figure 8 of *Liang et al.*, 2004]. A two-dimensional model, which determines the ozone abundances between latitudes more accurately, is needed to verify if the temperature profiles are responsible for this $\sim 1\%$ difference in the enrichments of stratospheric ozone.

The enrichments of heavy ozone are the most prominent feature in the isotopic chemistry in the stratosphere. This large oxygen isotopic effect can be transferred to other long-lived molecules such as CO_2 . Therefore, their isotopic composition can be used to trace detailed chemical and dynamical processes in the stratosphere and mesosphere. A similar mechanism has been applied to CO_2 [e.g., *Yung et al.*, 1991; *Yung et al.*, 1997], and the measured profile of $\text{C}^{16}\text{O}^{18}\text{O}$ is explained. *Barth and Zahn* [1997] extended this mechanism to $\text{C}^{16}\text{O}^{17}\text{O}$. They were able to calculate the observed slope of ~ 2 in three-isotope plots of oxygen in CO_2 , though several assumptions must be made to reproduce this slope. In a companion paper

[*Liang et al.*, 2005], we remove the assumptions by *Barth and Zahn* [1997] and successfully reproduce the slope of ~ 1.7 in the observed enrichments of CO_2 .

Bibliography

- Allen, M., Y. L. Yung, and J. W. Waters, Vertical Transport and Photochemistry in the Terrestrial Mesosphere and Lower Thermosphere (50-120 km), *Journal of Geophysical Research-Space Physics*, *86*, 3617-3627, 1981.
- Anbar, A. D., M. Allen, and H. A. Nair, Photodissociation in the Atmosphere of Mars - Impact of High-Resolution, Temperature-Dependent CO₂ Cross-Section Measurements, *Journal of Geophysical Research-Planets*, *98*, 10925-10931, 1993.
- Anderson, S. M., D. Hulsebusch, and K. Mauersberger, Surprising Rate Coefficients for Four Isotopic Variants of O+O₂+M, *Journal of Chemical Physics*, *107*, 5385-5392, 1997.
- Anderson, S. M., F. S. Klein, and F. Kaufman, Kinetics of the Isotope Exchange-Reaction of ¹⁸O with NO and O₂ at 298-K, *Journal of Chemical Physics*, *83*, 1648-1656, 1985.
- Arnold, I., and F. J. Comes, Temperature-Dependence of the Reactions O(³P) + O₃ ⇒ 2O₂ and O(³P) + O₂+M ⇒ O₃ + M, *Chemical Physics*, *42*, 231-239, 1979.
- Badger, R. M., A. C. Wright, and R. F. Whitlock, Absolute Intensities of Discrete and Continuous Absorption Bands of Oxygen Gas at 1.26 and 1.065 μm and Radiative Lifetime of ¹Λ_g State of Oxygen, *Journal of Chemical Physics*, *43*, 4345, 1965.
- Barth, V., and A. Zahn, Oxygen Isotope Composition of Carbon Dioxide in the Middle Atmosphere, *Journal of Geophysical Research-Atmospheres*, *102*, 12995-13007, 1997.

- Bhattacharya, S. K., S. Chakraborty, J. Savarino, and M. H. Thiemens, Low-Pressure Dependency of the Isotopic Enrichment in Ozone: Stratospheric Implications, *Journal of Geophysical Research-Atmospheres*, *107*, 2002.
- Blake, G. A., M. C. Liang, C. G. Morgan, and Y. L. Yung, A Born-Oppenheimer Photolysis Model of N₂O Fractionation, *Geophysics Research Letters*, *30*, art. no.-1656, 2003.
- Brock, J. C., and R. T. Watson, Ozone Photolysis - Determination of the O(³P) Quantum Yield at 266-nm, *Chemical Physics Letters*, *71*, 371-375, 1980.
- Fairchild, C. E., E. J. Stone, and G. M. Lawrence, Photofragment Spectroscopy of Ozone in UV Region 270-310 nm and at 600 nm, *Journal of Chemical Physics*, *69*, 3632-3638, 1978.
- Freeman, D. E., K. Yoshino, J. R. Esmond, and W. H. Parkinson, High-Resolution Absorption Cross-Section Measurements of Ozone at 195-K in the Wavelength Region 240-350 nm, *Planetary and Space Science*, *32*, 239, 1984.
- Gao, Y. Q., W. C. Chen, and R. A. Marcus, A Theoretical Study of Ozone Isotopic Effects Using a Modified ab initio Potential Energy Surface, *Journal of Chemical Physics*, *117*, 1536-1543, 2002.
- Gao, Y. Q., and R. A. Marcus, Strange and Unconventional Isotope Effects in Ozone Formation, *Science*, *293*, 259-263, 2001.
- Gao, Y. Q., and R. A. Marcus, On the Theory of the Strange and Unconventional Isotopic Effects in Ozone Formation, *Journal of Chemical Physics*, *116*, 137-154, 2002.

- Hathorn, B. C., and R. A. Marcus, An Intramolecular Theory of the Mass-Independent Isotope Effect for Ozone. I, *Journal of Chemical Physics*, *111*, 4087-4100, 1999.
- Hathorn, B. C., and R. A. Marcus, An Intramolecular Theory of the Mass-Independent Isotope Effect for Ozone. II. Numerical Implementation at Low Pressures Using a Loose Transition State, *Journal of Chemical Physics*, *113*, 9497-9509, 2000.
- Heidenreich, J. E., and M. H. Thiemens, The Non-Mass-Dependent Oxygen Isotope Effect in the Electrodissociation of Carbon-Dioxide - a Step toward Understanding Nomad Chemistry, *Geochimica et Cosmochimica Acta*, *49*, 1303-1306, 1985.
- Hippler, H., R. Rahn, and J. Troe, Temperature and Pressure-Dependence of Ozone Formation Rates in the Range 1-1000-bar and 90-370-K, *Journal of Chemical Physics*, *93*, 6560-6569, 1990.
- Irion, F. W., M. R. Gunson, C. P. Rinsland, Y. L. Yung, M. C. Abrams, A. Y. Chang, and A. Goldman, Heavy Ozone Enrichments from Atmos Infrared Solar Spectra, *Geophysics Research Letters*, *23*, 2377-2380, 1996.
- Janssen, C., J. Guenther, D. Krankowsky, and K. Mauersberger, Relative Formation Rates of $^{50}\text{O}_3$ and $^{52}\text{O}_3$ in $^{16}\text{O}^{18}\text{O}$ Mixtures, *Journal of Chemical Physics*, *111*, 7179-7182, 1999.
- Janssen, C., J. Guenther, D. Krankowsky, and K. Mauersberger, Temperature Dependence of Ozone Rate Coefficients and Isotopologue Fractionation in ^{16}O - ^{18}O Oxygen Mixtures, *Chemical Physics Letters*, *367*, 34-38, 2003.
- Janssen, C., J. Guenther, K. Mauersberger, and D. Krankowsky, Kinetic Origin of the Ozone Isotope Effect: A Critical Analysis of Enrichments and Rate Coefficients, *Physical Chemistry Chemical Physics*, *3*, 4718-4721, 2001.

- Jiang, X., C. D. Camp, R. Shia, D. Noone, C. Walker, and Y. L. Yung, Quasi-Biennial Oscillation and Quasi-Biennial Oscillation-Annual Beat in the Tropical Total Column Ozone: A Two-Dimensional Model Simulation, *Journal of Geophysical Research-Atmospheres*, *109*, 2004.
- Johnston, J. C. and M. H. Thiemens, The Isotopic Composition of Tropospheric Ozone in Three Environments, *Journal of Geophysical Research-Atmospheres*, *102*, 25395-25404, 1997.
- Kaye, J. A., and D. F. Strobel, Enhancement of Heavy Ozone in the Earths Atmosphere, *Journal of Geophysical Research-Oceans and Atmospheres*, *88*, 8447-8452, 1983.
- Krankowsky, D., F. Bartecki, G. G. Klees, K. Mauersberger, K. Schellenbach, and J. Stehr, Measurement of Heavy Isotope Enrichment in Tropospheric Ozone, *Geophysics Research Letters*, *22*, 1713-1716, 1995.
- Krankowsky, D., P. Lämmerzahl, and K. Mauersberger, Isotopic Measurements of Stratospheric Ozone, *Geophysics Research Letters*, *27*, 2593-2595, 2000.
- Lämmerzahl, P., T. Röckmann, C. A. M. Brenninkmeijer, D. Krankowsky, and K. Mauersberger, Oxygen Isotope Composition of Stratospheric Carbon Dioxide, *Geophysics Research Letters*, *29*, 2002.
- Lee, L. C., T. G. Slanger, G. Black, and R. L. Sharpless, Quantum Yields for Production of O(¹D) from Photodissociation of O₂ at 1160-1770 Å, *Journal of Chemical Physics*, *67*, 5602-5606, 1977.
- Liang, M.-C., G. A. Blake, B. R. Lewis, and Y. L. Yung, Oxygen Isotopic Composition

- of Carbon Dioxide in the Middle Atmosphere *Proceedings of the National Academy of Sciences*, submitted, 2005.
- Liang, M. C., G. A. Blake, and Y. L. Yung, A Semianalytic Model for Photo-Induced Isotopic Fractionation in Simple Molecules, *Journal of Geophysical Research-Atmospheres*, *109 (D10)*, art. No. D10308, 2004.
- Mauersberger, K., Measurement of Heavy Ozone in the Stratosphere, *Geophysics Research Letters*, *8*, 935-937, 1981.
- Mauersberger, K., B. Erbacher, D. Krankowsky, J. Gunther, and R. Nickel, Ozone Isotope Enrichment: Isotopomer-Specific Rate Coefficients, *Science*, *283*, 370-372, 1999.
- Mauersberger, K., P. Lämmerzahl, and D. Krankowsky, Stratospheric Ozone Isotope Enrichments-Revisited, *Geophysics Research Letters*, *28*, 3155-3158, 2001.
- Meier, A., and J. Notholt, Determination of the Isotopic Abundances of Heavy O₃ as Observed in Arctic Ground-Based FTIR-Spectra, *Geophysics Research Letters*, *23*, 551-554, 1996.
- Miller, C. E., R. M. Onorato, M.-C. Liang, and Y. L. Yung, Extraordinary Isotopic Fractionation in Ozone Photolysis, *Geophysics Research Letters*, *32(14)*, L14815, doi:10.1029/2005GL023317, 2005.
- Morgan, C. G., M. Allen, M. C. Liang, R. L. Shia, G. A. Blake, and Y. L. Yung, Isotopic Fractionation of Nitrous Oxide in the Stratosphere: Comparison between Model and Observations., *Journal of Geophysical Research-Atmospheres*, *109 (D4)*, art. No. D04305, 2004.

- Morton, J., J. Barnes, B. Schueler, and K. Mauersberger, Laboratory Studies of Heavy Ozone, *Journal of Geophysical Research-Atmospheres*, *95*, 901-907, 1990.
- Nicolet, M., On the Molecular-Scattering in the Terrestrial Atmosphere - an Empirical-Formula for its Calculation in the Homosphere, *Planetary and Space Science*, *32*, 1467-1468, 1984.
- Parisse, C., J. Brion, and J. Malicet, UV Absorption Spectrum of Ozone: Structure Analysis and Study of the Isotope Effect in the Hartley System, *Chemical Physics Letters*, *248*, 31-36, 1996.
- Samson, J. A. R., G. H. Rayborn, and P. N. Pareek, Dissociative Photo-Ionization Cross-Sections of O₂ from Threshold to 120-Å, *Journal of Chemical Physics*, *76*, 393-397, 1982.
- Sander, S. P., and colleagues, *Chemical Kinetics and Photochemical Data for Use in Atmospheric Studies*, Evaluation No. 14, JPL Pub. 02-25, Jet Propulsion Laboratory (Pasadena), 2003.
- Sandor, B. J., R. T. Clancy, D. W. Rusch, C. E. Randall, R. S. Eckman, D. S. Siskind, and D. O. Muhleman, Microwave Observations and Modeling of O₂(¹Δ_g) and O₃ Diurnal Variation in the Mesosphere, *Journal of Geophysical Research-Atmospheres*, *102*, 9013-9028, 1997.
- Schueler, B., J. Morton, and K. Mauersberger, Measurement of Isotopic Abundances in Collected Stratospheric Ozone Samples, *Geophysics Research Letters*, *17*, 1295-1298, 1990.
- Sparks, R. K., L. R. Carlson, K. Shobatake, M. L. Kowalczyk, and Y. T. Lee, Ozone Photolysis - Determination of the Electronic and Vibrational-State Distributions of Primary Products, *Journal of Chemical Physics*, *72*, 1401-1402, 1980.

- Taherian, M. R., and T. G. Slanger, Products and Yields from O₃ Photodissociation at 1576-Å, *Journal of Chemical Physics*, *83*, 6246-6250, 1985.
- Thiemens, M. H., and J. E. Heidenreich, The Mass-Independent Fractionation of Oxygen - a Novel Isotope Effect and Its Possible Cosmochemical Implications, *Science*, *219*, 1073-1075, 1983.
- Thiemens, M. H., and T. Jackson, New Experimental-Evidence for the Mechanism for Production of Isotopically Heavy O₃, *Geophysics Research Letters*, *15*, 639-642, 1988.
- Turnipseed, A. A., G. L. Vaghjiani, T. Gierczak, J. E. Thompson, and A. R. Ravishankara, The Photochemistry of Ozone at 193 and 222 nm, *Journal of Chemical Physics*, *95*, 3244-3251, 1991.
- Wine, P. H., and A. R. Ravishankara, O₃ Photolysis at 248 nm and O(¹D₂) Quenching by H₂O, CH₄, H₂, and N₂O: O(³P_J) Yields, *Chemical Physics*, *69*, 365-373, 1982.
- Yoshino, K., J. R. Esmond, D. E. Freeman, and W. H. Parkinson, Measurements of Absolute Absorption Cross-Sections of Ozone in the 185-nm to 254-nm Wavelength Region and the Temperature-Dependence, *Journal of Geophysical Research-Atmospheres*, *98*, 5205-5211, 1993.
- Yoshino, K., D. E. Freeman, J. R. Esmond, and W. H. Parkinson, Absolute Absorption Cross-Section Measurements of Ozone in the Wavelength Region 238-335 nm and the Temperature-Dependence, *Planetary and Space Science*, *36*, 395-398, 1988.
- Yung, Y. L., W. B. Demore, and J. P. Pinto, Isotopic Exchange between Carbon-Dioxide and Ozone via O(¹D) in the Stratosphere, *Geophysics Research Letters*, *18*, 13-16, 1991.

Yung, Y. L., A. Y. T. Lee, F. W. Irion, W. B. DeMore, and J. Wen, Carbon Dioxide in the Atmosphere: Isotopic Exchange with Ozone and its Use as a Tracer in the Middle Atmosphere, *Journal of Geophysical Research-Atmospheres*, *102*, 10857-10866, 1997.

Yung, Y. L., and C. E. Miller, Isotopic Fractionation of Stratospheric Nitrous Oxide, *Science*, *278*, 1778-1780, 1997.

Yung, Y. L., J. S. Wen, J. P. Pinto, M. Allen, K. K. Pierce, and S. Paulson, HDO in the Martian Atmosphere - Implications for the Abundance of Crustal Water, *Icarus*, *76*, 146-159, 1988.

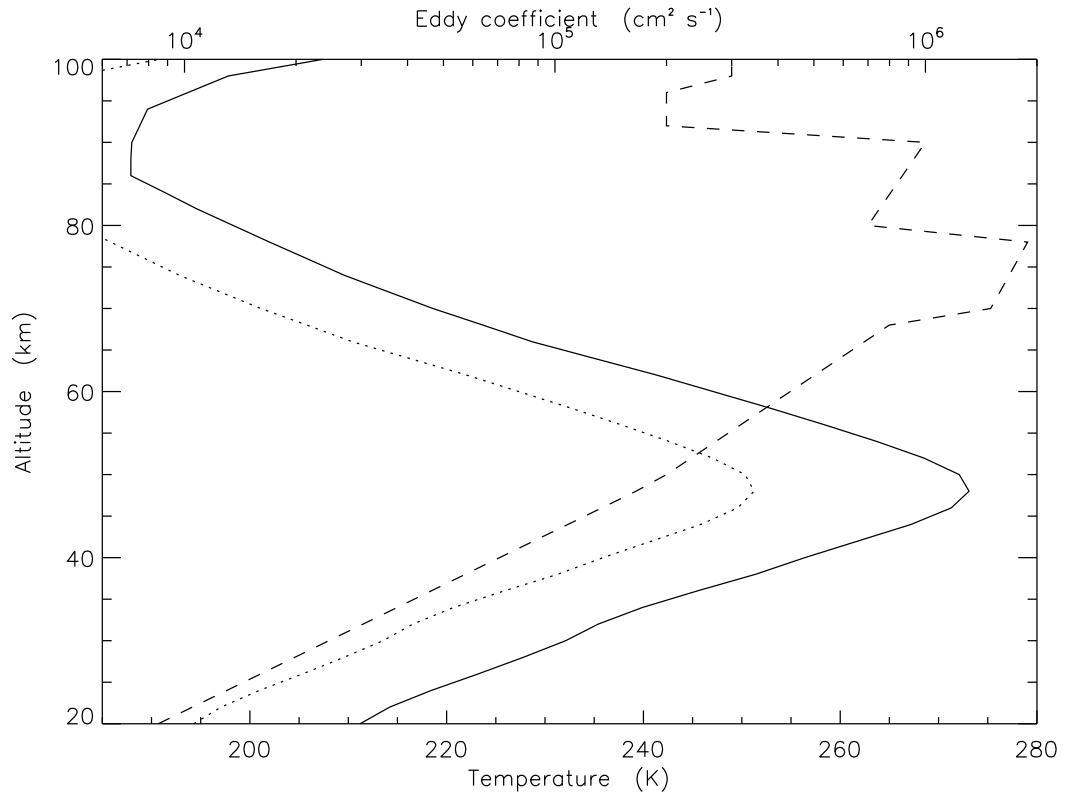


Figure 4.1 Ozone—Profiles of temperature (solid line) and eddy diffusion coefficient (dashed line) used in the calculation. These two profiles are taken from *Allen et al.* [1981]. Dotted line represents a temperature profile equal to the solid line reduced by 8%.

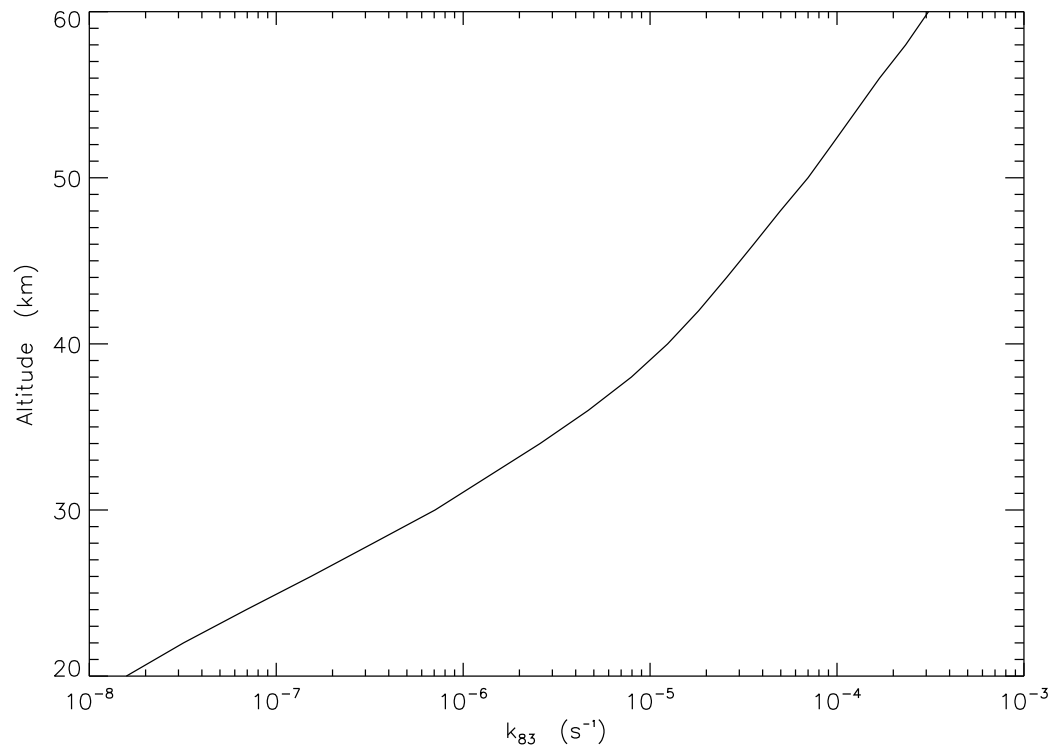


Figure 4.2 Ozone—Profile of rate coefficient k_{83} , which is used to account for the net loss of ozone by catalysis in the stratosphere. See text and Table 4.1 for details.

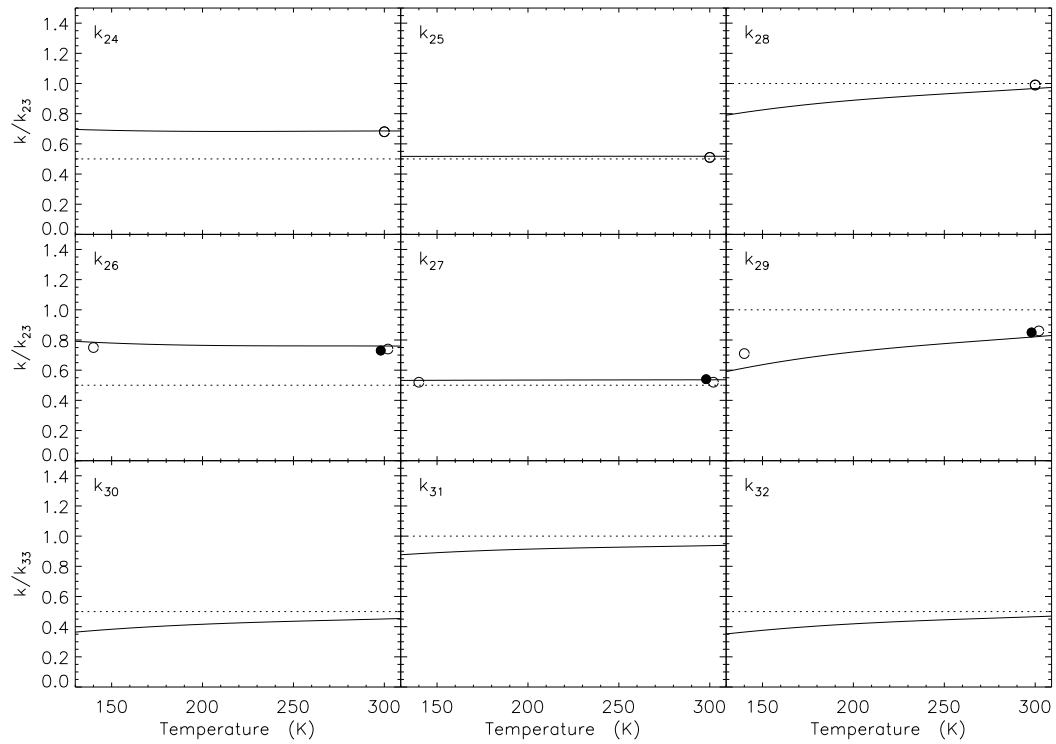


Figure 4.3 Ozone—Calculated ozone formation and oxygen exchange rate coefficients (solid lines). Null fractionation is shown by dotted lines for reference. The filled circles are laboratory measurements of *Mauersberger et al.* [1999] and *Janssen et al.* [1999]. The open circles are from the calculation by *Gao and Marcus* [2002].

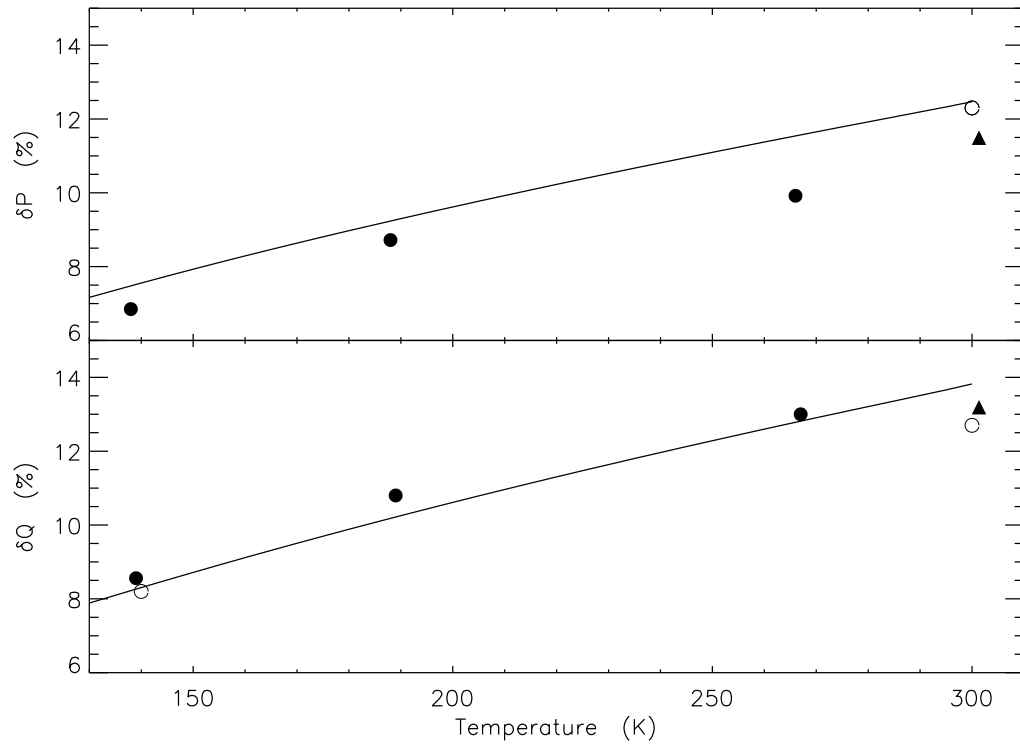


Figure 4.4 Ozone—Enrichments resulting from the formation processes. Filled symbols are laboratory measurements: circles were measured by *Morton et al.* [1990], and triangles by *Mauersberger et al.* [1999]. The open circles were calculated by *Gao and Marcus* [2002].

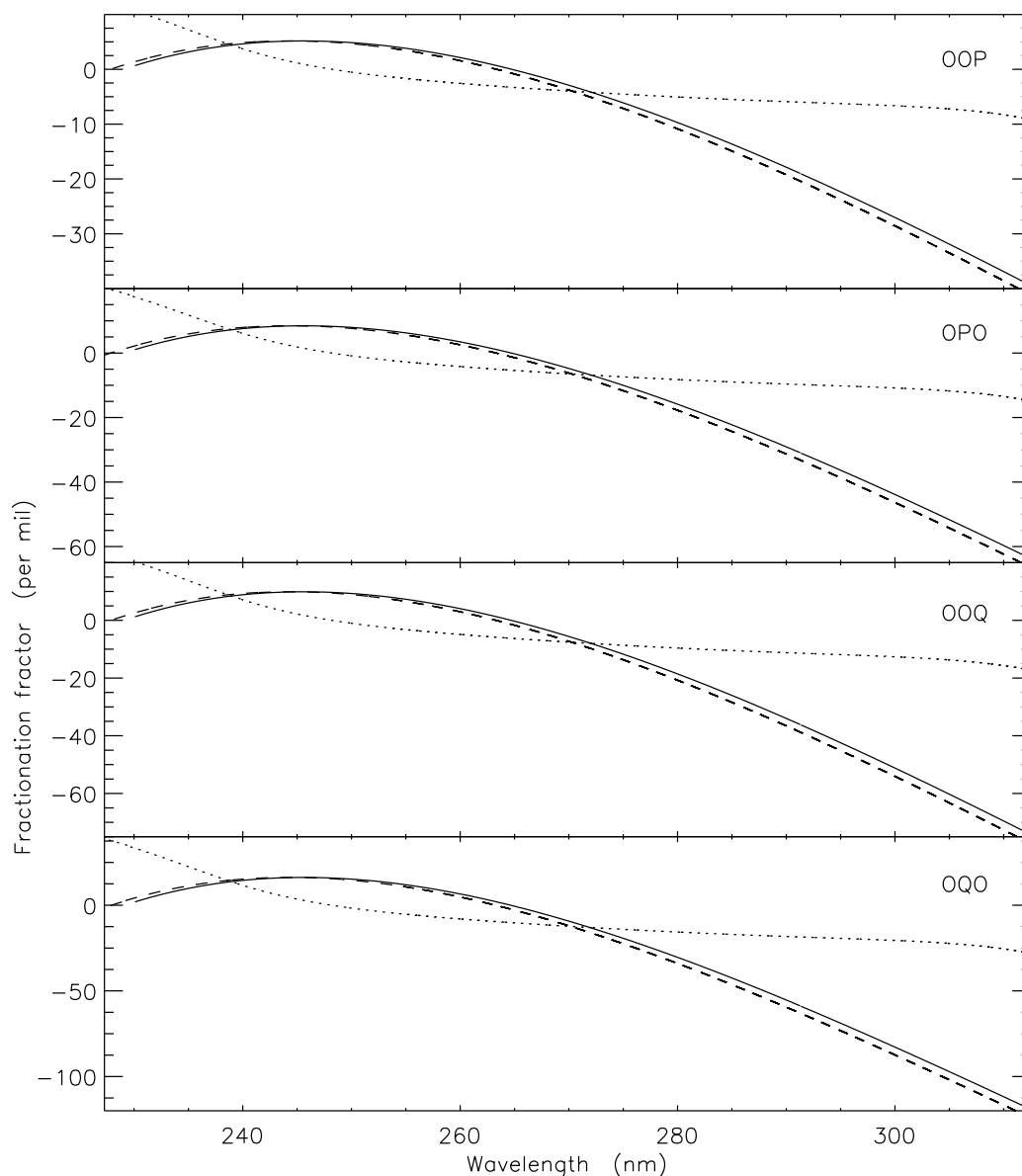


Figure 4.5 Ozone—Fractionation factors calculated using the MZPE model in the Hartley band at 195 (dashed lines) and 295 K (solid lines). Results calculated using the *Yung and Miller* [1997] model are shown by dotted lines. The fractionation factor is defined by $1000 \times (\sigma/\sigma_0 - 1)$, where σ_0 and σ are the photoabsorption cross sections of normal and isotopically substituted molecules, respectively.

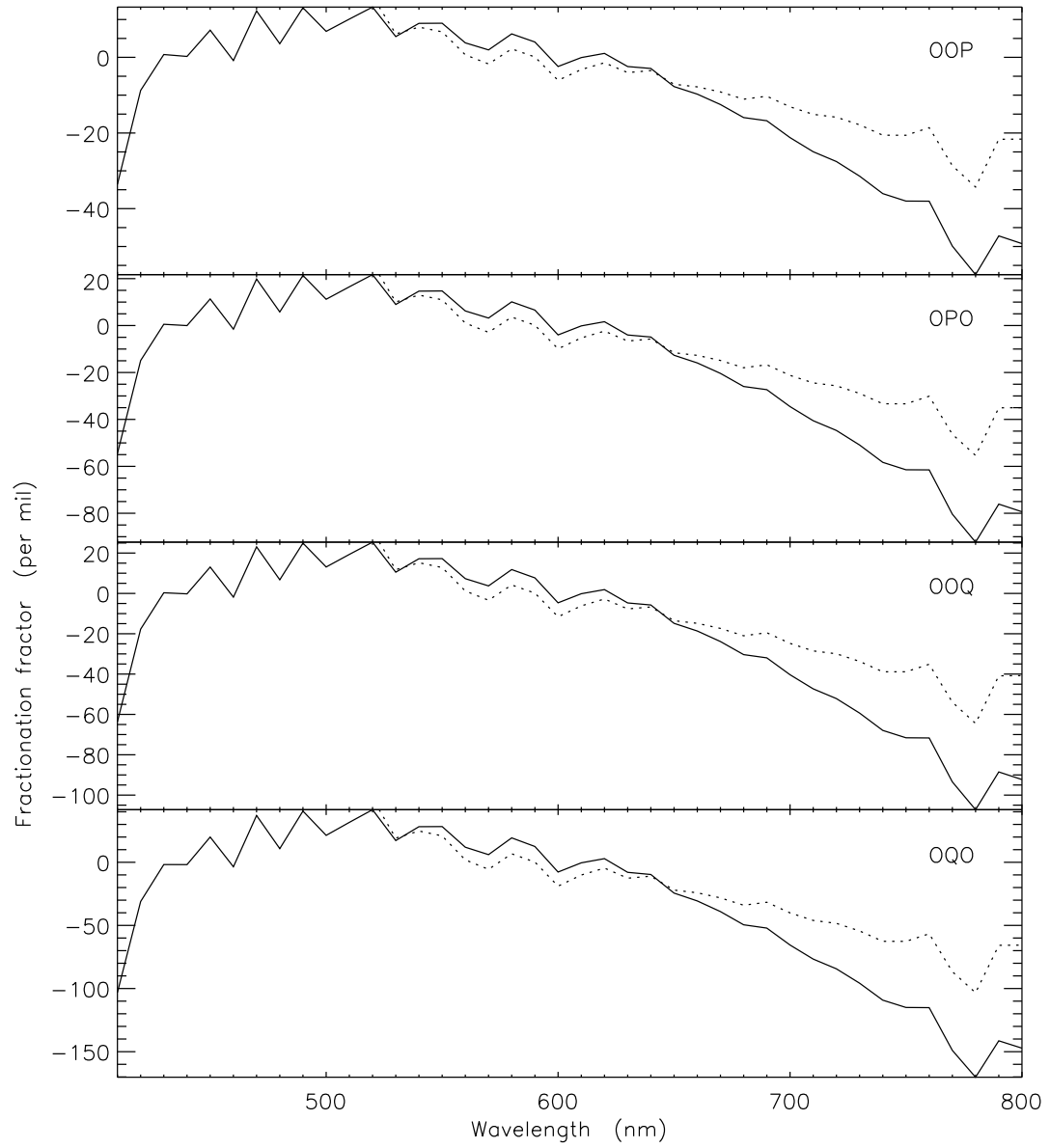


Figure 4.6 Ozone—Fractionation factors calculated using the MZPE model in the Chappuis band at 295 K (solid lines). Results calculated using the *Yung and Miller* [1997] model are shown by dotted lines.

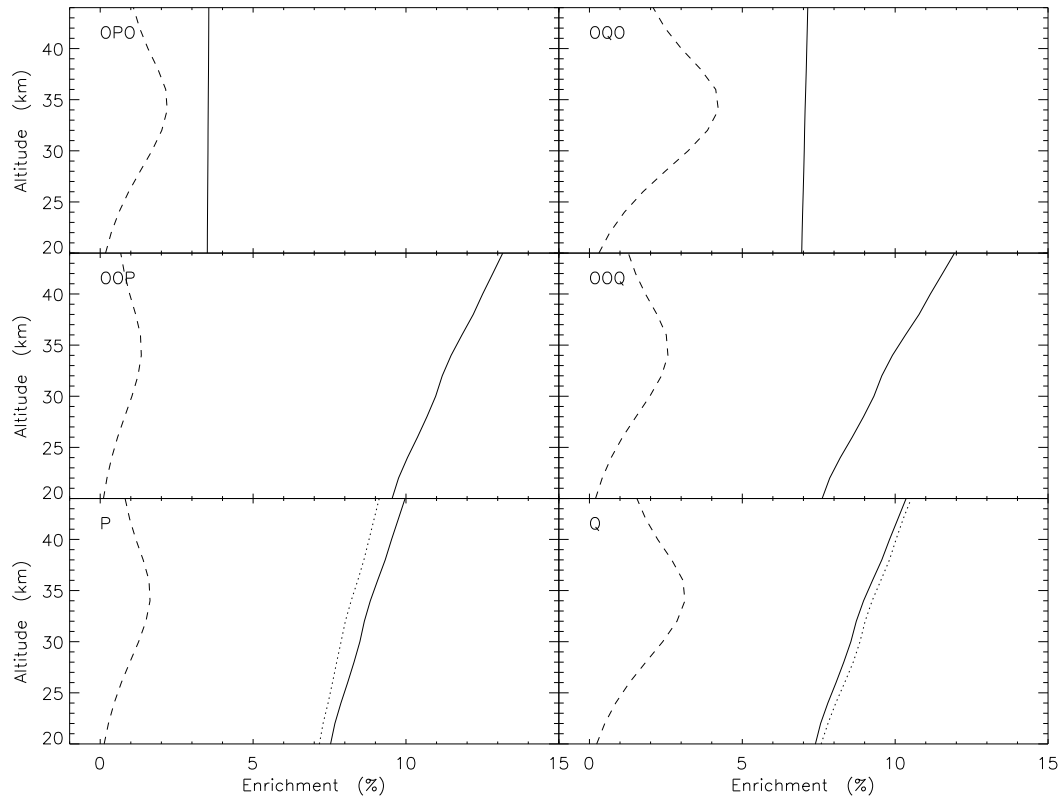


Figure 4.7 Ozone—Enrichments for the species indicated in the upper-left corner of each panel. Enrichments calculated using the formation and photolysis models are shown by solid and dashed lines, respectively. The dotted lines are the laboratory measurements [*Morton et al.*, 1990].

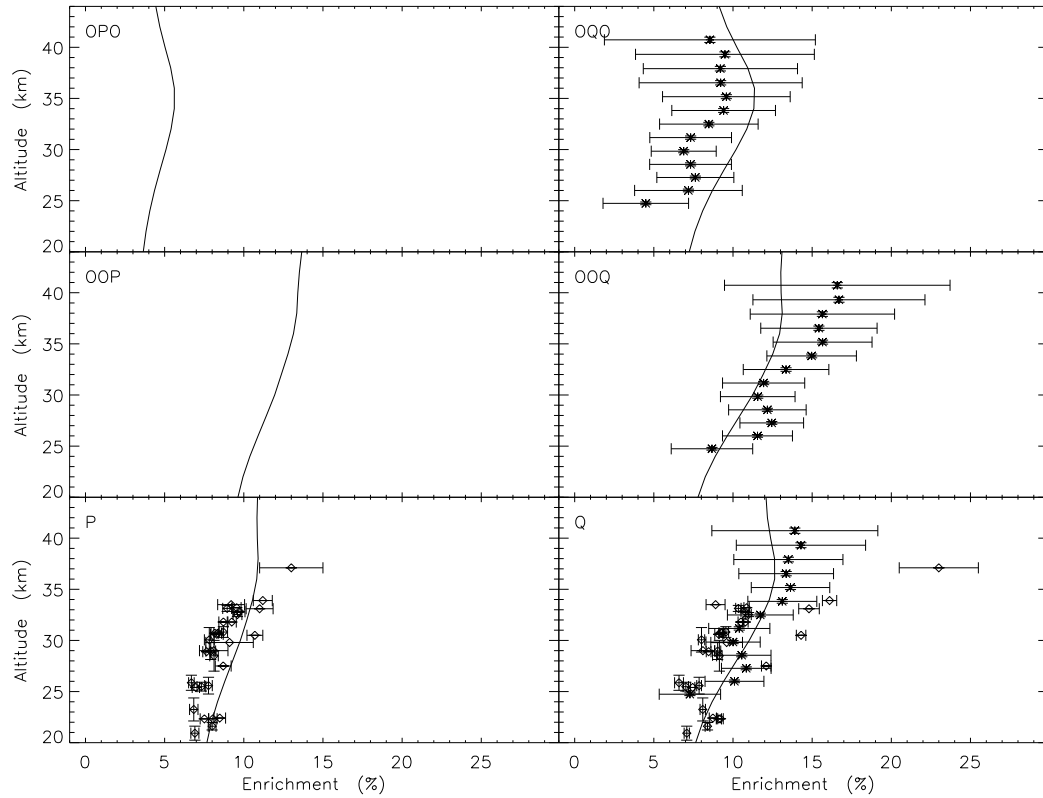


Figure 4.8 Ozone—Total enrichments calculated by integrating the formation and photolysis models. The error bars in the atmospheric measurements are for $1\text{-}\sigma$. The diamonds are mass-spectroscopic measurements [Krankowsky *et al.*, 2000; Mauersberger *et al.*, 2001; Lämmerzahl *et al.*, 2002], and asterisks are FTIR measurements by Irion *et al.* [1996]

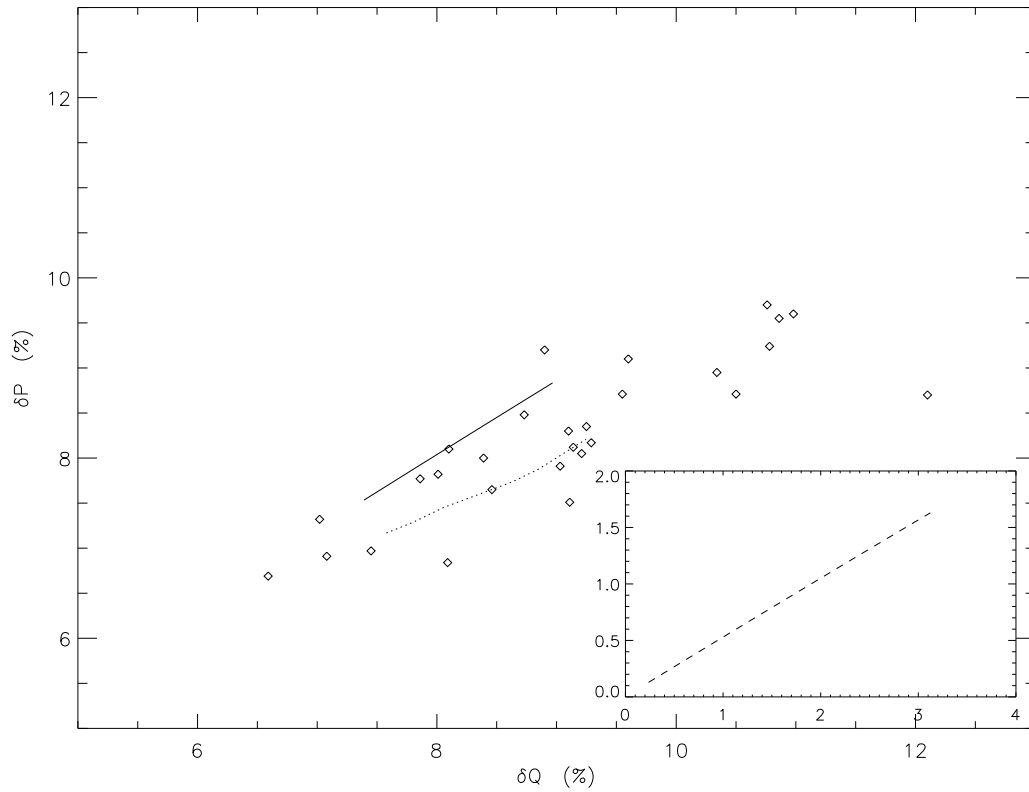


Figure 4.9 Ozone—Three-isotope plot of ozone in the regions between 20 and 35 km. Diamonds are balloon-borne mass spectrometer measurements [*Krankowsky et al.*, 2000; *Mauersberger et al.*, 2001; *Lämmerzahl et al.*, 2002]. The solid and dashed lines are the calculated formation- and photolysis-induced enrichments, respectively. The dotted line is the laboratory measurements [*Morton et al.*, 1990].

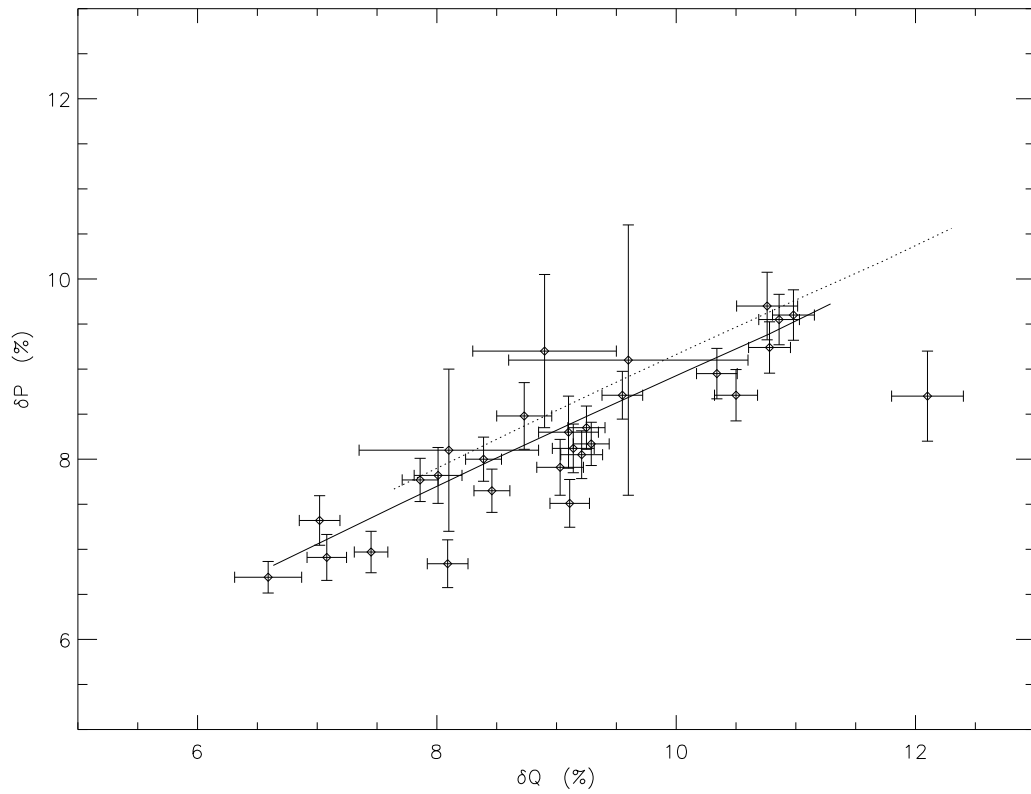


Figure 4.10 Ozone—Three-isotope plot of ozone in the regions between 20 and 35 km, using the temperature profile shown by dotted line in Figure 4.1. Dotted line shows the profiles obtained using the reference temperature profile. One- σ error bars are overplotted.

Table 4.1. Ozone—List of Chemical Reactions

	Reactant(s)		Product(s)	Rate Coefficient	Note(s)
R1	$O_3 + h\nu$	\rightarrow	$O_2(^1\Delta_g) + O(^1D)$	$J_1 = 4.21 \times 10^{-3}$	(1,5,6,14-17)
R2		\rightarrow	$O_2 + O$	$J_2 = 3.84 \times 10^{-4}$	(1,5,6,14-17)
R3	$OPO + h\nu$	\rightarrow	$OP(^1\Delta_g) + O(^1D)$	$\approx J_1$	Figure 4.5
R4		\rightarrow	$OP + O$	$\approx J_2$	Figure 4.6
R5	$OOP + h\nu$	\rightarrow	$O_2(^1\Delta_g) + P(^1D)$	$\approx \frac{1}{2}J_1$	Figure 4.5
R6		\rightarrow	$O_2 + P$	$\approx \frac{1}{2}J_2$	Figure 4.6
R7		\rightarrow	$OP(^1\Delta_g) + O(^1D)$	$= J_5 \approx \frac{1}{2}J_1$	Figure 4.5
R8		\rightarrow	$OP + O$	$= J_6 \approx \frac{1}{2}J_2$	Figure 6
R9	$OQO + h\nu$	\rightarrow	$OQ(^1\Delta_g) + O(^1D)$	$\approx J_1$	Figure 4.5
R10		\rightarrow	$OQ + O$	$\approx J_2$	Figure 4.6
R11	$OOQ + h\nu$	\rightarrow	$O_2(^1\Delta_g) + Q(^1D)$	$\approx \frac{1}{2}J_1$	Figure 4.5
R12		\rightarrow	$O_2 + Q$	$\approx \frac{1}{2}J_2$	Figure 4.6
R13		\rightarrow	$OQ(^1\Delta_g) + O(^1D)$	$= J_{11} \approx \frac{1}{2}J_1$	Figure 4.5
R14		\rightarrow	$OQ + O$	$= J_{12} \approx \frac{1}{2}J_2$	Figure 4.6
R15	$O_2 + h\nu$	\rightarrow	$2O$	$J_{15} = 1.42 \times 10^{-7}$	(1,8,9,11,18)
R16	$OP + h\nu$	\rightarrow	$O + P$	$= J_{15}$	assumed
R17	$OQ + h\nu$	\rightarrow	$O + Q$	$= J_{15}$	assumed
R18	$O_2 + h\nu$	\rightarrow	$O + O(^1D)$	$J_{18} = 6.50 \times 10^{-7}$	(1,8,9,11,18)
R19	$OP + h\nu$	\rightarrow	$O(^1D) + P$	$= \frac{1}{2}J_{18}$	assumed
R20		\rightarrow	$O + P(^1D)$	$= \frac{1}{2}J_{18}$	assumed
R21	$OQ + h\nu$	\rightarrow	$O(^1D) + Q =$	$= \frac{1}{2}J_{18}$	assumed
R22		\rightarrow	$O + Q(^1D)$	$= \frac{1}{2}J_{18}$	assumed
R23	$O + O_2 + M$	\rightarrow	$O_3 + M$	$k_{23} = 1.76 \times 10^{-27}T^{-2.6}$	(7)
R24	$O + OP + M$	\rightarrow	$OOP + M$	$\approx \frac{1}{2}k_{23}$	Figure 4.3
R25	$O + OP + M$	\rightarrow	$OPO + M$	$\approx \frac{1}{2}k_{23}$	Figure 4.3
R26	$O + OQ + M$	\rightarrow	$OOQ + M$	$\approx \frac{1}{2}k_{23}$	Figure 4.3
R27	$O + OQ + M$	\rightarrow	$OQO + M$	$\approx \frac{1}{2}k_{23}$	Figure 4.3
R28	$P + O_2 + M$	\rightarrow	$OOP + M$	$\approx k_{23}$	Figure 4.3
R29	$Q + O_2 + M$	\rightarrow	$OOQ + M$	$\approx k_{23}$	Figure 4.3
R30	$O + OP$	\rightarrow	$P + O_2$	$\approx \frac{1}{2}k_{33}$	Figure 4.3
R31	$P + O_2$	\rightarrow	$OP + O$	$\approx k_{33}$	Figure 4.3
R32	$O + OQ$	\rightarrow	$Q + O_2$	$\approx \frac{1}{2}k_{33}$	Figure 4.3
R33	$Q + O_2$	\rightarrow	$OQ + O$	$k_{33} = 2.01 \times 10^{-10}T^{-0.9}$	(2)
R34	$O + O_3$	\rightarrow	$2O_2$	$k_{34} = 8.00 \times 10^{-12}e^{-2060/T}$	(12)
R35	$O + OOP$	\rightarrow	$OP + O_2$	$= k_{34}$	assumed
R36	$O + OPO$	\rightarrow	$OP + O_2$	$= k_{34}$	assumed
R37	$O + OOQ$	\rightarrow	$OQ + O_2$	$= k_{34}$	assumed
R38	$O + OQO$	\rightarrow	$OQ + O_2$	$= k_{34}$	assumed
R39	$P + O_3$	\rightarrow	$OP + O_2$	$= k_{34}$	assumed

Table 4.1 (cont'd)

	Reactant(s)		Product(s)	Rate Coefficient	Note(s)
R40	Q + O ₃	→	OQ + O ₂	= k_{34}	assumed
R50	O(¹ D) + N ₂	→	O + N ₂	$k_{50} = 1.80 \times 10^{-11} e^{110/T}$	(12)
R51	P(¹ D) + N ₂	→	P + N ₂	= k_{50}	assumed
R52	Q(¹ D) + N ₂	→	Q + N ₂	= k_{50}	assumed
R53	O(¹ D) + O ₂	→	O + O ₂	$k_{53} = 3.20 \times 10^{-11} e^{70/T}$	(12)
R54	P(¹ D) + O ₂	→	P + O ₂	= k_{53}	assumed
R55	Q(¹ D) + O ₂	→	Q + O ₂	= k_{53}	assumed
R56 ^a	O ₂ (¹ Δ _g)	→	O ₂	$k_{56} = 2.58 \times 10^{-4}$	(4,13)
R57 ^a	OP(¹ Δ _g)	→	OP	= k_{56}	assumed
R58 ^a	OQ(¹ Δ _g)	→	OQ	= k_{56}	assumed
R59	O ₂ (¹ Δ _g) + O ₂	→	O ₂ + O ₂	$k_{59} = 3.60 \times 10^{-18} e^{-200/T}$	(12)
R60	OP(¹ Δ _g) + O ₂	→	OP + O ₂	= k_{59}	assumed
R61	OQ(¹ Δ _g) + O ₂	→	OQ + O ₂	= k_{59}	assumed
R62	O + O + M	→	O ₂ + M	$k_{62} = 4.30 \times 10^{-28} T^{-2}$	(3)
R63	O + P + M	→	OP + M	= k_{62}	assumed
R64	O + Q + M	→	OQ + M	= k_{62}	assumed
R83	O ₃ + X	→	PROD + X	k_{83}	Figure 4.2
R84	OPO + X	→	PROD + X	= k_{83}	assumed
R85	OOP + X	→	PROD + X	= k_{83}	assumed
R86	OQO + X	→	PROD + X	= k_{83}	assumed
R87	OOQ + X	→	PROD + X	= k_{83}	assumed

Note. — Electronic configurations are not shown for those atoms/molecules at their ground states. Units are s⁻¹ for photolysis reactions, cm³ s⁻¹ for two-body reactions, and cm⁶ cm⁻¹ for three-body reactions. The photolysis rate coefficients are given at the top of the model atmosphere. Note that O = ¹⁶O, P = ¹⁷O, and Q = ¹⁸O. R83-R87 denote a net loss of ozone by catalysis.

^aSpontaneous decay of excited O₂.

References. — (1) *Anbar et al.* [1993]; (2) *Anderson et al.* [1985]; (3) *Arnold and Comes* [1979]; (4) *Badger et al.* [1965]; (5) *Brock and Watson* [1980]; (6) *Fairchild et al.* [1978]; (7) *Hippler et al.* [1990]; (8) *Lee et al.* [1977]; (9) *Nicolet* [1984]; (10) *Parisse et al.* [1996]; (11) *Samson et al.* [1982]; (12) *Sander et al.* [2003]; (13) *Sandor et al.* [1997]; (14) *Sparks et al.* [1980]; (15) *Taherian and Slinger* [1985]; (16) *Turnipseed et al.* [1991]; (17) *Wine and Ravishankara* [1982]; (18) *Yung et al.* [1988].

Chapter 5

Oxygen Isotopic Composition of Carbon Dioxide in the Middle Atmosphere

Mao-Chang Liang, Geoffrey A. Blake, Brenton R. Lewis, and Yuk L.

Yung

Proceedings of the National Academy of Sciences, submitted

Abstract

The isotopic composition of long-lived trace gases provides a window into atmospheric transport and chemistry. Carbon dioxide is a particularly powerful tracer, because its abundance remains >100 ppmv in the mesosphere. We, for the first time, successfully reproduce the isotopic composition of CO₂ in the middle atmosphere. The mass-independent fractionation of oxygen in CO₂ can be fully explained by the exchange reaction with O(¹D). In the stratosphere, the major source of O(¹D) is O₃ photolysis. Higher in the mesosphere, we discover that the photolysis of ¹⁶O¹⁷O and ¹⁶O¹⁸O by solar Lyman- α radiation yields O(¹D) 10-100 times more enriched in ¹⁷O and ¹⁸O than that from ozone photodissociation. New laboratory and atmospheric measurements are proposed to test our model and validate the use of CO₂ isotopic fractionation as a tracer of atmospheric chemical and dynamical processes. Once fully understood, the “anomalous” oxygen signature in CO₂ can be used in turn to study biogeochemical cycles, in particular to constrain the gross carbon fluxes between the atmosphere and terrestrial biosphere.

5.1 Introduction

Of the many trace molecules that can be used to examine atmospheric transport processes and chemistry (e.g., CH₄, N₂O, SF₆, and the CFCs), carbon dioxide is unique in the middle atmosphere because of its high abundance (~370 ppmv in the stratosphere, dropping to ~100 ppmv at the homopause). The mass independent isotopic fractionation (MIF) of oxygen first discovered in ozone [*Mauersberger et al.*, 1981; *Thiemens and Heidenreich*, 1983] is thought to be partially transferred to carbon dioxide [*Thiemens et al.*, 1995; *Thiemens*, 1999] via the reaction O(¹D) + CO₂ in the middle atmosphere [*Yung et al.*, 1997]. Indeed,

while the reactions of trace molecules with $O(^1D)$ usually lead to their destruction, the $O(^1D) + CO_2$ reaction regenerates carbon dioxide. This “recycled” CO_2 is unique in its potential to trace the chemical (reactions involving $O(^1D)$ in either a direct or indirect way) and dynamical processes in the middle atmosphere. When transported to the troposphere, it will produce measurable effects in biogeochemical cycles involving CO_2 [Hoag *et al.*, 2005].

In particular, the extraordinary MIF seen initially in ozone [Mauersberger *et al.*, 1981; Thiemens and Heidenreich, 1983] has since been extended to long-lived trace molecules such as N_2O and CO_2 [see Thiemens, 1995 for a review]. The first stratospheric/mesospheric measurements of $\delta^{17}O(CO_2)$ and $\delta^{18}O(CO_2)$ at $30^\circ N$ by Thiemens *et al.* [1995] led to a suggestion that the MIF in stratospheric CO_2 is caused by isotopic exchange between CO_2 and O_3 , mediated by the reaction with $O(^1D)$ [Yung *et al.*, 1997].

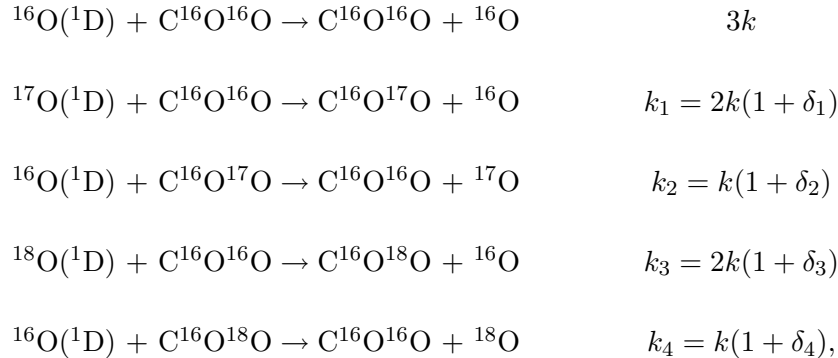
Subsequent stratospheric measurements at latitudes of $43.7^\circ N$ and $67.9^\circ N$ [Lämmerzahl *et al.*, 2002] revealed larger fractionations in both $\delta^{17}O(CO_2)$ and $\delta^{18}O(CO_2)$ than those seen at $30^\circ N$ at similar altitudes. Yung *et al.* [1997] suggested upwelling of tropospheric air from the tropics and downwelling at about $30^\circ N$ could dilute the magnitude of isotopic fractionation, further illustrating the critical role that transport plays in establishing the isotopic systematics of CO_2 in the stratosphere and mesosphere.

In three-isotope plots, the mass-dependent fractionation of oxygen has a slope of $\delta^{17}O/\delta^{18}O = m \approx 0.5$; yet least squares fits to the $30^\circ N$ and $43.7/67.9^\circ N$ CO_2 data sets give $m = 1.21 \pm 0.08$ and 1.71 ± 0.03 , respectively, while $m = 2.06 \pm 0.58$ for samples from the Arctic vortex [Alexander *et al.*, 2001] and 1.47 ± 0.14 from the lower stratosphere [Boering *et al.*, 2004]. Slopes near 1.6-1.7 have been successfully reproduced in the laboratory under \sim stratospheric conditions [Chakraborty and Bhattacharya, 2003]. Within the framework of Yung *et al.*’s mechanism [Yung *et al.*, 1997], the range of measured slopes reflects the

variety of transport histories of air parcels and sources of O(¹D), which have not yet been fully established in previous studies. The magnitude of $\delta^{17}\text{O}(\text{CO}_2)$ or $\delta^{18}\text{O}(\text{CO}_2)$ can, in principle, be used to determine how the air parcels are transported, but only if *all* sources of O(¹D) are accounted for. As we discuss below, while ozone photolysis is the dominant source of O(¹D) in the stratosphere, other sources must be considered at higher altitudes. These have not been included in previous models, and, as a result, the transport history of the air parcels as inferred by $\delta^{17}\text{O}(\text{CO}_2)$ or $\delta^{18}\text{O}(\text{CO}_2)$ alone tends to be ambiguous. This ambiguity can be largely resolved when both $\delta^{17}\text{O}(\text{CO}_2)$ and $\delta^{18}\text{O}(\text{CO}_2)$ are analyzed.

5.2 Exchange Reactions between O(¹D) and CO₂

The MIF of CO₂ is the consequence of the following reactions [Yung *et al.*, 1997]:



where O is either O(¹D) or O(³P) and δ_1 - δ_4 are the fractionation in the rate coefficients.

The resulting isotopic composition of CO₂ in equilibrium (in the absence of transport) is then determined simply by the isotopic composition of O(¹D), i.e., $[\text{C}^{16}\text{O}^{17}\text{O}]/[\text{C}^{16}\text{O}^{18}\text{O}] = (k_1 k_4)/(k_2 k_3)[{}^{17}\text{O}({}^1\text{D})]/[{}^{18}\text{O}({}^1\text{D})]$. However, the chemical exchange time $\tau_{exchange}$ is \gg vertical mixing time $\tau_{transport}$, and, as a result, the age of air can have a significant impact

on the magnitude of $\delta^{17}\text{O}(\text{CO}_2)$ and $\delta^{18}\text{O}(\text{CO}_2)$. For example, at an altitude of ~ 45 km, where $\text{O}(^1\text{D})$ peaks, τ_{exchange} is $\sim 10^8$ s while that for $\tau_{\text{transport}}$ is $\sim 10^7$ s; the “age” of air entering from the troposphere is $\sim 10^8$ s [Hall *et al.*, 1999]. During the time air ascends from the tropopause to this altitude, vertical mixing acts to dilute the isotopic fractionation of CO_2 . Thus, as the system approaches steady state, the isotopic composition of CO_2 is determined by the combination of the isotopic composition of $\text{O}(^1\text{D})$ and transport.

Limits to the slope m can be estimated by assuming isotopic equilibrium between CO_2 and $\text{O}(^1\text{D})$, since, in the homosphere, transport will only dilute the magnitude of $\delta^{17}\text{O}$ and $\delta^{18}\text{O}$. Based on Yung *et al.*'s mechanism, $\delta^{17}\text{O}$ and $\delta^{18}\text{O}$ can be approximated by

$$\delta^{17}\text{O}(\text{CO}_2) \approx \delta_1 - \delta_2 + \delta^{17}\text{O}(^1\text{D}) - \delta^{17}\text{O}(\text{CO}_2)_0 \quad (5.1)$$

$$\delta^{18}\text{O}(\text{CO}_2) \approx \delta_3 - \delta_4 + \delta^{18}\text{O}(^1\text{D}) - \delta^{18}\text{O}(\text{CO}_2)_0, \quad (5.2)$$

where $\delta^{17}\text{O}(\text{CO}_2)$ and $\delta^{18}\text{O}(\text{CO}_2)$ are the enrichments of CO_2 relative to the tropospheric values of $\delta^{17}\text{O}(\text{CO}_2)_0 \approx 9$ and $\delta^{18}\text{O}(\text{CO}_2)_0 \approx 17$ per mil. In this chapter, we follow the notation used in the companion paper [Liang *et al.*, 2005] that the enrichments are referenced to atmospheric O_2 , unless otherwise stated. (In the troposphere, $\delta^{17}\text{O}(\text{CO}_2)_0 \approx 21$ and $\delta^{18}\text{O}(\text{CO}_2)_0 \approx 41$ per mil, referenced to a more commonly used Vienna Standard Mean Ocean Water (V-SMOW).) If the reaction rate with $\text{O}(^1\text{D})$ is scaled by the reduced mass of each colliding pair, the δ_1 - δ_4 values are -21.8, -3.0, -41.6, and -5.8 per mil. The quenching reactions of $\text{O}(^1\text{D})$ with O_2/N_2 provide additional enrichments of 19.8/18.9 and 37.7/36.0 to $\delta^{17}\text{O}(^1\text{D})$ and $\delta^{18}\text{O}(^1\text{D})$, respectively, and since these effects are of opposite sign and similar in magnitude, the reduced mass effect in equations (5.1) and (5.2) is small. The slope m can thus be well approximated by $(\delta^{17}\text{O}(^1\text{D}) - \delta^{17}\text{O}(\text{CO}_2)_0)/(\delta^{18}\text{O}(^1\text{D}) - \delta^{18}\text{O}(\text{CO}_2)_0)$.

5.3 Sources of O(¹D)

More quantitative calculations of the three-isotope slope m are obtained via recent kinetic calculations modeling the isotopic fractionation of ozone versus altitude [*Liang et al.*, 2005]. Contributions to the enrichments of isotopically heavy ozone follow from two processes: chemical formation [*Gao and Marcus*, 2001] and UV photolysis [*Liang et al.*, 2004]. Using the model that reproduced the observed enrichments in a three-isotope plot of O₃ [*Liang et al.*, 2005], the computed equilibrium values of m (in the absence of transport) at altitudes between 30 and 60 km, where most of exchange reaction takes place, range from 1.3-3.0. Over the same altitude range (after taking transport into account) as that of the CO₂ measurements in the stratosphere, the slope m is 1.60, which is in good agreement with the measured value of ~ 1.7 [*Lämmerzahl et al.*, 2002].

At altitudes greater than 70 km, the photodissociation of O₂ becomes the dominant source of O(¹D). Exchange of O(¹D) with CO₂ at these altitudes could therefore modify the slope m if the O(¹D) from O₂ photolysis is isotopically distinct from that generated in the stratosphere. Using a semi-analytical calculation of the photolysis-induced fractionation [*Blake et al.*, 2003; *Liang et al.*, 2004] in the Schumann-Runge bands of O₂, the calculated enrichment of heavy O(¹D) is ≤ 100 per mil. However, a recent laboratory measurement of O₂ dissociation near Lyman- α (1215.67 Å) has shown that the cross section and O(¹D) yield are strong functions of wavelength, and suggests extremely large isotopic dependence [*Lacoursière et al.*, 1999]. Although the cross section near Lyman- α is 2-3 orders of magnitude less than those in the Schumann-Runge bands, the solar flux is correspondingly enhanced. For $T = 100 - 300$ K, we have computed the isotopic dependence of the O₂ dissociation cross section and O(¹D) yield near Lyman- α , using the model described in detail by *Lacoursière*

et al. [1999]. These cross sections, together with the solar spectrum, yield calculated values of $\delta^{17}\text{O}(^1\text{D})$ and $\delta^{18}\text{O}(^1\text{D})$ resulting from O_2 photolysis that peak at about 80 km with sizes of 3137.1 and 10578.6 per mil, respectively. These fractionations are enormous and give $m \approx 0.3$. Thus, even small amounts of mixing of mesospheric air with the $m = 1.6$ gas that characterizes the stratosphere can provide an explanation for the $m \leq 1.2$ fractionation observed in CO_2 by *Thiemens et al.* [1995]. We stress that Lyman- α photolysis of heavy O_2 as a source of $\text{O}(^1\text{D})$ has not been considered in previous models.

5.4 One-Dimensional Model

To provide a more quantitative assessment of the probable impact of the multiple sources of $\text{O}(^1\text{D})$, the results of a one-dimensional atmospheric model are summarized in Figure 5.1. The dominant slope of ~ 1.6 - 1.7 is produced by the $\text{O}(^1\text{D})$ from ozone photolysis, and reproduces the stratospheric data well. As the inset in Figure 5.1 shows, the heavy O atoms from O_2 Lyman- α photolysis can greatly modify the isotopic composition of CO_2 at altitudes >40 km. To provide a better agreement with the stratospheric data [*Lämmerzahl et al.*, 2002], the eddy coefficients below 40 km in this calculation have been reduced by 30% compared to those derived by *Allen et al.* [1981]. The disagreement of the model results with the measurements of *Thiemens et al.* [1995] is most likely due to circulation cells between the tropics and $\sim 30^\circ\text{N}$, where the air is significantly younger than that at higher latitudes and similar altitudes [*Yung et al.*, 1997; *Hall et al.*, 1999], but this difference cannot be resolved satisfactorily without two- or three-dimensional simulations. Indeed, we expect that multi-latitude and more mesospheric measurements of m , when combined with proper models, should be able to refine our understanding of atmospheric transport and

chemical processes – especially in the remote regions of the mesosphere.

5.5 Three-Box Model

Finally, we use a three-box model to evaluate the potential impact of transport on the slope and magnitude of the CO₂ isotopic fractionation. Box 1 (fresh air from the troposphere) has $\delta^{17}\text{O}(\text{CO}_2)_t = 9$ and $\delta^{18}\text{O}(\text{CO}_2)_t = 17$ per mil. Box 2 (the stratosphere) has $\delta^{17}\text{O}(\text{CO}_2)_s = \delta^{17}\text{O}({}^1\text{D}) = 93$ and $\delta^{18}\text{O}(\text{CO}_2)_s = \delta^{18}\text{O}({}^1\text{D}) = 69$ per mil, values defined by chemical equilibrium with O(¹D). Box 3 (the mesosphere) has $\delta^{17}\text{O}(\text{CO}_2)_m = \delta^{17}\text{O}({}^1\text{D}) = 3137$ and $\delta^{18}\text{O}(\text{CO}_2)_m = \delta^{18}\text{O}({}^1\text{D}) = 10579$ per mil, that predicted from the Lyman- α photolysis of O₂. The isotopic composition of CO₂ is determined by the mixing of air from these boxes, or

$$\delta^{17}\text{O}(\text{CO}_2) = x_t\delta^{17}\text{O}(\text{CO}_2)_t + x_s\delta^{17}\text{O}(\text{CO}_2)_s + x_m\delta^{17}\text{O}(\text{CO}_2)_m - \delta^{17}\text{O}(\text{CO}_2)_0 \quad (5.3)$$

$$\delta^{18}\text{O}(\text{CO}_2) = x_t\delta^{18}\text{O}(\text{CO}_2)_t + x_s\delta^{18}\text{O}(\text{CO}_2)_s + x_m\delta^{18}\text{O}(\text{CO}_2)_m - \delta^{18}\text{O}(\text{CO}_2)_0, \quad (5.4)$$

where x_t , x_s , and x_m are the fractions of air from boxes 1, 2, and 3, and $x_t + x_s + x_m =$

1. For atmospheric CO₂, $x_m \ll x_s < x_t$.

Figure 5.2 gives an illustration of this simple model. It is clear that the magnitude of $\delta^{17}\text{O}(\text{CO}_2)$ increases with the age of the air parcel, i.e., more CO₂ will exchange with O(¹D) from boxes 2 and 3. The solid line in this figure shows values of $\delta^{17}\text{O}(\text{CO}_2)$ obtained by varying x_t while $x_m = 0$. The symbols represent $\delta^{17}\text{O}(\text{CO}_2)$ with different degrees of mixing with box 3 after mixing of air from boxes 1 and 2.

The mixing of boxes 1 and 2 produces a slope of 1.6, as shown in the solid line of Figure 5.3. When mixing in air from box 3, the slope is modified, and the dotted line represents

the cases for which $(x_t, x_m) = (0.80, 0)$, $(0.75, 0.0005)$, and $(0.70, 0.001)$. Two extreme data points from Figure 5.1 overplotted by asterisks can be explained by $\sim 0.02\%$ mixing with box 3. Similar analysis can be applied to the rest of the data. In general, we predict that in the middle atmosphere the upwelling air would have CO_2 isotopic compositions characterized by ozone in the stratosphere, while that by O_2 photolysis would play a part in downwelling air.

In summary, we have demonstrated that the isotopic composition of CO_2 is potentially an exceptionally useful tracer in studying the dynamical and chemical processes in the middle atmosphere. Furthermore, this “recycled” CO_2 carries an isotopic composition distinct from that in the troposphere, and as such is a powerful tracer of biogeochemical CO_2 cycles – in particular those involving the terrestrial biosphere [Hoag *et al.*, 2005]. The large isotopic fractionation of O_2 resulting from the Lyman- α photolysis could be preserved in ice cores from polar regions in which downwelling air is prevalent [Luz *et al.*, 1999]. The observed depletion of $\delta^{18}\text{O}(\text{O}_2)$ at 53.3 and 59.5 km [Thiemens *et al.*, 1995] is likely the consequence of this O_2 Lyman- α photolysis. Experimentally, laboratory measurements of the dissociation cross sections of isotopically substituted O_2 near Lyman- α (1215.67 Å) are urgently needed. Observationally, more mesospheric measurements of CO_2 along with two- or three-dimensional atmospheric simulations will significantly expand our understanding of the dynamical and chemical history of trace molecules in the atmosphere.

Bibliography

- Alexander, B., M. K. Vollmer, T. Jackson, R. F. Weiss, and M. H. Thiemens, Stratospheric CO₂ Isotopic Anomalies and SF₆ and CFC Tracer Concentrations in the Arctic Polar Vortex, *Geophysics Research Letters*, 28, 4103-4106, 2001.
- Allen, M., Y. L. Yung, and J. W. Waters, Vertical Transport and Photochemistry in the Terrestrial Mesosphere and Lower Thermosphere (50-120 km), *Journal of Geophysics Research-Space Physics*, 86, 3617-3627, 1981.
- Blake, G. A., M. C. Liang, C. G. Morgan, and Y. L. Yung, A Born-Oppenheimer Photolysis Model of N₂O Fractionation, *Geophysics Research Letters*, 30, art. no.-1656, 2003.
- Boering, K. A., T. Jackson, K. J. Hoag, A. S. Cole, M. J. Perri, M. Thiemens, and E. Atlas, Observations of the Anomalous Oxygen Isotopic Composition of Carbon Dioxide in the Lower Stratosphere and the Flux of the Anomaly to the Troposphere, *Geophysics Research Letters*, 31, 2004.
- Chakraborty, S., and S. K. Bhattacharya, Experimental Investigation of Oxygen Isotope Exchange between CO₂ and O(¹D) and its Relevance to the Stratosphere, *Journal of Geophysics Research-Atmospheres*, 108, 2003.
- Clayton, R. N., T. K. Mayeda, and D. E. Brownlee, Oxygen Isotopes in Deep-Sea Spherules, *Earth and Planetary Science Letters*, 79, 235-240, 1986.

- Colegrov.Fd, Eddy Diffusion and Oxygen Transport in Lower Thermosphere, *Journal of Geophysics Research*, 70, 4931, 1965.
- Gao, Y. Q., and R. A. Marcus, Strange and Unconventional Isotope Effects in Ozone Formation, *Science*, 293, 259-263, 2001.
- Hall, T. M., D. W. Waugh, K. A. Boering, and R. A. Plumb, Evaluation of Transport in Stratospheric Models, *Journal of Geophysics Research-Atmospheres*, 104, 18815-18839, 1999.
- Hoag, K. J., C. J. Still, I. Y. Fung, and K. A. Boering, Triple Oxygen Isotope Composition of Tropospheric Carbon Dioxide as a Tracer of Terrestrial Gross Carbon Fluxes, *Geophysics Research Letters*, 32, 2005.
- Lacoursière, J., S. A. Meyer, G. W. Faris, T. G. Slanger, B. R. Lewis, and S. T. Gibson, The O(¹D) Yield from O₂ Photodissociation near H Lyman- α (121.6 nm), *Journal of Chemical Physics*, 110, 1949-1958, 1999.
- Lämmerzahl, P., T. Röckmann, C. A. M. Brenninkmeijer, D. Krankowsky, and K. Mauersberger, Oxygen Isotope Composition of Stratospheric Carbon Dioxide, *Geophysics Research Letters*, 29, 2002.
- Liang, M. C., G. A. Blake, and Y. L. Yung, A Semianalytic Model for Photo-Induced Isotopic Fractionation in Simple Molecules, *Journal of Geophysics Research-Atmospheres*, 109 (D10), art. No. D10308, 2004.
- Luz, B., E. Barkan, M. L. Bender, M. H. Thiemens, and K. A. Boering, Triple-Isotope Composition of Atmospheric Oxygen as a Tracer of Biosphere Productivity, *Nature*, 400, 547-550, 1999.

Mauersberger, K., Measurement of Heavy Ozone in the Stratosphere, *Geophysics Research Letters*, 8, 935-937, 1981.

Thiemens, M. H., Atmosphere Science - Mass-Independent Isotope Effects in Planetary Atmospheres and the Early Solar System, *Science*, 283, 341-345, 1999.

Thiemens, M. H., and J. E. Heidenreich, The Mass-Independent Fractionation of Oxygen - A Novel Isotope Effect and Its Possible Cosmochemical Implications, *Science*, 219, 1073-1075, 1983.

Thiemens, M. H., T. Jackson, E. C. Zipf, P. W. Erdman, and C. Vanegmond, Carbon-Dioxide and Oxygen-Isotope Anomalies in the Mesosphere and Stratosphere, *Science*, 270, 969-972, 1995.

Yung, Y. L., A. Y. T. Lee, F. W. Irion, W. B. DeMore, and J. Wen, Carbon Dioxide in the Atmosphere: Isotopic Exchange with Ozone and its Use as a Tracer in the Middle Atmosphere, *Journal of Geophysics Research-Atmospheres*, 102, 10857-10866, 1997.

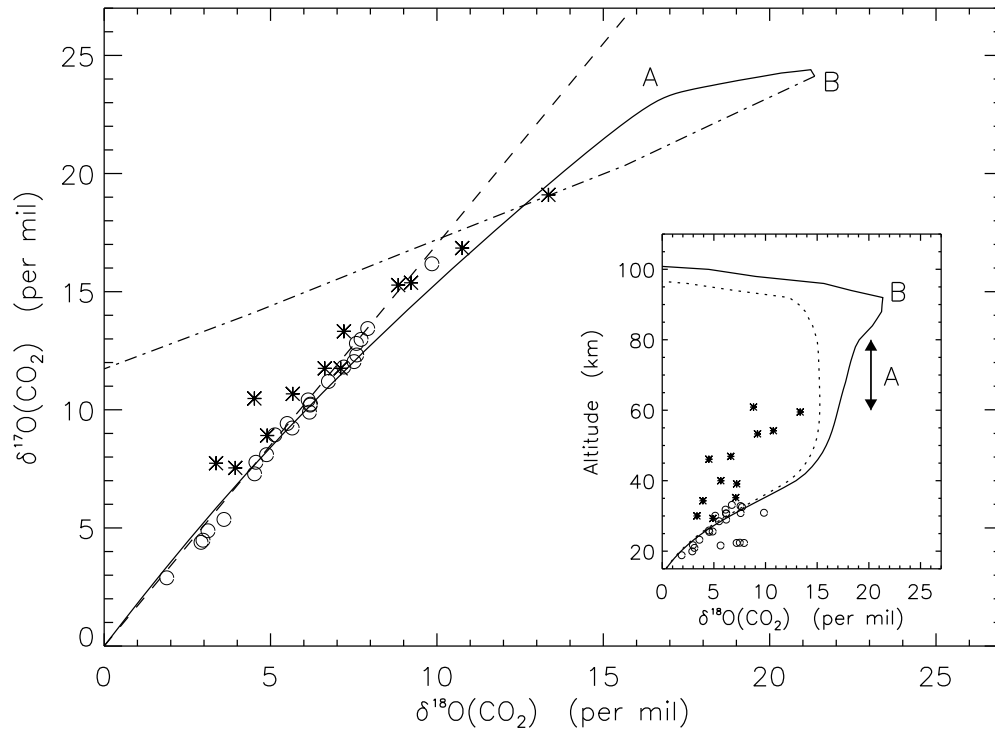


Figure 5.1 Carbon Dioxide—Three-isotope plot of oxygen in CO_2 , from which the tropospheric values have been subtracted. The atmospheric measurements are from *Lämmerzahl et al.* [2002] (circles) and from *Thiemens et al.* [1995] (asterisks). The solid line depicts the model, and the change in slope at A corresponds to altitudes of $\sim 60\text{--}80$ km. At higher altitudes (and for fractionations greater than these fiducial values), the slope $m(\text{A-B})$ is ~ 0.3 – as expected from oxygen photolysis. Another change of slope in the calculation occurs at B for altitudes of ~ 90 km and higher. Over this range, molecular diffusion dominates, and the slope becomes mass dependent, that is ~ 0.5 (dash-dotted line). Inset: vertical profiles of $\delta^{18}\text{O}(\text{CO}_2)$. The dotted line represents the results excluding the fractionation of $\text{O}(^1\text{D})$ from O_2 photolysis over the solar Lyman- α emission.

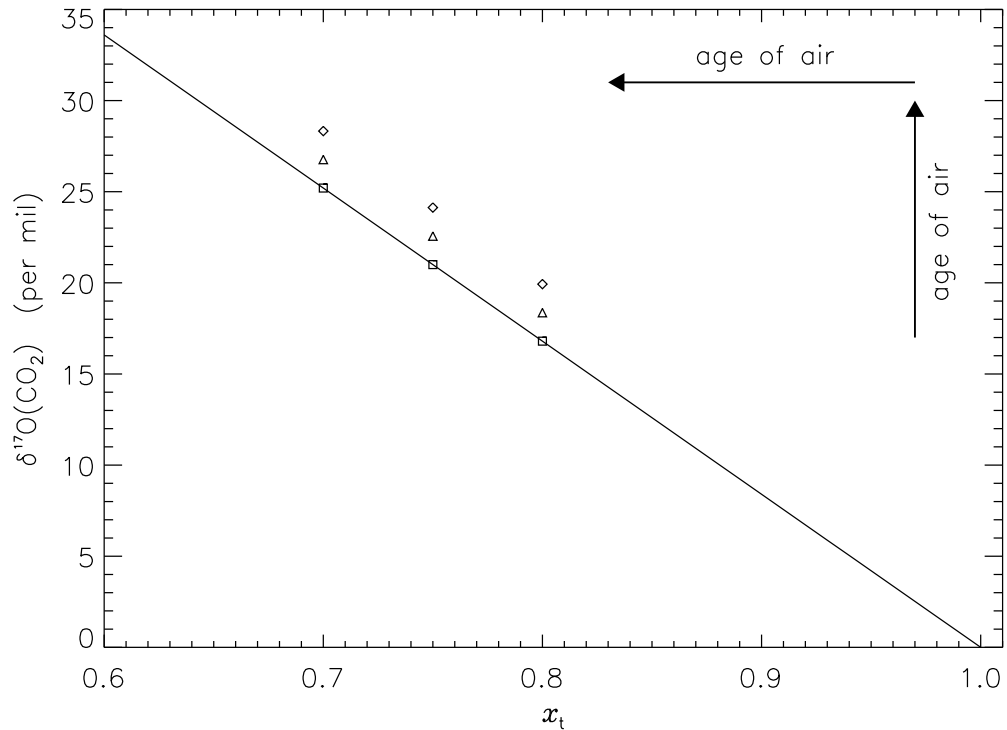


Figure 5.2 Carbon Dioxide—A three-box mixing model for CO_2 in the middle atmosphere. The solid line represents the mixing of boxes 1 (troposphere) and 2 (stratosphere) only, while the symbols denote additional mixing with box 3 to varying extent. Squares: no mixing with box 3. Triangles: 0.05% of air from box 3. Diamonds: 0.1% of air from box 3. The two arrows indicate the direction in which the fractionation changes as the age of the air is increased.

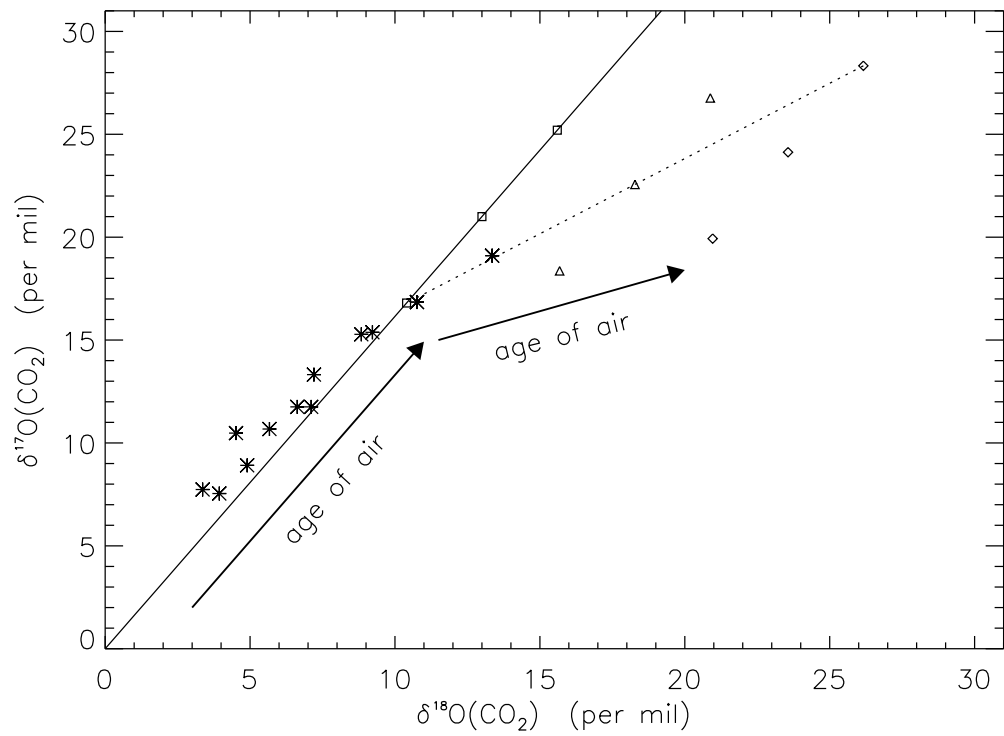


Figure 5.3 Carbon Dioxide—The notation and symbols are the same as those in Figures 5.1 and 5.2. The solid line illustrates the fractionation expected from the interaction of CO_2 and O_3 only, while the dotted line presents an example of how the three isotope slope can be flattened by the mixing of air from boxes 2 (stratosphere) and 3 (mesosphere).

Chapter 6

Production of Oxidants in the Atmosphere of a Snowball Earth

Mao-Chang Liang, Hyman Hartman, Robert E. Kopp, Joseph L. Kirschvink
and Yuk L. Yung

Proceedings of the National Academy of Sciences, submitted

Abstract

During the Proterozoic period, Earth experienced two intervals with one or more episodes of low-latitude glaciation, which were probable “Snowball Earth” events. Snowball conditions are associated with the nearly complete shutdown of the hydrological cycle and severe curtailment of biological activity. We show here that during such long and severe glacial intervals a weak hydrological cycle coupled with photochemical reactions involving water vapor would give rise to the sustained production and sequestration of hydrogen peroxide. This compound would be buried in the snow/ice and would accumulate over the lifetime of the Snowball. The accumulated oxidant would be released directly into the ocean and the atmosphere upon melting and could explain global oxidation events in the aftermath of the Snowball such as the Kalahari Manganese Field in South Africa and the Urucum Formation in Brazil. Low levels of peroxides generated during Archean and earliest Proterozoic non-Snowball glacial intervals could have driven the evolution of oxygen-mediating enzymes and thereby paved the way for the eventual appearance of oxygenic photosynthesis.

6.1 Introduction

While there have been many glacial events recorded in the history of the Earth [*Hambrey and Harland*, 1981; *Chumakov and Elston*, 1989; *Young et al.*, 1998], two major periods of low-latitude glacial episodes appear correlated with significant changes in the evolution of life. These “Snowball Earth” events appear to have been characterized by globally sub-freezing temperatures and the encasement of most of the surface of the earth, including the oceans, in ice [*Kirschvink*, 1992; *Hoffman and Schrag*, 2002]. The first known Snowball, the Paleoproterozoic Makganyene event, occurred approximately between 2.3 and 2.2 Ga.

At least two others may have occurred in the Cryogenian period of the Neoproterozoic, between about 740 and 630 Ma [*Hambrey and Harland, 1981; Chumakov and Elston, 1989; Bodiselitsch et al., 2005*]. The Paleoproterozoic Snowball appears to follow soon after the evolution of oxygenic photosynthesis and slightly predates the first clear fossil evidence for organelle-bearing eukaryotic cells [*Kopp et al., 2005*]. The Neoproterozoic Snowballs are followed soon after by the first fossil evidence for animal life. This article examines atmospheric photochemistry during the Paleoproterozoic Snowball Earth event, as well as the impact of this and four earlier glaciations on the evolution of cellular life.

Factors that initiate Snowball Earth conditions are as yet highly controversial. One mechanism that has been shown to work is the oxidation of atmospheric CH_4 , if CH_4 plays a key role in the greenhouse warming of the planet [*Pavlov et al., 2000*]. Biological activity and hydrological cycles during the Snowball would have been severely curtailed, while volcanic activity would have persisted [*Kirschvink, 1992*]. As ice cover and low temperatures would have greatly hindered silicate weathering, atmospheric accumulation of greenhouse gases, particularly CO_2 , would have eventually led to deglaciation [*Pierrehumbert, 2004*]. In Neoproterozoic time it would have taken about 30 Myr, a time scale consistent with iridium records (Bodiselitsch et al. 2005), to reach an atmospheric pressure of ~ 0.2 bar of CO_2 , needed to produce enough greenhouse warming to begin melting the equatorial ice. Due to the lower solar constant (85% vs. 96% of modern insolation), extrapolating this estimate to the Paleoproterozoic Snowball implies that nearly 100 Myr would have been necessary to reach the ~ 1 bar CO_2 needed to initiate the deglaciation. The rock record indicates that the atmosphere was oxygen poor before ~ 2.3 Ga, and that a burst of oxygen suddenly appeared afterward [*Karhu and Holland, 1996; Farquhar et al., 2000; Kirschvink et al., 2000*], coincident with the retreat of the Snowball [*Kirschvink et al., 2000*].

6.2 Hypothesis

We propose that the oxidants (mainly hydrogen peroxide) produced in the atmosphere of a Snowball Earth can be deposited in the snow/ice. The proposed mechanism is similar to that found in the Martian atmosphere, where oxidants such as H_2O_2 [Clancy *et al.*, 2004; Encrenaz *et al.*, 2004] can be formed in cold and dry environments [Hunten, 1979]. Due to the weak ice/water hydrological cycle during a Snowball, H_2O_2 , which has a freezing point of -1°C , close to that of water, can be preserved in the snow/ice. Upon the retreat of the Snowball, the deposited H_2O_2 would be released into the oceans and atmosphere, as occurs in the summertime in Greenland [Hutterli *et al.*, 2001]. Meltwater containing H_2O_2 would mix in the ocean and oxidize reduced solutes [Stumm and Morgan, 1996], including manganese, which would explain the post-glacial deposition of Mn oxides in the Kalahari Mn field [Cairncross *et al.*, 1997; Kirschvink *et al.*, 2000]. At present, the concentration of H_2O_2 in the snow is $\sim 20\ \mu\text{M}$ [Hutterli *et al.*, 2001], a mixing ratio of $\sim 5 \times 10^7$. With this concentration and $1\ \text{mm}\ \text{yr}^{-1}$ (limited by sublimation rate) [Hoffman *et al.*, 1998] ice/water cycles, the deposition rate of H_2O_2 would be $\sim 5 \times 10^7\ \text{molecules}\ \text{cm}^2\ \text{s}^{-1}$, or $\sim 10^{18}$ moles of H_2O_2 in 100 Myr (integrated over the whole planet), an order of magnitude lower than the required oxidants to explain the Kalahari Mn field [Kirschvink *et al.*, 2000]. However, the deposition rate of H_2O_2 could be greatly enhanced under low O_2 conditions.

6.3 Atmospheric Chemical Processes

To test our hypothesis, we perform a one-dimensional simulation of the chemical processes in the atmosphere of a Snowball Earth and exploit results reported recently by Tian *et al.* [Tian *et al.*, 2005] on the hydrodynamic escape of hydrogen into space. Our model

calculates the profiles of O, O(¹D), O₂, O₃, H, H₂, OH, HO₂, H₂O₂, CO, CO₂, HCO, and H₂CO. For simplicity, we fix H₂O with the profile in Figure 6.1, which is determined by its saturation relation. Our standard model assumes an N₂-based atmosphere with a surface pressure of 1 bar and vertical mixing coefficients of $2 \times 10^5 \text{ cm}^2 \text{ s}^{-1}$, close to present-day values [Allen *et al.*, 1981]. For the temperature profile, the surface temperature is taken to be 240 K [Hoffman *et al.*, 1998; Hyde *et al.*, 2000], with a vertical temperature gradient of -10 K km^{-1} (dry-adiabatic lapse rate) and a constant temperature of 150 K in regions where the extrapolation of the temperature with the assumed gradient yields values less than 150 K. We also assume a present-day solar UV spectrum. Initially, the atmosphere contains N₂ and H₂O only. The model starts with an upward H₂ and CO₂ fluxes of $10^{10} \text{ cm}^{-2} \text{ s}^{-1}$. Species other than H₂, H₂O, and H₂O₂ are impermeable at the boundary. We allow H₂ to escape to space hydrodynamically when the conditions of Tian *et al.* [Tian *et al.*, 2005] are met. With the present-day solar spectrum, hydrodynamic escape happens when the homopause ($\sim 65 \text{ km}$) mixing ratio of H₂ is >0.05 . For simplicity, we assume that H₂ escape with a flux of $10^{10} \text{ cm}^{-2} \text{ s}^{-1}$ is initiated when the H₂ mixing ratio is >0.1 and that it remains at this level as long as the ratio is >0.05 . We let the model run for 100 Myr. Vertical profiles of species important to this study are summarized in Figure 6.1.

Hydrogen peroxide can be deposited on ice by diffusional contact. This deposition rate is limited by the lifetime of H₂O₂ against photolysis in the atmosphere (~ 6 hours), equivalent to a travelling distance of $<1 \text{ km}$ for a diffusion coefficient of $2 \times 10^5 \text{ cm}^2 \text{ s}^{-1}$. This diffusional deposition of H₂O₂ is also sensitive to the H₂/O₂ ratio (Figure 6.2). With a ratio ~ 2 , the deposition rate is as high as $10^{10} \text{ cm}^{-2} \text{ s}^{-1}$. For ratios >5 , the rates are suppressed by a factor of >10 . The accumulation of H₂ in the atmosphere would soon stop the diffusional deposition of H₂O₂ if the replenishment of O₂ is insufficient to support an O₂ abundance

as high as that in Figure 6.1, because of the reaction $2\text{H}_2 + \text{O}_2 \rightarrow 2\text{H}_2\text{O}$. We find that the continuous accumulation and photolysis of CO_2 in the atmosphere can maintain such levels of O_2 ($2\text{CO}_2 \rightarrow 2\text{CO} + \text{O}_2$) via HOx chemistry [Liang *et al.*, 200]. Consequently, CO is in high abundance (Figure 6.1). In this standard model, the deposition rate of H_2O_2 by diffusion is $3 \times 10^8 \text{ cm}^{-2} \text{ s}^{-1}$. Assuming homogeneous co-condensation of H_2O and H_2O_2 (the ratio of the abundances of H_2O_2 and H_2O is $\sim 5 \times 10^{-6}$, see Figure 6.1) results in an average rainout rate of H_2O_2 of $5 \times 10^8 \text{ cm}^{-2} \text{ s}^{-1}$ for a 1 mm yr^{-1} hydrological cycle.

This standard model yields a burial rate of H_2O_2 of $\sim 10^9 \text{ cm}^{-2} \text{ s}^{-1}$. In 100 Myr, a total of ~ 5 moles cm^{-2} of H_2O_2 , or equivalent to ~ 0.1 bar of O_2 , can accumulate. We stress that the above calculated burial rate of H_2O_2 is a lower limit. With the present-day solar spectrum, the maximum photolysis rate of H_2O is $\sim 10^{12} \text{ cm}^{-2} \text{ s}^{-1}$. If UV photons directly irradiated of the snow/ice, H_2O_2 could be produced and preserved quickly in the firn. (The production of H_2O_2 in Antarctic seawater samples by direct sun light irradiation has been shown to be significant [Abele *et al.*, 1999].) This mechanism of depositing H_2O_2 would be insensitive to the abundance of atmospheric H_2 .

6.4 Biological Implications

The source of oxygen in the anaerobic environment of the Archean Earth has long been a mystery. Blankenship and Hartman [Blankenship and Hartman, 1998] suggested that H_2O_2 played a crucial role in the origin and evolution of oxygenic photosynthesis, since it is capable of being both a powerful oxidant and a reductant. The oxidation of H_2O_2 to O_2 is fully within the oxidative capabilities of reaction centers from existing anoxygenic photosynthetic bacteria [Blankenship and Hartman, 1998], and this process is similar to that

employed by the Mn-based enzyme, catalase, which catalyzes the reaction $2\text{H}_2\text{O}_2 \rightarrow 2\text{H}_2\text{O} + \text{O}_2$ [Penner-Hahn, 1992; Stumm and Morgan, 1996]. Hydrogen peroxide in the presence of ferrous ion produces the hydroxyl radical (and ferryl iron), which is lethal to the cell. Catalases and superoxide dismutase enzymes should have evolved to protect the cell against the effects of hydrogen peroxide and the hydroxyl radical. These enzymes evolved before the evolution of oxygenic photosynthesis and hence protected the first oxygen producing phototroph [Schopf, 1975].

Even when the concentration of H_2O_2 in snow and ice is as low as that in the modern Arctic or Antarctic, the release of H_2O_2 into the ocean upon melting after a glacial event smaller than a Snowball could gradually oxidize local environments and facilitate the evolution of oxygenic photosynthesis [Schopf, 1975]. The existence of the Pongola glaciation at ~ 2.9 Ga, and perhaps unrecognized earlier glacial episodes, argues that oxygen would also have been available to drive the evolution of enzymatic tolerance long before the appearance of the first oxygen-producing phototrophs [Schopf, 1975; Blankenship and Hartman, 1998]. Global oxidation, however, could happen only after planet-wide glaciations like Snowball Earth events.

We also find this total amount of H_2O_2 (when decomposed to O_2) deposited in the snow/ice is greater than that necessary to oxidize 4 billion tons of Mn in the Kalahari Mn Field [Kirschvink *et al.*, 2000]. Hydrogen peroxide in the snow/ice could not, however, be preserved in the places possessing high temperature variations. During summer at low latitudes, the deposited H_2O_2 could be released into ocean upon the melting of sea ice [Hyde *et al.*, 2000; Hoffman and Schrag, 2002], causing ions such as Mn^{2+} and Fe^{2+} to precipitate during the Snowball, thus strongly limiting the availability of H_2O_2 in these regions in the aftermath of the Snowball. The maximum amount of Mn and Fe available in the ocean is

$5\text{-}50\times 10^{18}$ and $2\text{-}5\times 10^{18}$ moles, respectively [Kirschvink *et al.*, 2000]. Such large deposition of Mn is not globally found, suggesting that the accumulation of Mn/Fe in some areas was insufficient during the Snowball.

We have demonstrated here that the generation of H_2O_2 through photolysis of H_2O is possible in the oxygen-poor early atmosphere of the Archean and early Paleoproterozoic periods [Kasting *et al.*, 1985; McKay and Hartman, 1991]. Hydrogen peroxide can be preserved only under very special conditions, such as during an intense glaciation. The low abundance of H_2O_2 is due primarily to its short atmospheric lifetime against UV photolysis, which necessitates its production close to the ground (hence, under low O_2 conditions), as well as a mechanism to trap it in the ice to store and concentrate it. During an ice age, the deposition rate can be enhanced greatly, as we discuss above. The process is even more noticeable after a Snowball, when the deposition of H_2O_2 is worldwide and extremely abundant. If this mechanism is correct, the smaller Urucom manganese deposits in Brazil suggest that the Sturtian hydrological cycle was more active than the hydrological cycle of the Paleoproterozoic Snowball Earth. A coupled chemistry and dynamics model is needed to quantify our calculation in detail and to provide a more accurate estimation of the deposition of hydrogen peroxide during Snowball Earth events.

Bibliography

- Abele, D., G. A. Ferreyra, and I. Schloss, H₂O₂ Accumulation from Photochemical Production and Atmospheric Wet Deposition in Antarctic Coastal and Off-Shore Waters of Potter Cove, King George Island, South Shetland Islands, *Antarctic Science*, 11, 131-139, 1999.
- Allen, M., Y. L. Yung, and J. W. Waters, Vertical Transport and Photochemistry in the Terrestrial Mesosphere and Lower Thermosphere (50-120 km), *Journal of Geophysical Research-Space Physics*, 86, 3617-3627, 1981.
- Blankenship, R. E., and H. Hartman, The Origin and Evolution of Oxygenic Photosynthesis, *Trends in Biochemical Sciences*, 23, 94-97, 1998.
- Bodiselsch, B., C. Koeberl, S. Master, and W. U. Reimold, Estimating Duration and Intensity of Neoproterozoic Snowball Glaciations from Ir Anomalies, *Science*, 308, 239-242, 2005.
- Cairncross, B., N. J. Beukes, and J. Gutzmer, *The Manganese Adventure: The South African Manganese Fields*, Associated Ore & Metal Corporation, Ltd., Johannesburg, South Africa, 1997.
- Chumakov, N. M., and D. P. Elston, The Paradox of Late Proterozoic Glaciations at Low Latitudes, *Episodes*, 12, 115-119, 1989.

- Clancy, R. T., B. J. Sandor, and G. H. Moriarty-Schieven, A Measurement of the 362 GHz Absorption Line of Mars Atmospheric H₂O₂, *Icarus*, 168, 116-121, 2004.
- Encrenaz, T., and colleagues, Hydrogen Peroxide on Mars: Evidence for Spatial and Seasonal Variations, *Icarus*, 170, 424-429, 2004.
- Farquhar, J., H. M. Bao, and M. Thiemens, Atmospheric Influence of Earth's Earliest Sulfur Cycle, *Science*, 289, 756-758, 2000.
- Hambrey, M. J., and W. B. Harland, *Earths Prepleistocene Glacial Record*, Cambridge Univ. Press, Cambridge, 1981.
- Hoffman, P. F., A. J. Kaufman, G. P. Halverson, and D. P. Schrag, A Neoproterozoic Snowball Earth, *Science*, 281, 1342-1346, 1998.
- Hoffman, P. F., and D. P. Schrag, The Snowball Earth Hypothesis: Testing the Limits of Global Change, *Terra Nova*, 14, 129-155, 2002.
- Hunten, D. M., Possible Oxidant Sources in the Atmosphere and Surface of Mars, *Journal of Molecular Evolution*, 14, 71-78, 1979.
- Hutterli, M. A., J. R. McConnell, R. W. Stewart, H. W. Jacobi, and R. C. Bales, Impact of Temperature-Driven Cycling of Hydrogen Peroxide (H₂O₂) between Air and Snow on the Planetary Boundary Layer, *Journal of Geophysical Research-Atmospheres*, 106, 15395-15404, 2001.
- Hyde, W. T., T. J. Crowley, S. K. Baum, and W. R. Peltier, Neoproterozoic 'Snowball Earth' Simulations with a Coupled Climate/Ice-Sheet Model, *Nature*, 405, 425-429, 2000.

- Karhu, J. A., and H. D. Holland, Carbon Isotopes and the Rise of Atmospheric Oxygen, *Geology*, *24*, 867-870, 1996.
- Kasting, J. F., H. D. Holland, and J. P. Pinto, Oxidant Abundances in Rainwater and the Evolution of Atmospheric Oxygen, *Journal of Geophysical Research-Atmospheres*, *90*, 497-510, 1985.
- Kirschvink, J. L., *The Proterozoic Biosphere: A Multidisciplinary Study*, Cambridge Univ. Press, Cambridge, 1992.
- Kirschvink, J. L., E. J. Gaidos, L. E. Bertani, N. J. Beukes, J. Gutzmer, L. N. Maepa, and R. E. Steinberger, Paleoproterozoic Snowball Earth: Extreme Climatic and Geochemical Global Change and Its Biological Consequences, *Proceedings of the National Academy of Sciences of the United States of America*, *97*, 1400-1405, 2000.
- Kopp, R. E., J. L. Kirschvink, J. A. Hilburn, and C. Z. Nash, The Paleoproterozoic Snowball Earth: A Climate Disaster Triggered by the Evolution of Oxygenic Photosynthesis, *Proceedings of the National Academy of Sciences of the United States of America*, , in press, 2005.
- Liang, M. C., B. F. Lane, R. T. Pappalardo, M. Allen, and Y. L. Yung, Atmosphere of Callisto, *Journal of Geophysical Research-Planets*, *110*, 2005.
- McKay, C. P., and H. Hartman, Hydrogen-Peroxide and the Evolution of Oxygenic Photosynthesis, *Origins of Life and Evolution of the Biosphere*, *21*, 157-163, 1991.
- Pavlov, A. A., J. F. Kasting, L. L. Brown, K. A. Rages, and R. Freedman, Greenhouse Warming by CH₄ in the Atmosphere of Early Earth, *Journal of Geophysical Research-Planets*, *105*, 11981-11990, 2000.

Penner-Hahn, J. E., *Manganese Redox Enzymes*, VCH Publishers, Inc., New York, 1992.

Pierrehumbert, R. T., High Levels of Atmospheric Carbon Dioxide Necessary for the Termination of Global Glaciation, *Nature*, *429*, 646-649, 2004.

Schopf, J. W., Precambrian Paleobiology - Problems and Perspectives, *Annual Review of Earth and Planetary Sciences*, *3*, 213-249, 1975.

Stumm, W., and J. J. Morgan, *Aquatic Chemistry: Chemical Equilibria and Rates in Natural Waters*, John Wiley & Sons., New York, 1996.

Tian, F., O. B. Toon, A. A. Pavlov, and H. D. Sterck, A Hydrogen-Rich Early Earth Atmosphere, *Science*, *308*, 1014-1017, 2005.

Young, G. M., V. von Brunn, D. J. C. Gold, and W. E. L. Minter, Earth's Oldest Reported Glaciation: Physical and Chemical Evidence from the Archean Mozaan Group (Similar to 2.9 Ga) of South Africa, *Journal of Geology*, *106*, 523-538, 1998.

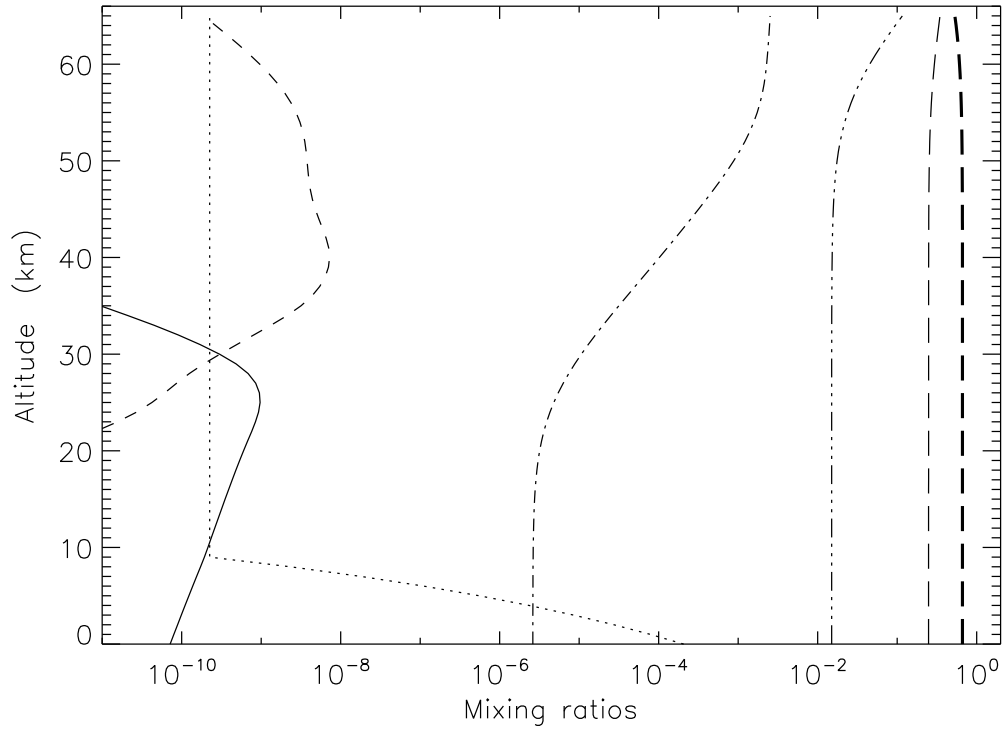


Figure 6.1 Snowball—Profiles of H_2O (dotted), H_2O_2 (solid), O_3 (dashed), O_2 (dash-dotted), H_2 (triple dot-dashed), CO (thin long-dashed), and CO_2 (thick long-dashed) calculated with the reference model, in which the surface temperature is 240 K, temperature gradient is -10 K km^{-1} , and constant temperature is 150 K above the tropopause ($\sim 10 \text{ km}$). The downward and escape fluxes of H_2O_2 and H_2 are $\sim 5 \times 10^8$ and $10^{10} \text{ cm}^{-2} \text{ s}^{-1}$, respectively. The mixing ratio of H_2O above the tropopause is set equal to that at the tropopause.

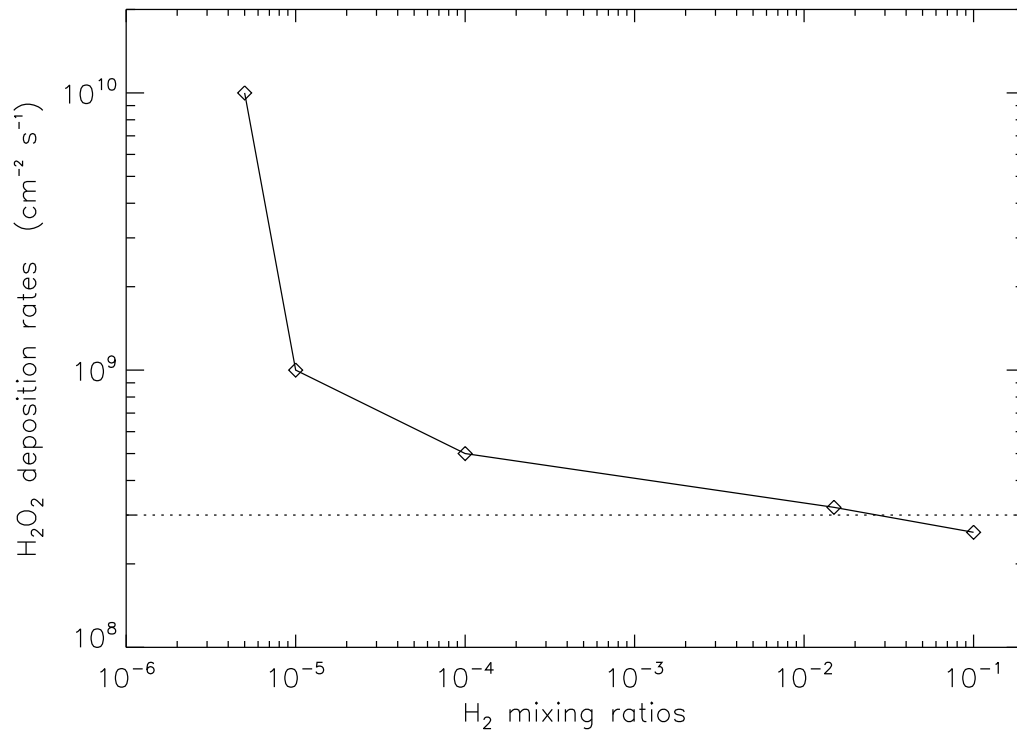


Figure 6.2 Snowball—Sensitivity of surface H₂ abundance on the deposition rate of H₂O₂ by diffusion. The abundance of O₂ as high as that in Figure 6.1 is maintained by CO₂ photolysis. Horizontal dotted line denotes the rate inferred by Kalahari Mn Field [*Kirschvink et al.*, 2000]; four billion tons of Mn were found over an area of 10^{6–7} km², which corresponds to an average deposition rate of $\sim 3 \times 10^8$ cm⁻² s⁻¹ in 100 Myr.

Part II

Jupiter and the Galilean Satellites

Chapter 7

Meridional Transport in the Stratosphere of Jupiter

Mao-Chang Liang, Run-Lie Shia, Anthony Y.-T. Lee, Mark Allen, A.

James Friedson, and Yuk L. Yung

The Astrophysical Journal Letters, 635, 177, 2005.

Abstract

The Cassini measurements of C_2H_2 and C_2H_6 at ~ 5 mbar provide a constraint on meridional transport in the stratosphere of Jupiter. We performed a two-dimensional photochemical calculation coupled with mass transport due to vertical and meridional mixing. The modeled profile of C_2H_2 at latitudes less than 70° follows the latitude dependence of the solar insolation, while that of C_2H_6 shows little latitude dependence, consistent with the measurements. In general, our model study suggests that the meridional transport timescale above 5-10 mbar altitude level is $\gtrsim 1000$ years and the time could be as short as 10 years below 10 mbar level, in order to fit the Cassini measurements. The derived meridional transport timescale above the 5 mbar level is a hundred times longer than that obtained from the spreading of gas-phase molecules deposited after the impact of the Shoemaker-Levy 9 comet. There is no explanation at this time for this discrepancy.

7.1 Introduction

Meridional advection and mixing processes in the atmosphere of Jupiter are poorly known. Based on the Voyager infrared spectrometer data, several efforts to derive the atmospheric circulation have been published [e.g., *Gierasch et al.*, 1986; *Conrath et al.*, 1990; *West et al.*, 1992]. The first direct and quantitative derivation of meridional transport processes is based on the introduction of aerosol debris into the atmosphere of Jupiter by comet Shoemaker-Levy 9 (SL9). *Friedson et al.* [1999] conclude that the advection by the residual circulation calculated by *West et al.* [1992] is insufficient to explain the temporal distribution of cometary debris. Meridional eddy mixing coefficients on the order of $1\text{-}10 \times 10^{10} \text{ cm}^2 \text{ s}^{-1}$ are inferred in the regions between ~ 10 and 100 mbar. Later, based on the time evolution

profiles of CO, CO₂, CS, HCN, and H₂O gas-phase molecules deposited after the SL9 impact, values of meridional eddy mixing coefficients as high as $2\text{-}5 \times 10^{11} \text{ cm}^2 \text{ s}^{-1}$ are derived for pressures between $\sim 0.1\text{-}0.5$ mbar [Lellouch *et al.*, 2002; Moreno *et al.*, 2003; Griffith *et al.*, 2004].

The Cassini measurements of stratospheric C₂H₂ and C₂H₆ [Kunde *et al.*, 2004] provide good tracers for characterizing mass transport in the upper atmosphere of Jupiter. However, the weighting function of these observations is such that they are most sensitive to the altitude level near 5 mbar. Kunde *et al.* show that at latitudes equatorward of $\sim 70^\circ$ the relative magnitude of the abundance (or emission line intensity) of C₂H₂ follows the latitudinal variation in solar insolation, while the abundance (or emission line intensity) of C₂H₆ is constant with latitude. Consequently, Kunde *et al.* conclude that the stratospheric meridional transport timescale at latitudes $< 70^\circ$ derived from these Cassini data sets falls between the lifetimes of C₂H₂ and C₂H₆. Due to the complexity in the auroral regions (contamination of line emissions from higher atmosphere due to temperature enhancement), we focus on the regions with latitude less than $\sim 70^\circ$ in this paper.

7.2 Two-Dimensional Transport Model

Because of the rapid rotation of Jupiter and its strong stratospheric zonal wind, the zonal variations in abundances should be minimized¹. Therefore, a two-dimensional (2-D) model including net meridional and vertical transport should be an adequate first-order simulation of these Cassini observations of the trace hydrocarbon species. In the 2-D mode, the

¹The rotation period and atmosphere-radiative timescale is ~ 10 hours and ~ 1000 days (at ~ 10 mbar) [Flasar, 1989], respectively.

Caltech/JPL coupled chemistry/transport code solves the mass continuity equation:

$$\frac{\partial n_i(y, z, t)}{\partial t} + \nabla \cdot \vec{\varphi}_i(y, z, t) = P_i(y, z, t) - L_i(y, z, t), \quad (7.1)$$

where n_i is the number density for the species i , φ_i the transport flux, P_i the chemical production rate, and L_i the chemical loss rate, all evaluated at time t , latitudinal distance y , and altitude z . Reported herein are results for diurnally averaged steady-state solutions, i.e., $\langle \partial n_i / \partial t \rangle \rightarrow 0$.

For one-dimensional (1-D) problems (y dependence in equation (7.1) vanishes), the Caltech/JPL code [e.g., see *Gladstone et al.*, 1996] integrates the continuity equation, including chemistry and vertical diffusion for each species using a matrix inversion method that allows large time steps. To take advantage of the computational efficiency of the 1-D solver, a “quasi 2-D” mode, which is a series of 1-D models at different latitudes coupled by meridional transport, has been developed. This quasi 2-D simulation has been tested against a case which has a known solution [*Shia et al.*, 1990]. Since the meridional transport in the stratosphere is not well understood, the quasi 2-D model uses a simple parameterization for mixing between the neighboring 1-D columns to simulate the meridional transport, i.e., $K_{yy} \partial n_i / \partial y$ is added to the results of the 1-D computations, where K_{yy} is the meridional mixing coefficient. Our work provides an order of magnitude estimate of the meridional transport in the stratosphere.

The vertical mixing coefficients (K_{zz}) and temperature profile are taken from *Gladstone et al.* [1996] and are assumed to be independent of latitude in the reference model. Sensitivities of the results due to the variations of temperature and K_{zz} profiles are also presented.

The meridional mixing K_{yy} will be determined by fitting the Cassini measurements [Kunde *et al.*, 2004]. As a first order approximation, the K_{yy} profile will be assumed also to be latitude-independent.

The model atmosphere is gridded latitudinally and vertically in 10 and 131 layers, respectively. The vertical grid size is chosen to insure that there are >3 grid points in one pressure scale height (to achieve good numerical accuracy). The latitude grid points are at 10, 30, 50, 70, and 85° in each hemisphere.

The photochemical reactions (P_i and L_i) are taken from Moses *et al.* [2000]. At all latitudes, the mixing ratio of CH₄ in the deep atmosphere is prescribed to be 2.2×10^{-3} , and the atomic hydrogen influx from the top atmosphere is fixed at $4 \times 10^9 \text{ cm}^{-2} \text{ s}^{-1}$ [e.g., see Gladstone *et al.*, 1996]. In order to prevent the solution from oscillating seasonally, the inclination angle of Jupiter is prescribed to be zero ($\sim 3^\circ$ actually).

7.3 Simulation Results

The Cassini measurements of the latitudinal distribution of C₂H₂ and C₂H₆ are reproduced in Figure 7.1; the contribution function for these is near 5 mbar [Kunde *et al.*, 2004]. Since the absolute abundances of C₂H₂ and C₂H₆ have not been determined from these measurements, the results shown are arbitrarily scaled following the approach of Kunde *et al.* Because the C₂H₂ abundances follow the latitudinal distribution of insolation (insolation is proportional to cosine of latitude), the meridional mixing timescale is expected to be longer than the C₂H₂ photochemical lifetime. On the other hand, since the C₂H₆ abundance appears to be constant with latitude, the meridional mixing timescale is expected to be shorter than the C₂H₆ photochemical lifetime.

A more quantitative estimate for K_{yy} can be derived from the 2-D model. A validation of the 2-D model is from a 1-D model for Jovian hydrocarbon chemistry [*Gladstone et al.*, 1996; *Moses et al.*, 2005], which reproduces extensive observations of hydrocarbon species as well as He 584 Å and H Lyman- α airglow emissions at low latitudes (observations are summarized in the Tables 1 and 5 of *Gladstone et al.* [1996] and Figure 14 of *Moses et al.* [2005]). The chemical loss timescales for C₂H₂ and C₂H₆ drawn from our current work are shown in Figure 7.2, along with vertical mixing timescales (also from our current work). At 5 mbar, the chemical loss timescales for C₂H₂ and C₂H₆ are about 10 and 2000 years, respectively. Therefore, to reproduce the Cassini distributions of C₂H₂ and C₂H₆, the meridional mixing time must fall within 10 and 2000 years at 5 mbar.

Many simulations were performed with the quasi-2D model to explore the sensitivities of the abundances C₂H₂ and C₂H₆ at 5 mbar to the choice of K_{yy} . The results were parameterized in terms of the ratio of the abundance at 70° latitude to the abundance at 10°. In general, the altitude variation of K_{yy} leading to a latitudinal gradient for C₂H₂ consistent with the Cassini observations also led to a sharp reduction in the C₂H₆ abundance from equator to near-pole. Alternatively, for many cases tested, if the C₂H₆ equator to near-pole variation was small, the same was true for the C₂H₂ equator to near-pole variation. Shown in Table 1 are the model results that most adequately reproduce the Cassini observations. We found that a ‘transition’ level somewhere around 5 and 10 mbar must be present, in order to match the Cassini measurements. Above the transition altitude, $K_{yy} \lesssim 10^9 \text{ cm}^2 \text{ s}^{-1}$. Below the transition altitude, $K_{yy} > 2 \times 10^{10} \text{ cm}^2 \text{ s}^{-1}$, consistent with the analysis of the temporal spreading of the SL9 debris [*Friedson et al.*, 1999]. It is interesting to note that the results of Friedson et al. predict a reversal in the direction of the meridional component of the annual-mean residual velocity across the 5 mbar level in the southern hemisphere.

This reversal represents a change with altitude in the relative contributions to the total annual-mean meridional heat flux from the component associated with the Eulerian-mean meridional velocity and the component associated with eddies. It is therefore possible that a change in the efficiency of meridional transport accompanies the reversal.

These model results can be understood in the context of the basic photochemistry controlling the production and loss of C_2H_2 and C_2H_6 as outlined in *Gladstone et al.* [1996]. In the atmosphere of Jupiter, most hydrocarbon compounds are synthesized in the regions above ~ 0.1 mbar (shown in the shaded area in Figure 7.2). Below 0.1 mbar, the production of C_2H_2 through CH_4 photolysis mediated reactions is insufficient, because the process requires UV photons with wavelengths < 130 nm, which has been self-shielded by CH_4 . In this region, the photolysis of C_2H_6 (< 160 nm), which decreases strongly toward lower regions of the atmosphere, dominates the production of C_2H_2 . The major chemical loss of C_2H_2 and C_2H_6 is through hydrogenation and photolysis, respectively. As a consequence of this chemistry, C_2H_2 is close to being in photochemical steady-state in the regions below ~ 5 mbar altitude level and its vertical gradient is large in this altitude range. Above 5 mbar level, transport is important for C_2H_2 (Figure 7.2). On the other hand, the abundance of C_2H_6 is controlled by transport and its vertical gradient is very small [e.g., see Figure 14 in *Gladstone et al.*, 1996]. Therefore, if meridional mixing is sufficiently rapid below the transition altitude to uniformly mix C_2H_6 with latitude, the tendency for uniform latitudinal mixing occurs also at 5 mbar. While above the transition altitude, uniform latitudinal mixing of C_2H_6 also results in uniform latitudinal mixing of C_2H_2 at 5 mbar.

Figure 7.3 shows the 2-D distribution of C_2H_2 and C_2H_6 calculated with the reference model, in which $K_{yy} = 2 \times 10^{10}$ below 5 mbar level and $2 \times 10^9 \text{ cm}^2 \text{ s}^{-1}$ above. Additional observations at different levels in the atmosphere can help constrain the 2-D dynamical

properties of the Jovian atmosphere.

In the above calculations whose results are summarized in Table 7.1, assumptions were made with respect to temperature and vertical eddy diffusion coefficients independent of latitudes and in the selection of chemistry reaction parameters. Several additional calculations were performed to assess the sensitivity of the derived values for K_{yy} with respect to these assumptions. In one sensitivity test, the temperature profile was progressively increased from 10° latitude so that by 85° , the temperature profile was 10% larger. Table 7.1, model G, shows that with the adjusted temperature distribution, the K_{yy} that best simulated the latitudinal variations in C_2H_2 and C_2H_6 in the Cassini observations is the same as derived above. This is consistent with the conclusions of *Moses and Greathouse* [2005], who found little sensitivity to temperature in their calculations. In a similar fashion, K_{zz} was modified linearly so that the value at 85° latitude was 10 times lower than the value at 10° latitude; enhanced K_{zz} at high latitudes cannot reproduce the measurements. The K_{yy} values that best simulated the Cassini observations (Table 7.1, model H) were again those derived earlier in this paper. Finally, the same result for K_{yy} was found when the model chemistry was updated to be consistent with the reaction coefficients in *Moses et al.* [2005] (Table 7.1, model F). Therefore, the conclusions in this paper for the magnitude of meridional mixing as a function of altitude are robust with regard to reasonable selection of atmospheric temperature, vertical mixing, and chemistry.

7.4 Conclusion

Our model simulation results have two implications. First, the meridional transport time as short as 10 years ($K_{yy} \approx 10^{11} \text{ cm}^2 \text{ s}^{-1}$) exists only in the altitude range below the 10 mbar

level. Second, above a transition level somewhere between 5 and 10 mbar, the meridional transport time is not shorter than ~ 1000 years ($K_{yy} \lesssim 10^9 \text{ cm}^2 \text{ s}^{-1}$). While these inferred K_{yy} values for the atmosphere at and below the 5-10 mbar level are consistent with the conclusions of *Friedson et al.* [1999] derived from an analysis of the SL9 debris evolution with time, the K_{yy} value above the transition level is much smaller than that ($\sim 10^{11} \text{ cm}^2 \text{ s}^{-1}$) derived from analyses of the time evolution of the distributions of gas-phase trace species deposited after the SL9 impact [*Lellouch et al.*, 2002; *Moreno et al.*, 2003; *Griffith et al.*, 2004]. There is no explanation at this time for this discrepancy.

It has been shown that CH_4 and C_2H_6 contribute to the heating and cooling of the stratosphere of Jupiter, respectively [*Yelle et al.*, 2001]. To a first order approximation, the cooling at/below 5 mbar level would be constant with latitude, being determined by two factors: the temperature and the abundance of C_2H_6 . These two are nearly constant between the equator and mid-latitudes [*Flasar et al.*, 2004; *Kunde et al.*, 2004; also Figure 7.3]. The heating function, however, is sensitive to the magnitude of the solar insolation and, consequently, it is a good approximation to assume that this function has the same latitude dependence as the solar insolation. Therefore, the global circulation could be driven by the differential heating between latitudes. This circulation driven by heating through absorption of radiation by gas-phase molecules will provide a first order estimate of the importance of aerosol heating in the stratosphere.

Bibliography

- Conrath, B. J., P. J. Gierasch, and S. S. Leroy, Temperature and Circulation in the Stratosphere of the Outer Planets, *Icarus*, 83, 255-281, 1990.
- Flasar, F. M., Temporal Behavior of Jupiter's Meteorology, in Time-Variable Phenomena in the Jovian System, M. J. S. Belton, R. A. West, and J. Rahe, eds., pp. 324-343, NASA SP-494, 1989.
- Flasar, F. M., and colleagues, An Intense Stratospheric Jet on Jupiter, *Nature*, 427, 132-135, 2004.
- Friedson, A. J., R. A. West, A. K. Hronek, N. A. Larsen, and N. Dalal, Transport and Mixing in Jupiter's Stratosphere Inferred from Comet S-L9 Dust Migration, *Icarus*, 138, 141-156, 1999.
- Gierasch, P. J., B. J. Conrath, and J. A. Magalhaes, Zonal Mean Properties of Jupiter's Upper Troposphere from Voyager Infrared Observations, *Icarus*, 67, 456-483, 1986.
- Gladstone, G. R., M. Allen, and Y. L. Yung, Hydrocarbon Photochemistry in the Upper Atmosphere of Jupiter, *Icarus*, 119, 1-52, 1996.
- Griffith, C. A., B. Bevard, T. Greathouse, E. Lellouch, J. Lacy, D. Kelly, and M. J. Richter, Meridional transport of HCN from SL9 impacts on Jupiter, *Icarus*, 170, 58-69, 2004.

- Kunde, V. G., and colleagues, Jupiter's Atmospheric Composition from the Cassini Thermal Infrared Spectroscopy Experiment, *Science*, *305*, 1582-1586, 2004.
- Lellouch, E., B. Bevard, J. I. Moses, G. R. Davis, P. Drossart, H. Feuchtgruber, E. A. Bergin, R. Moreno, and T. Encrenaz, The Origin of Water Vapor and Carbon Dioxide in Jupiter's Stratosphere, *Icarus*, *159*, 112-131, 2002.
- Moreno, R., A. Marten, H. E. Matthews, and Y. Biraud, Long-term Evolution of CO, CS and HCN in Jupiter after the Impacts of Comet Shoemaker-Levy 9, *Planetary and Space Science*, *51*, 591-611, 2003.
- Moses, J. I., B. Bevard, E. Lellouch, G. R. Gladstone, H. Feuchtgruber, and M. Allen, Photochemistry of Saturn's Atmosphere. I. Hydrocarbon Chemistry and Comparisons with ISO Observations, *Icarus*, *143*, 244-298, 2000.
- Moses, J. I., T. Fouchet, B. Bevard, G. R. Gladstone, E. Lellouch, and H. Feuchtgruber, Photochemistry and Diffusion in Jupiter's Stratosphere: Constraints from ISO Observations and Comparisons with Other Giant Planets, *J. Geophys. Res.*, *110*, E08001, doi:10.1029/2005JE002411, 2005.
- Moses, J. I., and T. K. Greathouse, Latitudinal and seasonal models of stratospheric photochemistry on Saturn: Comparison with infrared data from IRTF/TEXES, *Journal of Geophysics Research*, *110*, E09007, doi:10.1029/2005JE002450, 2005.
- Shia, R. L., Y. L. Ha, J. S. Wen, and Y. L. Yung, Two-dimensional Atmospheric Transport and Chemistry Model - Numerical Experiments with a New Advection Algorithm, *Journal of Geophysics Research*, *95*, 7467-7483, 1990.

West, R. A., A. J. Friedson, and J. F. Appleby, Jovian Large-scale Stratospheric Circulation, *Icarus*, 100, 245-259, 1992.

Yelle, R. V., C. A. Griffith, and L. A. Young, Structure of the Jovian Stratosphere at the Galileo Probe Entry Site, *Icarus*, 152, 331-346, 2001.

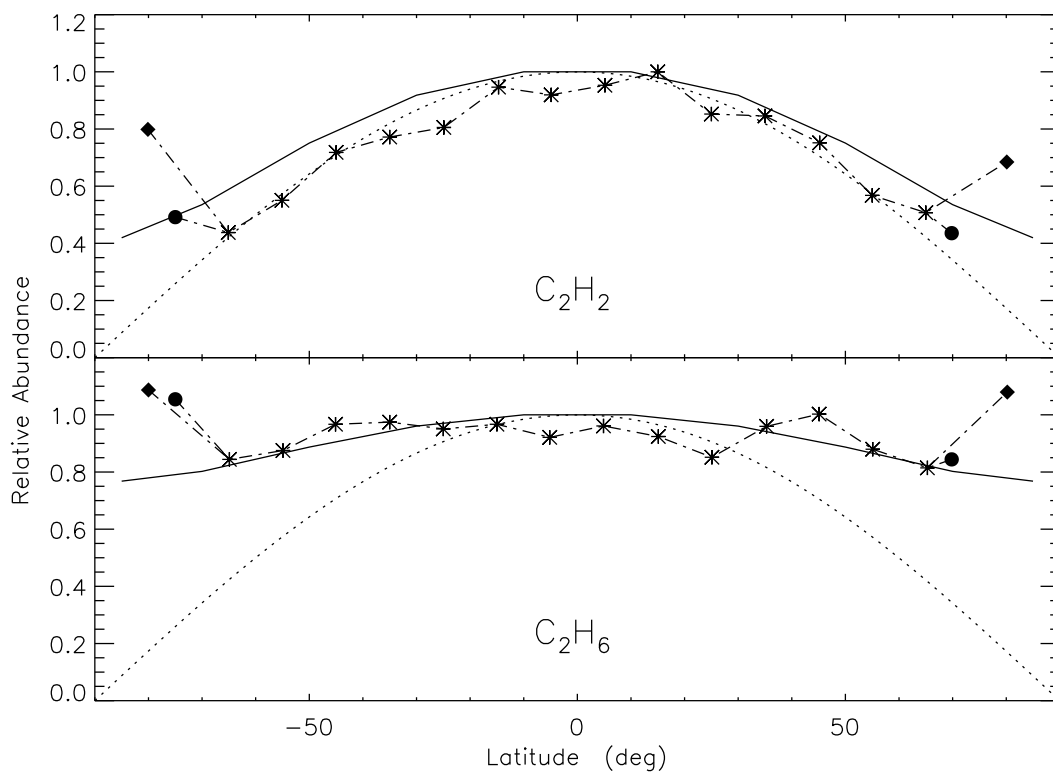


Figure 7.1 Jupiter—Relative abundances of C_2H_2 (upper) and C_2H_6 (lower) at 5 mbar as a function of latitude. Asterisks are the Cassini measurements [Kunde *et al.*, 2004]. Diamonds and circles are, respectively, high-latitude Cassini measurements that do include (diamonds) and do not include (circles) auroral longitudes. The calculated abundances of C_2H_2 and C_2H_6 are normalized to those at the equator. Solid line represents model results with the reference K_{yy} : constant $2 \times 10^{10} \text{ cm}^2 \text{ s}^{-1}$ below the 5 mbar altitude level and $2 \times 10^9 \text{ cm}^2 \text{ s}^{-1}$ above (model B). Dotted line represents the cosine function of latitude.

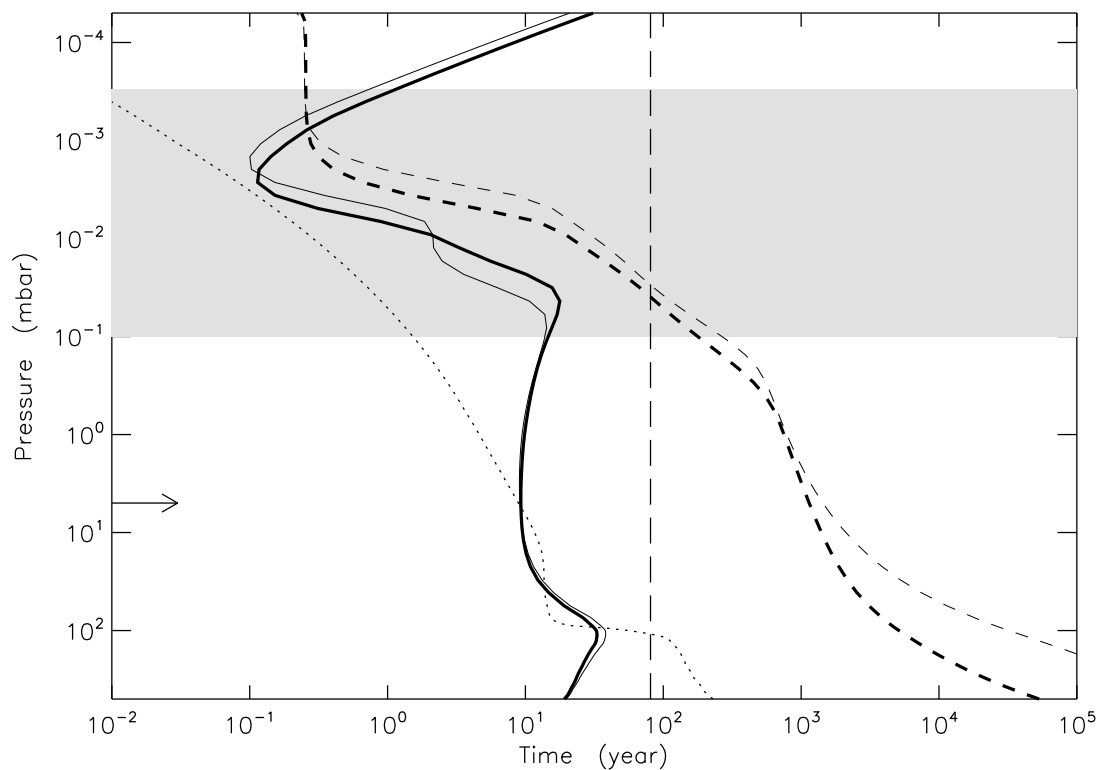


Figure 7.2 Jupiter—Timescales for the chemical loss of C_2H_2 (solid lines) and C_2H_6 (dashed lines) and for vertical transport (dotted line). The vertical transport timescale is defined by H^2/K_{zz} , where K_{zz} and H are the vertical diffusion coefficients of CH_4 and atmospheric scale height, respectively; values of time constants are derived from our reference model. Thick and thin lines represent values at latitudes 10° and 70° , respectively. The horizontal arrow indicates the 5 mbar level where the peak in the contribution function for the Cassini measurements of C_2H_2 and C_2H_6 lies. The vertical long-dashed line is a meridional mixing time equal to R_J^2/K_{yy} , where R_J is the radius of Jupiter and $K_{yy} = 2 \times 10^{10} \text{ cm}^2 \text{ s}^{-1}$. The shaded area shows the photochemical production region for the hydrocarbons.

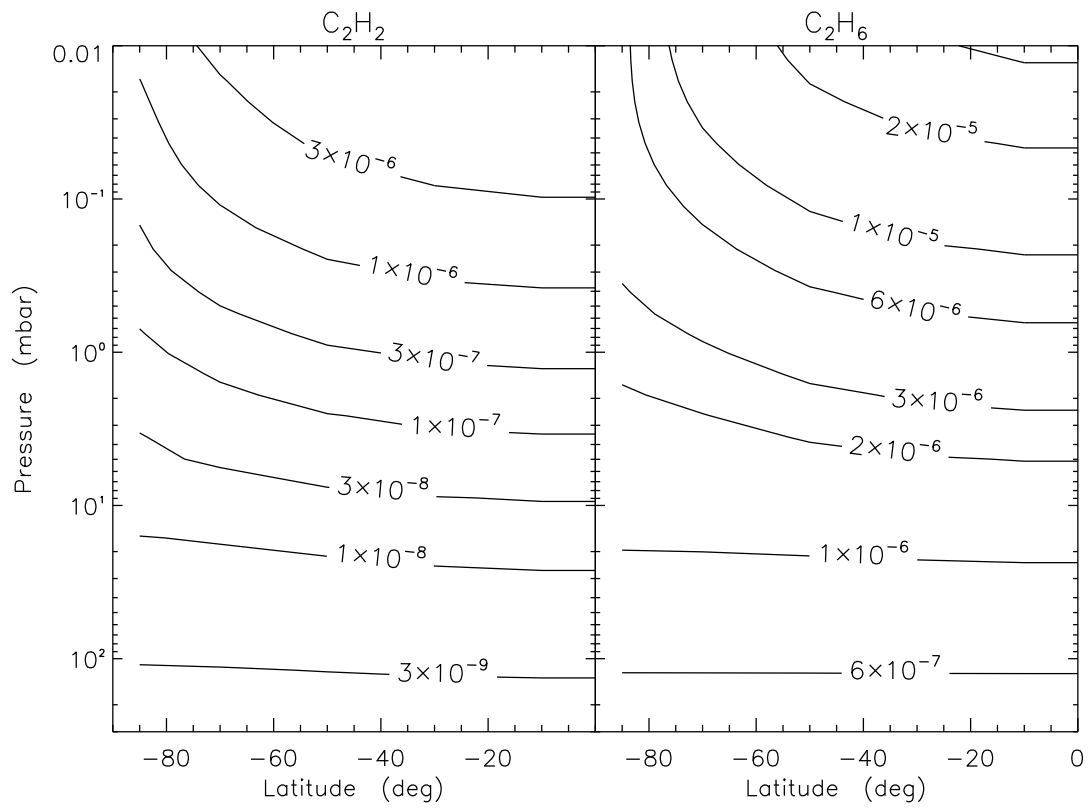


Figure 7.3 Jupiter—2-D volume mixing ratio profiles of C_2H_2 (left) and C_2H_6 (right) calculated with the reference K_{yy} (model B).

Table 7.1. Summary of Model Results

	Chemistry ^a	Temperature ^a	K_{zz} ^a	Transition ^b	K_{yy} below ^c	K_{yy} above ^c	C_2H_2 ^d	C_2H_6 ^d
Solar flux				0.34	0.34
Cassini				0.50	0.87
Model A	Standard	Standard	Standard	5	2×10^{10}	0	0.49	0.77
Model B	Standard	Standard	Standard	5	2×10^{10}	2×10^9	0.54	0.80
Model C	Standard	Standard	Standard	10	2×10^{10}	2×10^9	0.46	0.73
Model D	Standard	Standard	Standard	10	2×10^{11}	0	0.46	0.75
Model E	Standard	Standard	Standard	10	2×10^{11}	2×10^9	0.51	0.79
Model F	<i>Moses et al.</i> [2005]	Standard	Standard	5	2×10^{10}	2×10^9	0.59	0.84
Model G	Standard	$\times 1.1$	Standard	5	2×10^{10}	2×10^9	0.49	0.76
Model H	Standard	Standard	$\times 0.1$	10	2×10^{11}	2×10^9	0.48	0.91

^a Standard chemistry is taken from *Moses et al.* [2000]. Standard temperature and K_{zz} profiles are from *Gladstone et al.* [1996]. Modified chemistry is from *Moses et al.* [2005]. Reference temperature and K_{zz} profiles are set at equator (10°). The maximum changes in temperature (increase by 10%) and K_{zz} (reduced by a factor of 10) profiles are at 85° , with the change assumed to be linearly proportional to the angle of latitudes.

^b Transition level of K_{yy} profile. The level is given in units of mbar.

^c Values of K_{yy} below and above the transition level. K_{yy} is in units of $\text{cm}^2 \text{s}^{-1}$.

^d Ratio of abundance at $\pm 70^\circ$ latitude to abundance at the equator. Values for Cassini measurements are averaged at $\pm 70^\circ$.

Chapter 8

Atmosphere of Callisto

Mao-Chang Liang, Benjamin F. Lane, Robert T. Pappalardo, Mark Allen, and Yuk L. Yung

Journal of Geophysical Research-Planets, 110(E2) E02003, 2005.

Abstract

During the Galileo flybys of Callisto in 1999, a CO₂ atmosphere and an ionosphere were detected. Using the Caltech/Jet Propulsion Laboratory one-dimensional KINETICS model, we have successfully simulated the observed electron density within a factor of 2, while satisfying the observational constraints on carbon and oxygen atoms. We conclude that photoionization of CO₂ alone is insufficient to produce the observed electron density. An atmosphere 20-100 times denser than the CO₂ atmosphere must be introduced, as suggested by *Kliore et al.* [2002]. We show that an O₂-rich atmosphere is highly probable. However, the atomic oxygen produced from O₂ photodissociation is 2 orders of magnitude greater than the upper limit given by *Strobel et al.* [2002]. The introduction of reactive hydrogen chemistry assuming a surface abundance of H₂O of $\sim 2 \times 10^9 \text{ cm}^{-3}$ (4×10^{-8} mbar) is required to reduce the excess atomic O abundance. The calculated atomic O column density is $> 5 \times 10^{12} \text{ cm}^{-2}$, which is about the observed upper limit, suggesting we should be able to detect O in the atmosphere of Callisto.

8.1 Introduction

It is now known that all four Galilean satellites have tenuous atmospheres. On Io, SO₂ is derived from volcanic emission [*Pearl et al.*, 1979; *Lellouch*, 1996], while O₂ on Europa [*Hall et al.*, 1995] and atomic oxygen and hydrogen on Ganymede [*Barth et al.*, 1997] are most likely the result of radiolysis of surface ice [*Johnson*, 1998]. Recently, a thin CO₂ atmosphere was discovered on Callisto [*Carlson*, 1999] using Near-Infrared Mapping Spectrometer (NIMS) data from the Galileo spacecraft. Specifically, CO₂ airglow in the ν_3 band (4.3 μm) was seen in limb-scanning observations. The measured emission was

modeled as an isothermal layer at a temperature of 150 ± 50 K, and a surface pressure of 7.5×10^{-9} mbar. The inferred scale height of the atmospheric CO_2 is 23 km and the surface number density is $4 \times 10^8 \text{ cm}^{-3}$. The total column density of CO_2 is approximately $9.2 \times 10^{14} \text{ cm}^{-2}$. The stated uncertainties are 60% [Carlson, 1999].

During flybys of the Galileo spacecraft in 1999, an ionosphere on Callisto was detected only at the location where the trailing hemisphere was illuminated by the Sun [Gurnett *et al.*, 2000; Kliore *et al.*, 2002]. The electron density is determined by measuring the delay of radio signal between the Earth and the spacecraft, the technique of radio occultation. The inferred electron densities at 27.2 and 47.6 km are 15300 and 17400 cm^{-3} , respectively. The photoionization of CO_2 alone is insufficient to produce the observed electron density. By analogy with Europa, Kliore *et al.* [2002] proposed a primarily O_2 atmosphere, formed from the dissociation of H_2O sputtered from the surface [Hall *et al.*, 1995; Johnson *et al.*, 1998]. The estimated surface neutral density is on the order of 10^{10} cm^{-3} . However, species other than CO_2 have not been observed in the atmosphere; Strobel *et al.* [2002] reported upper limits of the abundances of O_2 and CO to be 10^{17} cm^{-2} and atomic carbon and atomic oxygen to be 10^{13} and $2.5 \times 10^{13} \text{ cm}^{-2}$, respectively. The latter two upper limits set strict constraints for the modeling work in this chapter.

Here, we examine a range of models for the atmosphere of Callisto that can reproduce the electron densities and satisfy the upper limits of the observations of O_2 , CO, O and C. The implications of the models are discussed.

8.2 Model Description

The one-dimensional Caltech/Jet Propulsion Laboratory KINETICS model is applied to the atmosphere of Callisto [e.g., see *Gladstone et al.*, 1996 for details of the model], and consists of 43 spherical layers along the radial direction from the surface to an altitude of 350 km. The bottom 5 layers are used to simulate enhanced chemistry for three-body reactions on the surface. The temperature profile is assumed to be isothermal at 150 K, and the surface pressure of CO₂ is fixed at 7.5×10^{-9} mbar [*Carlson*, 1999]. For this tenuous CO₂ atmosphere, the calculated electron density from CO₂ photoionization is an order of magnitude less than the measured density and peaks on the surface. Therefore, a neutral atmosphere denser than CO₂ must be introduced. We believe that an O₂ atmosphere is the most probable, and will examine this assumption in later sections. Such an atmosphere has been proposed by *Kliore et al.* [2002].

In order to match the observed electron density, the inferred surface density of O₂ is on the order of 10^{10} cm⁻³, which is ~ 20 times denser than that of CO₂. We therefore adopt surface densities of $\sim 7 \times 10^9$ and 4×10^8 cm⁻³ for O₂ and CO₂, respectively. The surface H₂O vapor pressure is taken to be $\sim 4 \times 10^{-8}$ mbar (2×10^9 cm⁻³). For the other lower boundary conditions, we set the transport flux to be zero and let the three-body reactions be more efficient on the surface. We adopt a rate coefficient of 10^{-20} cm⁶ s⁻¹ for three-body reactions on the surface (or an effective two-body rate coefficient of 10^{-10} cm³ s⁻¹), the number chosen to reach the kinetic limit of chemical reactions. This assumption of enhanced reactions on the surface may be reasonable if the surface/regolith is porous and can adsorb particles. Actually, $\text{H} + \text{O}_2 + \text{M} \rightarrow \text{HO}_2 + \text{M}$ is the most critical reaction affecting the model results. We take this as our reference model, which fulfills the observational constraints to a fair

degree. The results of relaxing the surface effect will be presented in later sections. For the upper boundary conditions, we assume the boundary is not permeable for species other than H, H₂, and O. The H and H₂, the two lightest neutral species, are allowed to escape with Jeans escape velocities: at 150 K they are $\sim 10^4$ and $\sim 10^3$ cm s⁻¹, respectively. The escape of O atoms occurs mainly by sputtering of energetic ions in the Jovian magnetosphere. The H escape is thus limited by the escape of atomic O. Since the atmosphere is tenuous, we believe that transport is dominated by molecular diffusion. Near the surface, the molecular diffusion coefficient for H is $\sim 10^9$ cm² s⁻¹. Hence, we omit eddy diffusion.

Table 8.1 lists the major chemical reactions in the model (minor reactions are not shown in the table). Because of a high electron density, the lifetimes of ions are ~ 400 s. The ions will quickly react with electrons before they diffuse away. We therefore assume a quasi-neutral atmosphere in our model, i.e., in each layer the electron density equals the cation density. The electrodynamic interaction between Callisto's ionosphere and the Jovian plasma is suggested to be minor [see *Strobel et al.*, 2002 for a detailed discussion]. This is also consistent with the results that there is no excess of electron density in the downstream as compared to the upstream of the plasma around Callisto [*Gurnett et al.*, 2000].

The solar flux values are taken from *Mount et al.* [1983], *Torr et al.* [1985], and the *WMO* [1985], and then scaled appropriately for the mean distance between the Sun and Callisto (5.2 AU). Callisto's ionosphere was detected in 1999, when the solar cycle was close to the solar maximum (the solar cycle reached its maximum in 2000). So the solar maximum flux is adopted to be our reference solar flux. The solar zenith angle is fixed at 80°, which is the mean angle of the observation of the ionosphere. The model results with solar mean and minimum fluxes are also shown.

8.3 General Results

8.3.1 Electron Density and Hydrogen Abundance

Profiles of the major constituents in our calculation are plotted in Figures 8.1 and 8.2. Figure 8.3 shows the total photoabsorption rates for O_2 , H_2O , CO_2 , and CO . The branching ratios of photoionization are about $\sim 10\%$ that of the total photoabsorption rates (e.g., see Table 8.1). Since we have assumed a quasi-neutral atmosphere, the major ion is O_2^+ (Figure 8.4). There are two sources of O_2^+ : the photoionization product of the most abundant molecule, O_2 , in the model and the charge exchange between H_2O^+ and O_2 . In order to better match the observed electron density profile, the required O_2 density is on the order of 10^9 cm^{-3} at 50 km above the surface. This corresponds to an O_2 column density of $2 \times 10^{16} \text{ cm}^{-2}$. Figure 8.4 shows the profiles of total electron density (dark solid line), O_2^+ (dashed line), H_2O^+ (dotted line), CO_2^+ (dash-dotted line), and O^+ (long-dashed line) during the solar flux maximum. We see that the modeled electron density agrees with the observation to within a factor of 2. Our model results support the assumption of an O_2 atmosphere on Callisto [*Kliore et al.*, 2002].

The O_2^+ is lost locally by recombination with electrons, the lifetime being ~ 400 s, while its parent molecule O_2 has a timescale of $\sim 10^7$ s against photoionization. As a result, the ions are $\sim 10^{-4}$ as abundant as their parents. Since the UV flux is limited and the atmosphere is optically thick at UV wavelengths, the observed electron density profile gives a strong constraint on the composition of the atmosphere on Callisto. As proposed by *Kliore et al.* [2002], H_2O , O , H_2 , OH , and H all have ionization cross sections similar to O_2 , and hence they are other possibilities for atmospheric constituents. Because of the low gravity (H and H_2 can escape readily), low temperature (H_2O vapor abundance is very sensitive

to temperature), and observationally constrained low O abundance [*Strobel et al.*, 2002], the assumption of an O₂ atmosphere on Callisto is the most plausible, which was also the proposed solution for the atmospheres of Ganymede and Europa [e.g., see *Hall et al.*, 1998 and references therein].

If the surface is not porous and cannot adsorb particles, the chemical reactions will not be enhanced. In this case, the electron profile is in better agreement with the measurements (see light solid line in Figure 8.4). The peak electron density is sensitive to solar zenith angle. Increasing the angle from 79 to 82° will move the peak upward by ~20 km; this brings the model into better agreement with the measurements [*Kliore et al.*, 2002]. The required surface densities of O₂ and H₂O are $3.2 \times 10^{10} \text{ cm}^{-3}$ and $4.8 \times 10^9 \text{ cm}^{-3}$, respectively. The values are 4 times greater than those of the reference model. The reason for this is that HO₂ is now formed inefficiently on the surface and subsequent chemistry resulting in the recycling of O₂ and H₂O is negligible (the last 3 reactions in Table 8.1). Consequently, O₂ and H₂O will be present in lower abundances in the upper atmosphere.

Though the model without enhanced surface reactions can better match the electron profiles, it is unlikely, as we will discuss later. In the upper atmosphere, the ultimate source of electrons (or ions) is photoionization of H and H₂. The electron density is determined by the reactions between H and H₂ photoionizations and the recombination of H₂⁺ plus e⁻, and it is estimated to be ~150 cm⁻³ at ~400 km above the surface, which is a factor of ~4 less than the observed value of ~400 cm⁻³ at an altitude of 535 km [*Gurnett et al.*, 2000]. The value is calculated by assuming a photoionization coefficient of $5 \times 10^{-9} \text{ s}^{-1}$, a density of 10^5 cm^{-3} , and a recombination rate coefficient of $2 \times 10^{-8} \text{ cm}^3 \text{ s}^{-1}$ [*Le Teuff et al.*, 2000]. The discrepancy can be explained by the fact that the density scale height in the upper atmosphere is significantly greater than that in the lower atmosphere, because H

and H_2 are the major species in the upper atmosphere. In our present model, we assume the density scale height is constant at ~ 30 km throughout the whole atmosphere.

The H atoms can be lost only by the enhanced three-body reactions on the surface and by Jeans escape, because H is unreactive in the atmosphere. Therefore, the H (and H_2) abundance will be high (see Table 8.2 and Figure 8.2). The abundances of H and H_2 should be extremely sensitive to the properties of the surface of Callisto. By observing the H profile, we can therefore quantify the communication processes between the surface and the atmosphere. The existence of enhanced surface reactions can also be tested by observing the abundance of O_3 . In the reference model, the abundance of O_3 is $\sim 5 \times 10^{12} \text{ cm}^{-2}$, while it is negligible without the enhanced surface reactions.

8.3.2 Carbon Dioxide and Carbon Monoxide

The profiles of density and photoabsorption rates of CO_2 and CO are shown in Figures 8.1 and 8.3, respectively. CO_2 is destroyed mainly by photodissociation, and can be recycled either by the reaction of CO with OH or by the three-body reaction of O and CO under the assumption of enhanced chemical reaction rates on the surface. CO is primarily formed by the CO_2 photodissociation. In vacuum, it is shown in Table 8.2 that CO has a lifetime against UV of a factor of 3 longer than that of CO_2 . This gives an upper limit for the CO abundance, under the conditions that enhanced chemical reaction rates on the surface and OH radicals or H_2O vapors are absent. The photoionization products of CO_2 and CO, CO_2^+ and CO^+ , are lost mostly by electron recombination and by charge exchange with O_2 , respectively. As a result, the CO_2 , CO, CO_2^+ , and CO^+ have lifetimes of $\sim 10^7$, 10^6 , 300, and 20 s. The calculated abundance of CO is shown in Table 8.2.

8.3.3 Atomic Carbon and Atomic Oxygen

The reported upper limits of the abundances of C and O strongly constrain the composition in the atmosphere of Callisto. Because of the high O₂ concentration, the C atoms have a lifetime of only ~ 100 s. The calculated C atom column density is about 10^8 cm⁻² (see Table 8.2). The abundance of O atoms depends on the H₂O vapor pressure in the atmosphere. The calculated profile of O using the reference model is shown in Figure 8.1. In the absence of H₂O in the atmosphere, the calculated O column density is about 10^{15} cm⁻², which is 2 orders of magnitude higher than the observed upper limit. By introducing an eddy diffusion of 10^{10} cm² s⁻¹, the calculated O column density is reduced to $\sim 3 \times 10^{13}$ cm⁻². This high eddy diffusion coefficient will transport the atomic O downward, and by the enhanced chemical processes on the surface O₂ can be recycled, but the abundance is still higher than the observed upper limit. Though eddy diffusion can reduce the O abundance through surface-mediated recombination, we argue that this assumption is not appropriate for two reasons. First, the electron density would be nearly constant below 100 km, while *Kliore et al.* [2002] observed an electron profile that increases sharply from the surface to 20-50 km. Second, the eddy velocity required is about 10% of the speed of the sound, a value that is unrealistic near the surface.

By the analogy with the atmospheres of Mars and Ganymede, we introduce HO_x chemistry for removing O [*McElroy and Donahue*, 1972; *Yung and McElroy*, 1977]. With the assumption of H₂O surface abundance equal to 4×10^{-8} mbar, the modeled O abundance drops by 2 orders of magnitude to nearly the observed upper limit. This value of H₂O is close to the saturation vapor pressure at 150 K [*Yung and McElroy*, 1977]. When we increase the abundance of H₂O, the O abundance is not seriously affected. The reason is that H₂O becomes the major UV absorber. The results shown in Table 8.2 reflect this

dependence. When the H₂O to O₂ abundance is ≤ 0.5 , a factor of 2 decrease in H₂O will result in an order of magnitude increase in the O abundance. This relation saturates for an H₂O to O₂ ratio > 0.5 . We list the model C and O column densities as well as the observed upper limits in Table 8.2. It is shown that in all cases the calculated O abundance is not far from the observed upper limit.

8.4 Discussion

For the tenuous atmosphere of Callisto, the heat conduction time is about 100 s, which is significantly less than the 17-day rotational period of Callisto. Along with a low visual albedo of 0.2 on Callisto, the surface and the atmosphere near the surface at the day side would be, on average, about 150 K, consistent with an insignificance of condensed O₂ on the surface of Callisto [Spencer and Calvin, 2002]. This confirms that the H₂O vapor pressure of 4×10^{-8} mbar adopted by the model is reasonable.

Galileo high-resolution imaging of Callisto [Moore *et al.*, 1999] reveals that the satellite's cratered surface is dominated by smooth, dark material which appears to mantle and subdue the satellite's topography (see Figure 8.5). Landslide deposits within some craters attest to the mobility of the dark material and its tendency to slough downhill off of topographic highs. High-standing crater rims, central peaks, and relatively steep interior crater walls are relatively bright. These bright areas are probably where water-ice is cold trapped, as seen by Spencer and Calvin [2002]. Callisto's craters commonly show gullied, crenulate walls and rims which are knobby and discontinuous. Irregularly shaped pits ~ 1 km in size are observed in some regions (Figure 8.5), and these suggest undermining and collapse of near-surface material, as through loss of a volatile substrate.

Therefore, the dark areas are the likely regions that provide the required H₂O vapor pressure, and the bright regions are a probable H₂O source. Diffusion from cold to warm regions can deliver the required H₂O. In order to study the process quantitatively, we follow the approach of *Moore et al.* [1996] and apply Fick's law to model the water diffusive flux F :

$$F = D \frac{\epsilon}{\tau} \frac{\partial n(T)}{\partial x}. \quad (8.1)$$

Here x is the distance from the source, $n(T)$ the number density of H₂O vapor at temperature T , ϵ the porosity, and τ the tortuosity. The diffusion coefficient D is (Knudsen diffusion, i.e. dominated by gas-pore wall collisions)

$$D \approx 2\epsilon r_0 / 3\tau \sqrt{2kT/\pi m}, \quad (8.2)$$

where r_0 is the pore size, m the molecular mass of the diffusion component, and k the Boltzmann constant. Typically $r_0 \approx 6 \times 10^{-4}$ cm, $\epsilon \approx 0.5$, and $\tau \approx 5$ [see, e.g., *Weiss et al.*, 2000]. If we can assume a constant temperature gradient ($\partial T/\partial x$), Equation 8.1 can be rewritten:

$$F = D \frac{\epsilon}{\tau} \frac{\partial T}{\partial x} \frac{\partial n(T)}{\partial T}.$$

The saturation vapor density is given by $n(T) = (kT)^{-1} \exp[-5631.120592/T + 8.231199999 \ln(T) - 0.03861573356 T + 0.00002774937399 T^2 - 15.55895661] \text{ cm}^{-3}$, where T is in the unit of K [*Lebofsky*, 1975]. Figure 8.6 shows the calculated profiles of H₂O diffusive flux as a function of temperature for a temperature gradient of 200 K cm⁻¹. Two dotted lines represents an

H₂O dissociation rate of $5 \times 10^9 \text{ cm}^{-2} \text{ s}^{-1}$ and a temperature of 150 K in our reference model. Since most H₂O molecules are recycled by the enhanced chemical reactions on the surface, a diffusive flux of H₂O below $5 \times 10^9 \text{ cm}^{-2} \text{ s}^{-1}$ is the most likely. The actual value is determined by the loss rate of H₂O.

The loss of H₂O depends on the escape of O and H atoms. H atoms can be lost easily by Jeans escape, while O atoms can be removed only by ion recombination (e.g., O₂⁺ plus e⁻) and by the sputtering of energetic ions in the Jovian magnetosphere. In the model, about 10% of the O atoms in the upper atmosphere are produced by the dissociative recombination of O₂⁺ plus electron. Though they may have kinetics energy as large as 2.5 eV per atom or 7 km s^{-1} (higher than the escape velocity of 2.5 km s^{-1}), they cannot escape: the exobase in the model is at about 200 km above the surface, while the energetic O atoms are generated primarily at $\sim 50 \text{ km}$, where the electron density peaks. Thus, the only loss process for O atoms occurs by sputtering by energetic particles. The incident ion flux at Callisto's orbit is $2 \times 10^7 \text{ cm}^{-2} \text{ s}^{-1}$ [e.g., *Neubauer*, 1998], and the maximum sputtering flux under these conditions is calculated to be $6 \times 10^8 \text{ cm}^{-2} \text{ s}^{-1}$ for a sputtering yield of 30 [*Johnson and Leblanc*, 2001]. Over geological time, $\sim 20 \text{ m}$ of ice may be lost. This is an upper limit; *Strobel et al.* [2002] have argued that the interaction between the ionosphere of Callisto and the Jovian plasma is limited.

For the maximum sputtering flux, the H escape flux cannot be more than $10^9 \text{ cm}^{-2} \text{ s}^{-1}$. This implies that the temperature at the top of the atmosphere is $< 100 \text{ K}$. At Callisto, the maximum H₂O photolysis rate is $10^{10} \text{ cm}^{-2} \text{ s}^{-1}$. In our reference model, a significant amount of H₂O can be recycled because of enhanced recombination rates on the surface. If the surface is not porous and cannot efficiently adsorb particles, the O and H produced by H₂O photolysis must be removed from the atmosphere. Otherwise, the accumulation

rate of O_2 will be large. This corresponds to an escape flux of atoms about $10^{10} \text{ cm}^{-2} \text{ s}^{-1}$, which is at least 2 orders of magnitude greater than that by sputtering. We propose that this hypothesis can be tested by detecting the escape flux of O atoms and by observing the H (or H_2) abundance in the atmosphere of Callisto.

8.5 Summary

We have modeled the photochemistry of a hypothesized O_2 -rich atmosphere of Callisto and have successfully reproduced the observed electron profile [*Kliore et al.*, 2002]. Because of the observational constraint on the O atom abundance [*Strobel et al.*, 2002], we propose that H_2O vapor needs to be present in the atmosphere. The OH radicals from H_2O photolysis will remove the O atoms produced by O_2 photolysis. The inferred H_2O surface density is $\sim 2 \times 10^9 \text{ cm}^{-3}$ (4×10^{-8} mbar), while the calculated O column density is $\sim 10^{13} \text{ cm}^{-2}$. The latter should be detectable with the current instrumentation.

Bibliography

- Barth, C. A., C. W. Hord, A. I. F. Stewart, W. R. Pryor, K. E. Simmons, W. E. McClintock, J. M. Aiello, K. L. Naviaux, and J. J. Aiello, Galileo Ultraviolet Spectrometer Observations of Atomic Hydrogen in the Atmosphere of Ganymede, *Geophysics Research Letters*, *24*, 2147-2150, 1997.
- Brion, C. E., and F. Carnovale, The Absolute Partial Photoionization Cross-Section for the Production of the X2b1 State of H_2O^+ , *Chemical Physics*, *100*, 291-296, 1985.
- Carlson, R. W. A Tenuous Carbon Dioxide Atmosphere on Jupiter's Moon Callisto, *Science*, *283*, 820-821, 1999.
- Chan, W. F., G. Cooper, and C. E. Brion, The Electronic-Spectrum of Carbon-Dioxide - Discrete and Continuum Photoabsorption Oscillator-Strengths (6-203 eV), *Chemical Physics*, *178*, 401-413, 1993.
- Datz, S., R. Thomas, S. Rosen, M. Larsson, A. M. Derkatch, F. Hellberg, and W. van der Zande, Dynamics of Three-Body Breakup in Dissociative Recombination: H_2O^+ , *Physical Review Letters*, *85*, 5555-5558, 2000.
- DeMore, W. B., S. P. Sander, D. M. Golden, R. F. Hampson, M. J. Kurylo, C. J. Howard, A. R. Ravishankara, C. E. Kolb, and M. J. Molina, Chemical Kinetics and Photochemical

- Data for Use in Stratospheric Modeling. Evaluation number 12, *JPL Publication, 97-4*, Jet Propulsion Laboratory, Pasadena, CA., 1997.
- Dutuit, O., A. Tabchefouhaile, I. Nenner, H. Frohlich, and P. M. Guyon, Photodissociation Processes of Water-Vapor Below and Above the Ionization-Potential, *Journal of Chemical Physics, 83*, 584-596, 1985.
- Gladstone, G. R., M. Allen, and Y. L. Yung, Hydrocarbon Photochemistry in the Upper Atmosphere of Jupiter, *Icarus, 119*, 1-52, 1996.
- Gougousi, T., M. F. Golde, and R. Johnsen, Electron-Ion Recombination Rate Coefficient Measurements in a Flowing Afterglow Plasma, *Chemical Physics Letters, 265*, 399-403, 1997.
- Gurnett, D. A., A. M. Persoon, W. S. Kurth, A. Roux, and S. J. Bolton, Plasma Densities in the Vicinity of Callisto from Galileo Plasma Wave Observations, *Geophysics Research Letters, 27*, 1867-1870, 2000.
- Gutcheck, R. A., and E. C. Zipf, Excitation of CO Fourth Positive System by Dissociative Recombination of CO_2^+ Ions, *Journal of Geophysical Research, 78*, 5429-5436, 1973.
- Haddad, G. N., and J. A. R. Samson, Total Absorption and Photoionization Cross-Sections of Water-Vapor between 100-Å and 1000-Å, *Journal of Chemical Physics, 84*, 6623-6626, 1986.
- Hall, D. T., P. D. Feldman, M. A. McGrath, and D. F. Strobel, The Far-Ultraviolet Oxygen Airglow of Europa and Ganymede, *Astrophysical Journal, 499*, 475-481, 1998.

- Hall, D. T., D. F. Strobel, P. D. Feldman, M. A. McGrath, and H. A. Weaver, Detection of an Oxygen Atmosphere on Jupiter Moon Europa, *Nature*, *373*, 677-679, 1995.
- Hippler, H., R. Rahn, and J. Troe, Temperature and Pressure-Dependence of Ozone Formation Rates in the Range 1-1000-Bar and 90-370-K, *Journal of Chemical Physics*, *93*, 6560-6569, 1990.
- Huber, and Herzberg, *Constants of Diatomic Molecules*, Van Nostrand Reinhold Company, p. 158, 1979.
- Johnson, R.E., Sputtering and Desorption from Icy Surfaces, in *Solar System Ices*, edited by B. Schmitt, pp. 303-334, Kluwer Academic Publishers, Netherlands, 1998.
- Johnson, R. E., and F. Leblanc, The Physics and Chemistry of Sputtering by Energetic Plasma Ions, *Astrophysics and Space Science*, *277*, 259-269, 2001.
- Johnson, R. E., R. M. Killen, J. H. Waite, and W. S. Lewis, Europa's Surface Composition and Sputter-Produced Ionosphere, *Geophysics Research Letters*, *25*, 3257-3260, 1998.
- Katayama, D. H., R. E. Huffman, and C. L. Obryan, Absorption and Photoionization Cross-Sections for H₂O and D₂O in Vacuum Ultraviolet, *Journal of Chemical Physics*, *59*, 4309-4319, 1973.
- Kliore, A. J., A. Anabtawi, R. G. Herrera, S. W. Asmar, A. F. Nagy, D. P. Hinson, and F. M. Flasar, Ionosphere of Callisto from Galileo Radio Occultation Observations, *Journal of Geophysics Research-Space Physics*, *107*, art. no.-1407, 2002.
- Kronebush, P. L., and J. Berkowitz, Photodissociative Ionization in the 21-41 eV Region:

- O₂, N₂, CO, NO, CO₂, H₂O, NH₃, and CH₄, *International Journal of Mass Spectrometry and Ion Physics*, *22*, 283-306, 1976.
- Lawrence, G. M., Production of O(¹S) from Photodissociation of CO₂, *Journal of Chemical Physics*, *57*, 5616, 1972a.
- Lawrence, G. M., Photodissociation of CO₂ to Produce CO(a³Π), *Journal of Chemical Physics*, *56*, 3435, 1972b.
- Le Teuff, Y. H., T. J. Millar, and A. J. Markwick, The UMIST Database for Astrochemistry 1999, *Astronomy and Astrophysics Supplement Series*, *146*, 157, 2000.
- Lebofsky, L.A., Stability of frosts in the Solar System, *Icarus*, *25*, 205-217, 1975.
- Lellouch, E., Urey Prize Lecture - Io's Atmosphere: Not Yet Understood, *Icarus*, *124*, 1-21, 1996.
- Masuoka, T., Single-Photoionization and Double-Photoionization Cross-Sections of Carbon-Dioxide (CO₂) and Ionic Fragmentation of CO₂⁺ and CO₂⁺⁺, *Physical Review A*, *50*, 3886-3894, 1994.
- Masuoka, T., and E. Nakamura, Single-Photoionization, Double-Photoionization, and Triple-Photoionization Cross-Sections of Carbon-Monoxide (CO) and Ionic Fragmentation of CO⁺, CO₂⁺, and CO₃⁺, *Physical Review A*, *48*, 4379-4389, 1993.
- Masuoka, T., and J. A. R. Samson, Dissociative and Double Photo-Ionization of CO from Threshold to 90-Å, *Journal of Chemical Physics*, *74*, 1093-1097, 1981.
- McElroy, M. B., and T. M. Donahue, Stability of Martian Atmosphere, *Science*, *177*, 986, 1972.

- Miller, T. M., R. E. Wetterskog, and J. F. Paulson, Temperature-Dependence of the Ion-Molecule Reactions $N^+ + CO$, $C^+ + NO$, and C^+ , CO^+ , $CO_2^+ + O_2$ from 90-450 K, *Journal of Chemical Physics*, *80*, 4922-4925, 1984.
- Moore, J. M., M. T. Mellon, and A. P. Zent, Mass Wasting and Ground Collapse in Terrains of Volatile-Rich Deposits as a Solar System-Wide Geological Process: The Pre-Galileo View, *Icarus*, *122*, 63-78, 1996.
- Moore, J. M., E. Asphaug, D. Morrison, J. R. Spencer, C. R. Chapman, R. J. Sullivan, F. C. Chuang, J. E. Klemaszewski, R. Greeley, K. C. Bender, P. E. Geissler, P. Helfenstein, and C. B. Pilcher, Mass Movement and landform Degradation of the Icy Galilean Satellites: Results of the Galileo Nominal Mission, *Icarus*, *140*, 294-312, 1999.
- Moses, J. I., E. Lellouch, B. Bezard, G. R. Gladstone, H. Feuchtgruber, and M. Allen, Photochemistry of Saturn's Atmosphere II. Effects of an Influx of External Oxygen, *Icarus*, *145*, 166-202, 2000.
- Mount, G. H., and G. J. Rottman, The Solar Absolute Spectral Irradiance 1150-3173-a - May 17, 1982, *Journal of Geophysical Research-Oceans and Atmospheres*, *88*, 5403-5410, 1983.
- Mul, P. M., J. W. McGowan, P. Defrance, and J. B. A. Mitchell, Merged Electron-Ion Beam Experiments .5. Dissociative Recombination of OH^+ , H_2O^+ , H_3O^+ and D_3O^+ , *Journal of Physics B: Atomic, Molecular and Optical Physics*, *16*, 3099-3107, 1983.
- Neubauer, F. M., The sub-Alfvénic interaction of the Galilean satellites with the Jovian magnetosphere, *Journal of Geophysical Research-Planets*, *103*, 19843-19866, 1998.
- Okabe, H., *Photochemistry of Small Molecules*, Wiley, New York, 1978.

- World Meteorological Organization, Report No. 16-Atmospheric Ozone, 1, 1985.
- Pearl, J., R. Hanel, V. Kunde, W. Maguire, K. Fox, S. Gupta, C. Ponnampereuma, and F. Raulin, Identification of Gaseous SO₂ and New Upper Limits for Other Gases on Io, *Nature*, 280, 755-758, 1979.
- Shaw, D. A., D. M. P. Holland, M. A. Hayes, M. A. Macdonald, A. Hopkirk, and S. M. McSweeney, A Study of the Absolute Photoabsorption, Photoionization and Photodissociation Cross-Sections and the Photoionization Quantum Efficiency of Carbon-Dioxide from the Ionization Threshold to 345-Angstrom, *Chemical Physics*, 198, 381-396, 1995.
- Sheehan, C. H., and J. P. St-Maurice, Dissociative Recombination of N₂⁺, O₂⁺, and NO⁺: Rate Coefficients for Ground State and Vibrationally Excited Ions, *Journal of Geophysics Research-Space Physics*, 109, art. no.-A03302, 2004.
- Skrzypkowski, M. P., T. Gougousi, R. Johnsen, and M. F. Golde, Measurement of the Absolute Yield of CO(a³Π)+O Products in the Dissociative Recombination of CO₂⁺ Ions with Electrons, *Journal of Chemical Physics*, 108, 8400-8407, 1998.
- Spencer, J. R., and W. M. Calvin, Condensed O₂ on Europa and Callisto, *Astron. J.*, 124, 3400-3403, 2002.
- Strobel, D. F., J. Saur, P. D. Feldman, and M. A. McGrath, Hubble Space Telescope Space Telescope Imaging Spectrograph Search for an Atmosphere on Callisto: A Jovian Unipolar Inductor, *Astrophysical Journal*, 581, L51-L54, 2002.
- Tan, K. H., C. E. Brion, P. E. Vanderleeuw, and M. J. Vanderwiell, Absolute Oscillator-Strengths (10-60 eV) for Photoabsorption, Photoionization and Fragmentation of H₂O, *Chemical Physics*, 29, 299-309, 1978.

- Torr, M. R., and D. G. Torr, Ionization Frequencies for Solar Cycle-21 - Revised, *Journal of Geophysics Research-Space Physics*, *90*, 6675-6678, 1985.
- Van brunt, R. J., Whitehead, R. G. Hirsch, and F. W. Powell, Photoionization of N₂, O₂, NO, CO, and CO₂ by Soft X-Rays, *Journal of Chemical Physics*, *57*, 3120, 1972.
- Vejby-Christensen, L., L. H. Andersen, O. Heber, D. Kella, H. B. Pedersen, H. T. Schmidt, and D. Zajfman, Complete Branching Ratios for the Dissociative Recombination of H₂O⁺, H₃O⁺, and CH₃⁺, *Astrophysical Journal*, *483*, 531-540, 1997.
- Weiss, B. P., Y. L. Yung, and K. H. Nealson, Atmospheric Energy for Subsurface Life on Mars? *Proceedings of the National Academy of Sciences of The United States of America*, *97*, 1395-1399, 2000.
- Weller, C. S., and M. A. Biondi, Measurements of Dissociative Recombination of CO₂⁺ Ions with Electrons, *Physical Review Letters*, *19*, 59, 1967.
- Wight, G. R., M. J. Vanderwiell, and C. E. Brion, Dipole Excitation, Ionization and Fragmentation of N₂ and CO in 10-60 eV Region, *Journal of Physics B: Atomic, Molecular and Optical Physics*, *9*, 675-689, 1976.
- Yung, Y. L., and W. B. DeMore, *Photochemistry of Planetary Atmospheres*, Oxford University Press, New York, pp. 258-260, 1999.
- Yung, Y. L., and M. B., McElroy Stability of an Oxygen Atmosphere on Ganymede, *Icarus*, *30*, 97-103, 1977.

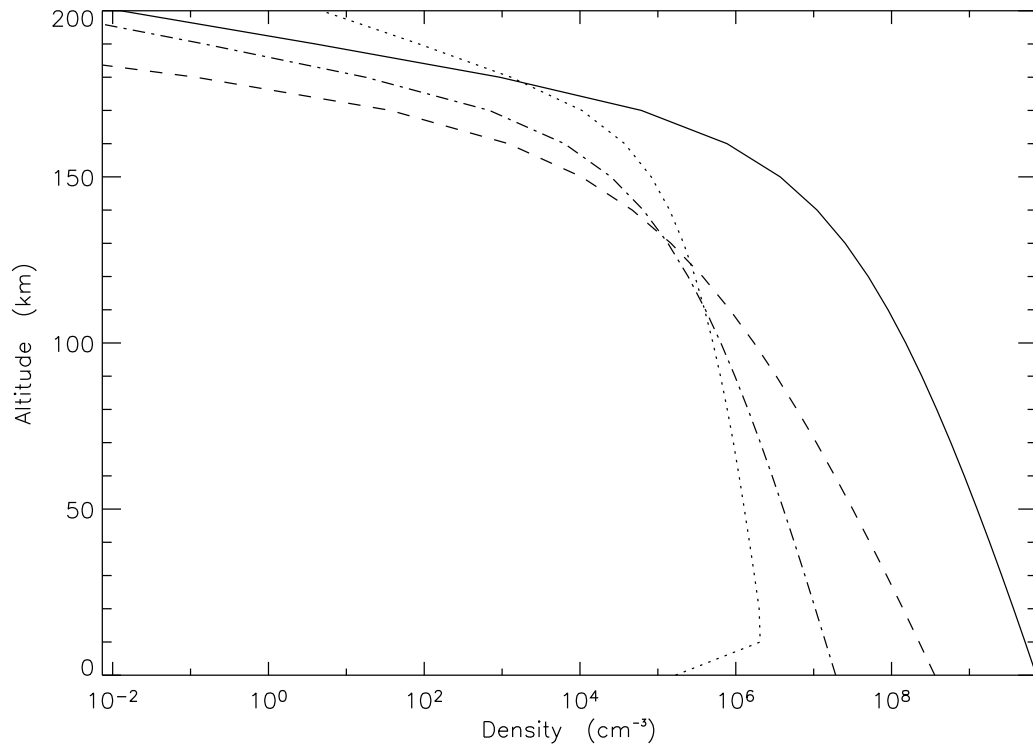


Figure 8.1 Callisto—Vertical profiles of oxides: O₂ (solid line), O (dotted line), CO₂ (dashed line), and CO (dash-dotted line).

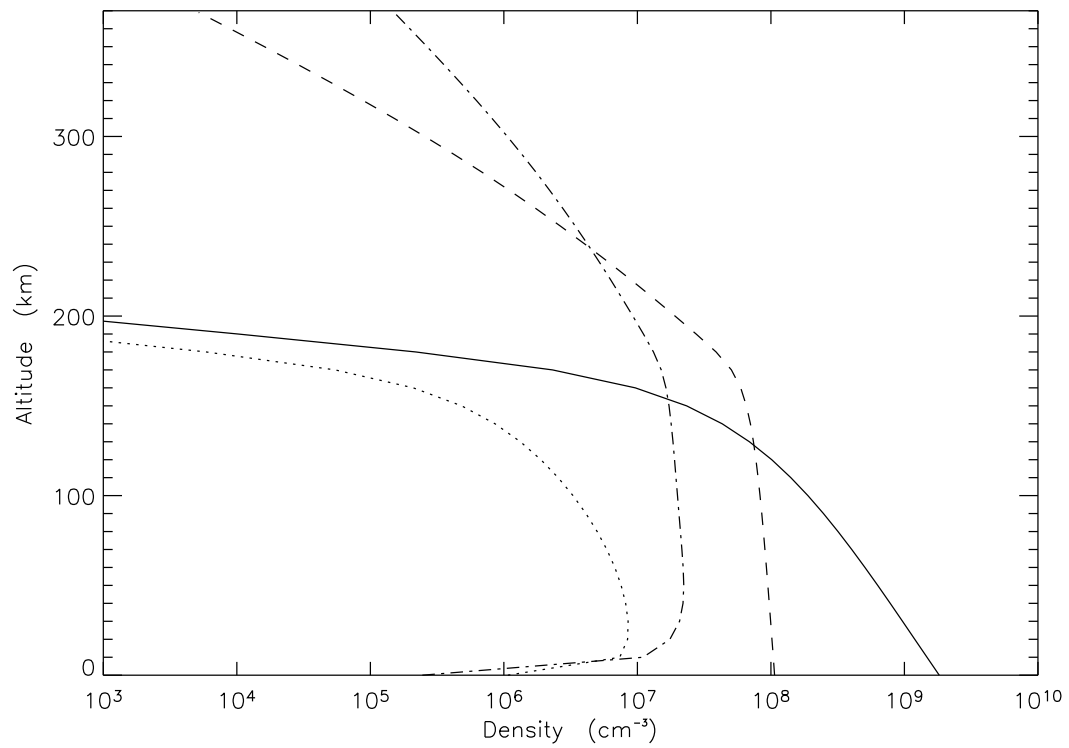


Figure 8.2 Callisto—Vertical profiles of H₂O (solid line), OH (dotted line), H₂ (dashed line), and H (dash-dotted line).

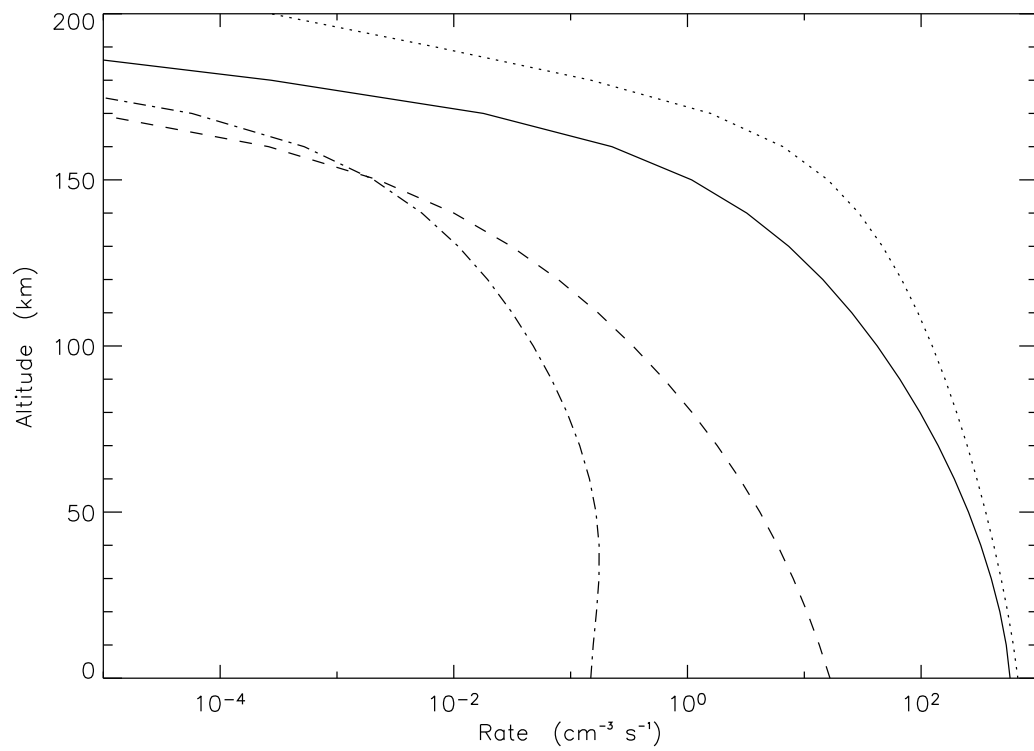


Figure 8.3 Callisto—Vertical profiles of total photoabsorption rates for O_2 (solid line), H_2O (dotted line), CO_2 (dashed line), and CO (dash-dotted line).

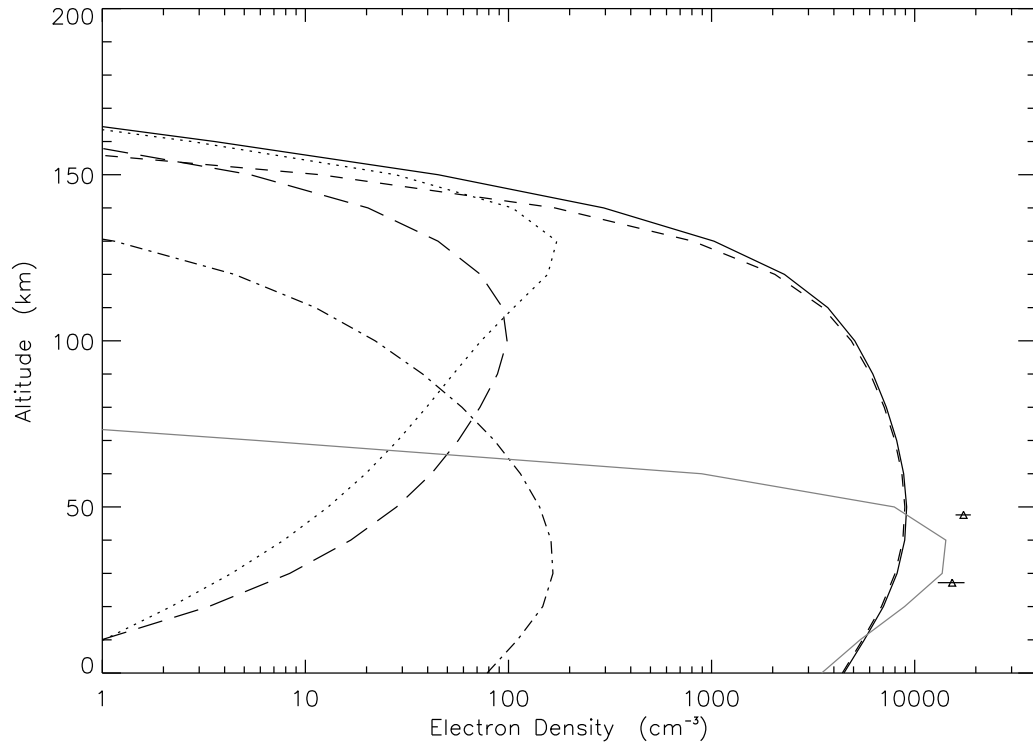


Figure 8.4 Callisto—Vertical profiles of total electron density (dark solid line), O_2^+ (dashed line), H_2O^+ (dotted line), CO_2^+ (dash-dotted line), and O^+ (long-dashed line) in our reference model (enhanced surface chemical reactions). A model with no chemical reactions enhanced on the surface is shown for comparison (light solid line). Triangles are Galileo spacecraft flyby experiments. The reported error bars are overplotted.

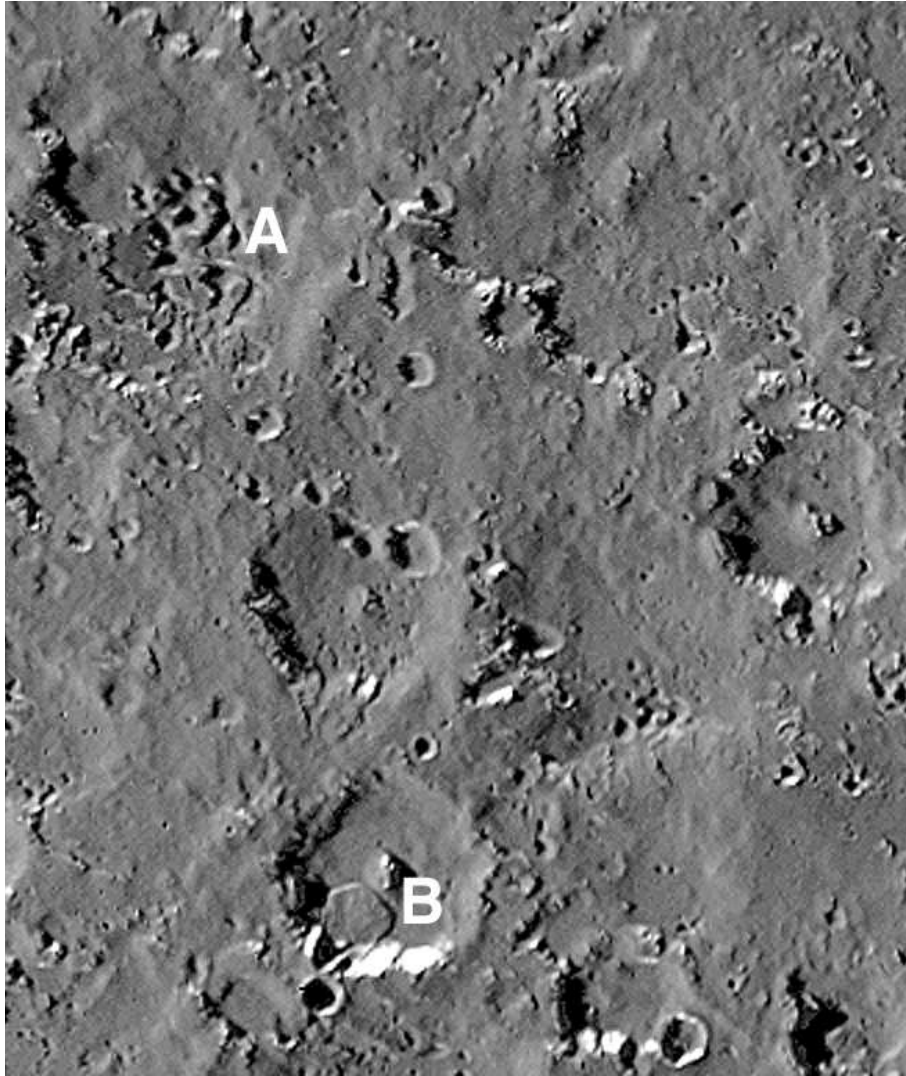


Figure 8.5 Callisto—Callisto’s surface shows abundant evidence for mass wasting of a dark mantling material. Pits (at A) suggest ground collapse due to loss of subsurface volatiles. A 4 km wide landslide deposit (at B) attests to the mobility of the dark material. Bright crater walls and local topographic highs are probably exposures of water frost cold trapped on relatively bright “bedice” which is believed to underlie the dark mantle. (Galileo Solid State Imager observation C9CSCRATER01, image s0401505526; resolution 160 m/pixel.)

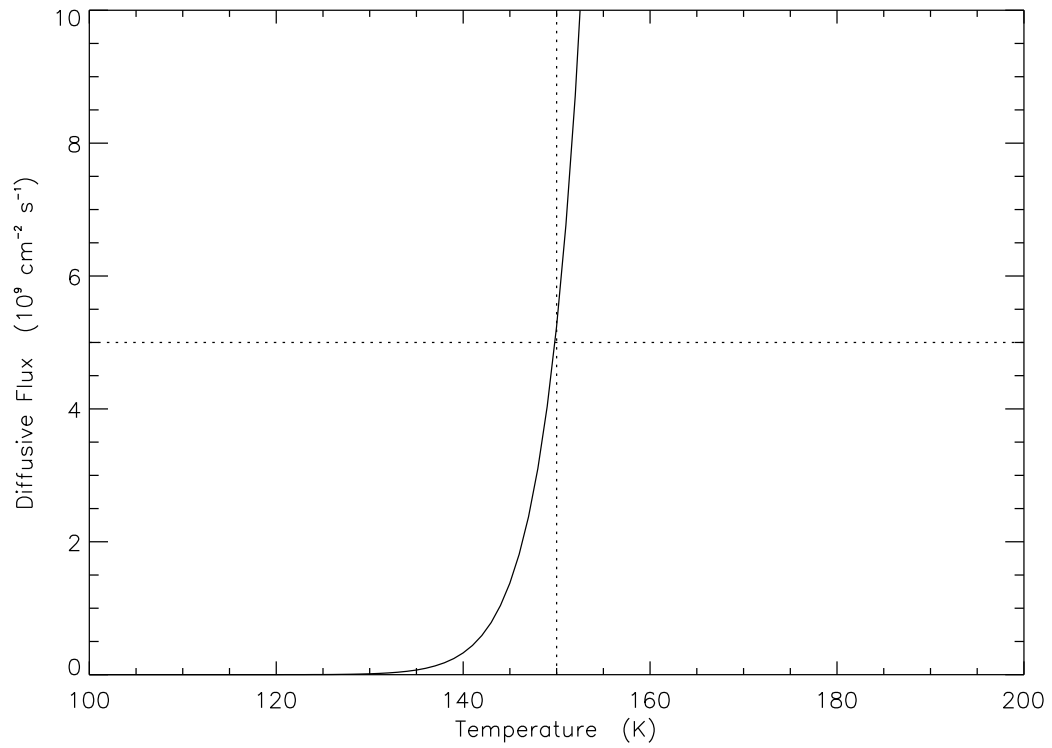


Figure 8.6 Callisto—Profiles of H_2O diffusive flux as a function of temperature for temperature gradient of 200 K cm^{-1} . The two dotted lines represents maximum H_2O diffusion rates (horizontal line) and the required surface temperature of 150 K (vertical line).

Table 8.1. Callisto—Lists of Major Reactions

Reactants	Products	Rate Coefficients ^a	References
CO + hν	→ C + O	6.2×10^{-8}	19
CO + hν	→ CO ⁺ + e ⁻	2.2×10^{-8}	10,12,16,17,26,29
CO ₂ + hν	→ CO + O	2.9×10^{-8}	19,30
CO ₂ + hν	→ CO + O(¹ D)	4.6×10^{-8}	19,30
CO ₂ + hν	→ CO + O(¹ S)	1.0×10^{-7}	13,14,21
CO ₂ + hν	→ CO ₂ ⁺ + e ⁻	4.6×10^{-8}	2,15,22,30
O ₂ + hν	→ 2 O	7.3×10^{-8}	19,30
O ₂ + hν	→ O + O(¹ D)	1.8×10^{-7}	19,30
O ₂ + hν	→ O ₂ ⁺ + e ⁻	3.6×10^{-8}	30
O ₃ + hν	→ O ₂ + O(¹ D)	2.8×10^{-4}	30
H ₂ O + hν	→ H + OH	5.7×10^{-7}	19,30
H ₂ O + hν	→ H ₂ O ⁺ + e ⁻	2.7×10^{-8}	19,30
C + O ₂	→ O + CO	1.6×10^{-11}	1,5,8,11,12,25
O + OH	→ O ₂ + H	4.9×10^{-11}	19,30
O(¹ D) + CO ₂	→ O + CO ₂	$7.4 \times 10^{-11} e^{120/T}$	30
O(¹ D) + O ₂	→ O + O ₂	$3.2 \times 10^{-11} e^{70/T}$	30
O(¹ D) + H ₂ O	→ 2 OH	2.2×10^{-10}	4,19,30
O(¹ S) + M	→ O + M	1.0×10^{-10}	estimate

Table 8.1 (cont'd)

Reactants	Products	Rate Coefficients ^a	References
CO + OH	→ CO ₂ + H	1.5 × 10 ⁻¹³	19,30
CO ⁺ + O ₂	→ CO + O ₂ ⁺	3.1 × 10 ⁻¹⁰	18
CO ₂ ⁺ + e ⁻	→ CO + O	4.0 × 10 ⁻⁷	6,7,24,28,30
O ₂ ⁺ + e ⁻	→ 2 O	3.2 × 10 ⁻⁷	23,30
H ₂ O ⁺ + O ₂	→ H ₂ O + O ₂ ⁺	4.6 × 10 ⁻⁷	31
H ₂ O ⁺ + e ⁻	→ O + 2 H	2.9 × 10 ⁻⁷	3,20,27
H ₂ O ⁺ + e ⁻	→ O + H ₂	4.7 × 10 ⁻⁸	3,20,27
H ₂ O ⁺ + e ⁻	→ OH + H	8.9 × 10 ⁻⁸	3,20,27
O + O ₂ + M	→ O ₃ + M	1.8 × 10 ⁻²⁷ T ^{-2.62}	9,19,30
H + O ₂ + M	→ HO ₂ + M	1.7 × 10 ⁻³¹	4,30
O + HO ₂	→ OH + O ₂	1.1 × 10 ⁻¹⁰	4,30
OH + HO ₂	→ H ₂ O + O ₂	2.5 × 10 ⁻¹⁰	4,30

^aUnits are s⁻¹ for photolysis reactions, cm³ s⁻¹ for two-body reactions, and cm⁶ cm⁻¹ for three-body reactions. The photolysis rate coefficients are given at the top of the model atmosphere.

References. — (1) *Brion and Carnovale* [1985]; (2) *Chan et al.* [1993]; (3) *Datz et al.* [2000]; (4) *DeMore et al.* [1997]; (5) *Dutuit et al.* [1985]; (6) *Gougousi et al.* [1997]; (7) *Gutcheck and Zipf* [1973]; (8) *Haddad and Samson* [1986]; (9) *Hippler et al.* [1990]; (10) *Huber and Herzberg* [1979]; (11) *Katayama et al.* [1973]; (12) *Kronebush and Berkowitz* [1976]; (13) *Lawrence* [1972a]; (14) *Lawrence* [1972b]; (15) *Masuoka* [1994]; (16) *Masuoka and Nakamura* [1993]; (17) *Masuoka and Samson* [1981]; (18) *Miller et al.* [1984]; (19) See references in *Moses et al.* [2000]; (20) *Mul et al.* [1983]; (21) *Okabe* [1978]; (22) *Shaw et al.* [1995]; (23) *Sheehan and St Maurice* [2004]; (24) *Skrzypkowski et al.* [1998]; (25) *Tan et al.* [1978]; (26) *Van brunt et al.* [1972]; (27) *Vejby-Christensen et al.* [1997]; (28) *Weller and Biondi* [1967]; (29) *Wight et al.* [1976]; (30) See references in *Yung and DeMore* [1999]; (31) *Le Teuff et al.* [2000].

Table 8.2. Callisto—Abundances of C, O, CO, H, and H₂

	H ₂ O ^a	C ^b	O ^b	CO ^b	H ^b	H ₂ ^b
obs. ^c	...	$< 10^{13}$	$< 2.5 \times 10^{13}$	$< 10^{17}$
max. ^d	0	1.8×10^8	1.6×10^{15}	4.3×10^{13}
	0.10	6.4×10^8	1.2×10^{14}	2.4×10^{14}	2.4×10^{14}	8.1×10^{14}
	0.25	1.2×10^8	1.3×10^{13}	6.0×10^{13}	3.5×10^{14}	3.2×10^{15}
	0.50	4.4×10^7	7.6×10^{12}	2.6×10^{13}	4.0×10^{14}	7.1×10^{15}
	1.00	1.5×10^7	5.6×10^{12}	1.1×10^{13}	4.6×10^{14}	1.4×10^{16}
	wet ^e	5.9×10^6	2.3×10^{13}	2.4×10^{13}	1.2×10^{17}	4.0×10^{15}
avg. ^d	0.25	6.7×10^7	1.1×10^{13}	4.6×10^{13}	2.5×10^{14}	2.7×10^{15}
min. ^d	0.25	2.4×10^7	8.3×10^{12}	2.8×10^{13}	1.6×10^{14}	1.8×10^{15}

^aThe near surface H₂O vapor abundance. The values are relative to the O₂ density of $7.4 \times 10^9 \text{ cm}^{-3}$. A value of 0.25 is adopted as our reference model.

^bThe column integrated density in units of cm^{-2} . H and H₂ are allowed to escape.

^cThe observed upper limits of column density for C, O, and CO [*Strobel et al.*, 2002].

^dThe calculated abundances for maximum, averaged and minimum solar fluxes.

^e“wet” refers to the model where three-body chemical reactions are not enhanced on the surface. In this model, the best fits of O₂ and H₂O surface densities are 3.2×10^{10} and $4.8 \times 10^9 \text{ cm}^{-3}$, respectively.

Part III

Extrasolar “Hot Jupiters”

Chapter 9

Source of Atomic Hydrogen in the Atmosphere of HD 209458b

Mao-Chang Liang, Christopher D. Parkinson, Anthony Y.-T. Lee, Yuk
L. Yung, and Sara Seager

The Astrophysical Journal Letters, 596, 247, 2003.

Abstract

Atomic hydrogen loss at the top of HD 209458b’s atmosphere has been recently suggested [Vidal-Madjar *et al.*, 2003]. We have developed a one-dimensional model to study the chemistry in the upper atmosphere of this extrasolar “hot Jupiter.” The three most abundant elements (other than He), as well as four parent molecules, are included in this model: H, C, O, H₂, CO, H₂O, and CH₄. The higher temperatures (~ 1000 K) and higher stellar irradiance ($\sim 6 \times 10^5$ W m⁻²) strongly enhance and modify the chemical reaction rates in this atmosphere. The main result is that the production of atomic hydrogen in the atmosphere is mainly driven by H₂O photolysis and reaction of OH with H₂ and is *insensitive* to the exact abundances of CO, H₂O, and CH₄.

9.1 Introduction

Since the discovery of the first extrasolar planet, 51 Peg b, in 1995 [Mayor and Queloz, 1995], a total of 155 planets have so far been discovered [e.g., Butler *et al.*, 2003; Udry *et al.*, 2002; Marcy *et al.*, 2005, and references therein] and analyzed statistically in order to characterize the formation environment [Fischer *et al.*, 2002; Santos *et al.*, 2003]. The formation of gas giants is thought to be complete in 10 Myr, before the disappearance of the gaseous stellar accretion disk, at distances > 5 AU from the parent star. They are then pulled to their present positions by tidal interactions between the gas disk and planet [e.g., Pollack *et al.*, 1996; Ward, 1997].

Edge-on planetary systems provide a unique opportunity to investigate planetary atmospheres. HD 209458b is such a planet, providing the first extrasolar planetary detection using the light curve obtained during a planetary transit of its parent star [Charbonneau *et*

al., 2000; *Henry et al.*, 2000]. The orbital parameters were accurately determined by *Charbonneau et al.* [2000], *Henry et al.* [2000], and *Mazeh et al.* [2000]. Strong absorption lines are required to make an atmospheric detection, and *Seager and Sasselov* [2000] theoretically characterized the most prominent absorption features; for example, Na I and K I doublet resonance and He I $2^3S - 2^3P$ triplets. *Charbonneau et al.* [2002] detected the Na I doublet at 589.3 nm in HD 209458b with $\sim 4\sigma$ confidence level. Following this, *Vidal-Madjar et al.* [2003] made the first observation of the extended upper atmosphere of HD 209458b with a $\sim 4\sigma$ detection of the H I atomic hydrogen absorption of the stellar Lyman- α line. They reported an absorption of $\sim 15 \pm 4\%$ and claimed that this should be taking place beyond the Roche limit, thus implying hydrodynamic escape of hydrogen atoms from HD 209458b’s atmosphere.

The temperature and UV flux of close-in planets are high. This motivates us to study the chemistry that may be important in this “hot Jupiter.” Here, we consider a simple hydrocarbon/oxygen chemistry model to determine a source of atomic hydrogen in the atmosphere of HD 209458b and represent the first effort to investigate the UV enhanced chemical processes in “hot Jupiters.”

9.2 Model

Our model is based on the four parent molecules H_2 , CO, H_2O , and CH_4 , and is a derivative of the Caltech/JPL KINETICS model for the Jovian atmosphere. HD 209458b orbits at a distance of 0.05 AU. As HD 209458 is a G0 solar-type dwarf star, it is justified to use the solar spectrum. We expect the atmosphere to have a temperature of ~ 1000 K and an incident UV flux (< 1800 Å) $\sim 2 \times 10^{15}$ photons $cm^{-2} s^{-1}$. By comparison, the UV flux at

Jupiter is a factor of $\sim 10^4$ lower.

A one-dimensional radiative transfer model is applied to the atmosphere with 80 layers. The main UV absorber in this model is H_2O , $\sim 100\%$. The strong UV absorbers, e.g., metals, are ignored in this study. A total of 253 chemical reactions involving C-H-O molecules are taken from the literature. The reaction rates are determined from laboratory measurements made mainly at room temperature. In this work, the chemical reactions are at much higher temperatures. Without any accurate measurements of the reaction rates under appropriate conditions, we adopt either the derived temperature-dependent rate constant, which is measured at lower temperature, or use the results of theoretical calculation to estimate the temperature-dependence [e.g., *Yung and DeMore, 1999*].

Hydrocarbons—The hydrocarbon photochemical scheme used here is a simplified version of the Jovian atmospheric model described in *Strobel [1973]* and *Gladstone et al. [1996]*. The photodissociation of CH_4 and the subsequent reactions of these species with hydrogen produce all the other hydrocarbons present in a Jovian-type atmosphere. For lower temperatures and weaker stellar irradiation, the main source of H is from H_2 and CH_4 photodissociation and the main sink is via C_2H_2 , which acts as a catalyst in recombining H. HD 209458b receives much greater stellar irradiation and is therefore much hotter than Jupiter. In this case, the formation of H is greatly enhanced by the photolysis of H_2O and reactions between O and OH radicals and H_2 . The sink for H is more complex (see § 9.3.3).

Oxygen—O is similar in abundance to C and represents a cosmic abundance of the parent molecules. The atmospheric H_2O abundance will be controlled mainly by the comparative richness of these two species. The amount of H_2O and CO governs the amount of atomic oxygen present and the related reactions are of great interest. The oxygen related reactions are taken from *Moses et al. [2000]*.

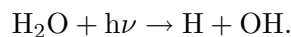
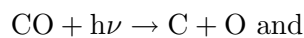
Model Atmosphere—Three models are investigated in this paper. Our reference model uses solar abundances, and is shown in Figure 9.1 (model A). We also consider 2 other cases, model B and model C, in which H₂O and CO abundances are 10 times lower, respectively. We have taken the 1 bar level to be “0” km, and all heights are referenced from this level. The temperature-pressure profile and chemical abundances are based on *Seager et al.* [2000], in which the stellar irradiance is uniformly distributed over the whole planet, and the cloud as shielding and scattering stellar light is not considered, and the temperature decreases from the bottom to the top of the atmosphere. The abundances of CO and H₂O are 3.6×10^{-4} and 4.5×10^{-4} , respectively. These values are similar to solar abundances. The CH₄ abundance is determined by the thermodynamic equilibrium chemistry in the deep atmosphere. We adopt the value 3.9×10^{-8} , which is at the lower end of the model by *Seager and Sasselov* [2000]. The temperature-pressure profiles are uncertain, because the global circulation and high temperature condensation [*Seager and Sasselov*, 2000; *Sudarsky et al.*, 2000] are not constrained in generating the model atmosphere. Various temperature-pressure profiles have been verified and will be presented in a more comprehensive paper. The eddy diffusion is proportional to $n^{-\alpha}$ (n is the number density), where α is taken to be $\sim 0.6 - 0.7$.

9.3 Results

9.3.1 OH and O Radicals

Figure 9.2 shows the OH and O radicals in our models. OH and O are the most important radicals, as they drive most of the chemical reactions. O, for example, drives most of the formation of OH radicals in the water-poor atmosphere. These species are produced

photochemically; for example,



CO photolysis is an important source of O, and H₂O is the main source of OH. As a consequence of H₂O and CO photolysis, O increases with altitude, while OH increases with altitude until the ~ 10 nbar level. The decline of OH above 10 nbar is due to OH photodissociation. Interestingly, the mixing ratio of OH radicals is not sensitive to the abundance of CO and H₂O. With an order of magnitude change in H₂O (model B) or CO (model C), OH changes by a factor of $\lesssim 3$ only. However, O is sensitive to both CO and H₂O concentrations and preferentially forms OH. From Figure 9.2 we see that OH is not sensitive to the H₂O abundance, that is controlled by the comparative richness of cosmic C and O. Under high stellar UV irradiation, a fraction of CO will be photodissociated. The resulting O will react with H₂ to form OH, which eventually forms H₂O by reacting with H₂.

9.3.2 CO₂ and CH₄

CO₂ is formed mainly via the reaction of CO and OH. Figure 9.3 shows the vertical profiles of CO₂ for our three models. The CO₂ mixing ratio is enhanced in the upper atmosphere. At pressures of ~ 10 nbar for model A, the CO₂ mixing ratio is only about 2 orders of magnitude less than its progenitor, CO. The CO₂ abundance in the model is rather insensitive to the abundance of H₂O. An order of magnitude decrease in H₂O results in only a factor of ~ 3 decrease in CO₂ abundance (see models A and B in Figure 9.3). However, the CO₂

abundance varies approximately linearly with the abundance of CO (see models A and C in Figure 9.3).

The photochemical formation of CH₄ is initiated by the downward flux of C atoms produced in the photolysis of CO in the upper atmosphere. This obtains the following sequence of reactions:

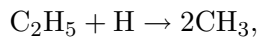
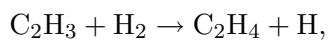
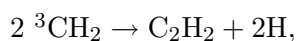
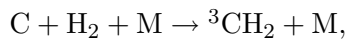


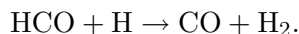
Figure 9.3 shows the vertical profiles of CH₄ in our models. We see that the CH₄ mixing ratio increases by a factor of 5-100 from the bottom to the 0.1 mbar level (see Figure 9.3). Above this level, CH₄ rapidly decreases due to photodissociation.

The CH₄ mixing ratio is increased by a factor ~ 2 when we lower the H₂O abundance by an order of magnitude (see models A and B in Figure 9.3). We suggest this increase is due to less UV shielding by water above. The CH₄ mixing ratio is decreased by an order of magnitude when we lower the CO abundance by an order of magnitude. The reason is that CO photolysis is the source of the C in CH₄.

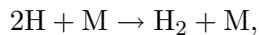
9.3.3 H and H₂O

Figure 9.3 shows the mixing ratios for H and H₂O. The most striking feature is the production of H (all three models). In our 1-D model, the production rate of atomic hydrogen is insensitive to the exact abundances of CO and H₂O. With an order of magnitude change in the abundance of either CO or H₂O, the atomic hydrogen changes by only a small factor, $\sim 1-2$. This implies the production of H in three models is limited by the availability of UV photons. The H production is also insensitive to the abundance of CH₄. CH₄ abundance has been increased to be as high as CO, and the H mixing ratio is only changed by a small factor. However, temperature-pressure profiles can significantly modify the H production. A more comprehensive discussion will be given in a separate paper [*Liang et al.*, in preparation]. The mixing ratio of H exceeds 1% at the top of atmosphere. At the top of the atmosphere (< 1 nbar), H₂ will be photolyzed and is a source of H. This atomic hydrogen will fuel the hydrodynamic loss process, as suggested by [*Vidal-Madjar et al.*, 2003] and is discussed in more detailed in a paper by *Parkinson et al.* [in preparation].

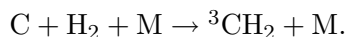
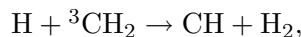
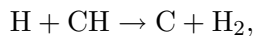
Figure 9.4 shows the production rate of H and the photolysis rate of H₂O. The rates are insensitive to the abundance of CO, but are sensitive to the abundance of H₂O. By comparing the H₂O photolysis rate with H production rate, it is evident that production of H is mainly driven by H₂O photolysis and the reaction of OH with H₂. Below ~ 1 mbar, HCO plays a role in the removal of H via



In the upper atmosphere, H atom recombination and reactions with CH and $^3\text{CH}_2$ will drive the loss of H via



and



The timescale for producing H is of order of 10^5 sec, \sim one day. Since the planet is suggested to be tidally locked, the temperature difference between day- and night-side could be as high as ~ 1000 K. Hence, the wind speed is a few km s^{-1} [Showman and Guillot, 2002; Cho *et al.*, 2003]. The global circulation timescale is calculated to be about one day. The mixing ratio of the produced H is likely to be overestimated.

9.4 Conclusion

We have considered a series of possible chemical reactions using various models for a “hot Jupiter.” We have shown the mechanism for producing atomic hydrogen. The production of H is *insensitive* to the exact abundances of CO, H_2O , and CH_4 . Lowering H_2O or CO by an order of magnitude changes the concentration of H by only a factor of $\lesssim 2$. However, the production rate of H is sensitive to the temperature profile. A 30% change in the temperature will result in $\sim 50\%$ change in the H concentration.

Our calculations show that the H mixing ratio at ~ 1 mbar is $\sim 10^{-3}$ and exceeds

1% at the top of the atmosphere. Being less gravitationally bound, the atomic hydrogen formed at the top of atmosphere can escape hydrodynamically as putatively suggested by the observations of *Vidal-Madjar et al.* [2003]. Since these close-in gas-rich giant planets are probably tidally locked, it is of interest to simulate the differences in chemical processes between the day and night sides and the global transport of heat and mass as well. In addition, high temperature condensations and strong UV absorbers other than H₂O are of another important factors in controlling the evolution and chemical reactions in the atmosphere.

Bibliography

- Butler, R. P., Marcy, G. W., Vogt, S. S., Fischer, D. A., Henry, G. W., Laughlin, G., Wright, J. T., Seven New Keck Planets Orbiting G and K Dwarfs, *Astrophysical Journal*, 582, 455-466, 2003.
- Charbonneau, D., Brown, T. M., Latham, D. W., Mayor, M., Detection of Planetary Transits Across a Sun-like Star, *Astrophysical Journal Letters*, 529, L45-48, 2000.
- Charbonneau, D., Brown, T. M., Noyes, R. W., Gilliland, R. L., Detection of an Extrasolar Planet Atmosphere, *Astrophysical Journal*, 568, 377-384, 2002.
- Cho, J. Y.-K., Menou, K., Hansen, B. M. S.; Seager, S., The Changing Face of the Extrasolar Giant Planet HD 209458b, *Astrophysical Journal Letters*, 587, L117-120, 2003.
- Fischer, D. A., Marcy, G. W., Butler, R. P., Laughlin, G., Vogt, S. S., A Second Planet Orbiting 47 Ursae Majoris, *Astrophysical Journal*, 564, 1028-1034, 2002.
- Gladstone, G. R., Allen, M., Yung, Y. L., Hydrocarbon Photochemistry in the Upper Atmosphere of Jupiter, *Icarus*, 119, 1-52, 1996.
- Henry, G. W., Marcy, G. W., Butler, R. P., Vogt, S. S., A Transiting "51 Peg-like" Planet, *Astrophysical Journal Letters*, 529, L41-44, 2000.
- Marcy, G. W., Butler, R. P., Vogt, S. S., Fischer, D. A., Henry, G. W., Laughlin, G., Wright,

- J. T., Johnson, J. A., Five New Extrasolar Planets, *Astrophysical Journal*, 619, 570-584, 2005.
- Mayor, M., & Queloz, D., A Jupiter-Mass Companion to a Solar-Type Star, *Nature*, 378, 355-359, 1995.
- Mazeh et al., The Spectroscopic Orbit of the Planetary Companion Transiting HD 209458, *Astrophysical Journal Letters*, 532, L55-58, 2000.
- Moses, J. I., Lellouch, E., Bézard, B., Gladstone, G. R., Feuchtgruber, H., Allen, M., Photochemistry of Saturn's Atmosphere. II. Effects of an Influx of External Oxygen, *Icarus*, 145, 166-202, 2000.
- Pollack, J. B., Hubickyj, O., Bodenheimer, P., Lissauer, J. J., Podolak, M., Greenzweig, Y., Formation of the Giant Planets by Concurrent Accretion of Solids and Gas, *Icarus*, 124, 62-85, 1996.
- Santos, N. C., Israelian, G., Mayor, M., Rebolo, R., Udry, S., Statistical Properties of Exoplanets. II. Metallicity, Orbital Parameters, and Space Velocities, *Astronomy and Astrophysics*, 398, 363-376, 2003.
- Seager, S., & Sasselov, D. D., Theoretical Transmission Spectra during Extrasolar Giant Planet Transits, *Astrophysical Journal*, 537, 916-921, 2000.
- Seager, S., Whitney, B. A., Sasselov, D. D., Photometric Light Curves and Polarization of Close-in Extrasolar Giant Planets, *Astrophysical Journal*, 540, 504-520, 2000.
- Showman, A. P., Guillot, T., Atmospheric circulation and tides of "51 Pegasus b-like" planets, *Astronomy and Astrophysics*, 385, 166-180, 2002.

- Strobel, D., The Photochemistry of Hydrocarbons in the Jovian Atmosphere, *Journal of the Atmospheric Sciences*, 30, 489-498, 1973.
- Sudarsky, D., Burrows, A., & Pinto, P., Albedo and Reflection Spectra of Extrasolar Giant Planets, *Astrophysical Journal*, 538, 885-903, 2000.
- Udry, S., Mayor, M., Naef, D., Pepe, F., Queloz, D., Santos, N. C., Burnet, M., The CORALIE Survey for Southern Extra-solar Planets. VIII. The Very Low-mass Companions of HD 141937, HD 162020, HD 168443 and HD 202206: Brown Dwarfs or “Superplanets”?, *Astronomy and Astrophysics*, 390, 267-279, 2002.
- Vidal-Madjar, A., des Etangs, A. Lecavelier, Desert, J.-M., Ballester, G. E., Ferlet, R., Hebrard, G., Mayor, M., An Extended Upper Atmosphere around the Extrasolar Planet HD209458b, *Nature*, 422, 143-146, 2003.
- Ward, W. R., Protoplanet Migration by Nebula Tides, *Icarus*, 126, 261-281, 1997.
- Yung, Y.-L., DeMore, W. B. 1999, Photochemistry of Planetary Atmospheres (New York: Oxford Uni. Press)

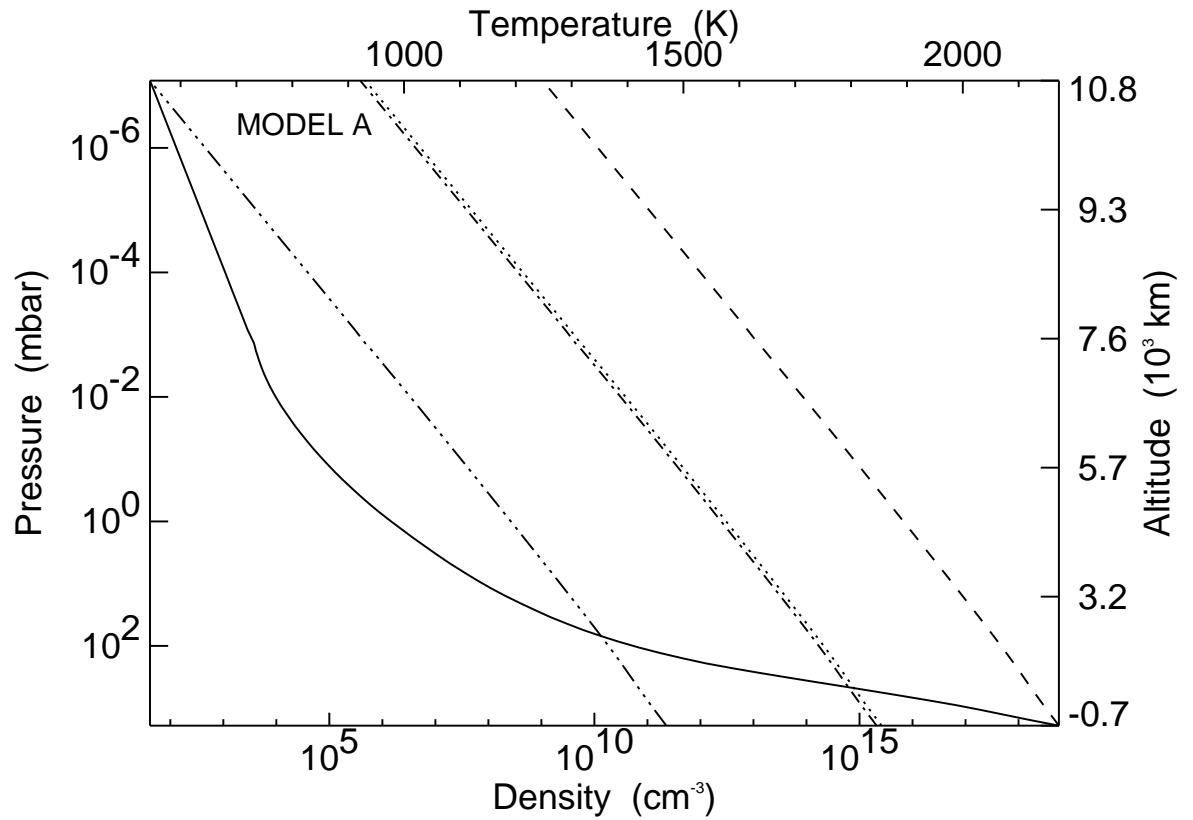


Figure 9.1 HD 209458b—Vertical profile of temperature (solid line), total density (dashed line), and initial constituent number densities (H_2O : dotted line, CO: dash-dot line, CH_4 : dash-dot-dot line).

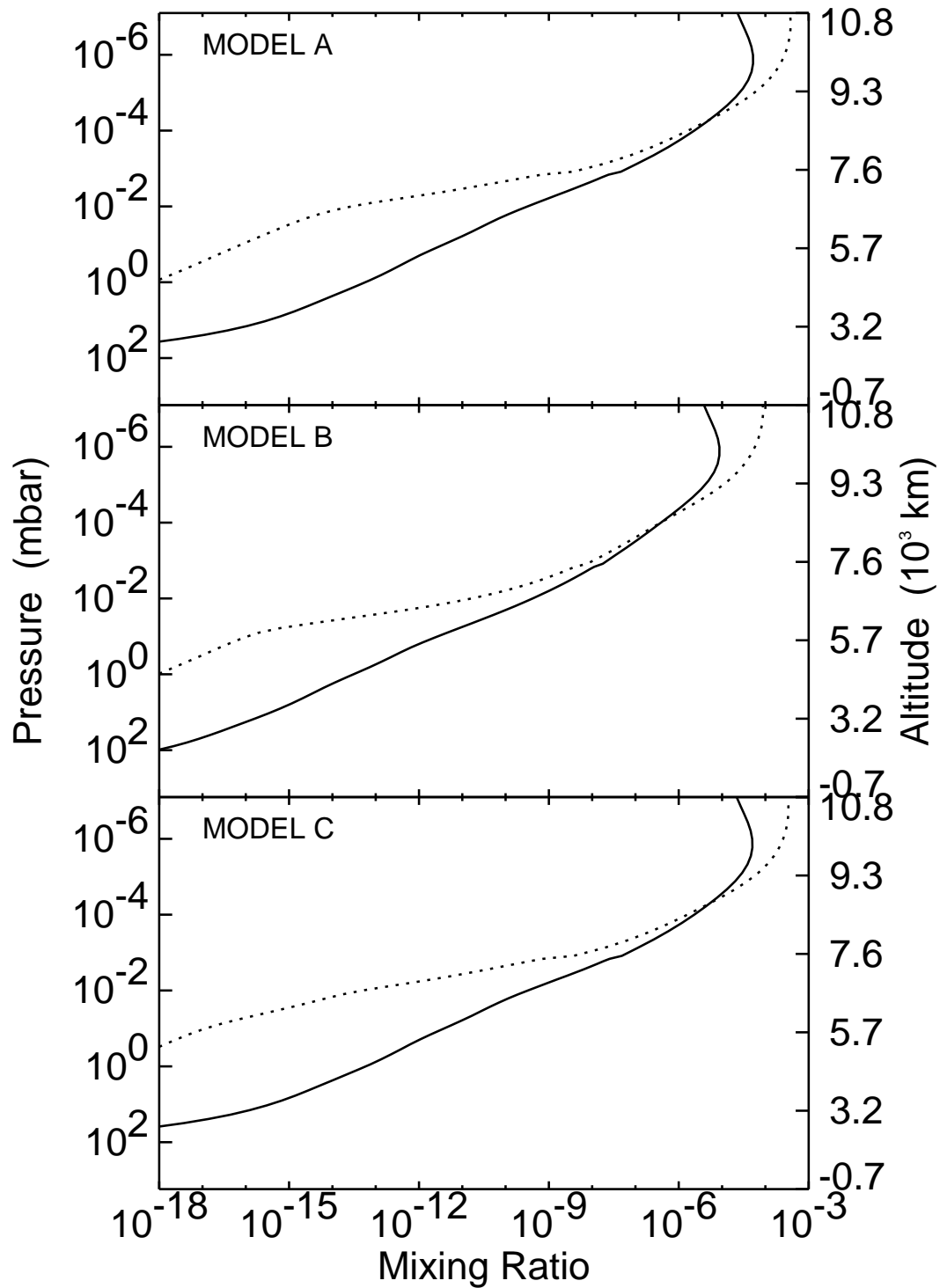


Figure 9.2 HD 209458b—Comparison of mixing ratios of OH (solid line) and O (dotted line) radicals in models A, B, and C.

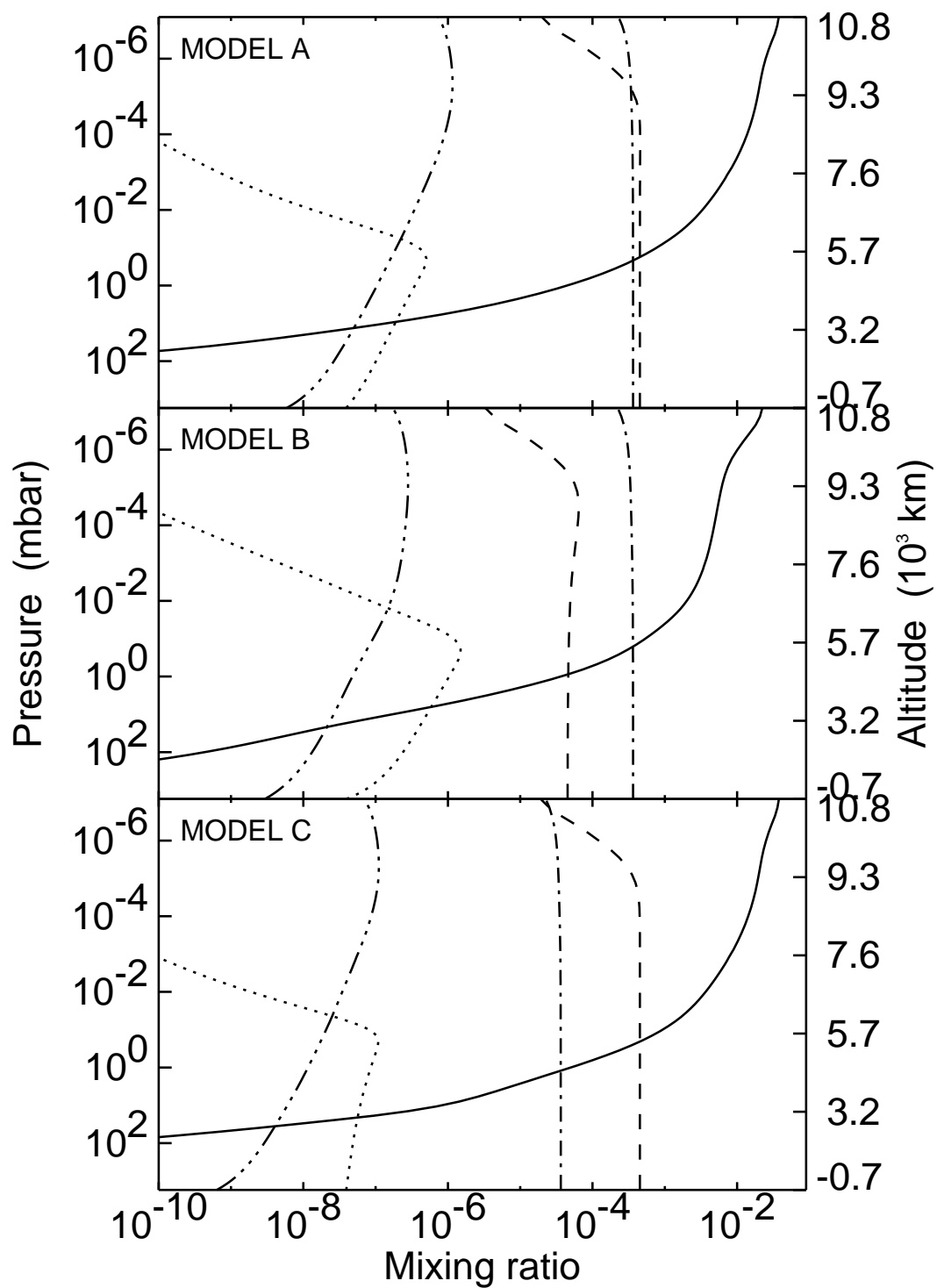


Figure 9.3 HD 209458b—Comparison of mixing ratios of H (solid line), CH_4 (dotted line), H_2O (dashed line), CO (dash-dot line), and CO_2 (dash-dot-dot line) in models A, B, and C.

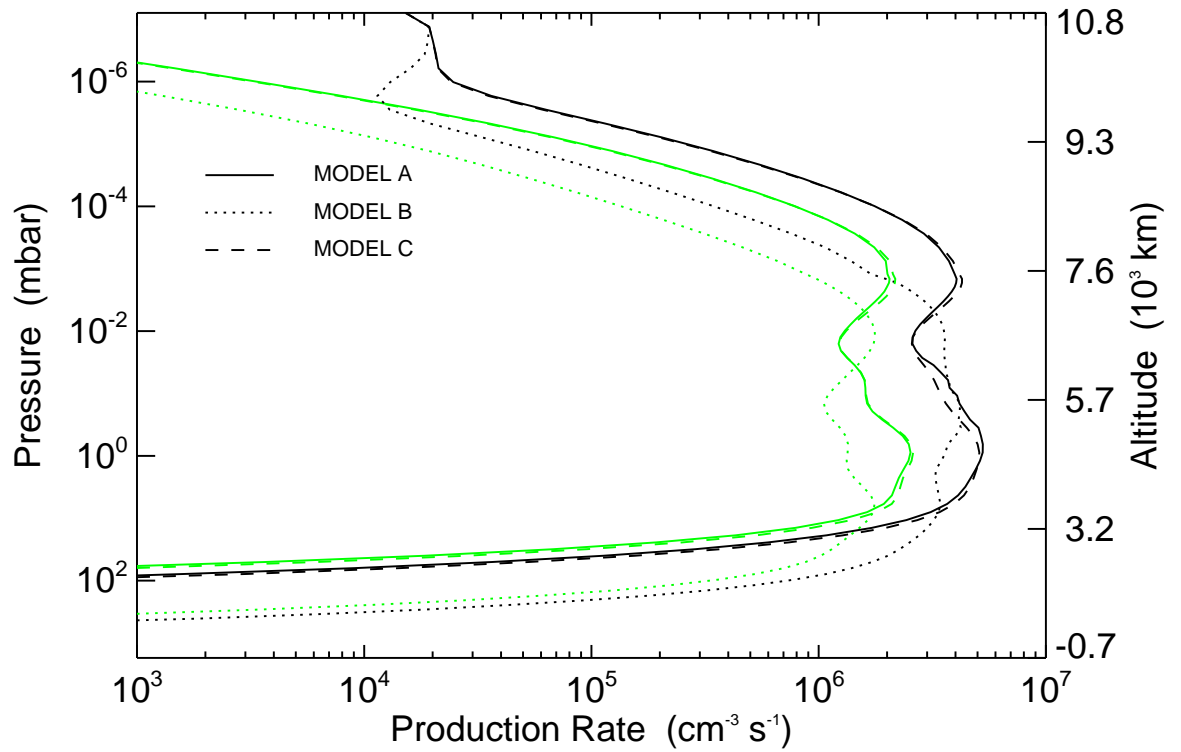


Figure 9.4 HD 209458b—Production rate of H (dark lines) and photolysis rate of H_2O (gray lines) in models A, B, and C.

Chapter 10

On the Insignificance of Photochemical Hydrocarbon Aerosols in the Atmospheres of Close-in Extrasolar Giant Planets

Mao-Chang Liang, Sara Seager, Christopher D. Parkinson, Anthony
Y.-T. Lee, and Yuk L. Yung

The Astrophysical Journal Letters, 605, 61, 2004.

Abstract

The close-in extrasolar giant planets (CEGPs) reside in irradiated environments much more intense than that of the giant planets in our solar system. The high UV irradiance strongly influences their photochemistry, and the general current view is that this high UV flux should greatly enhance the photochemical production of hydrocarbon aerosols. In this chapter, we investigate hydrocarbon aerosol formation in the atmospheres of CEGPs. We find that the abundances of hydrocarbons in the atmospheres of CEGPs are significantly less than that of Jupiter except for models in which the CH_4 abundance is unreasonably high (as high as CO) for the hot (effective temperatures $\gtrsim 1000$ K) atmospheres. Moreover, the hydrocarbons will be condensed out to form aerosols only when the temperature-pressure profiles of the species intersect with the saturation profiles—a case almost certainly not realized in the hot CEGPs’ atmospheres. Hence, our models show that photochemical hydrocarbon aerosols are insignificant in the atmospheres of CEGPs. In contrast, Jupiter and Saturn have a much higher abundance of hydrocarbon aerosols in their atmospheres, which are responsible for strong absorption shortward of 600 nm. Thus the insignificance of photochemical hydrocarbon aerosols in the atmospheres of CEGPs rules out one class of models with low albedos and featureless spectra shortward of 600 nm.

10.1 Introduction

Hazes and clouds¹ in the atmospheres of Jovian planets can strongly affect the ability to determine atmospheric composition at ultraviolet to infrared wavelengths. At wavelengths shorter than ~ 600 nm, the atmospheric line features in the Jovian planets are “washed

¹“Hazes” refers to the diffuse and optically thin aerosol distribution, while “clouds” refers to the optically thick regions [*West et al.*, 1986].

out” by the hazes/clouds in the atmospheres of planets [e.g., *Karkoschka and Tomasko, 1993; Karkoschka, 1998*]. The main chemical compositions of the hazes/clouds on Jupiter are believed to be $\text{H}_2\text{O-NH}_3$, NH_4SH , NH_3 , N_2H_4 , and hydrocarbons from several bar to ~ 0.1 mbar [*Weidenschilling and Lewis, 1973; Strobel, 1983; West et al., 1986; Pryor and Hord, 1991; Gladstone et al., 1996; Banfield et al., 1998a, 1998b; Wong et al., 2003*]. Saturn may have a composition profile similar to Jupiter since both have similar 300-1000 nm spectra [e.g., *Karkoschka, 1998*]. Saturn’s albedo has been successfully modeled by assuming a dichotomy in the aerosol distribution between the troposphere and stratosphere, where the number density of aerosols is much lower in the stratosphere [*Karkoschka and Tomasko, 1993*]. It is found that the stratospheric aerosols are very dark at ~ 300 nm, implying the presence of hydrocarbon aerosols.

Since the recent increase in sample size of extrasolar planets [e.g., *Udry et al., 2002; Butler et al., 2003*], the planetary formation environment has been statistically analyzed, although not conclusively [*Fischer et al., 2002; Santos et al., 2003*]. The close-in extrasolar giant planets (CEGPs, with semi-major axes $\lesssim 0.05$ AU, also known as “hot Jupiters”) are of particular interest since they have more active chemical processes in their atmospheres [e.g., *Liang et al., 2003*], and the evolution of the atmospheres can currently be studied observationally [e.g., *Vidal-Madjar et al., 2003, 2004*]. A number of simulations in the atmospheres of CEGPs have been performed to study the albedos and reflection spectra by including the formation of high temperature condensates, such as silicates [e.g., *Sudarsky et al., 2000; Seager et al., 2000*]. The importance and existence of the atmospheric aerosols have been addressed and discussed widely in recent years [e.g., *Baraffe et al., 2003*], and it is generally believed that more UV flux will result in more aerosols. The UV input to Jovian atmospheres results in photochemical aerosols which significantly affect the ultraviolet-

visible spectra and albedos. Hence, we were motivated to simulate the formation of various molecules, e.g., hydrocarbons, ammonia, and sulfuric acid, which are the possible sources of aerosols in the atmospheres of CEGPs. In this chapter, we focus on hydrocarbons and hydrocarbon aerosol formation.

10.2 Model

The one-dimensional Caltech/Jet Propulsion Laboratory KINETICS model is applied to HD 209458b's atmosphere, which is divided into 80 plane-parallel layers along the radial direction. The planet is probably tidally locked and our simulation is performed on the day side. The model assumes the four parent molecules: H_2 , CO , H_2O , and CH_4 . The abundances of CO and H_2O for the reference model (model A) are 3.6×10^{-4} and 4.5×10^{-4} , respectively. The CH_4 abundance is taken to be 3.9×10^{-8} , which is near the lower bound predicted by *Seager and Sasselov* [2000]. The temperature-pressure profiles are not certain, because the global circulation and high temperature condensates are not constrained in generating the model atmosphere. Our reference profile (solid curve in Figure 10.1) is a derivative of a cloud-free and high temperature condensate-free model. The stellar irradiance is assumed to be uniformly distributed over the whole planet; this gives the lower bound to the temperature profile in the atmosphere of HD 209458b. In view of the aforementioned uncertainty, two alternative temperature profiles, which assume the redistribution of the stellar irradiance evenly only on the day side, are examined [*Barman et al.*, 2002; *Fortney et al.*, 2003].

A one-dimensional, photochemical-diffusive, diurnally averaged numerical model for hydrocarbon photochemistry has been presented by *Gladstone et al.* [1996] for the atmosphere

of Jupiter. In that study, important chemical cycles and pathways involving C₁-C₄ species are identified. Included in this analysis are sensitivity studies on a standard reference model with respect to variations in the eddy-diffusion profile, solar flux, atomic hydrogen influx, latitude, temperature, and important chemical reaction rates. The model reproduces extensive observations of hydrocarbon species as well as He 584 Å and H Lyman-α airglow emissions on Jupiter. Due to the incomplete laboratory measurements of reaction rates and photodissociation quantum yields in the C₃ and higher hydrocarbons, we use a simplified version of the hydrocarbon photochemical model presented by *Gladstone et al.* [1996]. The hydrocarbon chemistry up to the C₂ hydrocarbons is modeled thoroughly in the atmosphere of HD 209458b. The C₁ and C₂ hydrocarbons are the fundamental ingredient for building up more complex hydrocarbons, e.g., benzene and polycyclic aromatic hydrocarbons (PAHs), through long chain polyynes and polymerization. The chemical pathways among the C₁ and C₂ compounds in the atmospheres of CEGPs were first pointed out by *Liang et al.* [2003], and are fundamentally different from the pathways on the colder Jovian planets [*Gladstone et al.*, 1996]. The full version of the hydrocarbon photochemical model is also verified. The oxygen related photochemistry is taken from *Moses et al.* [2000].

Figure 10.1 shows the temperature profiles for our three models [*Seager and Sasselov*, 2000; *Barman et al.*, 2002; *Fortney et al.*, 2003]. For each case, we have examined five different initial chemical abundances for CH₄, CO, and H₂O as tabulated in Table 10.1. Due to the unconstrained CH₄ abundance, we have varied it by several orders of magnitudes to study its sensitivity in the formation of hydrocarbons. However, we expect CO to be the dominant reservoir of carbon for the range of temperatures in the atmospheres of CEGPs and assume this in our reference model A. The models of *Barman et al.* [2002] and *Fortney et al.* [2003] go only to 1 and 0.1 μbar pressure levels, respectively; and, we assume the profiles

are isothermal above these pressure levels. The parameters for the reference eddy-diffusion profile ($\kappa = \kappa_0(n/n_0)^{-\alpha}$, where n is number density) are taken to be $\kappa_0 = 2.4 \times 10^7 \text{ cm}^2 \text{ s}^{-1}$, $n_0 \approx 6 \times 10^{18} \text{ cm}^{-3}$, and $\alpha = 0.56$. We also varied κ_0 and α to test the sensitivity of the results on eddy-diffusion (see Table 10.2). The fiducial eddy-diffusion used here is consistent with the upper limit estimates from *Showman and Guillot* [2002].

10.3 Results

Our modeling shows that gas phase hydrocarbons are most likely present in very low abundances in the atmospheres of CEGPs. This result is in contrast to the high abundances of hydrocarbons on the solar Jovian planets. The major pathways of forming C_1 and C_2 hydrocarbons are given in Figure 10.2. The vertical profiles of the three main hydrocarbons for various models are shown in Figure 10.3 and the maximum and column integrated hydrocarbons are tabulated in Table 10.2. The hydrocarbons are produced and concentrated mainly in the middle atmosphere, around 0.1 mbar. Because the framework of hydrocarbon formation on the Jovian planets is well understood, we explain our results in comparison to the photochemical production of hydrocarbons on the Jovian planets.

There are two known chemical schemes for the formation of hydrocarbons in the Jovian atmospheres and their satellites. The first is via the synthesis of long chain polyynes from C_2H_2 [*Allen et al.*, 1980]. The second is the polymerization of C_2H_2 to form ring compounds [*Wong et al.*, 2000]. In both cases, C_2H_2 plays a crucial role. Therefore, to explain why hydrocarbon aerosols are not formed in CEGPs, we have to explain why C_2H_2 concentrations are so low. This is due primarily to the high temperatures in the atmospheres of CEGPs and secondarily to the high UV flux. Both the high temperatures and high UV fluxes are

a direct consequence of the CEGPs' closer proximity to their parent stars.

One reason for low hydrocarbon abundances in CEGPs is because the abundance of CH_4 is many orders of magnitudes lower than that in the Jovian atmospheres. The CH_4 abundance is important because in the Jovian atmospheres hydrocarbon formation is driven by the photodissociation of CH_4 and the subsequent reactions of the products [e.g., *Gladstone et al.*, 1996]. The three species, C_2H_2 , C_2H_4 , and C_2H_6 , are important for forming more complex hydrocarbons and hydrocarbon aerosols. The primary reservoir of C in CEGPs is CO, not CH_4 as in the Jovian planets. This is due to the much higher temperatures in the atmospheres of CEGPs (effective temperatures $\gtrsim 1000$ K) compared to Jupiter (effective temperature ~ 130 K). *Liang et al.* [2003] showed that C compounds are initiated by C atoms produced by the photolysis of CO in the upper atmosphere. The hydrocarbons (C_2H_2 , C_2H_4 , and C_2H_6) are formed along with CH_4 from the C atoms.

A second reason for the low abundance of hydrocarbons is that hydrogenation of C_2H_2 to CH_4 by the pathways given in *Liang et al.* [2003] (see also Chapter 5 of *Yung and DeMore* [1999]) rapidly removes C_2H_2 . As pointed out by *Liang et al.* [2003], the CEGPs have a high concentration of H atoms formed via an H_2O -mediated process. Hydrogenation is the dominant removal process of C_2H_2 in CEGPs and is driven by the high concentration of H atoms. Unlike the colder Jovian atmospheres, the hydrocarbon loss via photolysis is minor in the atmospheres of CEGPs. A key reaction in the hydrogenation of C_2H_2 to CH_4 is the reaction $\text{C}_2\text{H}_3 + \text{H}_2 \rightarrow \text{C}_2\text{H}_4 + \text{H}$. The reaction that breaks the H_2 bond is fast for the high temperatures in the atmospheres of CEGPs; however, in the colder atmospheres of the Jovian planets this reaction is the major bottleneck to hydrogenation of C_2H_2 . Hydrogenation as a cause of low hydrocarbon abundances is therefore related to the high temperatures in the atmospheres of CEGPs which are hot enough not only for the

rapid hydrogenation rate but also for H₂O to be present in vapor form. In contrast to the Jovian planets and their satellites, water is frozen into ice at about 1 bar and not available for photolysis.

To show the robustness of the result of low hydrocarbon abundances in the atmospheres of CEGPs, we varied the input parameters to our photochemical model. We find that over a broad range of input parameters, i.e., initial chemical abundances and temperature and eddy-diffusion profiles, the hydrocarbon formation in the atmospheres of CEGPs never exceeds that of Jupiter. In our model with extremely abundant CH₄ (model E), the column integrated hydrocarbon abundance is about 0.5 that of Jupiter's (see Table 10.2). However, this is an extreme and highly unlikely CH₄ abundance—the hot atmospheric temperatures favor CO as the dominant reservoir of C.

10.4 Discussion

Using a simplified version of the Caltech/JPL KINETICS model, we have shown that the concentrations of the C₂H_{2n} species (see Table 10.2) are insignificant in the atmospheres of CEGPs. These C₂H_{2n} compounds are important sources for forming more complex C_xH_y species, such as benzene and PAHs, which will lead to the formation of hydrocarbon aerosols [e.g., *Richter and Howard*, 2000, 2002]. Although we have used a simplified photochemical model that captures the main reactions, we have tested models A-E using the reference temperature profile (solid-line in Figure 10.1), incorporating the full version of hydrocarbon model by *Gladstone et al.* [1996]. Even for this case, we find that the C₆H₆ abundance for model A is seven orders of magnitudes less than that of Jupiter and is two orders of magnitudes less for model E. Sulfur and nitrogen containing compounds are other potential

sources for aerosols and we plan to explore their photochemistry in a later paper.

The CEGPs are extremely close to the parent star; in such an extreme environment, the C_xH_y compounds will be lost either primarily by reactions with atomic hydrogen or also by photolysis. The production of atomic hydrogen is a consequence both of the high temperatures that allow the presence of H_2O vapor and of the high UV flux that causes the photolysis of H_2O . Therefore, the lifetime of the C_xH_y compounds in the atmospheres of CEGPs is predicted to be much shorter than that on Jupiter. Specifically, the lifetimes of the hydrocarbons are $\lesssim 10^3$ s, which are significantly shorter than the simulated circulation timescale of \sim one day [*Showman and Guillot, 2002; Cho et al., 2003*]. Hence the abundances of the hydrocarbons will be affected by a factor of “a few” through the relatively longer lifetime of the atomic hydrogen [\sim 1 day, *Liang et al., 2003*].

The condensation temperatures for hydrocarbons (e.g., C_4H_2 and C_4H_{10}) are below 200 K at \sim 1 mbar [*Moses et al., 2000*]. These temperatures are far colder than expected in the atmospheres of CEGPs [*Seager and Sasselov, 2000; Barman et al., 2002; Fortney et al., 2003*]. Nevertheless, we verified this by considering the saturation profiles together with the temperature profiles and found that the required saturation pressure for CEGPs is far more than that present in the atmospheres of CEGPs.

Using the measured Rayleigh scattering cross sections of He and H_2 [*Chan and Dalgarno, 1965; Ford and Browne, 1973*], the pressure level with optical depth unity is \sim 1 bar at 300 nm and increases rapidly at longer wavelengths (Rayleigh scattering cross section $\propto \lambda^{-4}$). Without the shielding from the atmospheric aerosols and in the absence of high-temperature condensate clouds, we may be able to observe the atmospheric composition at short wavelengths up to the Rayleigh scattering limit.

In this chapter, we have emphasized photolytically driven processes involving neutral

species. We have not considered the possibility of ion-neutral chemistry, such as that found in the polar region of Jupiter [*Wong et al.*, 2003]. This may be important in the atmospheres of CEGPs if the planet possesses a magnetic field. If the hydrocarbon aerosols can be formed in the polar region, then global circulation will redistribute them to lower latitudes. Stellar wind may be another source of energetic charged particles that could result in the formation of aerosols. Another subject not addressed in this work is the formation of aerosols by heterogeneous nucleation in the presence of pre-existing solid dust grains. In this case, the formation of aerosols would be sensitive to the amount of dust particles in the atmosphere.

Additionally, we find that the mixing ratios of C, O, S, and C₂H₂ (other than H) are high at the top of the atmosphere, implying that these particles can readily escape. The recent tentative detection of C and O in the extended upper atmosphere of HD 209458b by *Vidal-Madjar et al.* [2004] supports this assertion and we comment that hydrodynamically escaping atmospheric species will yield new information on the evolution of CEGPs.

Bibliography

- Allen, M., Pinto, J. P., Yung, Y. L., Titan - Aerosol Photochemistry and Variations Related to the Sunspot Cycle, *Astrophysical Journal Letters*, *242*, L125-128, 1980.
- Banfield, D., Conrath, B. J., Gierasch, P. J., Nicholson, P. D., Matthews, K., Near-IR Spectrophotometry of Jovian Aerosols-Meridional and Vertical Distributions, *Icarus*, *134*, 11-23, 1998a.
- Banfield, D., Gierasch, P. J., Bell, M., Ustinov, E., Ingersoll, A. P., Vasavada, A. R., West, R. A., Belton, M. J. S., Jupiter's Cloud Structure from Galileo Imaging Data, *Icarus*, *135*, 230-250, 1998b
- Baraffe, I., Chabrier, G., Barman, T. S., Allard, F., and Hauschildt, P. H., Evolutionary Models for Cool Brown Dwarfs and Extrasolar Giant Planets. The Case of HD 209458, *Astronomy and Astrophysics*, *402*, 701-712, 2003.
- Barman, T. S., Hauschildt, P. H., Schweitzer, A., Stancil, P. C., Baron, E., Allard, F., Non-LTE Effects of Na I in the Atmosphere of HD 209458b, *Astrophysical Journal Letters*, *569*, L51-54, 2002.
- Butler, R. P., Marcy, G. W., Vogt, S. S., Fischer, D. A., Henry, G. W., Laughlin, G., Wright, J. T., Seven New Keck Planets Orbiting G and K Dwarfs, *Astrophysical Journal*, *582*, 455-466, 2003.

- Chan, Y. M., Dalgarno, A., The Refractive Index of Helium, *Proc. Phys. Soc.*, 85, 227-230, 1965.
- Cho, J. Y.-K., Menou, K., Hansen, B. M. S., Seager, S., The Changing Face of the Extrasolar Giant Planet HD 209458b, *Astrophysical Journal Letters*, 587, L117-120, 2003.
- Fischer, D. A., Marcy, G. W., Butler, R. P., Laughlin, G., Vogt, S. S., A Second Planet Orbiting 47 Ursae Majoris, *Astrophysical Journal*, 564, 1028-1034, 2002.
- Ford, A. L., Browne, J. C., Rayleigh and Raman Cross Sections for the Hydrogen Molecule, *Atomic Data*, 5, 305-313, 1973.
- Fortney, J. J., Sudarsky, D., Hubeny, I., Cooper, C. S., Hubbard, W. B., Burrows, A., Lunine, J. I., On the Indirect Detection of Sodium in the Atmosphere of the Planetary Companion to HD 209458, *Astrophysical Journal Letters*, 589, L615-622, 2003.
- Gladstone, G. R., Allen, M., Yung, Y. L., Hydrocarbon Photochemistry in the Upper Atmosphere of Jupiter, *Icarus*, 119, 1-52, 1996.
- Karkoschka, E., Methane, Ammonia, and Temperature Measurements of the Jovian Planets and Titan from CCD-Spectrophotometry, *Icarus*, 133, 134-146, 1998.
- Karkoschka, E., Tomasko, M. G., Saturn's Upper Atmospheric Hazes Observed by the Hubble Space Telescope, *Icarus*, 106, 428-441, 1993.
- Liang, M. C., Parkinson, C. D., Lee, A. Y.-T., Yung, Y. L., Seager, S., Source of Atomic Hydrogen in the Atmosphere of HD 209458b, *Astrophysical Journal Letters*, 596, L247-250, 2003.

- Moses, J. I., Lellouch, E., Bézard, B., Gladstone, G. R., Feuchtgruber, H., Allen, M.,
Photochemistry of Saturn's Atmosphere. II. Effects of an Influx of External Oxygen,
Icarus, *145*, 166-202, 2000.
- Pryor, W. R., Hord, C. W., A Study of Photopolarimeter System UV Absorption Data on
Jupiter, Saturn, Uranus, and Neptune - Implications for Auroral Haze Formation, *Icarus*,
91, 161-172, 1991.
- Richter, H., Howard, J. B., Formation of Polycyclic Aromatic Hydrocarbons and Their
Growth to Soot: A Review of Chemical Reaction Pathways, *Progress in Energy and
Combustion Science*, *26*, 565-608, 2000.
- Richter, H., Howard, J. B., Formation and Consumption of Single-Ring Aromatic Hydrocar-
bons and their Precursors in Premixed Acetylene, Ethylene and Benzene Flames, *Phys.
Chem. Chem. Phys.*, *4*, 2038-2055, 2002.
- Santos, N. C., Israelian, G., Mayor, M., Rebolo, R., Udry, S., Statistical Properties of
Exoplanets. II. Metallicity, Orbital Parameters, and Space Velocities, *Astronomy and
Astrophysics*, *398*, 363-376, 2003.
- Seager, S., & Sasselov, D. D., Theoretical Transmission Spectra during Extrasolar Giant
Planet Transits, *Astrophysical Journal*, *537*, 916-921, 2000.
- Seager, S., Whitney, B. A., Sasselov, D. D., Photometric Light Curves and Polarization of
Close-in Extrasolar Giant Planets, *Astrophysical Journal*, *540*, 504-520, 2000.
- Showman, A. P., Guillot, T., Atmospheric circulation and tides of "51 Pegasus b-like"
planets, *Astronomy and Astrophysics*, *385*, 166-180, 2002.

- Strobel, D., The Photochemistry of Hydrocarbons in the Jovian Atmosphere, *Journal of the Atmospheric Sciences*, 30, 489-498, 1973.
- Sudarsky, D., Burrows, A., & Pinto, P., Albedo and Reflection Spectra of Extrasolar Giant Planets, *Astrophysical Journal*, 538, 885-903, 2000.
- Udry, S., Mayor, M., Naef, D., Pepe, F., Queloz, D., Santos, N. C., Burnet, M., The CORALIE Survey for Southern Extra-solar Planets. VIII. The Very Low-mass Companions of HD 141937, HD 162020, HD 168443 and HD 202206: Brown Dwarfs or “Superplanets”?, *Astronomy and Astrophysics*, 390, 267-279, 2002.
- Vidal-Madjar, A., des Etangs, A. Lecavelier, Desert, J.-M., Ballester, G. E., Ferlet, R., Hebrard, G., Mayor, M., An Extended Upper Atmosphere around the Extrasolar Planet HD209458b, *Nature*, 422, 143-146, 2003.
- Vidal-Madjar, A., Desert, J.-M., Lecavelier des Etangs, A., Hebrard, G., Ballester, G. E., Ehrenreich, D., Ferlet, R., McConnell, J. C., Mayor, M., Parkinson, C. D., Detection of Oxygen and Carbon in the Hydrodynamically Escaping Atmosphere of the Extrasolar Planet HD 209458b, *Astrophysical Journal Letters*, 604, L69-72, 2004.
- Weidenschilling, S. J., Lewis, J. S., Atmospheric and Cloud Structures of the Jovian Planets, *Icarus*, 20, 465-476, 1973.
- West, R. A., Strobel, D. F., Tomasko, M. G., Clouds, Aerosols, and Photochemistry in the Jovian Atmosphere, *Icarus*, 65, 161-217, 1986.
- Wong, A.-S., Lee, A. Y.-T., Yung, Y. L., Ajello, J. M., Jupiter: Aerosol Chemistry in the Polar Atmosphere, *Astrophysical Journal Letters*, 534, L215-217, 2000.

Wong, A.-S., Yung, Y. L., Friedson, A. J., Benzene and Haze Formation in the Polar Atmosphere of Jupiter, *Geophysics Research Letters*, 30(8), 1447, doi:10.1029/2002GL016661, 2003.

Yung, Y. L., DeMore, W. B. 1999, Photochemistry of Planetary Atmospheres (New York: Oxford Uni. Press)

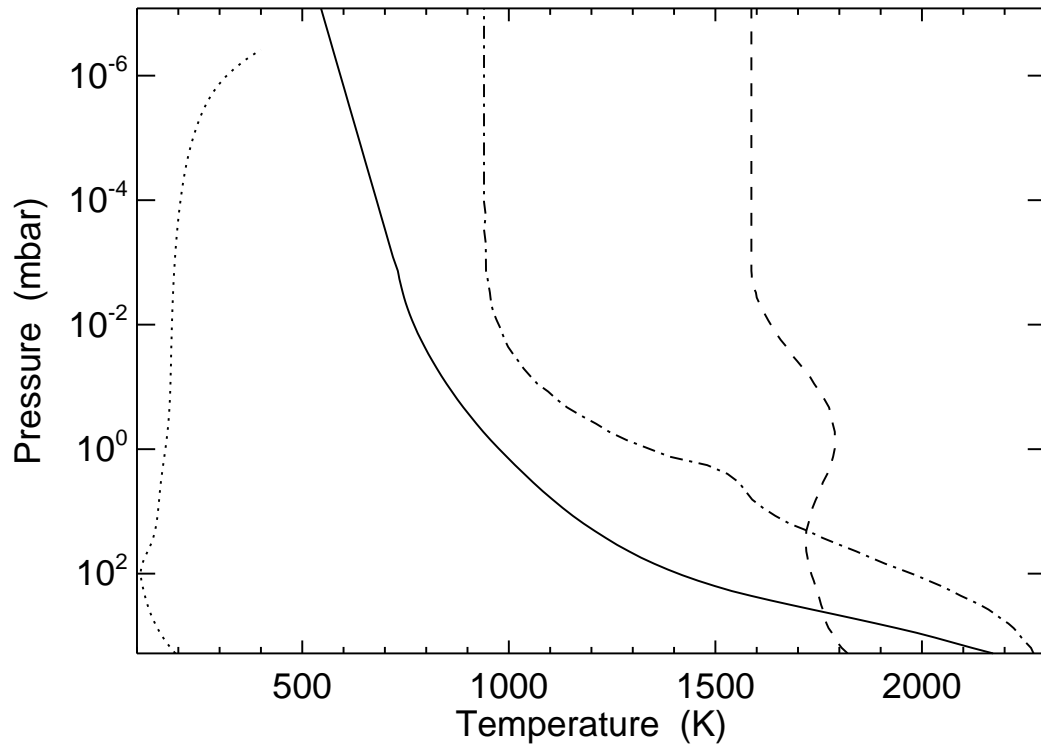


Figure 10.1 HD 209458b—Vertical temperature profiles of the reference model (solid line), *Barman et al.* [2002, dashed line], *Fortney et al.* [2003, dash-dotted], and Jupiter (dotted line). We assume the profiles of *Barman et al.* [2002] and *Fortney et al.* [2003] are isothermal above their reported pressure levels.

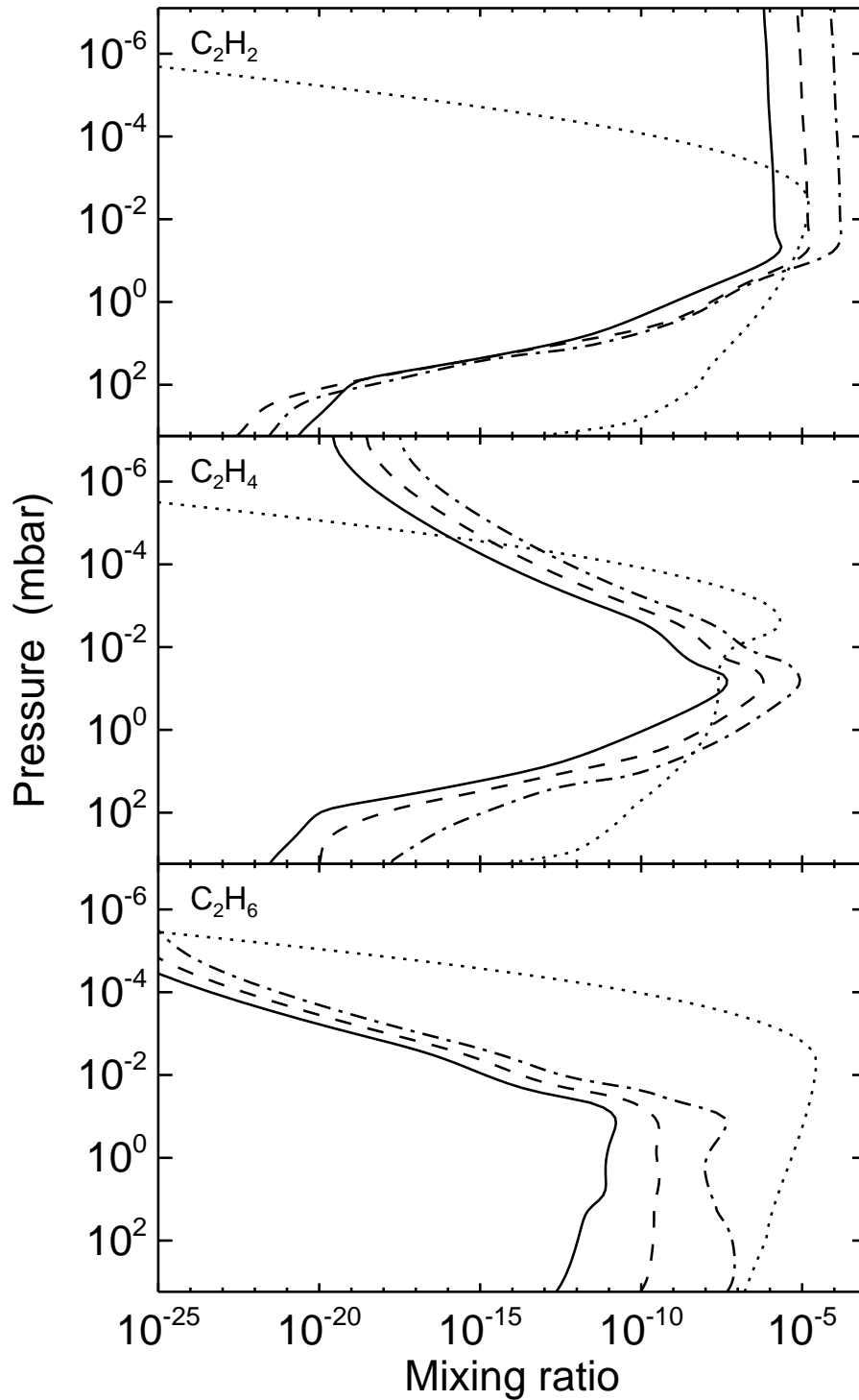


Figure 10.3 HD 209458b—Comparison of volume mixing ratios of C_2H_2 (upper panel), C_2H_4 (middle panel), and C_2H_6 (lower panel) for models A, D, E, and Jupiter (solid, dashed, dash-dotted, and dotted lines, respectively). The high C_2H_2 mixing ratio at the top of the atmosphere is due to the high photolysis rate of CO.

Table 10.1. HD 209458b—Initial Chemical Abundances of CH₄, CO, and H₂O for Models A-E.

Model	CH ₄	CO	H ₂ O
A	3.9×10^{-8}	3.6×10^{-4}	4.5×10^{-4}
B	3.9×10^{-8}	3.6×10^{-4}	4.5×10^{-5}
C	3.9×10^{-8}	3.6×10^{-5}	4.5×10^{-4}
D	3.9×10^{-5}	3.6×10^{-4}	4.5×10^{-4}
E	3.6×10^{-4}	3.6×10^{-4}	4.5×10^{-4}

Table 10.2. HD 209458b—Mixing Ratios of CH₄, C₂H₂, C₂H₄, and C₂H₆ for Models A-E at 0.1 mbar. Jupiter’s Results at 2 μ bar are Included for Comparison.

Model ^a	CH ₄	C ₂ H ₂	C ₂ H ₄	C ₂ H ₆	Total ^b
Jupiter	1×10^{-3}	1×10^{-5}	3×10^{-8}	2×10^{-5}	1
A 1	3×10^{-6}	8×10^{-7}	3×10^{-8}	2×10^{-11}	7×10^{-4}
^d A 1	2×10^{-6}	6×10^{-7}	3×10^{-8}	1×10^{-11}	7×10^{-4}
^e A 1	4×10^{-6}	9×10^{-7}	4×10^{-8}	2×10^{-11}	1×10^{-3}
^f A 1	5×10^{-7}	1×10^{-7}	4×10^{-9}	1×10^{-12}	1×10^{-4}
B 1	9×10^{-6}	2×10^{-6}	1×10^{-7}	6×10^{-11}	2×10^{-3}
C 1	5×10^{-7}	1×10^{-7}	4×10^{-9}	1×10^{-12}	7×10^{-5}
D 1	3×10^{-5}	5×10^{-6}	5×10^{-7}	3×10^{-10}	7×10^{-3}
E 1	3×10^{-4}	2×10^{-5}	6×10^{-6}	4×10^{-8}	0.4
E 2	2×10^{-4}	9×10^{-6}	1×10^{-5}	1×10^{-9}	0.3
E 3	4×10^{-4}	2×10^{-5}	1×10^{-5}	9×10^{-9}	0.6

Note. — The hydrocarbons have maximum mixing ratios at about 0.1 mbar in the atmosphere of HD 209458b, while on Jupiter the maxima are at about 2 μ bar (see Figure 10.3).

^a1: reference temperature profile (Seager & Sasselov, 2000). 2: Barman et al. (2002) temperature profile. 3: Fortney et al. (2003) temperature profile.

^bTotal: column integrated abundances of hydrocarbons (C₂H₂ + C₂H₄ + C₂H₆) at < 2 bar. The abundance is normalized to 2×10^{-7} which is the value calculated in the atmosphere of Jupiter (e.g., Gladstone et al. 1996).

^dExponent of eddy-diffusion is taken to be 0.65.

^eEddy-diffusion is a factor of two smaller than the reference eddy-diffusion.

^fEddy-diffusion is a factor of ten greater than the reference eddy-diffusion.